Title

Underlying Mechanisms of Vascular Disease in Hutchinson-Gilford Progeria Syndrome

Author

Kim, Paul

Publication Date

2024

Peer reviewed|Thesis/dissertation

UNIVERSITY OF CALIFORNIA

Los Angeles

Underlying Mechanisms of Vascular Disease in Hutchinson-Gilford Progeria Syndrome

A dissertation submitted in partial satisfaction

of the requirements for the degree Doctor of Philosophy

in Bioengineering

by

Paul Kim

2024

ABSTRACT OF THE DISSERTATION

Underlying Mechanisms of Vascular Disease in
Hutchinson-Gilford Progeria Syndrome

by

Paul Kim

Doctor of Philosophy in Bioengineering

University of California, Los Angeles, 2024

Professor Loren G. Fong, Co-Chair

Professor Dino Di Carlo, Co-Chair

Children with Hutchinson-Gilford progeria syndrome (HGPS) display symptoms resembling accelerated aging, with most succumbing in their mid-teens to complications from arteriosclerotic lesions in major arteries. HGPS arises from a *de novo* mutation in the *LMNA* gene, such as the Gly608Gly mutation, which creates an aberrant splice donor site, resulting in a deletion of 50 amino acids in prelamin A and the production of mutant protein called progerin. Progerin, unlike mature lamin A, retains a farnesyl lipid anchor, which contributes to cellular toxicity. In HGPS, a prominent vascular anomaly is reduced numbers of smooth muscle cells (SMCs) in the medial layer of large arteries, promoting arteriosclerotic disease. In order to study the underlying mechanisms of vascular disease in HGPS, we created a mouse model of HGPS ($Lmna^{G609G}$) which exhibits disease phenotypes reminiscent of human HGPS, including the hallmark vascular disease. We also created an *in vitro* doxycycline-inducible cell culture system to investigate properties of progerin by studying the effects of progerin on the nuclear lamina meshwork, nuclear mechanics,

integrity of the nuclear envelope, their relationship to nuclear morphology, DNA damage, and cell viability.

In this dissertation, my goal was to understand the mechanisms underlying vascular pathology in HGPS, focusing on the interactions between progerin, lamin B1, and the integrity of the nuclear lamina meshwork in vascular SMCs. In Chapter 2, we investigated the role of mechanical stress on the vascular disease and showed that disrupting the LINC complex in smooth muscle cells reduces SMC loss in *Lmna*^{G609G} mice. In Chapter 3, we hypothesized that progerin weakens the structural integrity of the nuclear envelope. Indeed, we showed that progerin resulted in nuclear membrane ruptures and found that it was responsible for vascular pathology *in vivo*. In Chapter 4, we investigated a more fundamental question—how does progerin induce abnormal biological effects in cells? We discovered that progerin forms an abnormal meshwork, characterized by clusters of large meshwork gaps. Unexpectedly, progerin had a dominant-negative effect on the nuclear lamina, thus further disrupting nuclear integrity. In Chapter 5, I summarize our key findings and discuss our current view on the mechanisms of vascular smooth muscle cell loss in HGPS.

The dissertation of Paul Kim is approved.

Amy C. Rowat

Stephen G. Young

Dino Di Carlo, Committee Co-Chair

Loren G. Fong, Committee Co-Chair

University of California, Los Angeles

2024

Table of Contents

List of Figures

Acknowledgements

I am profoundly grateful for the support and guidance of many individuals who have made my journey towards completing this PhD not only possible but also a rewarding experience. Among them, I want to give special thanks to Dr. Loren Fong and Dr. Stephen Young, whose insights and expertise have been invaluable throughout my research. I would also like to thank Dr. Dino Di Carlo and Dr. Amy Rowat for their mentoring and support.

Additionally, I extend my gratitude to all the former and current members of the lab. I feel incredibly fortunate to have worked alongside such wonderful individuals who not only contributed to my scientific growth but also made my days in the lab enjoyable. The daily interactions, the shared challenges, and the collective triumphs have enriched this journey immeasurably.

Lastly, I want to thank the UCLA Vascular Biology Training Grant (Ruth L. Kirschstein National Research Service Award T32HL069766) for their financial support and mentoring during my graduate studies.

Chapter 2 is a reprint of Kim PH, Luu J, Heizer P, Tu Y, Weston TA, Chen N, Lim C, Li RL, Lin PY, Dunn JCY, Hodzic D, Young SG, Fong LG, "Disrupting the LINC complex in smooth muscle cells reduces aortic disease in a mouse model of Hutchinson-Gilford progeria syndrome" from *Science Translational Medicine*. 2018 Sep 26;10(460) [doi: 10.1126/scitranslmed.aat7163]. Chapter 3 is a reprint of Kim PH, Chen NY, Heizer PJ, Tu Y, Weston TA, Fong JL, Gill NK, Rowat AC, Young SG, Fong LG, "Nuclear membrane ruptures underlie the vascular pathology in a mouse model of Hutchinson-Gilford progeria syndrome" *JCI Insight*. 2021 Aug 23;6(16) [doi: 10.1172/jci.insight.151515]. Chapter 4 is adapted from a manuscript in press Kim PH, Kim JR, Tu Y, Jung H, Jeong JY, Tran AP, Presnell A, Young SG, Fong LG, "Progerin Forms an Abnormal

Meshwork and Has a Dominant-negative Effect on the Nuclear Lamina" *Proc. Natl. Acad. Sci USA*. 2024. All the reprints used in this dissertation do not require a special permission from publishers with proper acknowledgements of the original sources of publication as an author of the articles.

VITA

University of California, Los Angeles **09/2019–06/2022**

Los Angeles, CA

Master of Science in Bioengineering

College of William and Mary **09/2005–06/2009**

Williamsburg, VA

Bachelor of Science in Molecular Biology and Architectural Art

Selected Publications

1. **Kim PH**, Kim JR, Tu Y, Jung H, Jeong JY, Tran AP, Presnell A, Young SG, Fong LG. Progerin forms abnormal meshwork and has a dominant-negative effect on the nuclear lamina. *Proc. Natl. Acad. Sci USA*. 2024. *In press.*
2. Kim JR, **Kim PH**, Presnell A, Tu Y, Young SG. Revisiting the truncated lamin A produced by a commonly used strain of Lmna knockout mice. *Nucleus*. 2023 Dec;14(1).
3. Yang Y, Beigneux AP, Song W, Nguyen LP, Jung H, Tu Y, Weston TA, Tran CM, Xie K, Yu RG, Tran AP, Miyashita K, Nakajima K, Murakami M, Chen YQ, Zhen EY, Kim JR, **Kim PH**, Birrane G, Tontonoz P, Ploug M, Konrad RJ, Fong LG, Young SG. Hypertriglyceridemia in Apoa5-/- mice results from reduced amounts of lipoprotein lipase in the capillary lumen. *J Clin Invest*. 2023 Dec 1;133(23).
4. **Kim PH**, Chen NY, Heizer PJ, Tu Y, Weston TA, Fong JL, Gill NK, Rowat AC, Young SG, Fong LG. Nuclear membrane ruptures underlie the vascular pathology in a mouse model of Hutchinson-Gilford progeria syndrome. *JCI Insight*. 2021 Aug 23;6(16).

5. Chen NY, **Kim PH**, Tu Y, Yang Y, Heizer PJ, Young SG, Fong LG. Increased expression of LAP2β eliminates nuclear membrane ruptures in nuclear lamin-deficient neurons and fibroblasts. *Proc. Natl. Acad. Sci USA*. 2021 Jun 22;118(25).
6. Chen NY, **Kim PH**, Fong LG, Young SG. Nuclear membrane ruptures, cell death, and tissue damage in the setting of nuclear lamin deficiencies. *Nucleus*. 2020 Dec;11(1):237-249.
7. Chen NY, Yang Y, Weston TA, Belling JN, Heizer P, Tu Y, **Kim P**, Edillo L, Jonas SJ, Weiss PS, Fong LG, Young SG. An absence of lamin B1 in migrating neurons causes nuclear membrane ruptures and cell death. *Proc. Natl. Acad. Sci USA*. 2019 Dec 17;116(51):25870-25879.
8. Gill NK, Ly C, **Kim PH**, Saunders CA, Fong LG, Young SG, Luxton GWG, Rowat AC. DYT1 Dystonia Patient-Derived Fibroblasts Have Increased Deformability and Susceptibility to Damage by Mechanical Forces. *Front Cell Dev Biol*. 2019;7:103.
9. Chen NY, **Kim P**, Weston TA, Edillo L, Tu Y, Fong LG, Young SG. Fibroblasts lacking nuclear lamins do not have nuclear blebs or protrusions but nevertheless have frequent nuclear membrane ruptures. *Proc. Natl. Acad. Sci USA*. 2018 Oct 2;115(40):10100-10105.
10. **Kim PH**, Luu J, Heizer P, Tu Y, Weston TA, Chen N, Lim C, Li RL, Lin PY, Dunn JCY, Hodzic D, Young SG, Fong LG. Disrupting the LINC complex in smooth muscle cells reduces aortic disease in a mouse model of Hutchinson-Gilford progeria syndrome. *Science Translational Medicine*. 2018 Sep 26;10(460).

Chapter 1:

Introduction

Nuclear Lamina

The nuclear lamina is an intricate meshwork of intermediate filament proteins located beneath the inner nuclear membrane, playing a vital role in maintaining the structural integrity and functionality of the nucleus in eukaryotic cells (Figure 1.1). First identified in the late 1970s, the nuclear lamina has since been recognized as a fundamental component in a range of cellular processes including chromatin organization, DNA replication, and the regulation of gene expression (R. D. Goldman, Gruenbaum, Moir, Shumaker, & Spann, 2002).

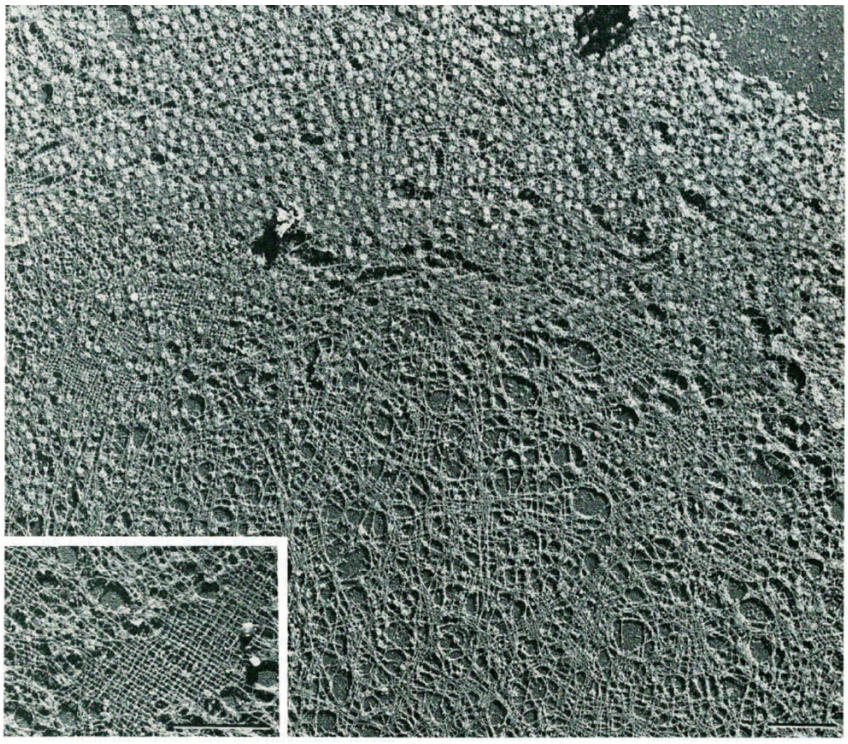

Figure 1.1. Electron microscopy image of *Xenopus* oocyte. Image reveals the nuclear lamina meshwork of *Xenopus* oocytes prepared by free-dried/metal-shadow method. Insert visualizes a well-preserved area of the meshwork with nuclear pore complexes mechanically removed showing two sets of near-orthogonal filaments. The figure adapted from (Aebi, Cohn, Buhle, & Gerace, 1986)

Molecular Composition and Structure

The nuclear lamina is primarily composed of nuclear lamins. Nuclear lamins are type V intermediate filament proteins, primarily classified into A-type and B-type lamins based on their biochemical properties and expression patterns (Lin & Worman, 1993). A-type lamins, comprising lamins A and C—splice variants produced from the *LMNA* gene—are predominantly expressed in differentiated cells and are essential for cellular responses to mechanical stimuli (Burke & Stewart, 2013). B-type lamins, which include lamins B1 and B2—encoded by *LMNB1* and *LMNB2*—are expressed ubiquitously and are crucial from early embryonic development through to adulthood (Harborth, Elbashir, Bechert, Tuschl, & Weber, 2001).

The nuclear lamins form a fibrous network that interfaces with both chromatin and the inner nuclear membrane, providing mechanical support and regulating nuclear size and shape (Fawcett, 1966). This network is dynamically reorganized during the cell cycle; it disassembles during mitosis and reassembles in the daughter cells, a process regulated by phosphorylation through cell cycle-dependent kinases (Gerace & Blobel, 1980).

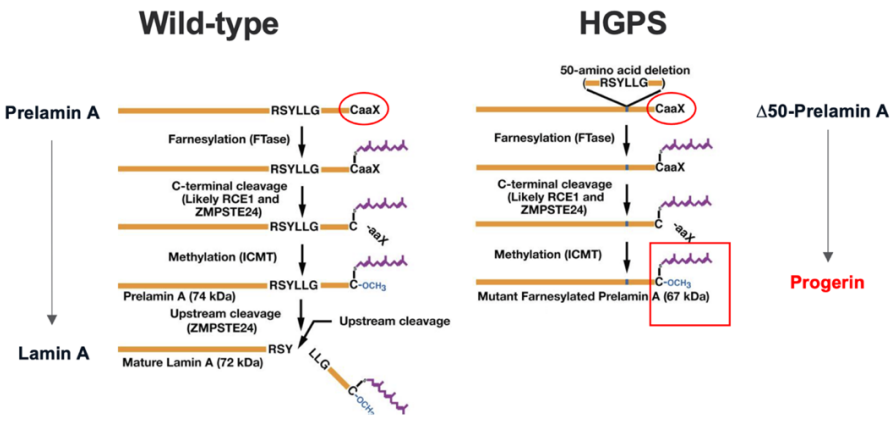

Figure 1.2. A schematic diagram showing lamin A and progerin processing. Prelamin A, which consists of 664 amino acids, typically undergoes four post-translational modifications in wild-type

cells (left panel). Initially, the cysteine in the CaaX motif is farnesylated by farnesyltransferase (FTase). Next, the -aaX amino acids are cleaved off. Following this, the now exposed farnesylcysteine is methylated. Finally, ZMPSTE24 cleaves and degrades the terminal 15 amino acids, including the farnesylcysteine methyl ester, resulting in the production of mature lamin A, comprising 646 amino acids. In the context of Hutchinson-Gilford progeria syndrome (HGPS) (right panel), a point mutation leads to the deletion of 50 amino acids in prelamin A (amino acids 607–656), eliminating the site for the terminal ZMPSTE24-mediated endoproteolytic cleavage. As a result, the farnesylated mutant prelamin A, known as progerin, accumulates within the cells, preventing the formation of mature lamin A. The figure adapted with permission from (S. G. Young, L. G. Fong, & S. Michaelis, 2005).

Biological Functions and Significance

Beyond their main role of structural support for the nucleus, nuclear lamins are involved in various fundamental biological processes, including DNA repair, replication, and the regulation of gene expression through their interaction with chromatin and transcription factors (Reddy et al., 2008). For instance, lamin A/C interacts with specific gene regions, influencing the organization of heterochromatin and thus playing a direct role in the silencing or activation of gene expression (Shumaker et al., 2006). The importance of lamins is further highlighted in the context of laminopathies, a diverse group of genetic disorders caused by mutations in the lamin genes. These include diseases such as Emery-Dreifuss muscular dystrophy, familial partial lipodystrophy, and Hutchinson-Gilford progeria syndrome, each characterized by defects in tissue integrity and cellular function that reflect the mechanical and regulatory roles of lamins (Worman & Bonne, 2007). The study of HGPS has particularly illuminated the role of A-type lamins in aging and cellular senescence. Progerin's incorporation into the nuclear lamina causes significant alterations

in nuclear architecture, which contributes to the premature aging phenotype observed in HGPS patients (M Eriksson et al., 2003). Research in this area not only deepens our understanding of premature aging but also sheds light on the processes of normal aging (R D Goldman et al., 2004).

Pathogenesis of SMC Loss in HGPS

Hutchinson-Gilford progeria syndrome is marked by premature aging and severe cardiovascular complications, predominantly atherosclerosis, which manifest much earlier than in the general population. One of the central features of cardiovascular disease in HGPS is the progressive loss of smooth muscle cells in the vascular media, which is hypothesized to underlie the accelerated development of atherosclerosis in HGPS (Varga et al., 2006). In HGPS, the loss of vascular SMCs is attributed to the deleterious effects of the mutant lamin A protein, progerin. This mutant protein induces multiple cellular defects including disrupted nuclear morphology, impaired mechanical stability, and altered gene expression (Capell et al., 2005; Kim et al., 2018a). SMCs in the arterial wall are particularly susceptible to these disruptions, resulting in SMC death, which compromises their ability to contract and respond to vascular stress (Hamczyk et al., 2019). Research has shown that progerin expression leads to increased DNA damage, disruption of tissue repair mechanisms, and enhanced senescence and apoptosis of vascular SMCs (Varga et al., 2006). The reduction in SMCs results in weakening of the arterial wall, decreased elasticity, and increased fibrosis, which in turn facilitates the early onset and rapid progression of atherosclerotic lesions.

Recently, researchers from South Korea discovered a novel compound called Progerinin, which has been shown to reduce progerin expression and improve the loss of vascular smooth muscle cells in both *in vitro* and *in vivo* HGPS models. Subsequently, they found significant improvements in cardiac parameters such as stroke volume, ejection fraction, and fractional shortening in Progerinin-treated *Lmna*$^{G606G/+}$ mice. Their studies further highlighted the significant

correlation between the health of vascular smooth muscle cells and cardiovascular disease (Kang et al., 2023).

From a different perspective, the Cao group explored the influence of progerin on endothelial cells and its role in cardiovascular disease in HGPS patients. They developed 3D tissue-engineered blood vessels (viTEBVs) using induced pluripotent stem cell–derived smooth muscle cells (viSMCs) and endothelial cells (viECs) from HGPS patients. These tissue-engineered blood vessels, containing HGPS cells, exhibited markers of cardiovascular disease associated with the endothelium and showed a decrease in vasoconstriction and vasodilation. Notably, viTEBVs with HGPS viECs and healthy viSMCs only showed reduced vasodilation. Furthermore, viTEBVs composed of HGPS endothelial cells, regardless of whether the viSMCs were healthy or HGPS-derived, produced the proteins VCAM1 and E-selectin, which are indicators of inflammation. In summary, their model demonstrated the significant impact of HGPS endothelial cells on cardiovascular disease (Atchison et al., 2020).

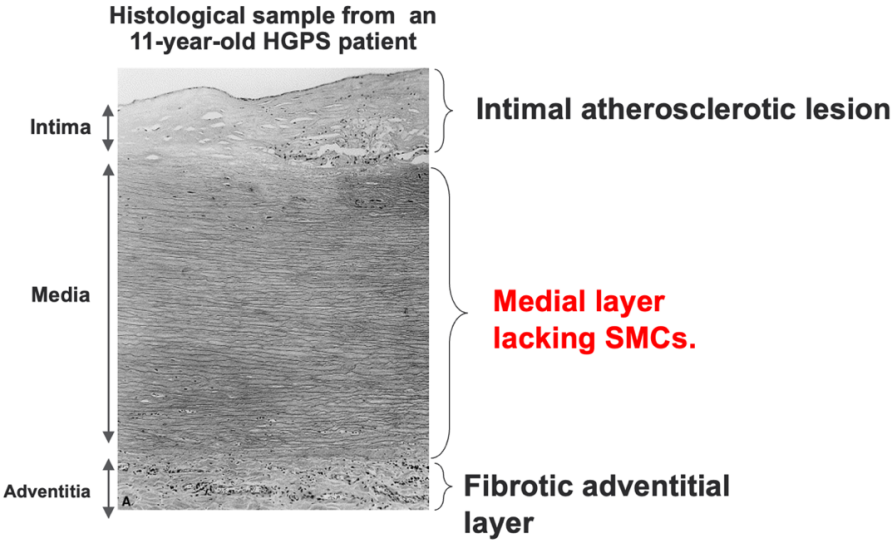

Figure 1.3. Aorta section from a 11-year-old HGPS patient stained with H&E. Atherosclerotic aorta showing relative acellularity of intima and media with round cell infiltration in the adventitia

below. The figure adapted from (W. E. Stehbens, Wakefield, Gilbert-Barness, Olson, & Ackerman, 1999).

Cardiovascular Disease in HGPS Patients: An Insight for Studying Normal-aging Associated Heart Disease.

Complications from cardiovascular disease is the primary cause of death in patients with Hutchinson-Gilford progeria syndrome, making it imperative to understand the underlying mechanisms to develop effective therapies. Over the past two decades, research has shown that HGPS patients exhibit multiple key cardiovascular issues; including accelerated atherosclerosis, vascular stiffening, significant fibrosis in the medial and adventitial layers, calcification, loss of vascular smooth muscle cells, left ventricular diastolic dysfunction, and cardiac valve disease (Figure 1.3). These conditions collectively lead to premature death from myocardial infarction or stroke (Benedicto, Dorado, & Andres, 2021; Merideth et al., 2008). Notably, the cardiovascular pathology in HGPS shares many similarities with that observed in normal aging (Olive et al., 2010).

Like typical aging, noninvasive imaging and autopsies of HGPS patients show atherosclerosis and cardiovascular calcification (Merideth et al., 2008). F. L. Debusk reported in a study of four HGPS cases that the majority of these patients succumb to heart failure or myocardial infarction primarily due to coronary atherosclerosis, with varying degrees of generalized atherosclerosis affecting the large arteries (Debusk, 1972). Common to both HGPS and normal aging is the calcification that affects the aorta and mitral valves, contributing to cardiovascular disease-associated morbidity in both populations. In a review of 12 HGPS patient autopsies, P. B. Baker et al. reported common findings of atherosclerosis-related coronary artery occlusion and calcification of the aortic and mitral valves (Baker, Baba, & Boesel, 1981).

Moreover, HGPS is characterized by vessel stiffening, measured noninvasively by pulse wave velocity (PWV), a reliable indicator of cardiac events independent of blood pressure (Gordon et al., 2012; Hamczyk et al., 2018). A study by M. Gerhard-Herman et al. involving a 21-patient cohort revealed that all HGPS patients exhibited significant vascular stiffening, with carotid-femoral PWV values comparable to those of adults older than 60 years, corroborated by other studies (Gerhard-Herman et al., 2012). Consequently, HGPS has been classified as a disease of vascular stiffening akin to cardiovascular diseases (CVD) seen in normal aging. PWV and arterial wall echo-density are now primary cardiovascular metrics for assessing the effectiveness of treatments in HGPS clinical trials (Benedicto et al., 2021).

Another similarity between HGPS and normal aging is the expression of progerin in both populations (Lopez-Otin, Blasco, Partridge, Serrano, & Kroemer, 2013). Although present at levels 50 times lower than in HGPS patients, progerin is detected in normal individuals from an early age (Gordon et al., 2014b). This is attributed to a classic pre-mRNA splicing mutation in HGPS, which activates a sporadic intronic splice site also present in normal individuals (Cao et al., 2011; McClintock et al., 2007; Scaffidi & Misteli, 2006). Even small accumulations of progerin can exert significant toxic effects due to its dominant-negative function. There is considerable evidence linking progerin to various aspects of generalized aging and cardiovascular health, particularly noting the similarity of atherosclerotic plaques in HGPS to those found in aging individuals (Olive et al., 2010). Moreover, vascular stiffening in HGPS mirrors that seen in normal aging, evidenced by increased PWV in both groups (Gordon et al., 2012).

Although many cardiovascular alterations in HGPS mimic those seen in physiological aging, HGPS patients lack many of the classical cardiovascular risk factors. For example, like healthy children, they exhibit similar levels of mean plasma cholesterol, low-density and high-

density lipoprotein-bound cholesterol, triglycerides, and median C-reactive protein. Therefore, studying the mechanisms of CVD in HGPS offers a unique opportunity to understand the mechanisms of CVD in non-HGPS individuals in the absence of confounding risk factors or chronic diseases that typically influence cardiovascular health (Gordon et al., 2014b).

Current HGPS Therapeutic Approaches

The treatment of Hutchinson-Gilford progeria syndrome primarily focuses on managing symptoms and improving quality of life, as there is currently no cure for the disease. (Gordon et al., 2012) Currently, the only FDA approved treatment is Lonafarnib. This is a farnesyltransferase inhibitor that has shown promising results in clinical trials. Lonafarnib can prevent the farnesylation of progerin, the toxic protein responsible for HGPS. The most significant outcome of the lonafarnib clinical trials was the observed increase in survival. Children with HGPS treated with lonafarnib had a statistically significant increase in survival rates compared to those who were not treated with the drug. A retrospective cohort study demonstrated that lonafarnib treatment led to a 3-year increase in survival on average (Gordon et al., 2018). It has also been observed to improve cardiovascular status, increase weight gain, and enhance the overall skeletal structure in children with HGPS (Ullrich et al., 2013).

Another therapeutic direction involves targeting the aberrant splicing of prelamin A using morpholino antisense oligonucleotides, antidiabetic metformin, and the proteasome inhibitor MG132, which have shown to transcriptionally reduce the RNA-binding protein splicing factor SRSF in HGPS fibroblasts. Moreover, RNA therapeutics like SRP-2001 and L-B143 have dramatically decreased progerin transcripts and protein expression in critical tissues, significantly extending the lifespan of progeria mouse models (Koblan et al., 2021; Puttaraju et al., 2021).

Recently, two research teams independently suggested a CRISPR/Cas9-based approach for treating Hutchinson-Gilford progeria syndrome (HGPS) by specifically halting the production of lamin A and progerin, while preserving lamin C (Beyret et al., 2019; Santiago-Fernandez et al., 2019). This is based on findings that lamin A is not essential in mice (Fong, Ng, et al., 2006; Lee et al., 2016). While this method has shown promise in enhancing health and prolonging the lifespan of progeria mice models (*Lmna*$^{G609G/G609G}$), its effects on humans remain uncertain. Additionally, the limited efficiency and potential for unintended insertions and deletions (indels) with the standard CRISPR/Cas9 system present significant challenges for clinical translation (Cong et al., 2013).

Significance of This Dissertation

The integration of multiple advanced methodologies in our study provided a comprehensive understanding of smooth muscle cell pathology in Hutchinson-Gilford progeria syndrome. The use of genetically engineered mouse models and *in vitro* doxycycline-inducible aortic SMCs illuminated the systemic impact and progression of SMC dysfunction in a living organism. These observations underscored the importance of SMC integrity to vascular health and how their degeneration significantly contributes to the vascular phenotype associated with HGPS.

Our *in vitro* doxycycline-inducible system offered a controlled environment to dissect the cellular mechanisms at play, specifically focusing on the induced expression of progerin. This system highlighted the direct consequences of progerin on SMC, including changes in DNA damage, p53 pathway activation, nuclear membrane ruptures, nuclear morphology, nuclear stiffness, cell death, and lamina structure which were not easily observable in a complex organismal model. Moreover, the controlled expression of progerin also allowed for the

observation of cellular responses over time, providing insight into the dynamics of disease progression at the cellular level.

The quantitative western blotting of mouse tissues validated the protein-level changes associated with disease states corresponding to animal's age. These quantitative analyses were essential for drawing connections between molecular alterations and the phenotypic traits observed in the aorta from *Lmna*$^{G606G/+}$ and *Zmpste24*$^{-/-}$ *Lmna*$^{G606G/+}$ compound mutant mouse models.

Examination of progeria mouse aorta sections stained with collagen type-8 antibody revealed that there were regional differences in SMC loss and adventitia thickening. Aorta wall near inner curvature of ascending aorta and branching points in aortic arch exhibited significantly more SMC loss and adventitia thickening. Moreover, these effected areas shared a remarkable resemblance with atherosclerosis mouse models in terms of where atherosclerotic lesions formed. This fascinating result elucidate the role of mechanical stress on VSMC death. The application of a custom-built cell stretching device revealed the sensitivity of progerin-SMCs to mechanical stress and confirmed our initial hypothesis. This aspect of the study pointed to the mechanosensitive of these cells, suggesting that mechanical forces could exacerbate the pathological features of HGPS or, conversely, could be targeted for therapeutic benefit. Understanding the mechanical properties of SMCs in the context of HGPS could lead to novel approaches for managing or mitigating the vascular aspects of the syndrome. And these findings allowed us to develop a transgenic mouse model to test our hypothesis.

Atomic force microscopy (AFM), Airyscan high-resolution confocal microscopy, and STED microscopy were pivotal in providing high-resolution insights into the structural integrity and nuclear lamin organization in SMCs. AFM detailed the intrinsic properties of the progerin expressing cells, which are crucial for understanding the enhanced susceptibility of vascular tissues

in HGPS patients to mechanical stress and strain. Meanwhile, Airyscan high-resolution confocal microscopy and STED microscopy allowed us to visualize nuclear lamina abnormalities that underlie the disrupted functions observed in HGPS SMCs, offering potential targets for molecular interventions.

Through the utilization of all the methodologies mentioned above, the significance of this dissertation lies in its comprehensive elucidation of the unique characteristics of the aorta, particularly in its expression levels of lamin proteins and the implications of these findings on vascular health. Unlike other tissues, the aorta is distinguished by its exceptionally high expression of lamin A and comparatively low levels of lamin B1. This distinctive profile not only underscores the unique structural and functional attributes of the aorta but also highlights its potential vulnerability to age-related changes. Central to this research is the discovery of progerin accumulation with advancing age. Progerin is found to progressively increase, while lamin B1 levels simultaneously decrease. These changes are shown to have profound pathological consequences.

Progerin accumulation disrupts the nuclear meshwork, leading to structural abnormalities that compromise the integrity of the nuclear envelope. This dissertation carefully details how these structural anomalies elicit nuclear membrane ruptures, which in turn exacerbate DNA damage and increase cell death rates. These cellular malfunctions are particularly critical in vascular smooth muscle cells, which are integral to the aorta's function and overall vascular health. The detailed analysis provided in this research demonstrates that the disruption caused by progerin not only impacts cellular architecture but also induces a cascade of detrimental effects, such as nuclear bleb and NM ruptures that compromise cell viability and function.

References

Aebi, U., Cohn, J., Buhle, L., & Gerace, L. (1986). The nuclear lamina is a meshwork of intermediate-type filaments. *Nature, 323*(6088), 560-564. doi:10.1038/323560a0

Atchison, L., Abutaleb, N. O., Snyder-Mounts, E., Gete, Y., Ladha, A., Ribar, T., . . . Truskey, G. A. (2020). iPSC-Derived Endothelial Cells Affect Vascular Function in a Tissue-Engineered Blood Vessel Model of Hutchinson-Gilford Progeria Syndrome. *Stem Cell Reports, 14*(2), 325-337. doi:10.1016/j.stemcr.2020.01.005

Baker, P. B., Baba, N., & Boesel, C. P. (1981). Cardiovascular abnormalities in progeria. Case report and review of the literature. *Arch Pathol Lab Med, 105*(7), 384-386.

Benedicto, I., Dorado, B., & Andres, V. (2021). Molecular and Cellular Mechanisms Driving Cardiovascular Disease in Hutchinson-Gilford Progeria Syndrome: Lessons Learned from Animal Models. *Cells, 10*(5). doi:10.3390/cells10051157

Beyret, E., Liao, H. K., Yamamoto, M., Hernandez-Benitez, R., Fu, Y., Erikson, G., . . . Izpisua Belmonte, J. C. (2019). Single-dose CRISPR-Cas9 therapy extends lifespan of mice with Hutchinson-Gilford progeria syndrome. *Nat Med, 25*(3), 419-422. doi:10.1038/s41591-019-0343-4

Burke, B., & Stewart, C. L. (2013). The nuclear lamins: flexibility in function. *Nat Rev Mol Cell Biol, 14*(1), 13-24. doi:10.1038/nrm3488

Cao, K., Graziotto, J. J., Blair, C. D., Mazzulli, J. R., Erdos, M. R., Krainc, D., & Collins, F. S. (2011). Rapamycin reverses cellular phenotypes and enhances mutant protein clearance in Hutchinson-Gilford progeria syndrome cells. *Sci Transl Med, 3*(89), 89ra58. doi:10.1126/scitranslmed.3002346

Capell, B. C., Erdos, M. R., Madigan, J. P., Fiordalisi, J. J., Varga, R., Conneely, K. N., . . . Collins, F. S. (2005). Inhibiting farnesylation of progerin prevents the characteristic nuclear blebbing of Hutchinson-Gilford progeria syndrome. *Proc. Natl. Acad. Sci. USA, 102*(36), 12879-12884.

Cong, L., Ran, F. A., Cox, D., Lin, S., Barretto, R., Habib, N., . . . Zhang, F. (2013). Multiplex genome engineering using CRISPR/Cas systems. *Science, 339*(6121), 819-823. doi:10.1126/science.1231143

Debusk, F. L. (1972). The Hutchinson-Gilford progeria syndrome. *J. Pediatr., 80*, 697–724.

Dechat, T., Pfleghaar, K., Sengupta, K., Shimi, T., Shumaker, D. K., Solimando, L., & Goldman, R. D. (2008). Nuclear lamins: major factors in the structural organization and function of the nucleus and chromatin. *Genes Dev, 22*(7), 832-853. doi:10.1101/gad.1652708

Eriksson, M., Brown, W. T., Gordon, L. B., Glynn, M. W., Singer, J., Scott, L., . . . Collins, F. S. (2003). Recurrent *de novo* point mutations in lamin A cause Hutchinson–Gilford progeria syndrome. *Nature, 423*, 293–298.

Fawcett, D. W. (1966). On the occurrence of a fibrous lamina on the inner aspect of the nuclear envelope in certain cells of vertebrates. *Am J Anat, 119*(1), 129-145. doi:10.1002/aja.1001190108

Fong, L. G., Ng, J. K., Lammerding, J., Vickers, T. A., Meta, M., Cote, N., . . . Young, S. G. (2006). Prelamin A and lamin A appear to be dispensable in the nuclear lamina. *J Clin Invest, 116*(3), 743-752. doi:10.1172/jci27125

Gerace, L., & Blobel, G. (1980). The nuclear envelope lamina is reversibly depolymerized during mitosis. *Cell, 19*(1), 277-287. doi:10.1016/0092-8674(80)90409-2

Gerhard-Herman, M., Smoot, L. B., Wake, N., Kieran, M. W., Kleinman, M. E., Miller, D. T., . . . Gordon, L. B. (2012). Mechanisms of premature vascular aging in children with Hutchinson-Gilford progeria syndrome. *Hypertension, 59*(1), 92-97. doi:10.1161/HYPERTENSIONAHA.111.180919

Goldman, R. D., Gruenbaum, Y., Moir, R. D., Shumaker, D. K., & Spann, T. P. (2002). Nuclear lamins: building blocks of nuclear architecture. *Genes Dev, 16*(5), 533-547. doi:10.1101/gad.960502

Goldman, R. D., Shumaker, D. K., Erdos, M. R., Eriksson, M., Goldman, A. E., Gordon, L. B., . . . Collins, F. S. (2004). Accumulation of mutant lamin A causes progressive changes in nuclear architecture in Hutchinson-Gilford progeria syndrome. *Proc. Natl. Acad. Sci. USA, 101*, 8963-8968.

Gordon, L. B., Kleinman, M. E., Miller, D. T., Neuberg, D. S., Giobbie-Hurder, A., Gerhard-Herman, M., . . . Kieran, M. W. (2012). Clinical trial of a farnesyltransferase inhibitor in children with Hutchinson-Gilford progeria syndrome. *Proc Natl Acad Sci U S A, 109*(41), 16666-16671. doi:10.1073/pnas.1202529109

Gordon, L. B., Massaro, J., D'Agostino, R. B., Sr., Campbell, S. E., Brazier, J., Brown, W. T., . . . Kieran, M. W. (2014). Impact of farnesylation inhibitors on survival in Hutchinson-Gilford progeria syndrome. *Circulation, 130*(1), 27–34. doi:10.1161/circulationaha.113.008285

Gordon, L. B., Shappell, H., Massaro, J., D'Agostino, R. B., Sr., Brazier, J., Campbell, S. E., . . . Kieran, M. W. (2018). Association of Lonafarnib Treatment vs No Treatment With Mortality Rate in Patients With Hutchinson-Gilford Progeria Syndrome. *Jama, 319*(16), 1687-1695. doi:10.1001/jama.2018.3264

Hamczyk, M. R., Villa-Bellosta, R., Gonzalo, P., Andres-Manzano, M. J., Nogales, P., Bentzon, J. F., . . . Andres, V. (2018). Vascular Smooth Muscle-Specific Progerin Expression Accelerates Atherosclerosis and Death in a Mouse Model of Hutchinson-Gilford Progeria Syndrome. *Circulation, 138*(3), 266-282. doi:10.1161/CIRCULATIONAHA.117.030856

Harborth, J., Elbashir, S. M., Bechert, K., Tuschl, T., & Weber, K. (2001). Identification of essential genes in cultured mammalian cells using small interfering RNAs. *J Cell Sci, 114*(Pt 24), 4557-4565. doi:10.1242/jcs.114.24.4557

Kang, S. M., Seo, S., Song, E. J., Kweon, O., Jo, A. H., Park, S., . . . Park, B. J. (2023). Progerinin, an Inhibitor of Progerin, Alleviates Cardiac Abnormalities in a Model Mouse of Hutchinson-Gilford Progeria Syndrome. *Cells, 12*(9). doi:10.3390/cells12091232

Koblan, L. W., Erdos, M. R., Gordon, L. B., Collins, F. S., Brown, J. D., & Liu, D. R. (2021). Base editor treats progeria in mice. *Nature*. doi:10.1038/d41586-021-01114-8

Lee, J. M., Nobumori, C., Tu, Y., Choi, C., Yang, S. H., Jung, H. J., . . . Fong, L. G. (2016). Modulation of LMNA splicing as a strategy to treat prelamin A diseases. *J Clin Invest, 126*(4), 1592-1602. doi:10.1172/JCI85908

Lopez-Otin, C., Blasco, M. A., Partridge, L., Serrano, M., & Kroemer, G. (2013). The hallmarks of aging. *Cell, 153*(6), 1194-1217. doi:10.1016/j.cell.2013.05.039

McClintock, D., Ratner, D., Lokuge, M., Owens, D. M., Gordon, L. B., Collins, F. S., & Djabali, K. (2007). The mutant form of lamin A that causes Hutchinson-Gilford progeria is a biomarker of cellular aging in human skin. *PLoS One, 2*(12), e1269. doi:10.1371/journal.pone.0001269

Merideth, M. A., Gordon, L. B., Clauss, S., Sachdev, V., Smith, A. C., Perry, M. B., . . . Introne, W. J. (2008). Phenotype and course of Hutchinson-Gilford progeria syndrome. *N Engl J Med, 358*(6), 592-604. doi:10.1056/NEJMoa0706898

Olive, M., Harten, I., Mitchell, R., Beers, J. K., Djabali, K., Cao, K., . . . Gordon, L. B. (2010). Cardiovascular pathology in Hutchinson-Gilford progeria: correlation with the vascular pathology of aging. *Arterioscler Thromb Vasc Biol, 30*(11), 2301-2309. doi:10.1161/atvbaha.110.209460

Puttaraju, M., Jackson, M., Klein, S., Shilo, A., Bennett, C. F., Gordon, L., . . . Misteli, T. (2021). Systematic screening identifies therapeutic antisense oligonucleotides for Hutchinson-Gilford progeria syndrome. *Nat Med, 27*(3), 526-535. doi:10.1038/s41591-021-01262-4

Santiago-Fernandez, O., Osorio, F. G., Quesada, V., Rodriguez, F., Basso, S., Maeso, D., . . . Lopez-Otin, C. (2019). Development of a CRISPR/Cas9-based therapy for Hutchinson-Gilford progeria syndrome. *Nat Med, 25*(3), 423-426. doi:10.1038/s41591-018-0338-6

Scaffidi, P., & Misteli, T. (2006). Lamin A-dependent nuclear defects in human aging. *Science, 312*(5776), 1059-1063. doi:10.1126/science.1127168

Ullrich, N. J., Kieran, M. W., Miller, D. T., Gordon, L. B., Cho, Y. J., Silvera, V. M., . . . Kleinman, M. E. (2013). Neurologic features of Hutchinson-Gilford progeria syndrome after lonafarnib treatment. *Neurology, 81*(5), 427-430. doi:10.1212/WNL.0b013e31829d85c0

Varga, R., Eriksson, M., Erdos, M. R., Olive, M., Harten, I., Kolodgie, F., . . . Collins, F. S. (2006). Progressive vascular smooth muscle cell defects in a mouse model of Hutchinson-Gilford progeria syndrome. *Proc Natl Acad Sci U S A, 103*(9), 3250-3255. doi:10.1073/pnas.0600012103

Worman, H. J., & Bonne, G. (2007). "Laminopathies": a wide spectrum of human diseases. *Exp. Cell. Res., 313*(10), 2121–2133.

Young, S. G., Fong, L. G., & Michaelis, S. (2005). Prelamin A, Zmpste24, misshapen cell nuclei, and progeria--new evidence suggesting that protein farnesylation could be important for disease pathogenesis. *J Lipid Res, 46*(12), 2531-2558. doi:10.1194/jlr.R500011-JLR200

Chapter 2:

Disrupting the LINC Complex in Smooth Muscle Cells Reduces Aortic Disease in a Mouse Model of Hutchinson-Gilford Progeria Syndrome

PROGERIA

Disrupting the LINC complex in smooth muscle cells reduces aortic disease in a mouse model of Hutchinson-Gilford progeria syndrome

Paul H. Kim[1], Jennings Luu[1], Patrick Heizer[1], Yiping Tu[1], Thomas A. Weston[1], Natalie Chen[1], Christopher Lim[1], Robert L. Li[1], Po-Yu Lin[2], James C. Y. Dunn[2], Didier Hodzic[3], Stephen G. Young[1,4]*, Loren G. Fong[1]*

Hutchinson-Gilford progeria syndrome is a disorder of premature aging in children caused by de novo mutations in *LMNA* that lead to the synthesis of an internally truncated form of prelamin A (commonly called progerin). The production of progerin causes multiple disease phenotypes, including an unusual vascular phenotype characterized by the loss of smooth muscle cells in the arterial media and fibrosis of the adventitia. We show that progerin expression, combined with mechanical stress, promotes smooth muscle cell death. Disrupting the linker of the nucleoskeleton and cytoskeleton (LINC) complex in smooth muscle cells ameliorates the toxic effects of progerin on smooth muscle cells and limits the accompanying adventitial fibrosis.

INTRODUCTION

Hutchinson-Gilford progeria syndrome (HGPS), the classic progeroid disorder of children, elicits multiple disease phenotypes resembling premature aging (*1*–*6*). Affected children appear normal at birth but soon manifest failure to thrive (gaining ~0.44 kg/year), hair loss, sclerodermatous skin, joint contractures, and a variety of dental and bone abnormalities. However, certain hallmarks of physiologic aging (arthritis, cancer, and dementia) are absent, prompting some to refer to HGPS as a "segmental aging syndrome" (*7*). Children with HGPS die at a mean age of 14.6 years, generally from occlusive arteriosclerotic disease in the coronary and cerebral arteries (*6*, *8*). The classical form of HGPS is caused by a de novo mutation in *LMNA* that results in the synthesis of a mutant form of prelamin A, commonly called progerin (*3*, *9*).

LMNA normally yields two alternatively spliced transcripts, one for prelamin A (the precursor to mature lamin A) and the other for lamin C (*10*). Prelamin A terminates with a C-terminal *CaaX* motif, which triggers farnesylation of a C-terminal cysteine, endoproteolytic cleavage of the last three amino acid residues, carboxyl methylation of the newly exposed farnesylcysteine, followed by the release of 15 additional amino acids by ZMPSTE24 (*11*). The final ZMPSTE24 cleavage step removes the C-terminal farnesylcysteine methyl ester and releases mature lamin A. The posttranslational processing of prelamin A is thought to aid in the assembly of the nuclear lamina by targeting farnesyl–prelamin A to the inner nuclear membrane. Lamin C is 74 residues shorter than mature lamin A (including six unique amino acids at its C terminus) and does not undergo any of the aforementioned posttranslational processing steps. Lamins A and C, together with lamins B1 and B2, are the building blocks of the nuclear lamina—a filamentous meshwork lining the inner nuclear membrane (*12*)—in somatic cells. In interphase cells, the nuclear lamina interacts with nuclear chromatin, proteins of the inner nuclear membrane, nuclear pore complexes, and indirectly with the cytoskeleton via the LINC (linker of the nucleoskeleton and cytoskeleton) complex (*13*). Because of these physical interactions, defects in the nuclear lamina can affect multiple nuclear-related properties such as heterochromatin organization, nuclear membrane integrity, and gene expression (*14*–*20*).

The most common mutation underlying HGPS is a point mutation in *LMNA* codon 608 that promotes usage of an alternative splice donor site, leading to an in-frame deletion of 50 amino acids and the production of a mutant prelamin A (progerin) (*3*, *9*). The internal deletion does not affect prelamin A's *CaaX* motif but eliminates the upstream ZMPSTE24 cleavage site. Thus, progerin undergoes farnesylation and methylation but does not undergo the final endoproteolytic cleavage step mediated by ZMPSTE24, meaning that the C terminus of progerin retains its farnesylcysteine methyl ester. Progerin accumulates in the nuclear envelope (*16*, *21*), resulting in misshapen nuclei (*3*), DNA damage (*22*, *23*), increased sensitivity to mechanical strain (*24*, *25*), and cell senescence (*26*–*28*). Inhibiting the farnesylation of progerin with protein farnesyltransferase inhibitors minimizes several of these phenotypes (*21*, *29*–*31*).

Mice engineered to produce progerin, either globally or in specific tissues, exhibit a variety of disease phenotypes resembling those in children with HGPS: alopecia, loss of subcutaneous adipose tissue, skeletal abnormalities, retarded growth, and shortened life span (*32*–*38*). About 15 years ago, Varga *et al.* (*39*) generated a transgenic mouse with a 164.4-kb bacterial artificial chromosome (BAC) clone containing four genes, including *LMNA* modified to contain the most common HGPS point mutation. Although the transgenic line did not manifest some of the hallmarks of progeria such as skeletal abnormalities and shortened life span, it developed vascular pathology—loss of smooth muscle cells (SMCs) in the media of the aorta along with fibrosis of the adventitia. Studies using these mice were intriguing because they seemed potentially relevant to the vascular disease observed in children with HGPS. Children with HGPS develop atherosclerotic lesions within the arterial intima (*8*), but SMC loss and adventitial fibrosis have also been observed (*8*, *40*, *41*). The cause of SMC loss is unknown, but it has been speculated that mechanical stress plays a role (*8*, *25*, *39*, *41*).

[1]Department of Medicine, University of California, Los Angeles, Los Angeles, CA 90095, USA. [2]Department of Surgery, Stanford University School of Medicine, Palo Alto, CA 94305, USA. [3]Department of Developmental Biology, Washington University School of Medicine, St. Louis, MO 63110, USA. [4]Department of Human Genetics, University of California, Los Angeles, Los Angeles, CA 90095, USA.
*Corresponding author. Email: lfong@mednet.ucla.edu (L.G.F.); sgyoung@mednet.ucla.edu (S.G.Y.)

Over the past 7 years, other groups have observed aortic disease in mouse models of HGPS (*35*, *38*, *42*), but there has been little progress in understanding the etiology of the vascular lesions. For example, given that progerin is expressed in many tissues, it is unclear why the pathology is so obvious in the aorta but seemingly absent in other tissues. Also, why does progerin lead to SMC death, and what causes adventitial fibrosis? Do mechanical forces in large arteries contribute to SMC loss? Here, we investigated these topics using both cell culture and mouse models.

RESULTS

Vascular disease is present in the aorta of *Lmna*^{G609G} mice

To investigate the aortic pathology associated with HGPS, we studied a knock-in mouse model (*Lmna*^{G609G}) with a mutant *Lmna* allele harboring the most common point mutation found in children with HGPS (*38*). Both *Lmna*$^{G609G/+}$ and *Lmna*$^{G609G/G609G}$ mice developed progressive disease phenotypes (skeletal abnormalities and reduced body weight gain), but disease phenotypes appeared at an earlier age and progressed more rapidly in *Lmna*$^{G609G/G609G}$ mice (fig. S1A). Western blotting confirmed the synthesis of progerin and the absence of prelamin A in the aorta (Fig. 1A), and hematoxylin and eosin (H&E) staining revealed hallmark vascular phenotypes in the ascending thoracic aorta (loss of SMCs, adventitial thickening, and intact endothelium) (Fig. 1B). To quantify the vascular phenotype, we measured the density of SMC nuclei (nucleus per square micrometer media area) and adventitial area as a percentage of total area in 4-month-old *Lmna*$^{G609G/G609G}$ mice. In those mice, the density of SMC nuclei was reduced by >90% in the proximal ascending aorta, and the adventitial area was about three-fold greater than that in wild-type (WT) mice (Fig. 1C).

The vascular phenotype was also observed in other regions of the aorta. Disease was present in the mid-arch, proximal descending aorta, and the lower descending aorta (Fig. 1, D and E, and fig. S1B); the same pathology was observed in the brachiocephalic, right and

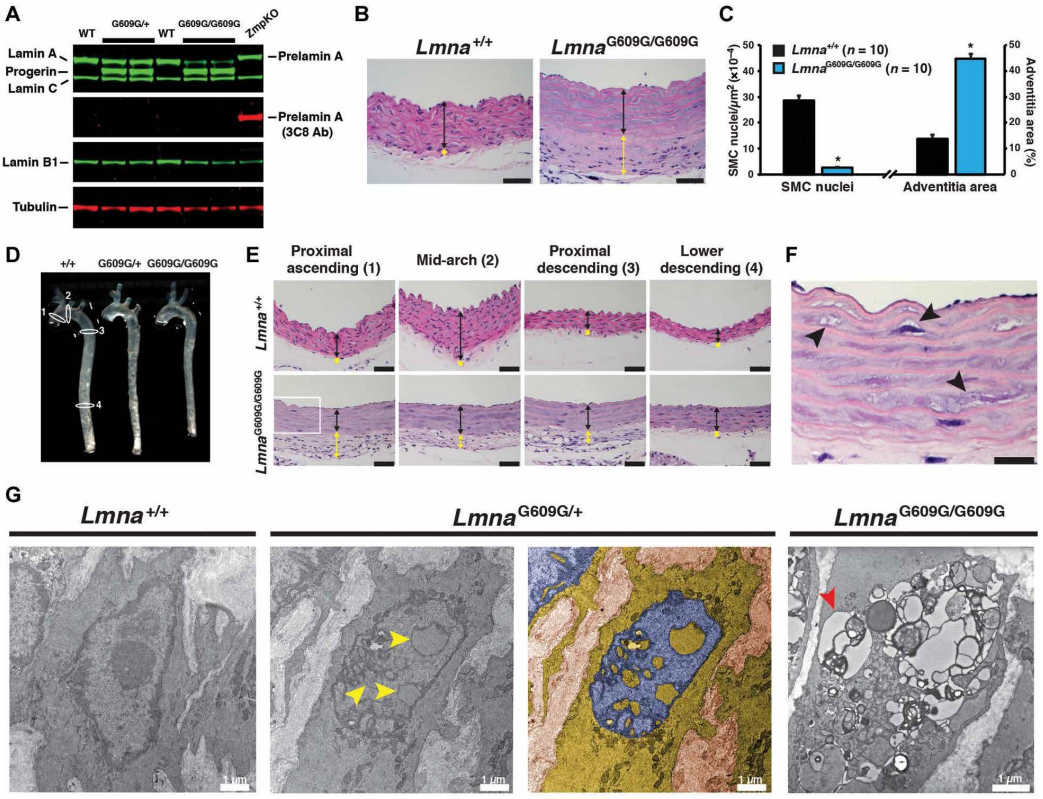

Fig. 1. Mice expressing progerin develop aortic pathology. (**A**) Western blot showing the synthesis of progerin but not prelamin A in aortas from *Lmna*$^{G609G/+}$ (G609G/+) and *Lmna*$^{G609G/G609G}$ (G609G/G609G) mice. Average progerin amounts (relative to tubulin) were 1.15 and 1.43 for heterozygous and homozygous G609G mice, respectively. KO, knockout; Ab, antibody. (**B**) Representative H&E-stained sections of the ascending aorta from 4-month-old *Lmna*$^{+/+}$ and *Lmna*$^{G609G/G609G}$ mice. Colored arrows identify the aortic media (black) and adventitia (yellow). Scale bars, 50 μm. (**C**) Bar graph showing SMC nuclei (left) and adventitial area (right) in the ascending aorta (inner curvature) of 4-month-old *Lmna*$^{G609G/G609G}$ mice (blue), compared with age-matched WT mice (black). Means ± SEM; $n = 10$ per group. *Lmna*$^{G609G/G609G}$ versus WT; *$P < 0.001$ (*t* test). (**D**) Thoracic aortas from WT (+/+), *Lmna*$^{G609G/+}$ (G609G/+), and *Lmna*$^{G609G/G609G}$ (G609G/G609G) mice. Numbered white ovals identify locations for sections in (E). (**E**) H&E-stained sections of four regions of the thoracic aorta from 4-month-old *Lmna*$^{+/+}$ and *Lmna*$^{G609G/G609G}$ mice. Colored arrows identify the adventitia (yellow) and media (black). Scale bars, 40 μm. (**F**) Enlarged image of the proximal ascending aorta [boxed area in (E)] showing vacuolated SMCs (black arrowheads). Scale bar, 20 μm. (**G**) Electron micrographs showing SMC nuclei in *Lmna*$^{+/+}$, *Lmna*$^{G609G/+}$, and *Lmna*$^{G609G/G609G}$ mice. Yellow arrowheads point to intranuclear vesicles in *Lmna*$^{G609G/+}$ aortas. A duplicate image is colorized to show the nucleoplasm (blue) and cytoplasm (yellow). Red arrowhead points to a cytoplasmic vacuole in a *Lmna*$^{G609G/G609G}$ aortic SMC.

left common carotid, and left subclavian arteries (fig. S1C). On H&E staining, the muscle layer of the aorta stained less red (Fig. 1E), and some SMCs contained vacuoles (Fig. 1F). No disease was detected in WT mice (Fig. 1E and fig. S1B) or in *Zmpste24*$^{-/-}$ mice (where there is an accumulation of the farnesylated form of WT prelamin A) (fig. S1D). The onset of aortic disease occurred after 2 months of age [aortas in 2-month-old *Lmna*$^{G609G/+}$ and *Lmna*$^{G609G/G609G}$ mice were free of obvious pathology (fig. S2A)]. We did not observe similar pathology in the parenchyma of other tissues (kidney and skeletal muscle) (fig. S2, B and C).

Lmna^{G609G} aortic SMCs contain intranuclear vesicles

Transmission electron microscopy identified two unusual features in *Lmna*^{G609G} aortic SMCs. The first was nuclei containing multiple intranuclear vesicles (Fig. 1G and fig. S3, A and B). The vesicles were bounded by inner and outer nuclear membranes, with heterochromatin lining the inner nuclear membrane, and occasionally containing cytoplasmic material. These structures were not observed in endothelial or adventitial cells (fig. S3C). The second unusual feature was that some SMCs contained multiple cytoplasmic vesicles (Fig. 1G and fig. S3B). Most of the vesicles appeared to be surrounded by a single lipid bilayer.

Collagen type VIII synthesis is increased in the aortic adventitia of *Lmna*^{G609G} mice

Previous histological studies showed increased collagen in diseased aortas (*38*, *39*). In keeping with those findings, we observed increased collagen content in aortas of *Lmna*$^{G609G/G609G}$ mice, as judged by Verhoeff-Van Gieson (VVG) and Masson's trichrome (MT) staining (Fig. 2A). To determine the type of collagen that accumulates in diseased aortas, we analyzed gene expression in different layers of the aorta (adventitia versus media). The layers were separated by enzymatic digestion (*43*) and validated by the expression of marker genes (*Col1a1* for the adventitia and *Acta2* for the media; Fig. 2B). The expression of *Col1a1*, *Col3a1*, *Col5a1*, and *Col8a1* was increased in the adventitia of *Lmna*$^{G609G/+}$ mice, with the largest increases relative to WT mice in the expression of *Col1a1* and *Col8a1* (3.8- and 17.2-fold, respectively). *Col1a1* and *Col8a1* were also increased in the aortic media, but expression was much lower than that in the adventitia. Immunofluorescence microscopy confirmed increased amounts of collagen types I and VIII protein in the aortic adventitia of *Lmna*$^{G609G/+}$ mice (Fig. 2C).

Lamin A and progerin are highly expressed in the aorta

The toxicity of progerin is dose-related. In cultured cells, increased amounts of progerin result in more misshapen nuclei, more DNA damage, and more rapid senescence (*18*, *30*). In mouse models, the severity of disease expression correlates with amounts of progerin expression (fig. S1A) (*32*, *33*, *35*). Given these observations, we suspected that tissues that express the highest amounts of progerin would be most likely to develop disease. Measuring progerin in tissues of *Lmna*^{G609G} mice would be the most straightforward approach to test this idea; however, we were concerned that progerin expression might be influenced by the disease itself: The emergence of disease might influence progerin by affecting *Lmna* splicing, cell viability, or protein turnover. To circumvent this possibility, we first measured lamin A amounts in WT mice, reasoning that lamin A expression in WT mice might correlate with progerin expression in *Lmna*^{G609G} mice. Lamin A expression was measured in the brain (cerebral cortex), liver, kidney, intercapsular brown adipose tissue, gonadal white adipose tissue, gallbladder, quadriceps, heart, skin, femur, and aorta (ascending, descending, and abdominal segments) by Western blotting (Fig. 3A) and normalized to tubulin, lamin C, or lamin B1 (Fig. 3, B to D). Lamin A expression in the different tissues was variable, differing as much as ~14-fold when normalized to tubulin. Low expression was found in the brain, liver, and kidney, whereas high expression was observed in the aorta, skin, and bone (Fig. 3B). Of note, the latter tissues are sites of pathology in HGPS, whereas the former tissues are not (*4*). The tissues with high amounts of lamin A (aorta, skin, and bone) also had a high lamin A/lamin C ratio (Fig. 3C).

The brain, a tissue that is spared in HGPS, expresses low amounts of lamin A relative to lamin B1 (*37*, *44*). When we ranked lamin A expression relative to lamin B1, the brain was the lowest and the aorta was the highest (Fig. 3D). Differences in expression were also evident at the transcript level (Fig. 3E). On the basis of the pattern of lamin A expression in WT mice, we predicted that we would find high amounts of progerin expression in the aorta of mice carrying the *Lmna*^{G609G} allele. This was the case; the tissue with the highest amounts of progerin in *Lmna*$^{G609G/+}$ mice was the aorta (fig. S4, A to D).

Lamin B1 amounts are low in aortic medial SMCs

A puzzling feature of the pathology in mouse models of HGPS is the loss of SMCs in the arterial media but the absence of obvious pathology in endothelial cells of the intima and cells of the adventitia. We hypothesized that the susceptibility of different cells to disease might be due to different amounts of lamin A expression. To explore this idea, we separated the media and adventitia layers and measured gene expression. Prelamin A transcript amounts were similar in the media and adventitia, but lamin B1 levels were about three- to four-fold higher in the adventitia than in the media (Fig. 3F). The higher lamin B1 expression in the adventitia was confirmed by Western blotting (fig. S4F) and immunofluorescence microscopy (Fig. 3G). The microscopy studies also showed that lamin B1 expression was higher in endothelial cells than in medial SMCs. Thus, SMCs have a far higher lamin A/lamin B1 ratio than endothelial cells and adventitial cells.

The vascular phenotype is more severe at curvatures and branches

Our experience in dissecting aortas from *Lmna*^{G609G} mice suggested that the aortic pathology was not uniformly distributed. To determine the distribution of aortic disease, we sectioned the proximal aorta down the midline and stained for CD31 (an endothelial cell marker) and collagen type VIII (a marker of adventitial fibrosis). In 12-month-old *Lmna*$^{G609G/+}$ mice and 4-month-old *Lmna*$^{G609G/G609G}$ mice, the pathology was more pronounced along the inner curvature of the ascending aorta and at major branch points (especially at the origin of the brachiocephalic artery) (Fig. 4, A to C). Quantitative studies in *Lmna*$^{G609G/+}$ (Fig. 4, D and E) and *Lmna*$^{G609G/G609G}$ (fig. S5, A to C) mice revealed that there was more adventitial fibrosis and a greater loss of SMCs in the media along the inner curvature of the aorta. Similar changes were previously noted along the posterior wall of the ascending aorta in mice expressing human progerin, but the changes were not quantified (*42*). Given that our Western blot and gene expression studies showed a correlation between high lamin A expression, low lamin B1 expression, and the extent of aortic pathology, we suspected that we might find distinct patterns of lamin A and lamin B1

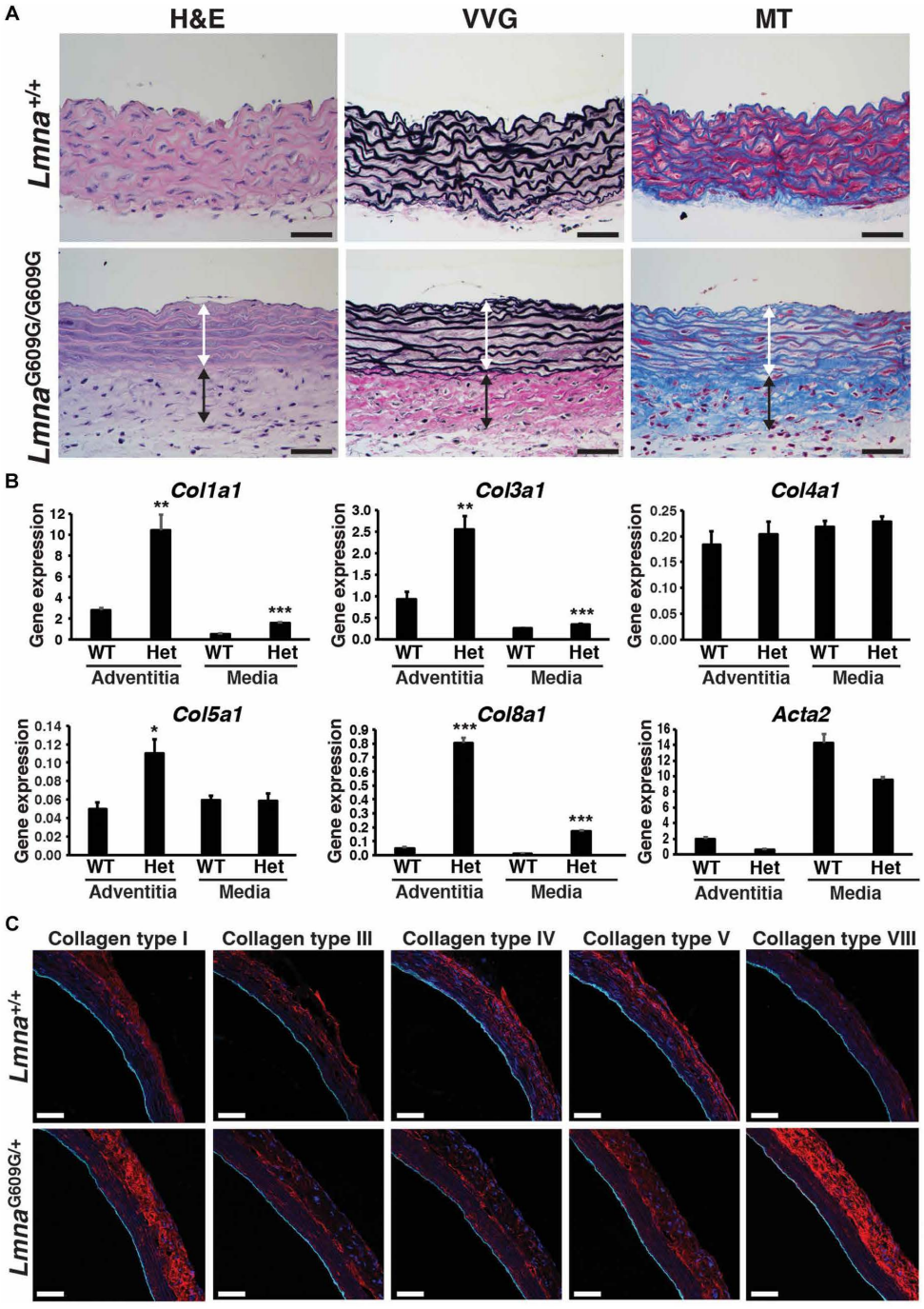

Fig. 2. Collagen synthesis is increased in the adventitia of *Lmna*^{G609G} mice. (**A**) Histochemical studies showing collagen content in the adventitia of aortas from 4-month-old *Lmna*$^{G609G/G609G}$ and *Lmna*$^{+/+}$ mice. H&E: blue, nuclei; pink, cytoplasm. VVG stain: black, elastic fibers and nuclei; red, collagen. MT stain: pink/red, cytoplasm; blue, collagen. Colored arrows identify the media (white) and adventitial (black) layers. Scale bars, 50 μm. (**B**) Reverse transcription polymerase chain reaction (RT-PCR) studies showing *Col1a1* and *Col8a1* expression in the adventitia of 12-month-old WT and *Lmna*$^{G609G/+}$ mice (means ± SEM; $n = 3$). *Lmna*$^{G609G/+}$ versus WT; $^{*}P < 0.05$, $^{**}P < 0.01$, and $^{***}P < 0.001$ (*t* test). (**C**) Serial frozen sections of the ascending aorta from 12-month-old WT and *Lmna*$^{G609G/+}$ mice stained with antibodies against collagen types I, III, IV, V, and VIII (red) and CD31 (cyan), examined by confocal fluorescence microscopy. Scale bars, 50 μm.

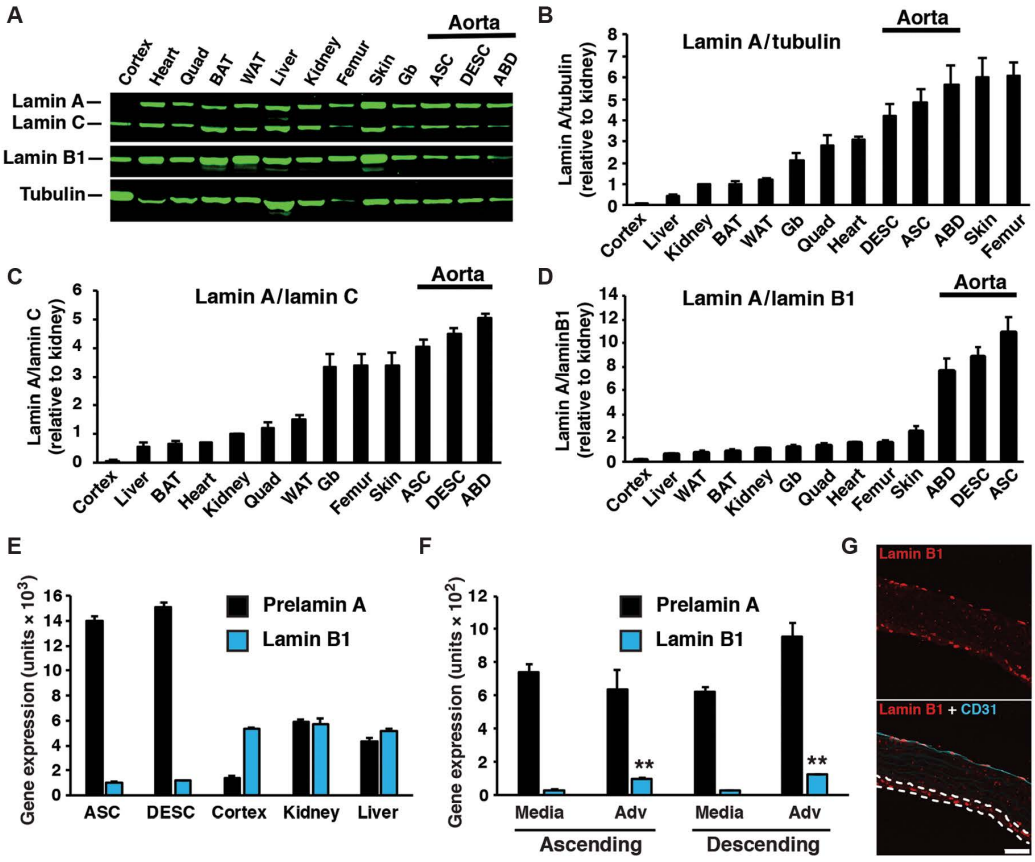

Fig. 3. Lamin A is expressed at high amounts in the aorta of WT mice. (**A**) Representative Western blot comparing lamin A, lamin C, and lamin B1 in different tissues from WT mice. Tubulin was measured as a loading control. Cortex, cerebral cortex; BAT, brown adipose tissue; WAT, white adipose tissue; Gb, gallbladder; ASC, ascending aorta; DESC, descending aorta; ABD, abdominal aorta. Graphs showing lamin A expression relative to tubulin (B), relative to lamin C (C), and relative to lamin B1 (D). For (**B**) to (**D**), tissues are arranged in ascending order of expression from left to right, with the expression in kidney set at a value of 1 (means ± SEM; $n = 4$ mice). (**E**) RT-PCR comparing the expression of prelamin A (black) and *Lmnb1* (blue) in tissues (means ± SEM; $n = 4$ mice). (**F**) RT-PCR comparing the expression of prelamin A (black) and *Lmnb1* (blue) in the media and adventitia (Adv) layers of WT mice (means ± SEM; $n = 4$ mice). Media versus adventitia; $^{**}P < 0.001$ (*t* test). (**G**) Confocal fluorescence microscopy images showing the expression of CD31 (cyan) and lamin B1 (red) in the ascending aorta of a WT mouse. In the merged image, the adventitia is outlined by dashed white lines (see fig. S4G). Scale bar, 50 μm.

expression in the inner and outer curvatures of the aorta. However, this was not the case (Fig. 4F).

Progerin expression induces hallmark HGPS phenotypes in cultured SMCs

The fact that the aortic pathology in the HGPS mice was greater in some locations than in others led us to suspect that local biomechanical forces are relevant to disease pathogenesis. The predilection of specific regions of the mouse aorta to atherosclerotic lesions near curvatures and branch points has been attributed to disturbed blood flow and dynamic changes in shear stress (*45*, *46*). To determine whether cells expressing progerin have increased sensitivity to mechanical forces, we developed a model system with cultured cells. Mouse SMCs stably expressing either human prelamin A or human progerin were grown on flexible polydimethylsiloxane (PDMS) membranes and exposed to repetitive biaxial stretch. In these studies, a doxycycline-inducible system was used to achieve a lamin A/lamin C profile similar to that in medial SMCs in vivo (lamin A/lamin C ratio of 3–4:1) (Fig. 3C). The expression of mature lamin A and progerin depended on doxycycline concentration in the medium, and the optimal expression for lamin A and progerin was achieved at 0.1 and 0.3 μg of doxycycline per milliliter, respectively (fig. S6A). The expression of progerin in SMCs resulted in "HGPS phenotypes"—misshapen nuclei (Fig. 5A) and markers of DNA damage [an accumulation of phosphorylated p53(Ser^{15}) and H2AXγ] (Fig. 5B). The increased DNA damage in progerin-expressing cells could not be attributed to the higher concentration of doxycycline required to induce progerin expression because DNA damage was not observed when WT cells were incubated with up to 3 μg of doxycycline per milliliter (fig. S6B).

Progerin expression promotes cell death in stretched SMCs

To determine whether biomechanical forces could contribute to SMC loss in HGPS mice, cells were cultured on flexible PDMS membranes

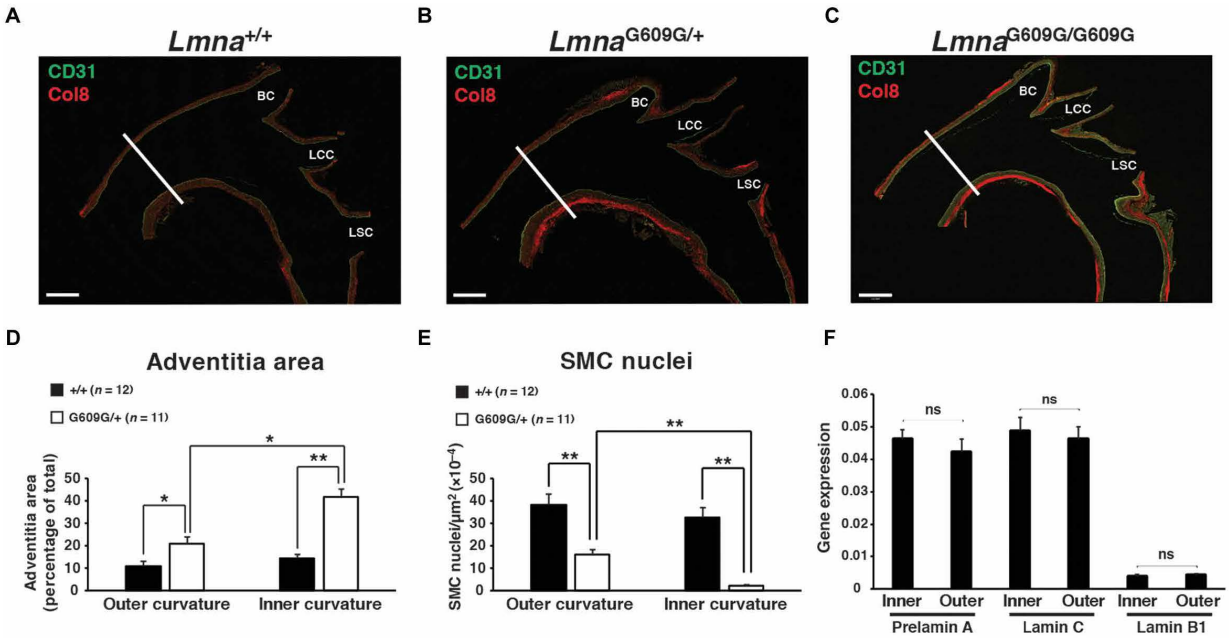

Fig. 4. Vascular pathology is more severe along the inner curvature of the ascending aorta and branches of the aortic arch. (**A** to **C**) Composite fluorescence microscopy images of the ascending thoracic aorta stained with antibodies against CD31 (green) and collagen type VIII (red) in 12-month-old *Lmna*$^{+/+}$ (A) and *Lmna*$^{G609G/+}$ (B) mice and in a 4-month-old *Lmna*$^{G609G/G609G}$ mouse (C). The white lines identify the location where the measurements were made. BC, brachiocephalic; LCC, left common carotid; LSC, left subclavian. Scale bars, 500 μm. (**D**) Bar graph showing adventitial area as a percentage of total area in WT (black) and *Lmna*$^{G609G/+}$ (white) mice at the outer and inner curvatures of the ascending aorta. (**E**) Bar graph showing the number of SMC nuclei relative to media area in WT (black) and *Lmna*$^{G609G/+}$ (white) mice at the outer and inner curvatures of the ascending aorta. Means ± SEM for WT (n = 12) and *Lmna*$^{G609G/+}$ (n = 11) mice; *P < 0.02 and **P < 0.001 (t test). (**F**) RT-PCR measuring prelamin A, lamin C, and *Lmnb1* expression at the inner and outer curvatures in WT mice (means ± SEM; n = 4). Inner versus outer; ns, not significant; P > 0.20 (t test).

and exposed to repetitive biaxial stretching (*25*). After 24 hours, ~40% of progerin-expressing SMCs detached from the membrane, as judged by cell protein (Fig. 5C). Collection of the detached cells and staining with trypan blue showed that the cells were nonviable. In contrast, SMCs that expressed WT prelamin A were unaffected and remained viable. To assess the effects of stretch before cell death and detachment, the cells were stained with propidium iodide (PI) (*25*) after stretching for 2 hours. PI staining increased to ~12% in progerin-expressing SMCs, whereas it increased to only ~1% in lamin A–expressing cells (fig. S6C). Similarly, reducing lamin B1 increased H2AXγ to a larger extent in progerin-expressing SMCs than in prelamin A–expressing cells (fig. S6D). Thus, progerin expression renders SMCs more susceptible to cell death in response to mechanical stress.

Disrupting the LINC complex reduces the toxic effects of progerin in cultured SMCs

The cell nucleus is connected to the cytoskeleton by the LINC complex (*13*), and this complex is known to transmit biomechanical forces to the cell nucleus. Two outer nuclear membrane proteins of the complex, Nesprin1 and Nesprin2, are tethered to the cytoskeleton. The KASH (Klarsicht/Anc-1, Syne Homology) domains of Nesprin1 and Nesprin2, located within the perinuclear space, interact with the Sun domains of Sun1 and Sun2. Sun1 and Sun2 traverse the inner nuclear membrane and interact with the nuclear lamina (*47*). The link between the cytoskeleton and the nuclear lamina can be disrupted by overexpressing the KASH domain of Nesprin2 (KASH2). KASH2 expression occupies the binding sites on the Sun proteins and thereby prevents Sun-Nesprin interactions within the perinuclear space (*48*). We predicted that KASH2 expression would reduce force transmission to the nucleus and limit the death of progerin-expressing cells during repetitive stretching. To test this possibility, we generated stable cell lines expressing either a KASH2-EGFP fusion protein (KASH2) or an inactive KASH2-EGFP mutant (ext-KASH2). KASH2 prevented the nuclear shape abnormalities that appear in progerin-expressing cells (Fig. 5D) and simultaneously reduced markers of DNA damage (Fig. 5E). Of note, these effects were observed in the absence of any effects on progerin (Fig. 5E). When progerin-expressing SMCs were exposed to repetitive stretching, the expression of KASH2 increased cell survival by 71% and reduced PI staining by ~60% (Fig. 5F and fig. S6C). These studies demonstrate that KASH2-mediated disruption of force transmission to the cell nucleus limits the toxicity of progerin in cultured SMCs.

Disrupting the LINC complex in aortic SMCs ameliorates SMC loss and adventitial fibrosis

The beneficial effects of KASH2 expression in progerin-expressing SMCs prompted us to test whether KASH2 expression in the SMCs of HGPS mice would ameliorate SMC loss in the medial layer of the aorta. We introduced a *Cre*-conditional KASH2-EGFP transgene (*49*) into *Lmna*$^{G609G/G609G}$ mice harboring an SMC-specific *Sm22-Cre* transgene (*50*). We bred three groups of mice: *Lmna*$^{+/+}$KASH2–EGFP^{+} *Sm22-Cre*$^{+}$ (WT), *Lmna*$^{G609G/G609G}$KASH2–EGFP^{+}*Sm22-Cre*$^{-}$ (MUT),

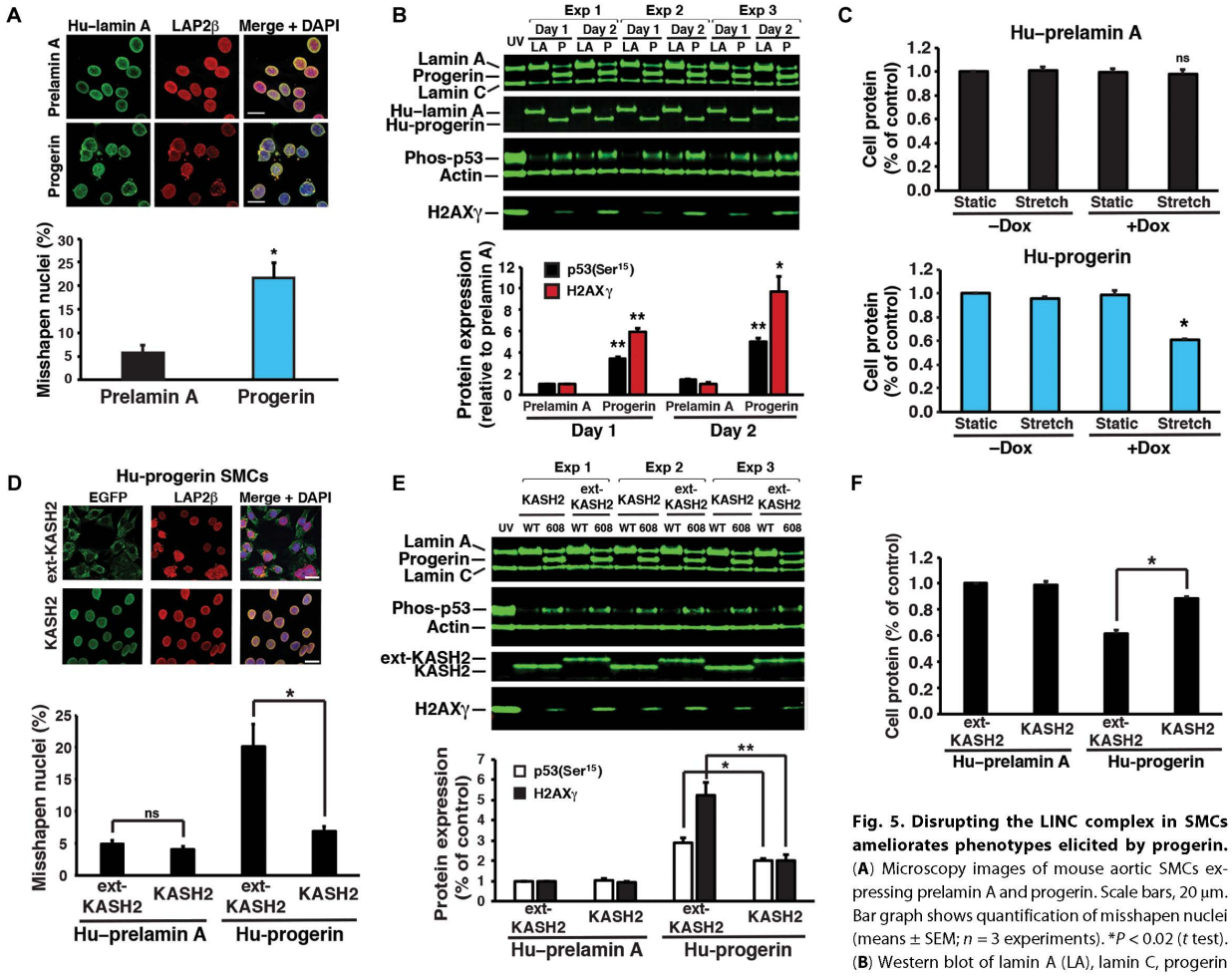

Fig. 5. Disrupting the LINC complex in SMCs ameliorates phenotypes elicited by progerin. (**A**) Microscopy images of mouse aortic SMCs expressing prelamin A and progerin. Scale bars, 20 μm. Bar graph shows quantification of misshapen nuclei (means ± SEM; $n = 3$ experiments). *$P < 0.02$ (t test). (**B**) Western blot of lamin A (LA), lamin C, progerin (P), phosphorylated p53 (Phos-p53), and H2AXγ expression in cells expressing lamin A or progerin. Cells exposed to ultraviolet (UV) light were included as a control. The bar graph shows the expression of p53 phosphorylation (black) and H2AXγ (red) after 1 or 2 days (means ± SEM; $n = 3$ experiments). Progerin versus prelamin A; *$P < 0.01$ and **$P < 0.001$ (t test). (**C**) Cell protein expressed relative to static cells (means ± SEM; $n = 3$ experiments) in prelamin A– and progerin-expressing SMCs exposed to uniaxial strain via stretching (6 mm, 0.5 Hz) or static conditions for 1 day. Stretch versus static; *$P < 0.001$ (t test). (**D**) Microscopy images of progerin-expressing cells transduced with enhanced green fluorescent protein (EGFP)–labeled KASH2 or EGFP-labeled ext-KASH2 (both in green). Nuclei were stained with DAPI (4′,6-diamidino-2-phenylindole) (blue) and LAP2β (red; a nuclear membrane marker). Scale bars, 20 μm. Bar graph shows quantification of misshapen nuclei in prelamin A– and progerin-expressing cells (means ± SEM; $n = 3$ experiments). KASH2 versus ext-KASH2; *$P < 0.02$ (t test). (**E**) Western blot showing lamin A, progerin, lamin C, phosphorylated p53, KASH2, and H2AXγ in unstrained, prelamin A (WT)– or progerin (608)–expressing cells. The bar graph shows the average expression of p53 phosphorylation (white) and H2AXγ (black) after 1 day (means ± SEM; $n = 3$ experiments). KASH2 versus ext-KASH2; *$P < 0.05$ and **$P < 0.01$ (t test). (**F**) Bar graph showing relative cell protein in progerin- and prelamin A–expressing stretched SMCs transfected with KASH2 or ext-KASH2 (means ± SEM; $n = 3$ experiments). KASH2 versus ext-KASH2; *$P < 0.001$ (t test).

and *Lmna*$^{G609G/G609G}$KASH2–EGFP^{+}*Sm22-Cre*$^{+}$ (MUT + KASH2). The specificity of the *Sm22-Cre* transgene was confirmed with mT/mG reporter mice (*51*). *Sm22-Cre*–mediated recombination occurred only in SMCs in the aortic medial layer, as judged by EGFP fluorescence (fig. S6E). KASH2 expression in the aorta of *Lmna*^{G609G} mice was confirmed by Western blotting, and this did not affect progerin expression (fig. S6F). Because all mice were collected at 4 months of age (before *Lmna*^{G609G} mice died of progeria disease), the study design did not permit us to determine the effects of KASH2 expression on mouse survival. However, KASH2 expression did not reduce body weights (fig. S6G).

KASH2 expression in MUT mice improved vascular pathology in the ascending aorta (inner and outer curvatures) and proximal descending thoracic aorta (Fig. 6). In the outer curvature of the ascending aorta (Fig. 6A), the density of SMC nuclei increased to 65% of that in WT mice, and adventitial fibrosis was eliminated (Fig. 6E). In the inner curvature, where the aortic pathology is more severe, the density of SMC nuclei increased about threefold but only to ~33% of the

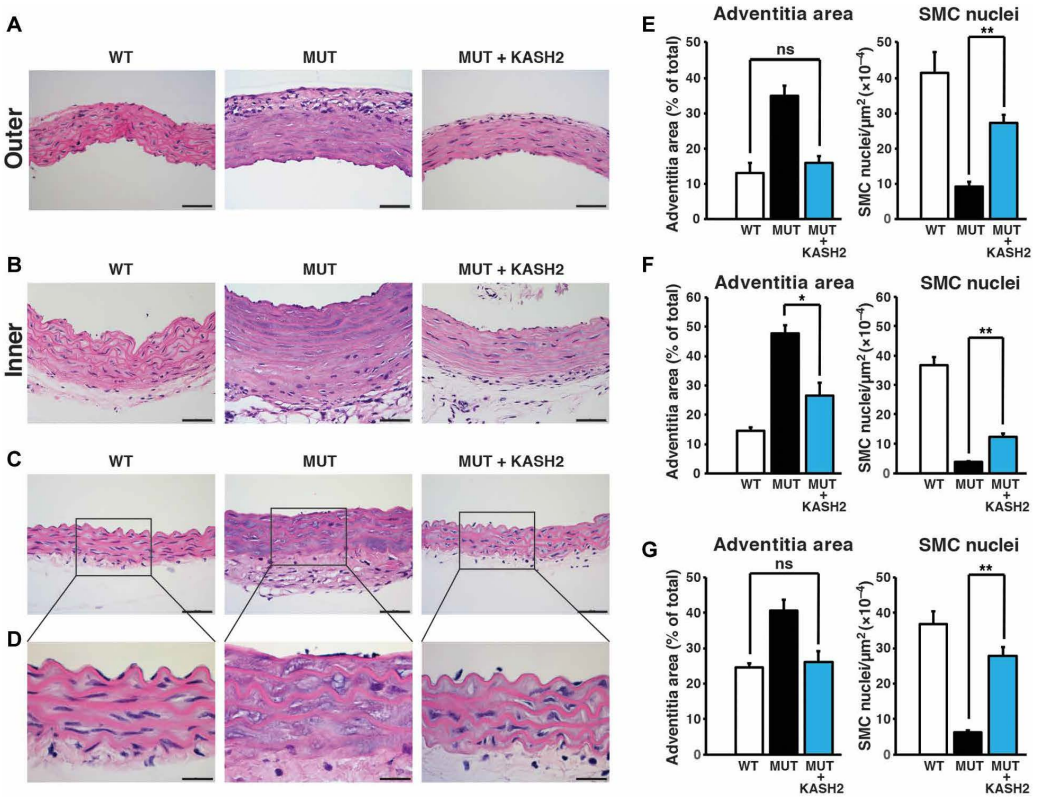

Fig. 6. The expression of the KASH2 domain in SMCs ameliorates aortic disease in *Lmna*$^{G609G/G609G}$ mice. (**A** to **D**) Representative photographs of H&E-stained cross sections at the outer (A) and inner (B) curvatures of the ascending aorta and proximal descending aorta (C and D) of WT (*Lmna*$^{+/+}$KASH2–EGFP^{+}*Sm22-Cre*$^{+}$), MUT (*Lmna*$^{G609G/G609G}$KASH2–EGFP^{+}*Sm22-Cre*$^{-}$), and MUT + KASH2 (*Lmna*$^{G609G/G609G}$KASH2–EGFP^{+}*Sm22-Cre*$^{+}$) mice. Scale bars, 50 μm (A to C) and 20 μm (D). (**E**) Adventitial area as a percentage of total area and numbers of SMC nuclei per media area at the outer ascending thoracic aorta (means ± SEM; $n = 6$ per group). (**F**) Adventitial area and numbers of SMC nuclei at the inner ascending thoracic aorta (means ± SEM; $n = 6$ per group). (**G**) Adventitial area and numbers of SMC nuclei in the proximal descending thoracic aorta (means ± SEM; $n = 6$ per group). *$P < 0.01$ and **$P < 0.001$; ns, not significant defined as $P > 0.40$ (*t* test).

density observed in the aorta of WT mice (Fig. 6, B and F). Nevertheless, adventitial fibrosis in the ascending aorta was greatly improved (~60% decrease) (Fig. 6F). In the descending aorta, where disease is less severe, the beneficial effects of KASH2 expression were striking (Fig. 6, C and D). The density of SMC nuclei in the medial layer of MUT + KASH2 aortas was 75% as high as that in WT mice, and adventitial fibrosis was eliminated (Fig. 6G). These studies demonstrate that force transmission from the cytoskeleton to the nucleus is a contributing factor to promoting SMC loss. Moreover, our results show that improved SMC survival prevents adventitial fibrosis, indicating that adventitial fibrosis in HGPS mice is secondary to the loss of SMCs.

DISCUSSION

The vascular pathology of HGPS has puzzled physicians and biomedical investigators for decades (*8*, *40*, *41*). Despite an absence of the typical risk factors for atherosclerosis, children with HGPS succumb to heart attacks or stroke, a consequence of occlusions in the coronary and cerebral arteries (*52*, *53*). The arterial pathology in HGPS must be caused by progerin, but the underlying mechanisms have remained unclear. In the current studies, we investigated the vascular pathology in HGPS mice and developed three insights into pathogenesis. The first relates to why the aorta develops disease while other tissues are spared. We found that the aorta produces more progerin than any other tissue—more than the skin and bone (two tissues affected by HGPS) and ~15-fold more than the kidney (an unaffected tissue). Electron micrographs of aortic SMCs of HGPS mice revealed striking abnormalities—intranuclear membrane vesicles and vacuoles in the cytoplasm. The second insight is that mechanical forces influence the distribution of vascular lesions. The vascular disease in HGPS mice is most severe along the inner curvature of the ascending aorta and at arterial branch points, where blood flow is disturbed and biomechanical forces are altered (*45*, *46*). The third insight is that reducing force transmission to the nucleus ameliorates the toxicity of progerin. In cultured SMCs, uncoupling the LINC complex with KASH2 (and thereby blunting force transmission to the cell nucleus) resulted in less DNA damage, fewer nuclear blebs, and reduced cell death. The expression of KASH2 in SMCs in HGPS mice markedly reduced SMC loss in the aortic media and reduced adventitial fibrosis.

Both the loss of aortic medial SMCs and the accompanying adventitial fibrosis depend on the dosage of progerin. The onset of vascular disease is earlier and disease progression is more rapid in homozygous HGPS mice than in heterozygous mice. The fact that disease severity depends on progerin dosage is not particularly surprising, given earlier studies showing that the amount of progerin expression affects the frequency of misshapen nuclei in cultured fibroblasts (*18*, *30*) and mouse experiments showing that the severity of nonvascular disease phenotypes depends on the extent of progerin expression (*32*, *33*, *35*). Of note, in humans, point mutations that increase progerin expression are associated with more severe disease (*54*).

Given the link between gene dosage and the severity of disease phenotypes, we suspected that we might encounter higher amounts of progerin expression in tissues that are susceptible to disease (aorta, skin, and bone) than in tissues that are spared (liver, kidney, and brain). This was the case. Of note, the higher amounts of progerin expression in the aorta, bone, and skin were not secondary to pathology in those tissues, but due to the intrinsic higher expression of lamin A in those tissues as found in WT mice (highest in skin, bone, and aorta and lowest in liver, kidney, and brain). The aorta was the third highest for lamin A expression in WT mice, behind skin and bone, but ranked first for progerin expression in HGPS mice. Those observations raise the possibility that progerin might accumulate in the aorta in HGPS mice, perhaps because of lower levels of turnover.

The distribution of vascular lesions was not uniform in the proximal aorta, suggesting that there are regional influences on lesion formation. The vascular disease was most severe along the inner curvature of the ascending aorta and at branches of the aortic arch—the very same locations where early atherosclerotic lesions develop in models of atherosclerosis. The nonrandom formation of atherosclerotic lesions is thought to be due to differences in flow patterns, where lesion formation coincides with areas of disturbed flow and oscillating low shear stress conditions—namely, at bends and branch points (*45*). The fact that HGPS vascular lesions develop in the same locations suggests that low shear stress contributes to the HGPS vascular phenotype. However, it is noteworthy that SMC loss and adventitial fibrosis also occur along the outer curvature of the ascending aorta (albeit to a lower extent), where shear stress and circumferential vessel strain are high. Thus, HGPS vascular lesions are not limited to regions of low shear stress and suggest that high vessel strain could also lead to SMC loss. Our in vitro mechanical stretch studies, which more closely model high vessel strain, support this proposal. In our studies, the combination of progerin expression and repetitive cell stretching resulted in greater cell toxicity than progerin expression alone.

Disrupting the LINC complex in SMCs with KASH2 expression ameliorated medial SMC loss and adventitial fibrosis throughout the aorta, but the greatest improvement was in regions with the least severe disease—the outer curvature of the ascending aorta and the descending aorta. In those regions, KASH2 expression in SMCs increased the density of medial SMCs to amounts approaching those in WT mice. Somewhat less expected was the significant reduction of adventitial fibrosis with KASH2. The *Sm22-Cre* transgene used to activate KASH2 expression is specific for medial SMCs in the aorta; hence, the improvement in adventitial fibrosis cannot be attributed to KASH2 expression in the mesenchymal cells of the adventitia. The simplest explanation is that collagen synthesis in the adventitia is activated in response to medial SMC death and weakening of the medial layer. In support of this idea, we observed an inverse relationship between medial SMC density and collagen type VIII staining in the aortic adventitia. Also, in earlier studies, Turlo *et al.* (*55*) observed aortic adventitial fibrosis in the setting of a genetic intervention (inactivation of β_1 integrin) that caused SMC death in the aortic media.

Nearly 20 years ago, Stehbens *et al.* (*41*) described SMC loss in the aorta in two autopsy cases of "progeria" (a firm diagnosis of HGPS was not established by genetic testing). In the more severe case, the medial layer of the aorta was nearly devoid of SMCs, and immunohistochemistry studies showed increased expression of collagen types I and III in the aortic intima. More recently, Olive *et al.* (*8*) examined atherosclerotic lesions in two children with bona fide HGPS (where a diagnosis of HGPS was confirmed by genetic testing). They observed loss of vascular SMCs in the aorta of one case, but both cases had adventitial fibrosis. Staining with Picrosirius red revealed increased amounts of collagen types I and III in the aorta. In our studies, *Col1a1* and *Col3a1* expression were increased in the aortic adventitia of HGPS mice, but the increase in *Col8a1* expression was the most impressive (17-fold greater than that in the aorta of WT mice). The expression of collagen type VIII in blood vessels is normally very low, but increased expression has been observed in the setting of vascular injury and atherosclerosis (*56*, *57*). Further studies will be required to determine whether increased levels of collagen type VIII also occur in other diseased tissues (skin and bone).

An intriguing issue is why medial SMCs in HGPS mice die, whereas the endothelial cells in the arterial intima and the mesenchymal cells of the adventitia remain viable. We doubt that these differences can be fully explained by differences in progerin expression. We found similar amounts of prelamin A transcripts in the media and adventitia of the mouse aorta, and the amounts of lamin A protein in the aorta media were only about twofold higher than that in the adventitia. We speculate that the peculiar susceptibility of medial SMCs to cell death could relate to low amounts of lamin B1 expression. By immunofluorescence microscopy, lamin B1 expression in medial SMCs is low—far lower than that in intimal endothelial cells or adventitial cells. Gene expression and Western blotting studies confirmed those findings. Low amounts of lamin B1 expression have been reported to cause stiffer cell nuclei (*58*) and to induce senescence (*59*)—similar to phenotypes elicited by progerin. We speculate that increased rigidity of cell nuclei in medial SMCs, where progerin expression is high and lamin B1 expression is low, renders the nucleus more susceptible to nuclear membrane ruptures (*20*, *60*), which could lead to DNA damage and cell death (*61*). Additional studies are required to investigate the role of lamin B1 in the increased mechanical sensitivity of SMCs.

The ultrastructural hallmark of aortic medial SMCs in HGPS mice are the intranuclear vesicles bounded by a double membrane and surrounded by heterochromatin. We suspect that these intranuclear vesicles, which are absent from intimal endothelial cells and adventitial cells, are the result of tubular invaginations of the nuclear envelope. In support of this idea, we have observed cytoplasmic contents inside the intranuclear vesicles. We do not understand the mechanism for the tubular invaginations, but one possibility is that high progerin expression leads to increased nuclear membrane synthesis (*62*), which, in turn, results in tubular invaginations. The consequences of deep nuclear membrane invaginations are unknown, but it is easy to imagine that these structures could disrupt chromatin architecture and gene expression. It is also conceivable that the transmission of cytoskeletal forces to intranuclear vesicles would be tangential to the surface of the nucleus (or would occur in multiple directions), increasing the likelihood of nuclear membrane ruptures.

We also observed SMCs containing multiple cytoplasmic vesicles, surrounded by a single lipid bilayer. We suspect that these represented dying cells with cytoplasmic autolysosomes (*63*).

In mouse models of atherosclerosis driven by hyperlipidemia, the atherosclerotic lesions preferentially form at the inner curvature of the ascending aorta and at branches of the aortic arch, sites of disturbed flow and oscillating shear stress (*45*). Those sites are identical to sites of vascular pathology in HGPS mice, implying that shear stress is a common factor in the pathogenesis of hyperlipidemia-driven atherosclerosis and the vascular pathology in HGPS. Although atherosclerosis is generally considered to be an intimal disease, the loss of SMCs in the media and the resultant weakening of the aorta could lead indirectly to more atheromas in the intima. Of note, Clarke *et al.* (*64*) have shown that inducing vascular SMC apoptosis in *Apoe*$^{-/-}$ mice (a model of atherosclerosis) induces intense intimal inflammation and characteristics of atherosclerotic plaque vulnerability (thin fibrous cap, inflammatory foci, large necrotic core, cellular debris, and depletion of matrix content). Alternatively, it is entirely possible that progerin expression in arterial endothelial cells, accompanied by increased biomechanical forces, leads to more subtle (less visible) changes in intimal endothelial cells that promote atherogenesis (increased lipoprotein uptake, more lipoprotein oxidation, and increased macrophage infiltration) (*65*). Additional studies will be required to assess the impact of progerin on arterial wall cell function and atherogenesis. Such studies will likely add to our understanding of vascular disease in children with HGPS and further define the relevance of HGPS vascular pathology to ordinary atherosclerosis in adults within the general population.

MATERIALS AND METHODS

Study design

The objective of the study was to investigate the vascular phenotype in HGPS. The vascular phenotype—defined as the loss of SMCs and fibrosis of the adventitia—was examined in the thoracic aorta of *Lmna*^{G609G} mice, a mouse model of HGPS. We hypothesized that high progerin expression combined with mechanical strain promote SMC loss. To test this hypothesis, we performed studies in cultured cells and mouse models. Unless otherwise specified, all cell culture studies were independently performed at least three times. Studies in animals were performed in group sizes listed in figure legends.

Mice

Zmpste24$^{-/-}$ and *Lmna*$^{G609G/G609G}$ mice have been described previously (*38*, *66*). Sm22α-*Cre* transgenic (stock no. 017491) and mT/mG reporter (stock no. 007676) mice were purchased from The Jackson Laboratory. The Sm22α-*Cre* mouse strain was genotyped by PCR with forward primer 5′-CAGACACCGAAGCTACTCTCCTTCC-3′ and reverse primer 5′-CGCATAACCAGTGAAACAGCATTGC-3′ [yielding a 500–base pair (bp) product]. The mT/mG mouse strain was genotyped with a mutant forward primer 5′-TAGAGCTTGCGGAACCCTTC-3′, a WT forward primer 5′-AGGGAGCTGCAGTGGAGTAG-3′, and a common reverse primer 5′-CTTTAAGCCTGCCCAGAAGA-3′ (128-bp product for the mutant allele and 212-bp product for the WT allele). The CAG-LacZ/EGFP-KASH2 transgenic mouse (*49*) was genotyped with forward primer 5′-GGA GTTCGTGACCGCCGCCGGGATCACTCT-3′ and reverse primer 5′-TTTAAACGGGCCCCCTAGGTGGGAGGTGGC-3′ (yielding a ~280-bp product). Mice were housed in a specific pathogen–free barrier facility with a 12-hour light/dark cycle. The mice were provided pelleted mouse chow (NIH-31) and water ad libitum and nutritional food cups as required for supportive care. All animal studies were approved by the UCLA's (University of California, Los Angeles) Animal Research Committee. Antibodies used for Western blotting and immunohistochemistry are reported in table S1; primers used for quantitative RT-PCR are listed in table S2.

Cells

Immortalized mouse aortic SMCs (#CRL-2797) were purchased from the American Type Culture Collection and cultured in Dulbecco's modified Eagle's medium (Gibco) containing 10% fetal bovine serum (HyClone), 1× nonessential amino acids (Gibco), 1 mM sodium pyruvate (Gibco), 2 mM glutamine (Gibco), and G418 (0.2 mg/ml; Gibco). The cells exhibit both synthetic and contractile phenotypes, as judged by a high proliferation rate and the absence of smooth muscle myosin heavy chain expression (*67*), and perinuclear distribution of vimentin (*68*), respectively. The cells were transduced with lentivirus by UCLA's Vector Core Facility. To produce UV-treated cells, SMCs in six-well dishes were exposed to UV light (100 mJ/cm^2) in a Stratalinker 2400 (Stratagene). Cells were transfected with 100 nM *Lmnb1* siRNA (small interfering RNA) (AM16706, Ambion) using RNAiMAX (Invitrogen) according to the manufacturer's instructions.

Stretching SMCs on PDMS membranes

Flexible PDMS membranes (1 mm thick) were prepared in 150-mm culture dishes with the Sylgard 184 silicone elastomer kit (#3097358-1004, Dow Corning). Membranes strips (7 × 0.8 cm) were activated with a plasma cleaner, treated with 2% 3-aminopropy-triethoxysilane at room temperature for 45 min, washed in ethanol, and then dried at 55°C for 30 min. The membranes were incubated with sulfo-SANPAH [sulfosuccinimidyl 6-(4′-azido-2′-nitrophenylamino)hexanoate] (0.5 mg/ml) in Hepes buffer and cross-linked with UV exposure (300 to 460 nm) for 30 s. The washed membranes were stored at 4°C in a collagen solution (100 μg/ml; 5005, PureCol; Advanced BioMatrix). Cells (1 × 10^5) were added to individual membrane strips in molds and incubated in media ± doxycycline for 24 hours and then clamped into a custom-built stretching device. The brackets holding the membranes were attached to an L12 linear actuator (Actuonix) controlled by a multifunction DAQ (data acquisition) device (National Instruments) and LabVIEW 2015 software (National Instruments). The membranes were stretched 6 mm at 0.5 Hz (24 hours) for the cell viability studies (trypan blue and cell protein measurements), 3 mm at 0.5 Hz (24 hours) for the DNA damage studies (Western blotting studies), and 2 mm at 0.5 Hz (2 hours) for the cell damage studies (PI studies). The milder conditions for the DNA and cell damage studies were to examine the effects of mechanical stress before cell death. To measure cell protein, membranes were washed with phosphate-buffered saline (PBS) and digested with 0.1 N NaOH, and protein content was measured with the DC protein assay kit (Bio-Rad). To stain cells with PI, we incubated membranes with freshly prepared PI (10 μg/ml; Thermo Fisher Scientific) and Hoechst 33342 (1 μg/ml; Thermo Fisher Scientific) in Dulbecco's PBS at room temperature for 15 min. The stained cells were washed, fixed, and analyzed by fluorescence microscopy.

Separation of aortic adventitia and media layers

The adventitia and media layers of the mouse aorta were separated by enzymatic digestion (*43*). Cleaned aortas were incubated in PBS

containing collagenase type II (1 mg/ml), soybean trypsin inhibitor (1 mg/ml), and elastase (2 mg/ml) (all from Worthington) at 37°C for 10 min. The digested aortas were placed into ice-cold PBS and cut into three segments of equal length, and the adventitia layer was unrolled from each segment. The adventitia and media (also including the endothelial cell layer) were processed immediately or frozen in liquid nitrogen for storage.

Statistical analysis

Statistical analyses were performed with Microsoft Excel for Mac 2011 and GraphPad Software. Experimental groups were analyzed by a two-tailed Student's *t* test. Individual subject-level data are reported in table S3.

SUPPLEMENTARY MATERIALS

www.sciencetranslationalmedicine.org/cgi/content/full/10/460/eaat7163/DC1

Materials and Methods

Fig. S1. Pathology in $Lmna^{G609G}$ mice.

Fig. S2. H&E staining of aortic tissue from young mice and nonaortic tissues from older $Lmna^{G609G/+}$ mice.

Fig. S3. Cell and nuclear morphology in $Lmna^{G609G}$ aortic SMCs.

Fig. S4. Nuclear lamin expression in the aorta of WT and $Lmna^{G609G/+}$ mice.

Fig. S5. Analysis of the vascular phenotype in the ascending aorta of $Lmna^{G609G/G609G}$ mice.

Fig. S6. Control studies for the lamin-inducible SMC system and the *Sm22-Cre*–dependent activation of KASH2 expression in the aorta.

Table S1. Antibodies used for Western blotting and immunohistochemistry.

Table S2. Quantitative RT-PCR primers.

Table S3. Individual subject-level data.

Reference (*69*)

REFERENCES AND NOTES

1. F. L. DeBusk, The Hutchinson-Gilford progeria syndrome. Report of 4 cases and review of the literature. *J. Pediatr.* **80**, 697–724 (1972).
2. P. K. Sarkar, R. A. Shinton, Hutchinson-Guilford progeria syndrome. *Postgrad. Med. J.* **77**, 312–317 (2001).
3. M. Eriksson, W. T. Brown, L. B. Gordon, M. W. Glynn, J. Singer, L. Scott, M. R. Erdos, C. M. Robbins, T. Y. Moses, P. Berglund, A. Dutra, E. Pak, S. Durkin, A. B. Csoka, M. Boehnke, T. W. Glover, F. S. Collins, Recurrent de novo point mutations in lamin A cause Hutchinson-Gilford progeria syndrome. *Nature* **423**, 293–298 (2003).
4. M. W. Kieran, L. Gordon, M. Kleinman, New approaches to progeria. *Pediatrics* **120**, 834–841 (2007).
5. L. B. Gordon, K. M. McCarten, A. Giobbie-Hurder, J. T. Machan, S. E. Campbell, S. D. Berns, M. W. Kieran, Disease progression in Hutchinson-Gilford progeria syndrome: Impact on growth and development. *Pediatrics* **120**, 824–833 (2007).
6. M. A. Merideth, L. B. Gordon, S. Clauss, V. Sachdev, A. C. M. Smith, M. B. Perry, C. C. Brewer, C. Zalewski, H. J. Kim, B. Solomon, B. P. Brooks, L. H. Gerber, M. L. Turner, D. L. Domingo, T. C. Hart, J. Graf, J. C. Reynolds, A. Gropman, J. A. Yanovski, M. Gerhard-Herman, F. S. Collins, E. G. Nabel, R. O. Cannon III, W. A. Gahl, W. J. Introne, Phenotype and course of Hutchinson-Gilford progeria syndrome. *N. Engl. J. Med.* **358**, 592–604 (2008).
7. G. M. Martin, J. Oshima, Lessons from human progeroid syndromes. *Nature* **408**, 263–266 (2000).
8. M. Olive, I. Harten, R. Mitchell, J. K. Beers, K. Djabali, K. Cao, M. R. Erdos, C. Blair, B. Funke, L. Smoot, M. Gerhard-Herman, J. T. Machan, R. Kutys, R. Virmani, F. S. Collins, T. N. Wight, E. G. Nabel, L. B. Gordon, Cardiovascular pathology in Hutchinson-Gilford progeria: Correlation with the vascular pathology of aging. *Arterioscler. Thromb. Vasc. Biol.* **30**, 2301–2309 (2010).
9. A. De Sandre-Giovannoli, R. Bernard, P. Cau, C. Navarro, J. Amiel, I. Boccaccio, S. Lyonnet, C. L. Stewart, A. Munnich, M. Le Merrer, N. Lévy, Lamin A truncation in Hutchinson-Gilford progeria. *Science* **300**, 2055 (2003).
10. F. Lin, H. J. Worman, Structural organization of the human gene encoding nuclear lamin A and nuclear lamin C. *J. Biol. Chem.* **268**, 16321–16326 (1993).
11. S. G. Young, L. G. Fong, S. Michaelis, Prelamin A, Zmpste24, misshapen cell nuclei, and progeria—New evidence suggesting that protein farnesylation could be important for disease pathogenesis. *J. Lipid Res.* **46**, 2531–2558 (2005).
12. N. Stuurman, S. Heins, U. Aebi, Nuclear lamins: Their structure, assembly, and interactions. *J. Struct. Biol.* **122**, 42–66 (1998).
13. M. Crisp, Q. Liu, K. Roux, J. B. Rattner, C. Shanahan, B. Burke, P. D. Stahl, D. Hodzic, Coupling of the nucleus and cytoplasm: Role of the LINC complex. *J. Cell Biol.* **172**, 41–53 (2006).
14. T. Sullivan, D. Escalante-Alcalde, H. Bhatt, M. Anver, N. Bhat, K. Nagashima, C. L. Stewart, B. Burke, Loss of A-type lamin expression compromises nuclear envelope integrity leading to muscular dystrophy. *J. Cell Biol.* **147**, 913–920 (1999).
15. E. C. Schirmer, T. Guan, L. Gerace, Involvement of the lamin rod domain in heterotypic lamin interactions important for nuclear organization. *J. Cell Biol.* **153**, 479–489 (2001).
16. R. D. Goldman, D. K. Shumaker, M. R. Erdos, M. Eriksson, A. E. Goldman, L. B. Gordon, Y. Gruenbaum, S. Khuon, M. Mendez, R. Varga, F. S. Collins, Accumulation of mutant lamin A causes progressive changes in nuclear architecture in Hutchinson-Gilford progeria syndrome. *Proc. Natl. Acad. Sci. U.S.A.* **101**, 8963–8968 (2004).
17. C. Coffinier, S. Y. Chang, C. Nobumori, Y. Tu, E. A. Farber, J. I. Toth, L. G. Fong, S. G. Young, Abnormal development of the cerebral cortex and cerebellum in the setting of lamin B2 deficiency. *Proc. Natl. Acad. Sci. U.S.A.* **107**, 5076–5081 (2010).
18. A. Chojnowski, P. F. Ong, E. S. M. Wong, J. S. Y. Lim, R. A. Mutalif, R. Navasankari, B. Dutta, H. Yang, Y. Y. Liow, S. K. Sze, T. Boudier, G. D. Wright, A. Colman, B. Burke, C. L. Stewart, O. Dreesen, Progerin reduces LAP2α-telomere association in Hutchinson-Gilford progeria. *eLife* **4**, e07759 (2015).
19. E. M. Hatch, M. W. Hetzer, Nuclear envelope rupture is induced by actin-based nucleus confinement. *J. Cell Biol.* **215**, 27–36 (2016).
20. C. M. Denais, R. M. Gilbert, P. Isermann, A. L. McGregor, M. te Lindert, B. Weigelin, P. M. Davidson, P. Friedl, K. Wolf, J. Lammerding, Nuclear envelope rupture and repair during cancer cell migration. *Science* **352**, 353–358 (2016).
21. M. P. Mallampalli, G. Huyer, P. Bendale, M. H. Gelb, S. Michaelis, Inhibiting farnesylation reverses the nuclear morphology defect in a HeLa cell model for Hutchinson-Gilford progeria syndrome. *Proc. Natl. Acad. Sci. U.S.A.* **102**, 14416–14421 (2005).
22. T. Misteli, P. Scaffidi, Genome instability in progeria: When repair gets old. *Nat. Med.* **11**, 718–719 (2005).
23. B. Liu, J. Wang, K. M. Chan, W. M. Tjia, W. Deng, X. Guan, J.-d. Huang, K. M. Li, P. Y. Chau, D. J. Chen, D. Pei, A. M. Pendas, J. Cadiñanos, C. López-Otín, H. F. Tse, C. Hutchison, J. Chen, Y. Cao, K. S. E. Cheah, K. Tryggvason, Z. Zhou, Genomic instability in laminopathy-based premature aging. *Nat. Med.* **11**, 780–785 (2005).
24. K. N. Dahl, P. Scaffidi, M. F. Islam, A. G. Yodh, K. L. Wilson, T. Misteli, Distinct structural and mechanical properties of the nuclear lamina in Hutchinson-Gilford progeria syndrome. *Proc. Natl. Acad. Sci. U.S.A.* **103**, 10271–10276 (2006).
25. V. L. R. M. Verstraeten, J. Y. Ji, K. S. Cummings, R. T. Lee, J. Lammerding, Increased mechanosensitivity and nuclear stiffness in Hutchinson-Gilford progeria cells: Effects of farnesyltransferase inhibitors. *Aging Cell* **7**, 383–393 (2008).
26. P. Scaffidi, T. Misteli, Reversal of the cellular phenotype in the premature aging disease Hutchinson-Gilford progeria syndrome. *Nat. Med.* **11**, 440–445 (2005).
27. P. Taimen, K. Pfleghaar, T. Shimi, D. Möller, K. Ben-Harush, M. R. Erdos, S. A. Adam, H. Herrmann, O. Medalia, F. S. Collins, A. E. Goldman, R. D. Goldman, A progeria mutation reveals functions for lamin A in nuclear assembly, architecture, and chromosome organization. *Proc. Natl. Acad. Sci. U.S.A.* **106**, 20788–20793 (2009).
28. G.-H. Liu, B. Z. Barkho, S. Ruiz, D. Diep, J. Qu, S.-L. Yang, A. D. Panopoulos, K. Suzuki, L. Kurian, C. Walsh, J. Thompson, S. Boue, H. L. Fung, I. Sancho-Martinez, K. Zhang, J. Yates III, J. C. Izpisua Belmonte, Recapitulation of premature ageing with iPSCs from Hutchinson-Gilford progeria syndrome. *Nature* **472**, 221–225 (2011).
29. J. I. Toth, S. H. Yang, X. Qiao, A. P. Beigneux, M. H. Gelb, C. L. Moulson, J. H. Miner, S. G. Young, L. G. Fong, Blocking protein farnesyltransferase improves nuclear shape in fibroblasts from humans with progeroid syndromes. *Proc. Natl. Acad. Sci. U.S.A.* **102**, 12873–12878 (2005).
30. M. W. Glynn, T. W. Glover, Incomplete processing of mutant lamin A in Hutchinson-Gilford progeria leads to nuclear abnormalities, which are reversed by farnesyltransferase inhibition. *Hum. Mol. Genet.* **14**, 2959–2969 (2005).
31. B. C. Capell, M. R. Erdos, J. P. Madigan, J. J. Fiordalisi, R. Varga, K. N. Conneely, L. B. Gordon, C. J. Der, A. D. Cox, F. S. Collins, Inhibiting farnesylation of progerin prevents the characteristic nuclear blebbing of Hutchinson-Gilford progeria syndrome. *Proc. Natl. Acad. Sci. U.S.A.* **102**, 12879–12884 (2005).
32. S. H. Yang, M. Meta, X. Qiao, D. Frost, J. Bauch, C. Coffinier, S. Majumdar, M. O. Bergo, S. G. Young, L. G. Fong, A farnesyltransferase inhibitor improves disease phenotypes in mice with a Hutchinson-Gilford progeria syndrome mutation. *J. Clin. Invest.* **116**, 2115–2121 (2006).
33. H. Sagelius, Y. Rosengardten, M. Hanif, M. R. Erdos, B. Rozell, F. S. Collins, M. Eriksson, Targeted transgenic expression of the mutation causing Hutchinson-Gilford progeria syndrome leads to proliferative and degenerative epidermal disease. *J. Cell Sci.* **121**, 969–978 (2008).
34. Y. Wang, A. A. Panteleyev, D. M. Owens, K. Djabali, C. L. Stewart, H. J. Worman, Epidermal expression of the truncated prelamin A causing Hutchinson–Gilford progeria syndrome: Effects on keratinocytes, hair and skin. *Hum. Mol. Genet.* **17**, 2357–2369 (2008).

35. F. G. Osorio, C. L. Navarro, J. Cadiñanos, I. C. López-Mejia, P. M. Quirós, C. Bartoli, J. Rivera, J. Tazi, G. Guzman, I. Varela, D. Depetris, F. de Carlos, J. Cobo, V. Andres, A. De Sandre-Giovannoli, J. M. P. Freije, N. Lévy, C. Lopez-Otin, Splicing-directed therapy in a new mouse model of human accelerated aging. *Sci. Transl. Med.* **3**, 106ra107 (2011).
36. E. Schmidt, O. Nilsson, A. Koskela, J. Tuukkanen, C. Ohlsson, B. Rozell, M. Eriksson, Expression of the Hutchinson-Gilford progeria mutation during osteoblast development results in loss of osteocytes, irregular mineralization, and poor biomechanical properties. *J. Biol. Chem.* **287**, 33512–33522 (2012).
37. J.-H. Baek, E. Schmidt, N. Viceconte, C. Strandgren, K. Pernold, T. J. C. Richard, F. W. Van Leeuwen, N. P. Dantuma, P. Damberg, K. Hultenby, B. Ulfhake, E. Mugnaini, B. Rozell, M. Eriksson, Expression of progerin in aging mouse brains reveals structural nuclear abnormalities without detectible significant alterations in gene expression, hippocampal stem cells or behavior. *Hum. Mol. Genet.* **24**, 1305–1321 (2015).
38. J. M. Lee, C. Nobumori, Y. Tu, C. Choi, S. H. Yang, H.-J. Jung, T. A. Vickers, F. Rigo, C. F. Bennett, S. G. Young, L. G. Fong, Modulation of *LMNA* splicing as a strategy to treat prelamin A diseases. *J. Clin. Invest.* **126**, 1592–1602 (2016).
39. R. Varga, M. Eriksson, M. R. Erdos, M. Olive, I. Harten, F. Kolodgie, B. C. Capell, J. Cheng, D. Faddah, S. Perkins, H. Avallone, H. San, X. Qu, S. Ganesh, L. B. Gordon, R. Virmani, T. N. Wight, E. G. Nabel, F. S. Collins, Progressive vascular smooth muscle cell defects in a mouse model of Hutchinson–Gilford progeria syndrome. *Proc. Natl. Acad. Sci. U.S.A.* **103**, 3250–3255 (2006).
40. W. E. Stehbens, S. J. Wakefield, E. Gilbert-Barness, R. E. Olson, J. Ackerman, Histological and ultrastructural features of atherosclerosis in progeria. *Cardiovasc. Pathol.* **8**, 29–39 (1999).
41. W. E. Stehbens, B. Delahunt, T. Shozawa, E. Gilbert-Barness, Smooth muscle cell depletion and collagen types in progeric arteries. *Cardiovasc. Pathol.* **10**, 133–136 (2001).
42. M. Song, H. San, S. A. Anderson, R. O. Cannon III, D. Orlic, Shear stress-induced mechanotransduction protein deregulation and vasculopathy in a mouse model of progeria. *Stem Cell Res. Ther.* **5**, 41 (2014).
43. A. A. Geisterfer, M. J. Peach, G. K. Owens, Angiotensin II induces hypertrophy, not hyperplasia, of cultured rat aortic smooth muscle cells. *Circ. Res.* **62**, 749–756 (1988).
44. H.-J. Jung, Y. Tu, S. H. Yang, A. Tatar, C. Nobumori, D. Wu, S. G. Young, L. G. Fong, New *Lmna* knock-in mice provide a molecular mechanism for the 'segmental aging' in Hutchinson–Gilford progeria syndrome. *Hum. Mol. Genet.* **23**, 1506–1515 (2014).
45. J.-J. Chiu, S. Chien, Effects of disturbed flow on vascular endothelium: Pathophysiological basis and clinical perspectives. *Physiol. Rev.* **91**, 327–387 (2011).
46. P. Assemat, K. K. Siu, J. A. Armitage, S. N. Hokke, A. Dart, J. Chin-Dusting, K. Hourigan, Haemodynamical stress in mouse aortic arch with atherosclerotic plaques: Preliminary study of plaque progression. *Comput. Struct. Biotechnol. J.* **10**, 98–106 (2014).
47. F. Haque, D. J. Lloyd, D. T. Smallwood, C. L. Dent, C. M. Shanahan, A. M. Fry, R. C. Trembath, S. Shackleton, SUN1 interacts with nuclear lamin A and cytoplasmic nesprins to provide a physical connection between the nuclear lamina and the cytoskeleton. *Mol. Cell. Biol.* **26**, 3738–3751 (2006).
48. P. J. Stewart-Hutchinson, C. M. Hale, D. Wirtz, D. Hodzic, Structural requirements for the assembly of LINC complexes and their function in cellular mechanical stiffness. *Exp. Cell Res.* **314**, 1892–1905 (2008).
49. D. Razafsky, C. Potter, D. Hodzic, Validation of a mouse model to disrupt LINC complexes in a cell-specific manner. *J. Vis. Exp.* **1**, e53318 (2015).
50. R. Holtwick, M. Gotthardt, B. Skryabin, M. Steinmetz, R. Potthast, B. Zetsche, R. E. Hammer, J. Herz, M. Kuhn, Smooth muscle-selective deletion of guanylyl cyclase-A prevents the acute but not chronic effects of ANP on blood pressure. *Proc. Natl. Acad. Sci. U.S.A.* **99**, 7142–7147 (2002).
51. M. D. Muzumdar, B. Tasic, K. Miyamichi, L. Li, L. Luo, A global double-fluorescent Cre reporter mouse. *Genesis* **45**, 593–605 (2007).
52. L. B. Gordon, I. A. Harten, M. E. Patti, A. H. Lichtenstein, Reduced adiponectin and HDL cholesterol without elevated C-reactive protein: Clues to the biology of premature atherosclerosis in Hutchinson-Gilford Progeria Syndrome. *J. Pediatr.* **146**, 336–341 (2005).
53. R. C. Hennekam, Hutchinson-Gilford progeria syndrome: Review of the phenotype. *Am. J. Med. Genet.* **140**, 2603–2624 (2006).
54. C. L. Moulson, L. G. Fong, J. M. Gardner, E. A. Farber, G. Go, A. Passariello, D. K. Grange, S. G. Young, J. H. Miner, Increased progerin expression associated with unusual LMNA mutations causes severe progeroid syndromes. *Hum. Mutat.* **28**, 882–889 (2007).
55. K. A. Turlo, J. Scapa, P. Bagher, A. W. Jones, R. Feil, R. J. Korthuis, S. S. Segal, M. L. Iruela-Arispe, β1-Integrin is essential for vasoregulation and smooth muscle survival in vivo. *Arterioscler. Thromb. Vasc. Biol.* **33**, 2325–2335 (2013).
56. N. E. Sibinga, L. C. Foster, C. M. Hsieh, M. A. Perrella, W. S. Lee, W. O. Endege, E. H. Sage, M. E. Lee, E. Haber, Collagen VIII is expressed by vascular smooth muscle cells in response to vascular injury. *Circ. Res.* **80**, 532–541 (1997).
57. J. Lopes, E. Adiguzel, S. Gu, S.-L. Liu, G. Hou, S. Heximer, R. K. Assoian, M. P. Bendeck, Type VIII collagen mediates vessel wall remodeling after arterial injury and fibrous cap formation in atherosclerosis. *Am. J. Path.* **182**, 2241–2253 (2013).
58. J.-W. Shin, K. R. Spinler, J. Swift, J. A. Chasis, N. Mohandas, D. E. Discher, Lamins regulate cell trafficking and lineage maturation of adult human hematopoietic cells. *Proc. Natl. Acad. Sci. U.S.A.* **110**, 18892–18897 (2013).
59. T. Shimi, V. Butin-Israeli, S. A. Adam, R. B. Hamanaka, A. E. Goldman, C. A. Lucas, D. K. Shumaker, S. T. Kosak, N. S. Chandel, R. D. Goldman, The role of nuclear lamin B1 in cell proliferation and senescence. *Genes Dev.* **25**, 2579–2593 (2011).
60. J. L. V. Broers, E. A. G. Peeters, H. J. H. Kuijpers, J. Endert, C. V. C. Bouten, C. W. J. Oomens, F. P. T. Baaijens, F. C. S. Ramaekers, Decreased mechanical stiffness in LMNA−/− cells is caused by defective nucleo-cytoskeletal integrity: Implications for the development of laminopathies. *Hum. Mol. Genet.* **13**, 2567–2580 (2004).
61. M. Raab, M. Gentili, H. de Belly, H.-R. Thiam, P. Vargas, A. J. Jimenez, F. Lautenschlaeger, R. Voituriez, A.-M. Lennon-Duménil, N. Manel, M. Piel, ESCRT III repairs nuclear envelope ruptures during cell migration to limit DNA damage and cell death. *Science* **352**, 359–362 (2016).
62. P. Jevtic, L. J. Edens, X. Li, T. Nguyen, P. Chen, D. L. Levy, Concentration-dependent effects of nuclear lamins on nuclear size in *Xenopus* and mammalian cells. *J. Biol. Chem.* **290**, 27557–27571 (2015).
63. D. J. Klionsky, E.-L. Eskelinen, V. Deretic, Autophagosomes, phagosomes, autolysosomes, phagolysosomes, autophagolysosomes… wait, I'm confused. *Autophagy* **10**, 549–551 (2014).
64. M. C. H, Clarke, N. Figg, J. J. Maguire, A. P. Davenport, M. Goddard, T. D. Littlewood, M. R. Bennett, Apoptosis of vascular smooth muscle cells induces features of plaque vulnerability in atherosclerosis. *Nat. Med.* **12**, 1075–1080 (2006).
65. A. J. Lusis, Atherosclerosis. *Nature* **407**, 233–241 (2000).
66. M. O. Bergo, B. Gavino, J. Ross, W. K. Schmidt, C. Hong, L. V. Kendall, A. Mohr, M. Meta, H. Genant, Y. Jiang, E. R. Wisner, N. van Bruggen, R. A. D. Carano, S. Michaelis, S. M. Griffey, S. G. Young, *Zmpste24* deficiency in mice causes spontaneous bone fractures, muscle weakness, and a prelamin A processing defect. *Proc. Natl. Acad. Sci. U.S.A.* **99**, 13049–13054 (2002).
67. S. S. M. Rensen, P. A. F. M. Doevendans, G. J. J. M. van Eys, Regulation and characteristics of vascular smooth muscle cell phenotypic diversity. *Neth. Heart J.* **15**, 100–108 (2007).
68. L. G. Fong, J. K. Ng, J. Lammerding, T. A. Vickers, M. Meta, N. Coté, B. Gavino, X. Qiao, S. Y. Chang, S. R. Young, S. H. Yang, C. L. Stewart, R. T. Lee, C. F. Bennett, M. O. Bergo, S. G. Young, Prelamin A and lamin A appear to be dispensable in the nuclear lamina. *J. Clin. Invest.* **116**, 743–752 (2006).
69. L. G. Fong, J. K. Ng, M. Meta, N. Coté, S. H. Yang, C. L. Stewart, T. Sullivan, A. Burghardt, S. Majumdar, K. Reue, M. O. Bergo, S. G. Young, Heterozygosity for *Lmna* deficiency eliminates the progeria-like phenotypes in *Zmpste24*-deficient mice. *Proc. Natl. Acad. Sci. U.S.A.* **101**, 18111–18116 (2004).

Acknowledgments: We thank D. Di Carlo (UCLA) for the use of the plasma cleaner and L. Edillo for assistance with quantification of misshapen nuclei. Virus production and transduction were performed by the Integrated Molecular Technologies Core (IMTC)/UCLA Vector Core, which is supported by CURE/P30 DK041301. **Funding:** This work was supported by the NIH (AG047192 and AG035626). **Author contributions:** Designing research studies: P.H.K., S.G.Y., and L.G.F. Conducting experiments: P.H.K., J.L., P.H., Y.T., T.A.W., C.L., N.C., R.L.L., and L.G.F. Providing reagents: P.-Y.L., J.C.Y.D., and D.H. Writing the manuscript: P.H.K., S.G.Y., and L.G.F. **Competing interests:** The authors declare that they have no competing interests. **Data and materials availability:** All data associated with this study are present in the paper or the Supplementary Materials.

Submitted 27 March 2018
Accepted 7 September 2018
Published 26 September 2018
10.1126/scitranslmed.aat7163

Citation: P. H. Kim, J. Luu, P. Heizer, Y. Tu, T. A. Weston, N. Chen, C. Lim, R. L. Li, P.-Y. Lin, J. C. Y. Dunn, D. Hodzic, S. G. Young, L. G. Fong, Disrupting the LINC complex in smooth muscle cells reduces aortic disease in a mouse model of Hutchinson-Gilford progeria syndrome. *Sci. Transl. Med.* **10**, eaat7163 (2018).

Science Translational Medicine
AAAS

www.sciencetranslationalmedicine.org/cgi/content/full/10/460/eaat7163/DC1

Supplementary Materials for

Disrupting the LINC complex in smooth muscle cells reduces aortic disease in a mouse model of Hutchinson-Gilford progeria syndrome

Paul H. Kim, Jennings Luu, Patrick Heizer, Yiping Tu, Thomas A. Weston, Natalie Chen, Christopher Lim, Robert L. Li, Po-Yu Lin, James C. Y. Dunn, Didier Hodzic, Stephen G. Young*, Loren G. Fong*

*Corresponding author. Email: lfong@mednet.ucla.edu (L.G.F.); sgyoung@mednet.ucla.edu (S.G.Y.)

Published 26 September 2018, *Sci. Transl. Med.* **10**, eaat7163 (2018)
DOI: 10.1126/scitranslmed.aat7163

The PDF file includes:

Other Supplementary Material for this manuscript includes the following:

(available at www.sciencetranslationalmedicine.org/cgi/content/full/10/460/eaat7163/DC1)

Table S3 (Microsoft Excel format). Individual subject-level data.

Materials and Methods

pTRIPZ-Prelamin A and pTRIPZ-progerin lentiviral vectors. A human prelamin A cDNA in pCMV-XL5 vector (#SC101048) was purchased from Origene. A human progerin cDNA was created by deleting 150 nucleotides (1818–1968) from the prelamin A cDNA with the QuikChange Lightening kit (Agilent) and mutagenic primers (forward primer, 5′-GCTCAGGAGCCCAGAGCCCCCAGAACTG-3′; reverse primer, 5′-CAGTTCTGGGGGCTCTGGGCTCCTGAGC-3′). The doxycycline-inducible vector pTRIPZ-hDDX5/17 (Addgene) was digested with restriction enzymes *Age*I and *Eco*RI to delete the red fluorescence protein and shRNA sequences and then gel-purified. The human prelamin A and progerin cDNAs were amplified with the Titanium Taq PCR kit (Clontech) and sequence-specific primers (forward primer, 5′-GTCAGATCGCACCGGATGGAGACCCCGTCCCAG-3′; and reverse primer, 5′-GTAGCCCCTTGAATTTTACATGATGCTGCAGTTCTGGGG-3′). The fragments were purified with UltraClean15 (Mo-bio) and subcloned into the prepared pTRIPZ vector with In-Fusion Cloning (Clontech). The products were amplified in XL10-Gold Ultracompetent cells (Agilent) and plasmids with the correct sequence were isolated with plasmid kits (Qiagen). Packaging of lentivirus and transduction of cells were performed by UCLA's Vector Core. Transduced cells were selected for two weeks with 1.5 μg/ml puromycin.

pLenti6-EGFP-KASH2 and pLenti6-EGFP-KASHext lentiviral vectors. The EGFP-KASH2 sequence was amplified from pEGFP-C1-KASH2 (*48*) with the TaKaRa LA PCR kit (Clontech) and sequence-specific primers (forward primer, 5′-ACACCGACTCTAGAGATGGTGAGCAAGGGCGAGGA-3′; and reverse primer, 5′-GCGGGCCCTCTAGACCTAGGTGGGAGGTGGCCCGT-3′). The EGFP-KASHext sequence was amplified from pEGFP-C1-KASHext (*48*) with the TaKaRa LA PCR kit (Clontech) and

sequence-specific primers (forward primer, 5′-ACACCGACTCTAGAGATGGTGAGCAAGGGCGAGGA-3′; and reverse primer, 5′-GCGGGCCCTCTAGACTTATCTAGATCCGGTGGATC-3′). The gel-purified fragments were subcloned into the pLenti6/v5-DEST plasmid (ThermoFisher) (linearized with *Bam*HI and *Xho*I), with In-Fusion Cloning (Clontech). The products were amplified in XL10-Gold Ultracompetent cells (Agilent) and plasmids with the correct sequences were isolated with plasmid kits (Qiagen). Packaging of lentivirus and transduction of pTRIPZ-prelamin A or pTRIPZ-progerin cells were performed by UCLA's Vector Core. Transduced cells were selected for two weeks with 2 μg/ml blasticidin.

Western blotting. Urea-soluble protein extracts from cells and tissues were prepared as described (*38*). Proteins were size-fractionated on 4–12% gradient polyacrylamide Bis-Tris gels (Invitrogen) and transferred to nitrocellulose membranes. The membranes were blocked with Odyssey Blocking solution (LI-COR Bioscience) for 1 h at RT and incubated with primary antibodies at 4° C overnight. After washing the membranes with PBS containing 0.2% Tween-20, they were incubated with infrared dye (IR)–labeled secondary antibodies at RT for 1 h. The IR signals were quantified with an Odyssey infrared scanner (LI-COR Biosciences). The antibodies and concentrations are listed in table S1.

Immunofluorescence microscopy. Cells on coverslips or tissue sections (6–10-μm-thick) on glass slides were fixed with 4% paraformaldehyde in PBS and permeabilized with 0.2% Triton. The cells were processed for immunofluorescence microscopy as described (*68, 69*). The antibodies and concentrations are listed in table S1. Confocal fluorescence microscopy images were obtained with a Zeiss LSM700 laser–scanning microscope and images along the *z*-axis were processed by Zen 2010 software (Zeiss) to generate maximum image projections. Nuclear

shape abnormalities in cells were scored by two independent trained observers blinded to genotype (*68, 69*). A minimum of 200 cells were scored for each group.

Histological analysis. Mice were perfused in situ with PBS followed by fixative solution (3% paraformaldehyde in PBS). The entire thoracic aorta was dissected free and incubated in fixative solution for 24–48 h at 4° C. Aortic rings (~2-mm-long) from the proximal ascending aorta, mid-arch, proximal descending, and mid-descending aorta were embedded in paraffin, and sections (4–6-μm) were stained with hematoxylin and eosin (H&E), Masson's trichrome, or Verhoeff-Van Gieson stain by UCLA's Translational Pathology Core Laboratory. The stained sections were coded, and photographs captured on a Nikon E600 light microscope with 20× and 40× objectives with a Nikon DS-Fi2 camera operated by NIS Elements software (Version 4.0). The images (tiff format) were imported into ImageJ1.50i, and the areas of the media and adventitia were measured. The number of nuclei in the media were counted and expressed as #nuclei/media area. Adventitial area was expressed as a percentage of total area [adventitia area/(adventitia area + media area)].

Quantitative real time-PCR. Total RNA was isolated and treated with DNase I (Ambion, Life Technologies). RNA was reverse-transcribed with random primers, oligo(dT), and SuperScript III (Invitrogen). qPCR reactions were performed on a 7900HT Fast Real-Time PCR system (Applied Biosystems) with SYBR Green PCR Master Mix (Bioline). Transcript amounts were determined by the comparative cycle threshold method and normalized to the expression of cyclophilin A. Primer sequences are listed in table S2.

Electron microscopy. Mice were perfused *in situ* with PBS followed by ice-cold fixative (3% paraformaldehyde in PBS). Aortic samples were incubated overnight in glutaraldehyde fixative solution containing 2.5% glutaraldehyde (EMS), 4% paraformaldehyde (EMS), 2.1% sucrose

(Sigma) and buffered with 0.1 M sodium cacodylate (Sigma). The following day, tissues were rinsed three times with 0.1 M sodium cacodylate and fixed with 2% osmium tetroxide (EMS) buffered with 0.1 M sodium cacodylate at RT for 1 h. The samples were rinsed three times with distilled water and stained overnight with 2% uranyl acetate at 4° C. The samples were rinsed three times with distilled water and dehydrated with increasing concentrations of acetone (30%, 50%, 70%, 85%, 95%, 100%; 3 × 10 min each) before infiltration with Spurr's epoxy resin (EMS) in acetone (33% for 2 h; 66% overnight; 100% for 4 h). The samples were flat-embedded in caps of BEEM capsules (EMS) and polymerized in a vacuum oven at 65° C for 24 h. The polymerized "pucks" were removed from the caps and glued onto the tops of polymerized BEEM capsules for trimming and sectioning. Sections (65-nm) were cut on a Leica UC6 ultramicrotome and picked up on freshly glow-discharged copper grids (Ted Pella) that were coated with formvar and carbon. Sections on grids were then stained with Reynold's lead citrate solution for 10 min. Images were acquired with an FEI T12 transmission electron microscope set to 120 kV accelerating voltage and a Gatan 2K × 2K digital camera (Electron Imaging Center) or with a JEOL 100CX electron microscope set at 60 kV on type 4489 EM film (BRI Electron Microscopy Core Facility). Film negatives were scanned to create digital files.

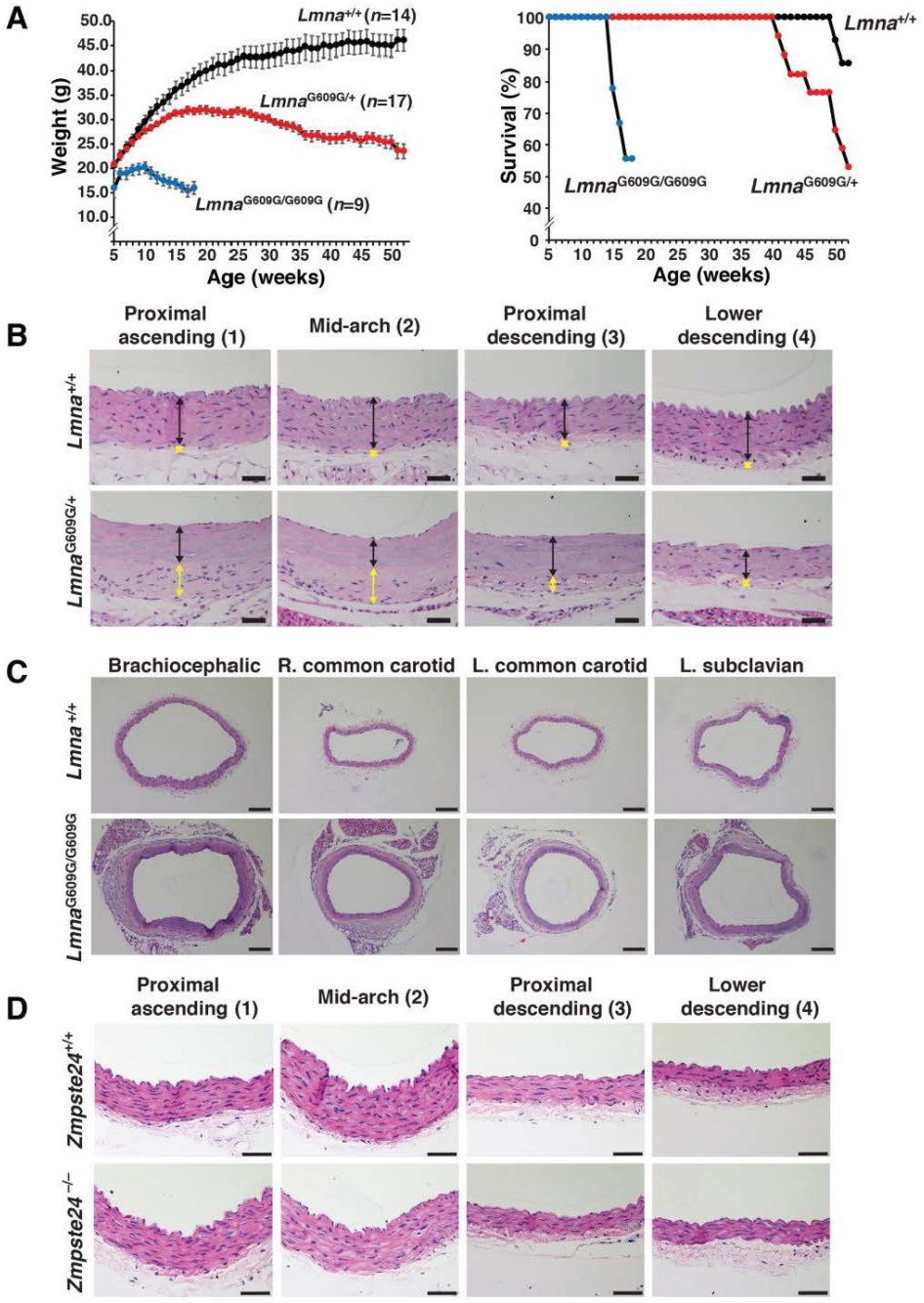

Fig. S1. Pathology in *Lmna*^{G609G} mice. (A) Body weight gain and survival curves for *Lmna*$^{+/+}$ (black line; n = 14), *Lmna*$^{G609G/+}$ (red line; n = 17), and *Lmna*$^{G609G/G609G}$ (blue line; n = 9) mice. (B) H&E-stained sections of different regions of the aorta in 12-month old *Lmna*$^{+/+}$ and *Lmna*$^{G609G/+}$ mice (proximal ascending, mid-arch, proximal descending, and lower descending). Colored arrows identify the media (black) and adventitia (yellow). Scale bars, 20 μm. (C) H&E-

stained sections of the brachiocephalic artery, right (R) common carotid, left (L) common carotid, and L. subclavian artery from 4.5-month-old *Lmna*$^{+/+}$ and *Lmna*$^{G609G/G609G}$ mice. Scale bars, 100 μm. (D) H&E-stained sections of the same regions described in panel B, but collected from 4.5-month-old *Zmpste24*$^{+/+}$ and *Zmpste24*$^{-/-}$ mice. Scale bars, 50 μm.

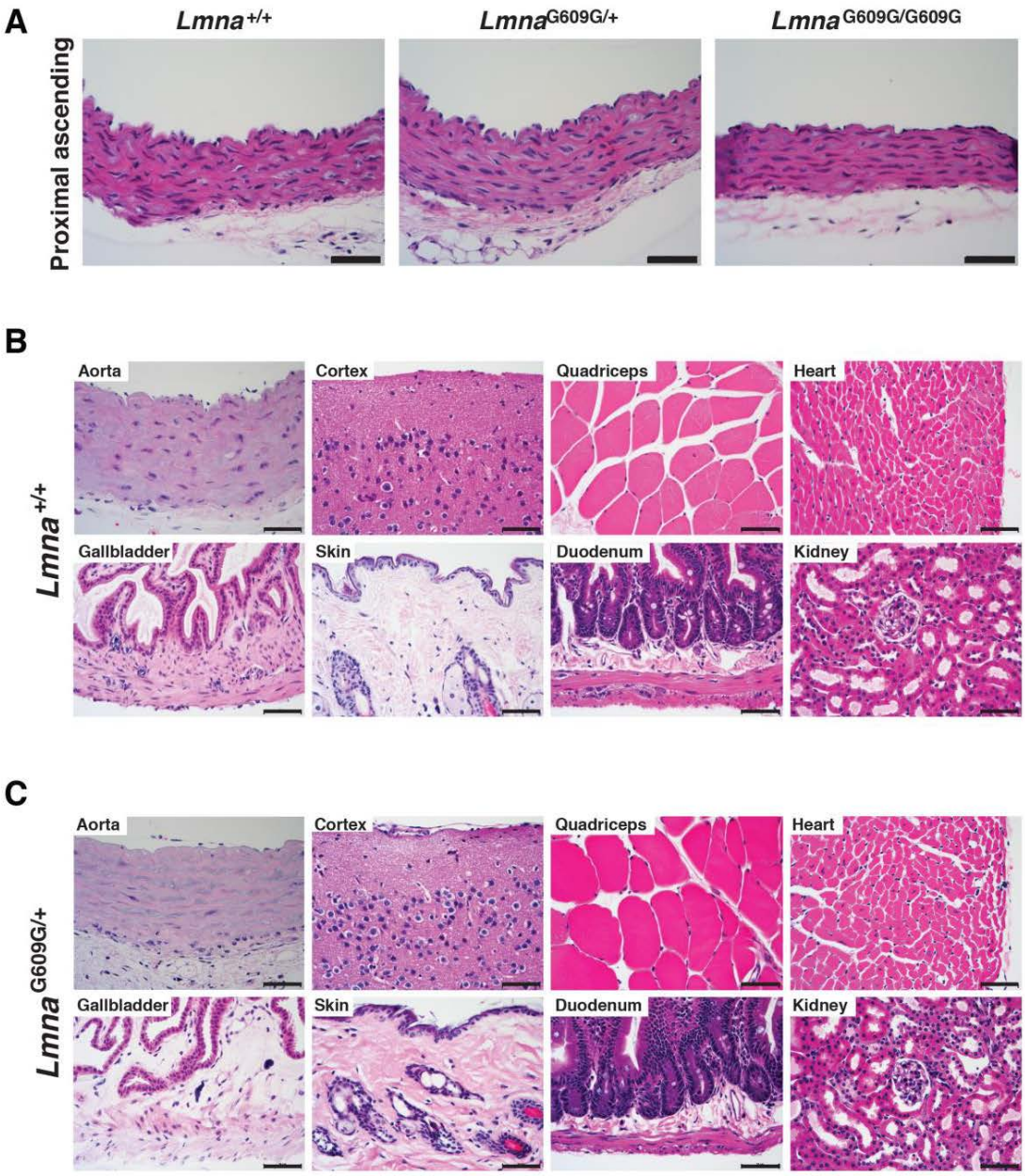

Fig. S2. H&E staining of aortic tissue from young mice and nonaortic tissues from older *Lmna*$^{G609G/+}$ mice. (A) H&E-stained sections of the proximal ascending aorta from 2-month-old wild-type, *Lmna*$^{G609G/+}$, and *Lmna*$^{G609G/G609G}$ mice. Scale bars, 50 μm. (B–C) H&E-stained sections of the proximal ascending aorta, cerebral cortex, quadriceps, heart, gallbladder, skin, duodenum, and kidney from 12-month-old wild-type (B) and *Lmna*$^{G609G/+}$ (C) mice. Scale bars, 50 μm.

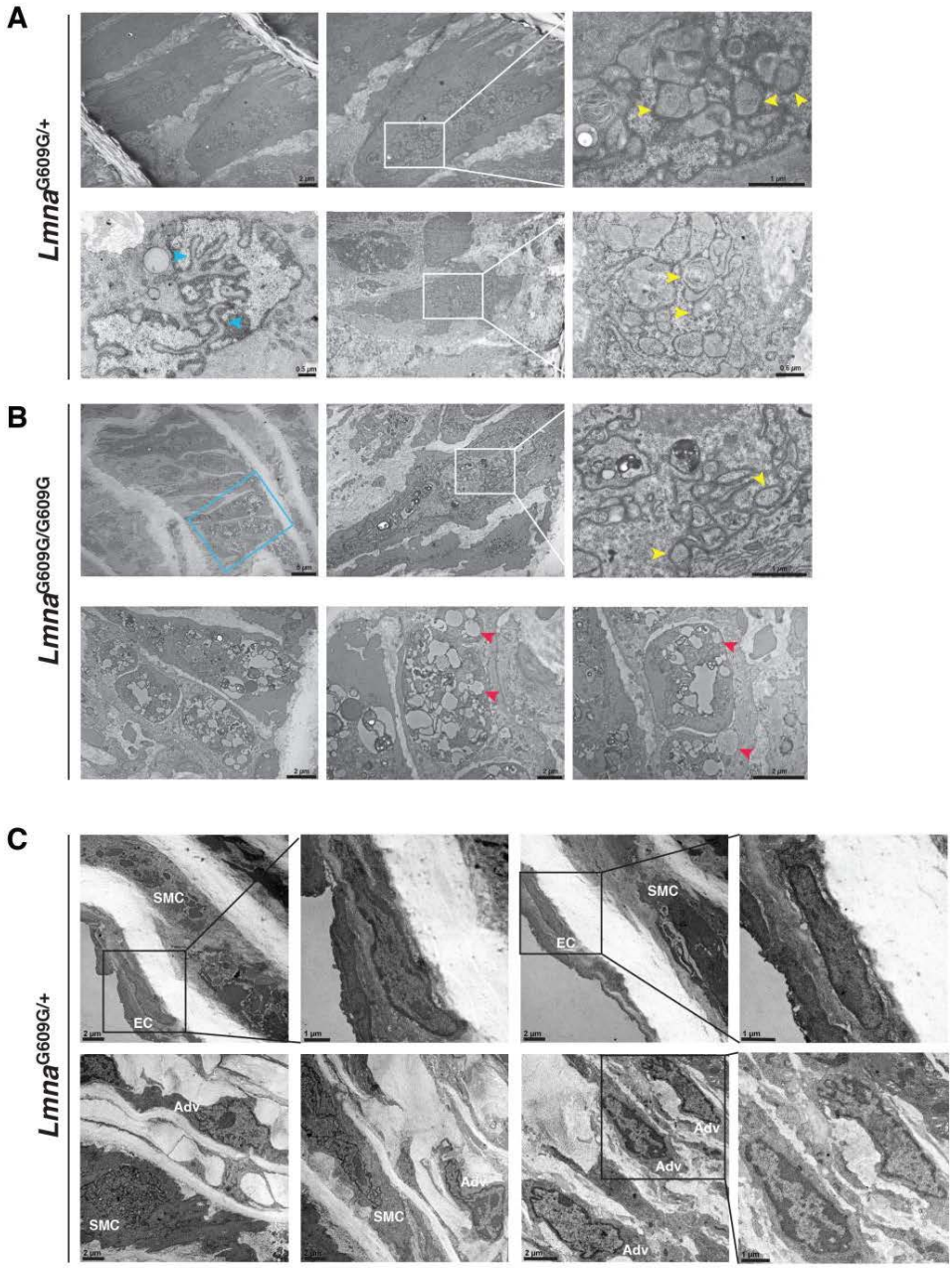

Fig. S3. Cell and nuclear morphology in *Lmna*^{G609G} aortic SMCs. Cell morphology in the thoracic aorta was examined by transmission electron microscopy. (A) Low- and high-magnification images of smooth muscle cells (SMCs) from 9-month-old *Lmna*$^{G609G/+}$ mice. The boxed areas in the middle panels are shown at higher magnification in images to the right. Yellow arrowheads point to intranuclear vesicles, some with cytoplasmic organelles. Blue

arrowheads point to intranuclear tubules. (B) Low- and high-magnification images of SMCs from a 3-month-old *Lmna*$^{G609G/G609G}$ mouse. The blue-colored box is shown at higher magnification in the lower panels. The white-colored box in the middle panel is shown at higher magnification in the image to the right. Yellow arrowheads point to intranuclear vesicles, and red arrowheads point to cytoplasmic vacuoles. (C) Low- and high-magnification images of endothelial cells (EC) (upper row) and adventitial cells (Adv) (lower row) from a 3-month-old *Lmna*$^{G609G/G609G}$ mouse. The black-colored boxes are shown at higher magnification in images to the right. Scale bars are shown in the images.

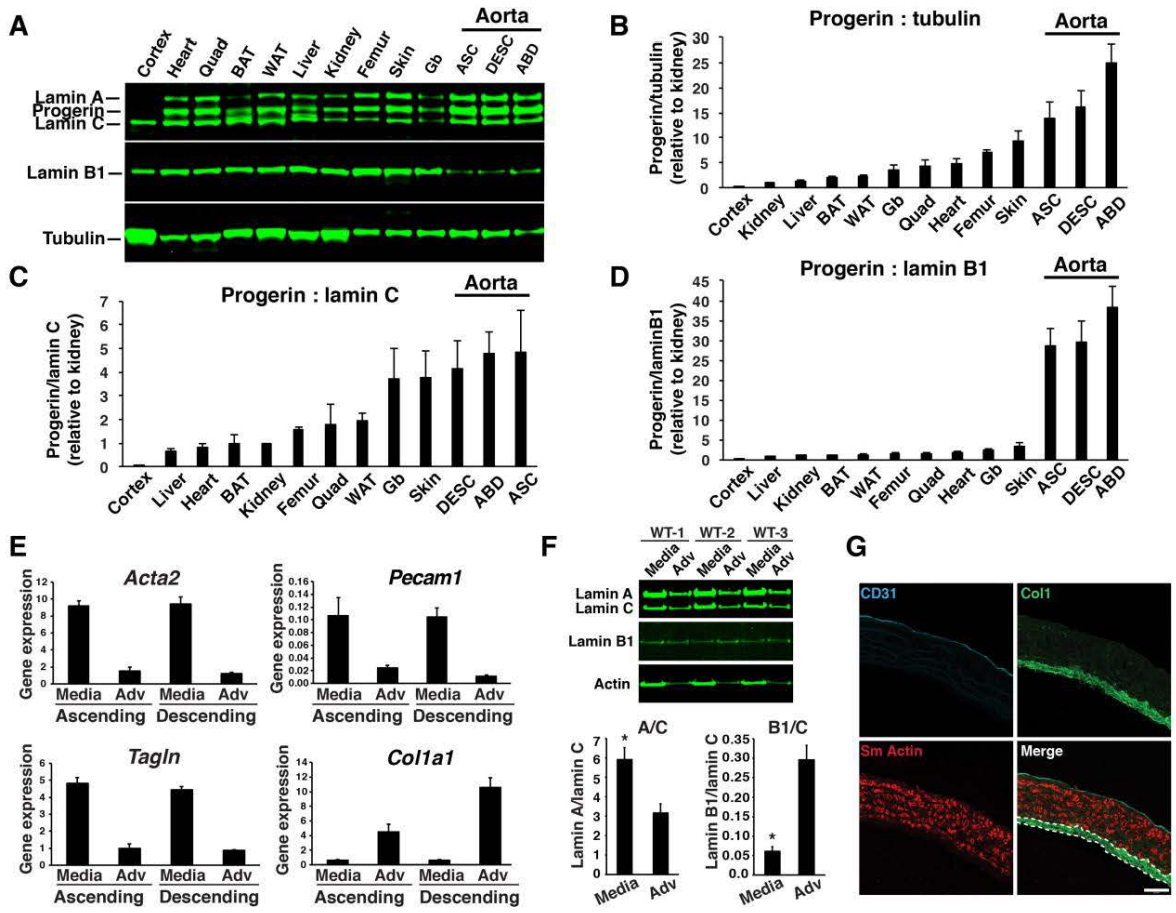

Fig. S4. Nuclear lamin expression in the aorta of WT and *Lmna*$^{G609G/+}$ mice. (A) Representative western blot comparing the expression of lamin A, progerin, lamin C, and lamin B1 in different tissues of *Lmna*$^{G609G/+}$ mice. Tubulin was measured as a loading control. Cortex, cerebral cortex; BAT, brown adipose tissue; WAT, white adipose tissue; Gb, gallbladder; ASC, ascending aorta; DESC, descending aorta; ABD, abdominal aorta. (B) Graph showing progerin expression relative to tubulin. (C) Graph showing progerin expression relative to lamin C. (D) Graph showing progerin expression relative to lamin B1. For panels B–D, tissues are arranged in ascending order from left to right with expression in kidney set at a value of one (means ± SEM; n = 3 mice). (E) Gene-expression studies to validate the isolation of the media and adventitial (Adv) layers (means ± SEM; n = 4 mice). *Acta2* and *Tagln* were measured to identify SMCs;

Pecam1 for endothelial cells; and *Col1a1* for adventitial cells. (F) Western blot comparing the expression of lamin A, lamin C, and lamin B1 in the media and adventitia (Adv) in wild-type mice. Bar graphs show the expression of lamin A (left) and lamin B1 (right) relative to lamin C (means ± SEM; $n = 3$). Media vs. adventitia; $^*P < 0.03$ (t test). (G) Confocal fluorescence microscopy to identify endothelial cells, smooth muscle cells, and adventitia with antibodies against CD31 (cyan), smooth muscle cell actin (red), and collagen type I (green), respectively. In the merged image, the adventitia is outlined by dashed white lines. Scale bars, 50 μm.

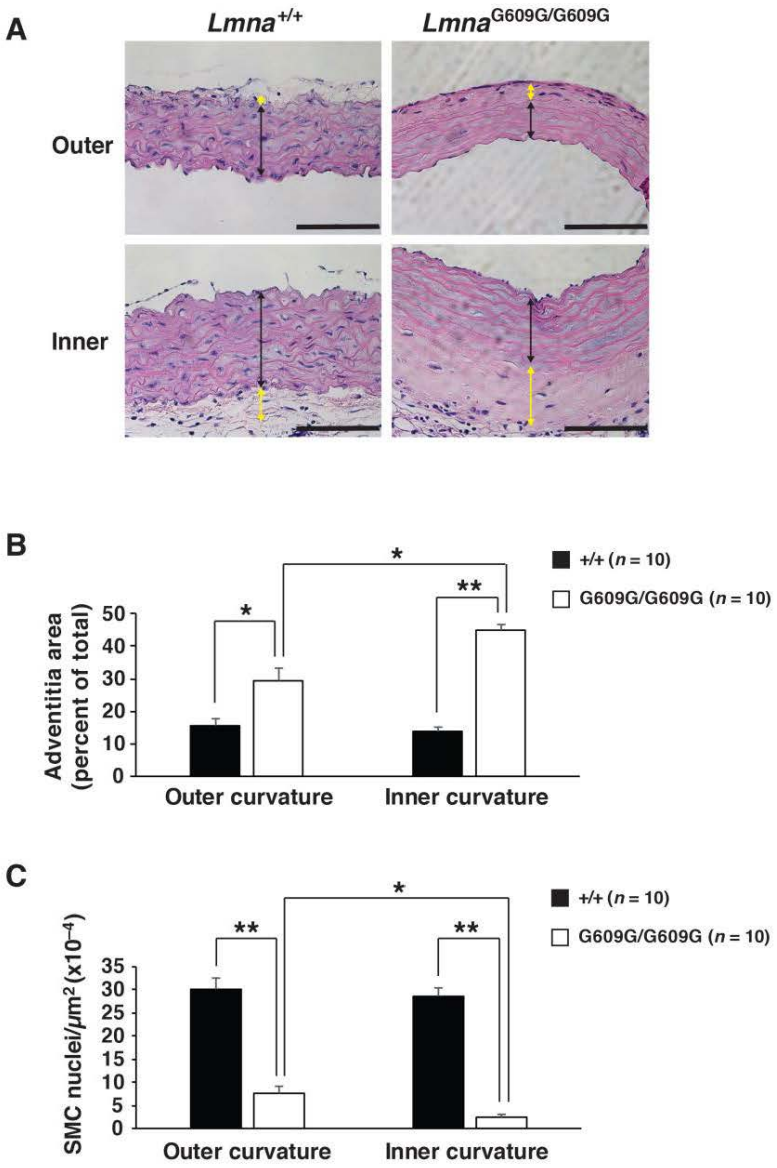

Fig. S5. Analysis of the vascular phenotype in the ascending aorta of *Lmna*$^{G609G/G609G}$ mice. The number of SMC nuclei and adventitial area were quantified at the inner and outer curvature of the ascending thoracic aorta in 4-month-old *Lmna*$^{G609G/G609G}$ mice. The white line in Fig. 4C shows the location where the measurements were made. (A) Representative H&E-stained sections of the inner and outer curvature of the ascending aorta in *Lmna*$^{+/+}$ and *Lmna*$^{G609G/G609G}$ mice. Colored arrows identify the media (black) and adventitia (yellow). Scale bars, 100 μm. (B) Bar graph showing adventitial area (as a percentage of total area) in wild-type (black) and

Lmna$^{G609G/G609G}$ (white) mice at the outer and inner curvature of the ascending aorta. (C) Bar graph showing the number of SMC nuclei (relative to media area) in wild-type (black) and *Lmna*$^{G609G/G609G}$ (white) mice at the outer and inner curvature of the ascending aorta. Means ± SEM for wild-type (n = 10) and *Lmna*$^{G609G/G609G}$ (n = 10) mice. *Lmna*$^{G609G/G609G}$ vs. wild-type; *$P < 0.01$ and **$P < 0.001$ (t test). Results for the inner curvature were reported in Fig. 1E.

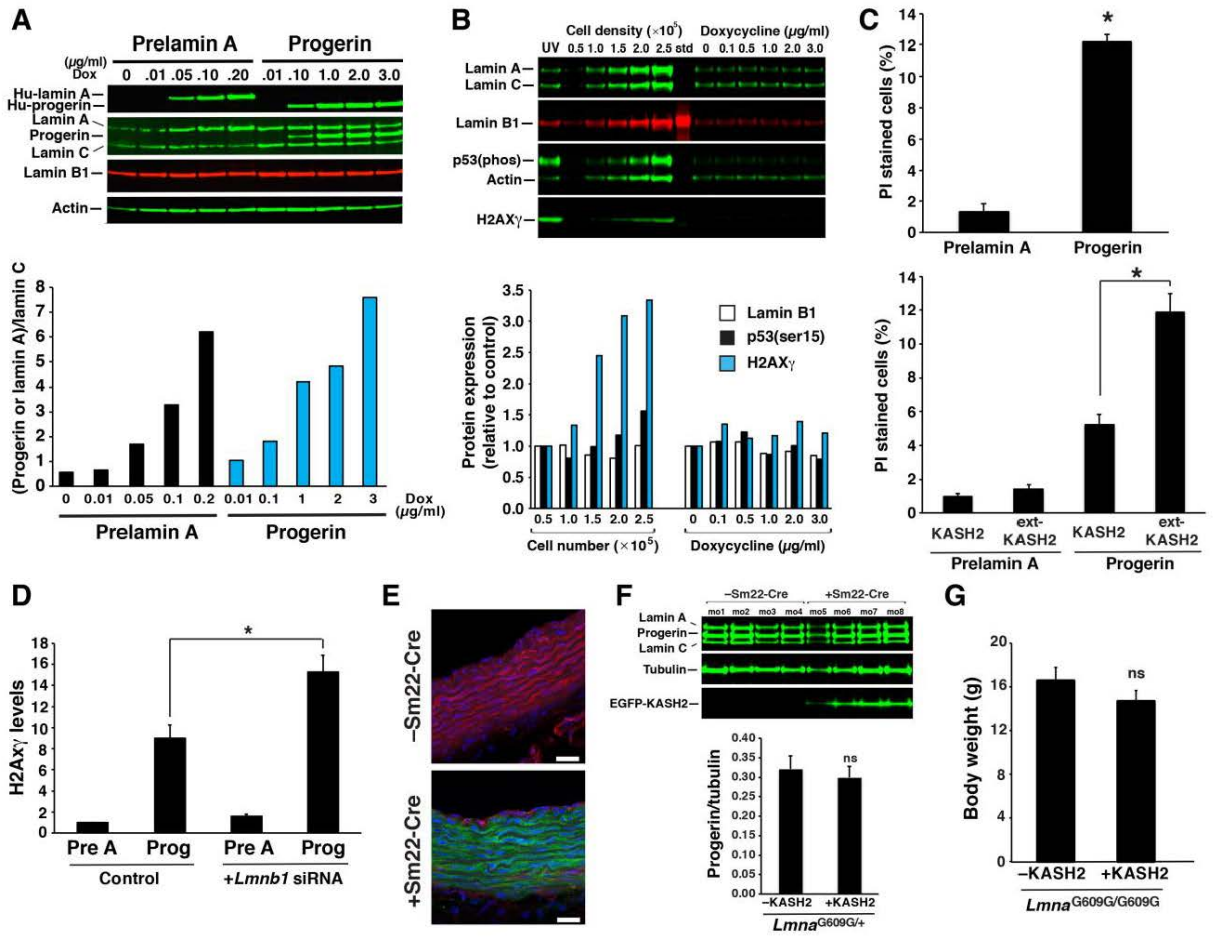

Fig. S6. Control studies for the lamin-inducible SMC system and the *Sm22-Cre*–dependent activation of KASH2 expression in the aorta. (A) Western blot comparing human lamin A and progerin expression in SMCs treated with doxycycline for 1-day. Lamin A and progerin were detected with an antibody specific for human lamin A (top panel). Total A-type lamins (lamin A, progerin, and lamin C) were measured with an antibody that recognizes both human and mouse lamin A/C (middle panel). The bar graph shows the amount of lamin A or progerin, relative to lamin C. (B) Western blot measuring H2AXγ expression in cells cultured at different densities and after treatment with doxycycline. The bar graph shows the expression of lamin B1 (white), phos-p53 (black), and H2AXγ (blue), relative to actin and normalized to either the 0.5×10^5 group or the no-doxycycline group (both set at a value of one). (C) Upper bar graph shows

propidium iodide (PI) staining in prelamin A-expressing cells and progerin-expressing cells after stretching for 2 h at 0.5 Hz (2-mm). The means ± SEM (n = 3 experiments) is shown. Lower bar graph shows the effects of KASH2 expression on PI staining in stretched progerin-expressing cells. Cells expressing the inactive KASH2 mutant (ext-KASH2) is included as a control. The means ± SEM (n = 3 experiments) is shown. *, $P < 0.05$ (t test). (D) Bar graph shows the effects of lamin B1 siRNA treatment on H2AXγ expression in prelamin A (Pre A) and progerin (Prog)-expressing cells. All cells were exposed to repetitive stretching (2-mm at 0.5Hz) for 2 h. SiRNA treatment reduced lamin B1 protein expression by 45% (n = 3). The bar graph shows H2AX-γ amounts relative to control-treated Pre A–expressing cells. The means ± SEM (n = 3 experiments) is shown. Control vs. *Lmnb1* siRNA-treated; *$P < 0.05$ (t test). (E) The expression pattern for the *Sm22-Cre* transgene was examined by intercrossing *Sm22-Cre* transgenic mice with the mT/mG reporter mouse. *Cre*-mediated recombination was identified by EGFP fluorescence (green). Scale bar, 20 μm. (F) Western blot shows the effects of KASH2–EGFP expression in SMCs (+Sm22-Cre) on progerin amounts in the aorta of $Lmna^{G609G/+}$ mice. The KASH2–EGFP fusion protein was detected with an antibody against GFP. Tubulin was used as a loading control. mo, mouse. Bar graph shows progerin amounts relative to tubulin. The means ± SEM (n = 4 mice/group) is shown. ns (nonsignificant), $P > 0.10$ (t test). (G) Bar graph shows the effects of KASH2 expression in SMCs (+KASH2) on body weight in $Lmna^{G609G/G609G}$ mice at 16-weeks of age. The means ± SEM (n = 6 mice/group) is shown. ns, $P > 0.10$ (t test).

Table S1. Antibodies used for Western blotting and immunohistochemistry.

Antibody Description	Species	Source	Catalog #	Use	Dilution
β-actin	Rabbit	Abcam	ab8227	WB, IF	1:3000
β-actin	Goat	Santa Cruz Biotech	SC1616	WB, IF	1:3000
CD31	Rat	BD Pharmingen	553370	IF	1:100
Collagen type I	Rabbit	Abcam	ab21286	IF	1:200
Collagen type III	Rabbit	Abcam	ab7778	IF	1:100
Collagen type IV	Rabbit	BioRad	2150-1470	IF	1:100
Collagen type V	Rabbit	Abcam	ab7046	IF	1:100
Collagen type VIII	Rabbit	Antibodies-online	ABIN1718654	IF	1:20
GFP	Rabbit	ThermoFisher	A11122	WB, IF	1:1000
GFP	Chicken	Aves Lab	GFP1020	WB, IF	1:1000
Human lamin A	Mouse	Millipore	MAB3211	WB, IF	1:1500
Lamin A/C	Goat	Santa Cruz Biotech	SC6215S	WB, IF	1:1000
Lamin A/C	Mouse	Santa Cruz Biotech	SC376248	WB, IF	1:1500
Lamin B1	Goat	Santa Cruz Biotech	SC6217	WB, IF	1:1500
LAP2β	Mouse	BD	611000	IF	1:2000

		Pharmingen			
Nesprin2	Rabbit	In-house	Not applicable	IF	1:1000
Phospho-H2AX	Mouse	Millipore	05-636	WB, IF	1:3000
p53(Ser15)	Rabbit	Cell Signaling Technology	9284	WB, IF	1:3000
Prelamin A (3C8)	Rat	In-house	Not applicable	WB	2 µg/ml
Sm-actin	Goat	Sigma	SAB2500963	IF	1:100
Tubulin	Rat	Novus Bio	NB600-506	WB	1:3000
Anti-rabbit IR800	Donkey	LI-COR	926-32213	WB	1:10000
Anti-goat IR800	Donkey	LI-COR	926-32214	WB	1:10000
Anti-rat IR800	Donkey	ThermoFisher	SA5-10032	WB	1:5000
Anti-mouse IR800	Donkey	ThermoFisher	SA5-10172	WB	1:5000
Anti-rabbit IR680	Donkey	LI-COR	926-32221	WB	1:5000
Anti-rat IR680	Goat	LI-COR	925-68076	WB	1:5000
Anti-chicken IR800	Goat	Rockland	603-131-126	WB	1:5000
Anti-chicken Alexa 488	Goat	Invitrogen	A11039	IF	1:2000
Anti-mouse Alexa 488	Donkey	Invitrogen	A21202	IF	1:2000
Anti-rabbit Alexa 488	Donkey	Invitrogen	A21206	IF	1:2000
Anti-goat Alexa 488	Donkey	Invitrogen	A11055	IF	1:2000
Anti-goat Alexa 555	Donkey	Invitrogen	A21432	IF	1:2000

Anti-rabbit Alexa 555	Donkey	Invitrogen	A31572	IF	1:200
Anti-rabbit Alexa 568	Donkey	Invitrogen	A10042	IF	1:2000
Anti-mouse Alexa 568	Donkey	Invitrogen	A10037	IF	1:2000
Anti-mouse Alexa 647	Donkey	Invitrogen	A31571	IF	1:2000
Anti-rabbit Alexa 647	Donkey	Invitrogen	A31573	IF	1:2000
Anti-goat Alexa 647	Donkey	Invitrogen	A21447	IF	1:2000
Anti-rat Alexa 650	Donkey	ThermoFisher	SA5-10029	IF	1:200

Table S2. Quantitative RT-PCR primers.

Gene	Forward	Reverse
Col1a1	TGACTGGAAGAGCGGAGAGT	GACGGCTGAGTAGGGAACAC
Col3a1	GACCAAAAGGTGATGCTGGACAG	CAAGACCTCGTGCTCCAGTTAG
Col4a1	ATGGCTTGCCTGGAGAGATAGG	TGGTTGCCCTTTGAGTCCTGGA
Col5a1	AGATGGCATCCGAGGTCTGAAG	GACCTTCAGGACCATCTTCTCC
Col8a1	GCTGCTGGGAATACTGTTCA	GGGTAGGTGTGGGTACTCTTT
Acta2	TCCCTGGAGAAGAGCTACGAACT	GATGCCCGCTGACTCCAT
Prelamin A	GGTTGAGGACAATGAGGATGA	TGAGCGCAGGTTGTACTCAG
Lmnb1	CAACTGACCTCATCTGGAAGAAC	TGAAGACTGTGCTTCTCTGAGC
Pecam1	CCTCAGTCGGCAGACAAGAT	ATGGATGCTGTTGATGGTGA
Tagln	CCGAAGCTACTCTCCTTCCA	GACTGCACTTCTCGGCTCAT
Lamin C	GACAATGAGGATGACGACGAG	TTAATGAAAAGACTTTGGCATGG
Ppia	TGAGCACTGGAGAGAAAGGA	CCATTATGGCGTGTAAAGTCA

Table S3. Individual subject-level data.
See Excel sheet.

Chapter 3:

Nuclear Membrane Ruptures Underlie the Vascular Pathology in a Mouse Model of Hutchinson-Gilford Progeria Syndrome

JCI insight

RESEARCH ARTICLE

Nuclear membrane ruptures underlie the vascular pathology in a mouse model of Hutchinson-Gilford progeria syndrome

Paul H. Kim,[1,2] Natalie Y. Chen,[1,3] Patrick J. Heizer,[1] Yiping Tu,[1] Thomas A. Weston,[1] Jared L.-C. Fong,[1] Navjot Kaur Gill,[3] Amy C. Rowat,[2,3] Stephen G. Young,[1,4] and Loren G. Fong[1]

[1]Department of Medicine, [2]Department of Bioengineering, [3]Department of Integrative Biology and Physiology, and [4]Department of Human Genetics, UCLA, Los Angeles, California, USA.

The mutant nuclear lamin protein (progerin) produced in Hutchinson-Gilford progeria syndrome (HGPS) results in loss of arterial smooth muscle cells (SMCs), but the mechanism has been unclear. We found that progerin induces repetitive nuclear membrane (NM) ruptures, DNA damage, and cell death in cultured SMCs. Reducing lamin B1 expression and exposing cells to mechanical stress – to mirror conditions in the aorta – triggered more frequent NM ruptures. Increasing lamin B1 protein levels had the opposite effect, reducing NM ruptures and improving cell survival. Remarkably, raising lamin B1 levels increased nuclear compliance in cells and was able to offset the increased nuclear stiffness caused by progerin. In mice, lamin B1 expression in aortic SMCs is normally very low, and in mice with a targeted HGPS mutation (*Lmna*^{G609G}), levels of lamin B1 decrease further with age while progerin levels increase. Those observations suggest that NM ruptures might occur in aortic SMCs in vivo. Indeed, studies in *Lmna*^{G609G} mice identified NM ruptures in aortic SMCs, along with ultrastructural abnormalities in the cell nucleus that preceded SMC loss. Our studies identify NM ruptures in SMCs as likely causes of vascular pathology in HGPS.

Introduction

Hutchinson-Gilford progeria syndrome (HGPS) is a pediatric progeroid disorder caused by a point mutation in *LMNA* (the gene for prelamin A and lamin C) that causes aberrant prelamin A splicing and the production of an internally truncated prelamin A protein (progerin) (1, 2). Progerin cannot undergo the proteolytic processing step by ZMPSTE24 that normally converts farnesyl–prelamin A to mature lamin A; thus, progerin retains a farnesyl lipid anchor at its carboxyl terminus (3). In HGPS fibroblasts, progerin accumulates at the nuclear periphery and leads to a high frequency of misshapen nuclei (1, 4). Children with HGPS develop several aging-like phenotypes, but the most devastating is atherosclerosis in the coronary and cerebral arteries, which often leads to death by the mid-teenage years (5). The atherosclerosis in HGPS is unusual in that it occurs in the absence of common risk factors (e.g., hypercholesterolemia, smoking, and diabetes mellitus) (6). Histopathologic studies uncovered another atypical feature of the arterial disease in HGPS: the loss of medial smooth muscle cells (SMCs) (7, 8).

The loss of SMCs in large arteries, accompanied by thickening of the adventitia, is also observed in transgenic and gene-targeted mouse models of HGPS (9–11). The severity of the arterial disease depends on levels of progerin expression; the arterial pathology is more severe — and the onset is earlier — in mice that have 2 targeted HGPS mutant alleles as compared with only 1 (12, 13). The arterial disease is less severe in HGPS mice treated with a farnesyltransferase inhibitor (14), an antisense oligonucleotide that alters RNA splicing and reduces progerin expression (11), or by inhibiting N-acetyltransferase 10 (15), endoplasmic reticulum stress (16), MMP13 (17), or ICMT (18).

Mechanical stress is relevant to the vascular pathology in HGPS. In cultured SMCs that express progerin, mechanical stretching increases DNA damage and cell death (12). Disrupting the linker of the nucleoskeleton and cytoskeleton (LINC) complex, which reduces force transmission to the nucleus (19, 20), reduces DNA damage and increases cell survival. Also, in gene-targeted mice expressing progerin (*Lmna*^{G609G}–knock-in mice), the loss of medial SMCs is most pronounced in segments of the aorta that are subjected to high hemodynamic stress (e.g., inner curvature of the ascending thoracic aorta) (12, 21). Of note, disrupting the LINC complex in the SMCs of *Lmna*^{G609G} mice markedly reduces arterial pathology (12).

Conflict of interest: The authors have declared that no conflict of interest exists.

Submitted: May 18, 2021
Accepted: July 1, 2021
Published: August 23, 2021

Reference information: *JCI Insight*. 2021;6(16):e151515. https://doi.org/10.1172/jci.insight.151515.

In *Lmna*^{G609G} mice, nuclear abnormalities and cell death are widespread in medial SMCs but absent in intimal endothelial cells (12), even though both cell types are subjected to pulsatile hemodynamic forces. One potential clue to this discrepancy relates to differences in the composition of the nuclear lamina. In both WT and *Lmna*^{G609G} mice, lamin B1 expression is very low in medial SMCs but is robust in endothelial cells (12). Lamin B1, like progerin, is tethered to the inner nuclear membrane (NM) by a farnesyl lipid anchor (22), but whether the physiologically low levels of lamin B1 in medial SMCs render cells more susceptible to progerin toxicity is unknown. Knocking down lamin B1 expression in cultured osteosarcoma cells was reported to trigger NM ruptures (23), but the relevance of that finding to aortic SMCs in vivo is open to question because plating cells on plastic dishes increases susceptibility to NM ruptures (24, 25). NM ruptures have been observed in cortical neurons of lamin B1–deficient mouse embryos (26), but the relevance of that finding to arterial SMCs is also questionable because embryonic neurons, unlike arterial SMCs, do not express lamin A or lamin C (27, 28), 2 nuclear lamins that are crucial for the integrity of the nuclear envelope.

We believe that the low levels of lamin B1 in arterial SMCs are normally well tolerated because SMCs produce high levels of lamin A and lamin C (12, 29). However, we suspected that the low levels of lamin B1, combined with progerin expression, could be relevant to the vascular pathology of HGPS. Specifically, we hypothesized that progerin expression in SMCs, particularly when the cells are subjected to mechanical stress, could reduce NM integrity and trigger NM ruptures, resulting in reduced cell survival. We also hypothesized that increasing lamin B1 expression in progerin-expressing SMCs (so as to model the situation in intimal endothelial cells) would render SMCs less susceptible to NM ruptures. In addressing our hypotheses, we were keenly aware that cell culture studies are an imperfect model for arterial SMCs and HGPS pathology. Therefore, we also examined, in *Lmna*^{G609G} mice, whether progerin triggers NM ruptures in arterial SMCs but not in endothelial cells, and whether the onset of NM ruptures in SMCs correspond temporally to the emergence of the hallmark arterial pathology of HGPS.

Results

Progerin expression causes NM ruptures in cultured SMCs. We generated aortic SMCs expressing nuclear-targeted GFP (Nuc-GFP) and doxycycline-inducible (Dox-inducible) constructs for WT prelamin A (PreA-SMC) or progerin (Prog-SMC). Dox levels were adjusted to achieve lamin A (or progerin) levels similar to those in aortas of WT mice (*Lmna*$^{+/+}$) or mice with a targeted HGPS mutation (*Lmna*$^{G609G/+}$) (Figure 1A). Both lamin A and progerin were located in the cell nucleus (Supplemental Figure 1A; supplemental material available online with this article; https://doi.org/10.1172/jci.insight.151515DS1). After 2 days, progerin increased the frequency of misshapen nuclei in both live SMCs (Figure 1B) and fixed cells (Supplemental Figure 1B). NM ruptures, evident from the escape of a nuclear-targeted fluorescent protein into the cytoplasm (23, 30, 31) (Figure 1C), were detected by fluorescence microscopy. In the absence of Dox, the frequency of NM ruptures was low in PreA-SMCs and Prog-SMCs (~3%) (Figure 1D). In the presence of Dox, 17% of Prog-SMCs exhibited a NM rupture, whereas only approximately 3% of PreA-SMCs had a rupture. In Prog-SMCs, the frequency of ruptures increased with higher levels of progerin expression (Supplemental Figure 1D).

To define the dynamics of NM ruptures, Prog-SMCs were monitored by time-lapse microscopy (images were taken every 10 minutes for 24 hours). Snapshots of Prog-SMCs at 1-hour intervals are shown in Figure 1E (also see Supplemental Video 1). Our analysis of time-lapse experiments (915 PreA-SMCs and 735 Prog-SMCs) revealed that NM ruptures were more frequent in Prog-SMCs than in PreA-SMCs (18% vs. 2.5%; $P < 0.001$) (Figure 1F) and often occurred repetitively (Figure 1G) (see Supplemental Videos 2 and 3). Cell death also occurred more frequently in Prog-SMCs with NM ruptures (25/141 cells vs. only 1/21 in PreA-SMCs; $P < 0.02$) (Figure 1H). NM ruptures were more frequent in Prog-SMCs that had a misshapen nucleus (Figure 1I). The results from individual experiments are shown in Supplemental Figure 1E.

Impact of lamin B1, mechanical stress, and progerin farnesylation on NM ruptures. To examine the effects of low lamin B1 expression and mechanical stress on NM ruptures — so as to model conditions in the aorta — Prog-SMCs and PreA-SMCs were treated with a *Lmnb1* siRNA (or a control siRNA), plated on collagen-coated polydimethylsiloxane (PDMS) membranes, and subjected to either uniaxial stretching (2 mm, 0.5 Hz for 2 hours) or static conditions. Western blots documented reduced lamin B1 levels in *Lmnb1* siRNA–treated cells (Supplemental Figure 2A). The lower levels of lamin B1 expression increased NM ruptures in Prog-SMCs by 58% in static conditions ($P < 0.05$) and 40% in stretch conditions ($P < 0.02$) (Figure 2A) but had no effect on ruptures in PreA-SMCs (Supplemental Figure 2B). Stretching increased NM ruptures in both untreated Prog-SMCs (1.6-fold vs. static Prog-SMCs; $P < 0.02$) and *Lmnb1* siRNA–treated Prog-SMCs

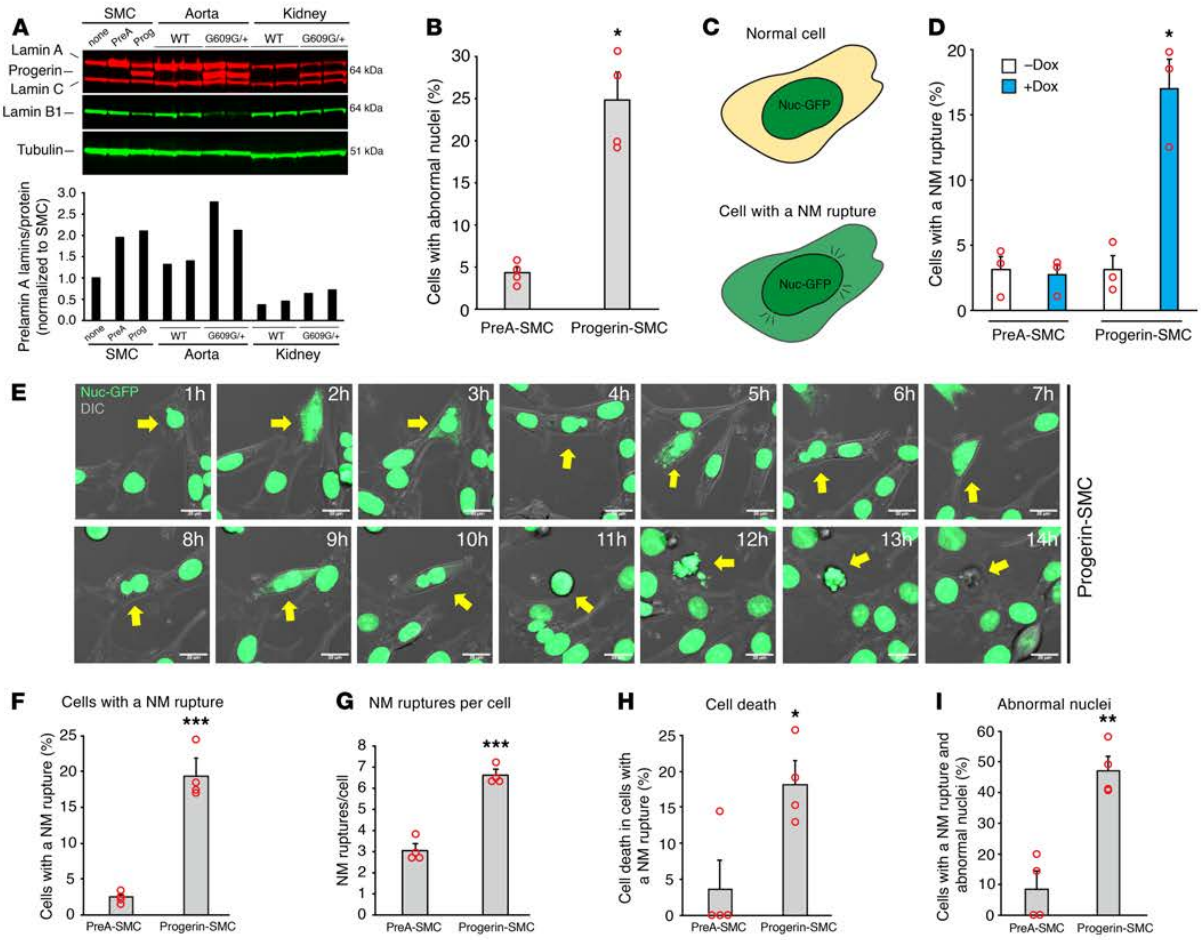

Figure 1. Progerin expression causes NM ruptures in cultured SMCs. (**A**) Western blot analysis of SMCs expressing prelamin A (PreA) and progerin (Prog), and in the aorta and kidney of WT and *Lmna*$^{G609G/+}$ mice. The bar graph shows the expression of lamin A plus progerin, relative to total protein (Supplemental Figure 1C). (**B**) Bar graph showing that progerin increases the frequency of abnormally shaped nuclei in SMCs, as judged by live-cell microscopy (mean ± SEM, n = 4 experiments; Student's t test, *P < 0.001). (**C**) Illustration depicting a NM rupture, defined as the escape of nuclear-targeted GFP (Nuc-GFP; green) into the cytoplasm (tan). (**D**) Bar graph showing that progerin causes NM ruptures in SMCs (mean ± SEM, n = 3 experiments; Student's t test, *P < 0.01). NM ruptures were measured in fixed cells 48 hours after adding Dox (blue). (**E**) Fluorescence microscopy images of live SMCs expressing progerin and Nuc-GFP (green) at 1-hour intervals. A DIC image (grey) is superimposed. The yellow arrow points to a cell followed for 14 hours by time-lapse microscopy (see Supplemental Video 1; images were captured every 10 minutes). The cell had several NM ruptures and eventually died. Scale bar: 20 μm. (**F**–**I**) Characteristics of NM ruptures in PreA-SMC and Progerin-SMC derived from time-lapse microscopy studies. Bar graphs show the percentage of cells with a NM rupture; the number of NM ruptures per cell; the percentage of cells with a NM rupture that die; and the percentage of cells with a NM rupture and abnormal-shaped nuclei (mean ± SEM, n = 4 experiments; Student's t test, *P < 0.02, **P < 0.002, ***P < 0.001). The results from the individual experiments are shown in Supplemental Figure 1E.

(2.3-fold vs. static Prog-SMCs; P < 0.0001). The expression of a nonfarnesylated (nf) progerin (nf-Prog), a progerin that terminated with –SSIM rather than –CSIM, a modification to the C-terminal CaaX signal sequence that blocks progerin farnesylation) (Supplemental Figure 2A), did not trigger NM ruptures in either static or stretched SMCs (Figure 2A).

The endosomal sorting complex required for transport III (ESCRT-III) protein complex plays a role in repairing NM ruptures (31, 32). Transcript levels for components of the ESCRT-III protein complex (*Vps20*, *Snf7b*, *Vps24*, *Vps2*, *Vps4*, and *Vps60*) were not different in Prog-SMCs and PreA-SMCs (Figure 2B).

Finding increased NM ruptures in stretched Prog-SMCs implied that mechanical strain contributes to ruptures. To explore that idea, we expressed a nuclear-targeted red fluorescence protein (RFP) (Nuc-RFP) in SMCs and then disrupted the LINC complex with a GFP-tagged Klarsicht/Anc-1, Syne homology (KASH) domain of nesprin-2 (GFP-KASH2) (33) (Figure 2C). NM ruptures, documented by the escape of Nuc-RFP into the cytoplasm, were reduced by KASH2 expression in Prog-SMCs (compared with

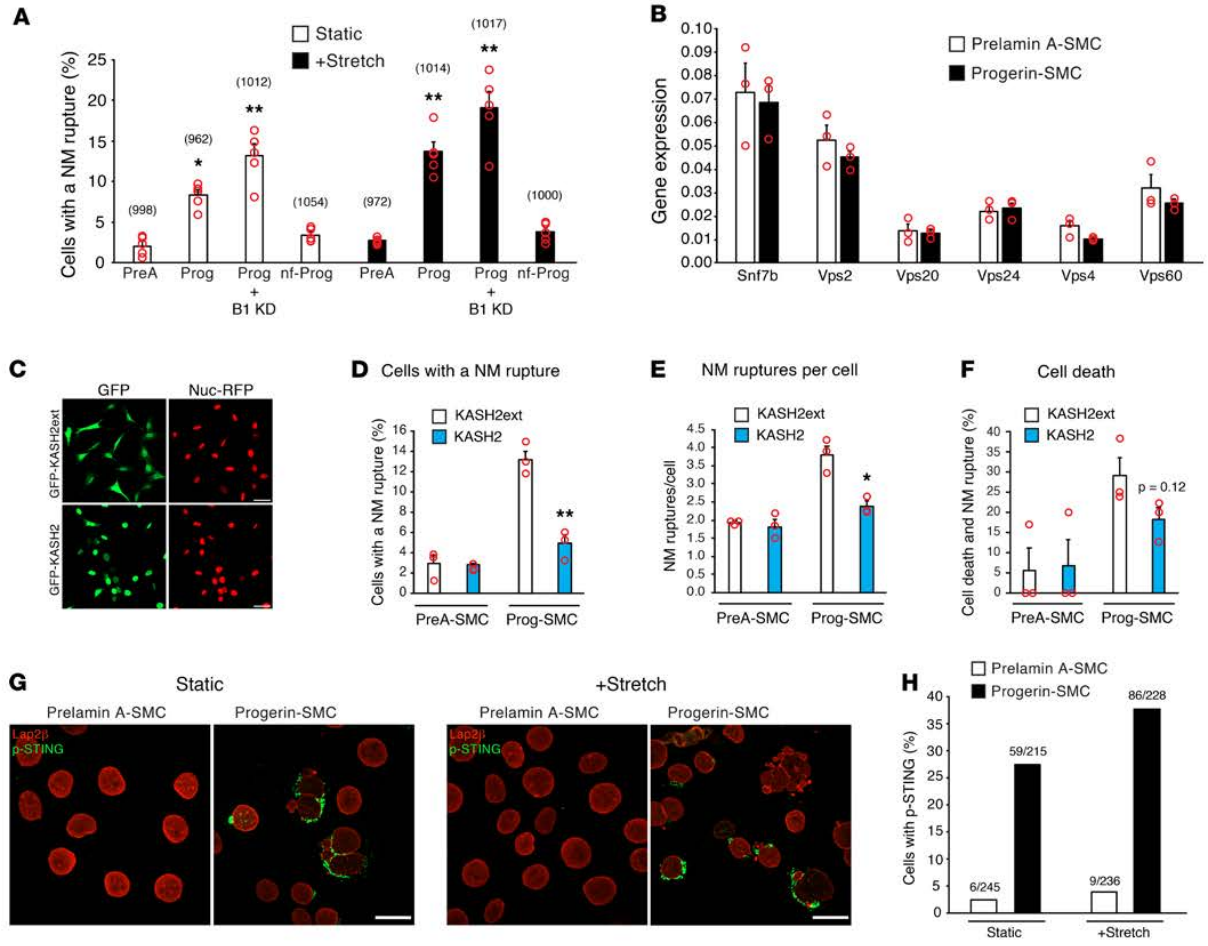

Figure 2. Impact of lamin B1, mechanical stress, and progerin farnesylation on NM ruptures. (**A**) Bar graph comparing the effects of prelamin A (PreA), progerin (Prog), lamin B1 knockdown (B1 KD), and nf-Prog on NM ruptures in static (white bars) and stretched (black bars) SMCs (mean ± SEM, $n = 5$ experiments). Differences were compared with static SMCs expressing prelamin A by 2-way ANOVA (*$P < 0.005$, **$P < 0.0001$). The total numbers of cells examined are shown in parentheses above each bar. (**B**) Bar graph showing transcript levels for genes involved in NM repair (mean ± SEM, $n = 3$ experiments; Student's t test, all nonsignificant). (**C**) Confocal fluorescence microscopy images showing SMCs expressing Nuc-RFP (red) and either GFP-KASH2ext (green) or GFP-KASH2 (green). Scale bar: 20 μm. (**D**–**F**) Characterization of NM ruptures in live PreA-SMCs and Prog-SMCs expressing KASH2ext (white bars) or KASH2 (blue bars). Bar graphs show the percentage of cells with a NM rupture; the number of NM ruptures per cell; and the percentage of cells with a NM rupture that die (mean ± SEM, $n = 3$ experiments; Student's t test, *$P < 0.01$, **$P < 0.005$). (**G**) Confocal fluorescence microscopy images showing increased phosphorylated-STING (p-STING; green) in Progerin-SMCs. SMCs were examined in both static (left) and stretched (right) conditions. PreA-SMCs were included as a control. Lap2β staining is shown in red. Scale bar: 20 μm. (**H**) Bar graph showing the percentage of cells staining positive for p-STING in PreA-SMCs (white bars) and Prog-SMCs (black bars) in static and stretched conditions in a representative experiment. The ratios above each bar show the number of cells positive for p-STING over the total number of cells assessed.

KASHext, an inactive KASH2 protein) (Figure 2, D and E). There was a trend of reduced cell death in KASH2-expressing Prog-SMCs but the differences did not achieve statistical significance ($P = 0.12$) (Figure 2F). KASH2 expression had no effect on NM ruptures in PreA-SMCs (Figure 2, D and E). The results from individual experiments are shown in Supplemental Figure 2C.

NM ruptures result in the intermixing of nuclear and cytoplasmic contents (23, 30, 34). To determine if NM ruptures activate the cGAS-STING pathway (32, 35), we assessed phosphorylated-STING by immunofluorescence microscopy. Phosphorylated-STING was detected at a higher frequency in both static and stretched Prog-SMCs (Figure 2, G and H).

Lamin B1 reduces progerin's toxicity and association with NMs. To determine if increasing lamin B1 levels alter the frequency of progerin-induced NM ruptures, we created Prog-SMCs harboring a Dox-inducible

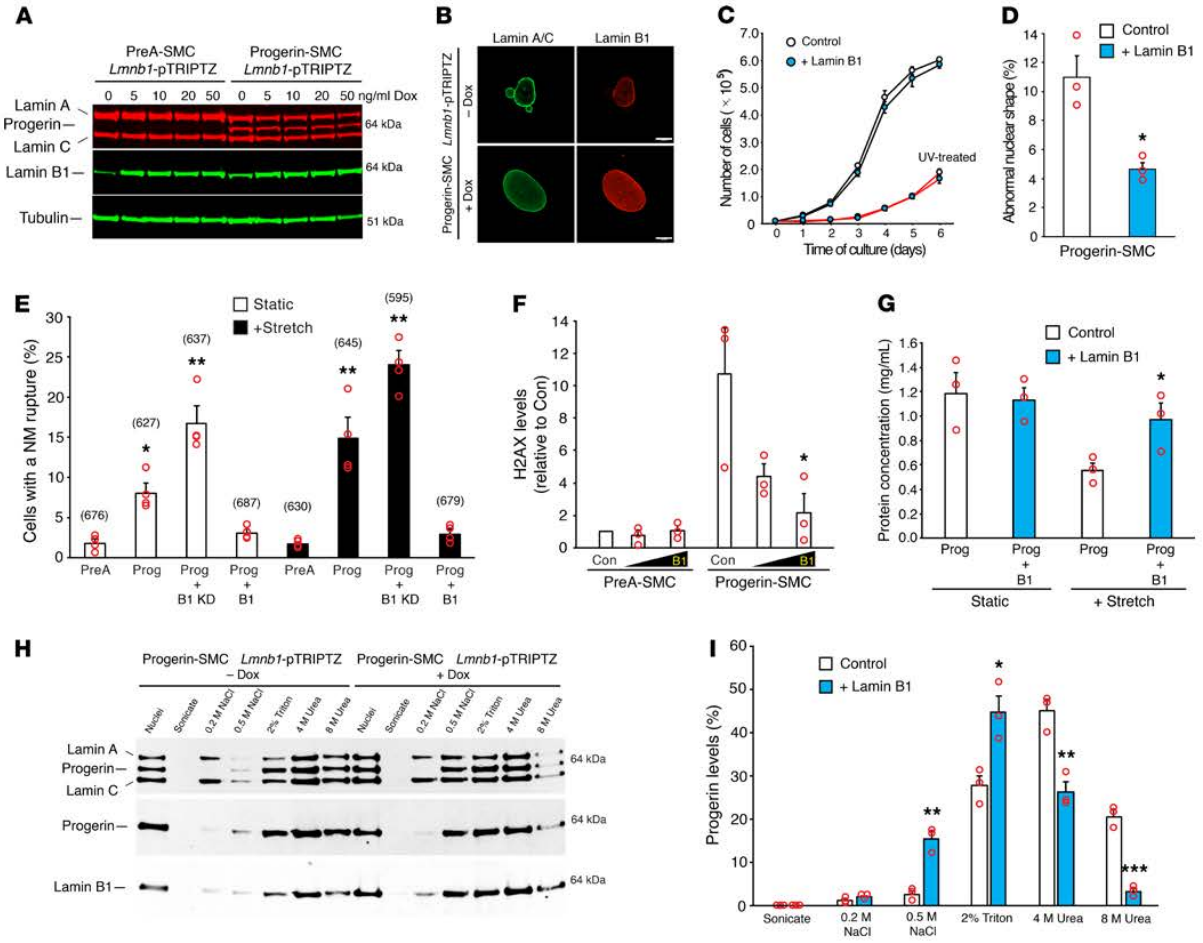

Figure 3. Lamin B1 reduces progerin's toxicity and association with NMs. (**A**) Western blot showing Dox-induced expression of mouse lamin B1 in PreA-SMCs and Prog-SMCs. (**B**) Microscopy images showing lamin B1 expression (red) in Prog-SMCs. Scale bar: 10 μm. (**C**) Growth curves showing that induced lamin B1 expression (blue circles) does not affect cell growth in control (black lines) or UV-treated SMCs (red lines). Mean ± SEM (n = 3 experiments). (**D**) Bar graph showing that lamin B1 overexpression (blue) reduces abnormal nuclear shape in Prog-SMCs (mean ± SEM, n = 3 experiments; Student's t test, $^*P < 0.02$). (**E**) Bar graph comparing the effects of lamin B1 knockdown (B1 KD) and lamin B1 overexpression (B1) on NM ruptures in Prog-SMCs under static (white bars) and stretched (black bars) conditions (mean ± SEM, n = 4 experiments). NM ruptures were compared with static PreA-SMCs by 2-way ANOVA ($^*P < 0.05$, $^{**}P < 0.0001$). The total numbers of cells examined are shown in parentheses above each bar. (**F**) Bar graph showing that lamin B1 reduces H2AX-γ levels in Prog-SMCs (mean ± SEM, n = 3 experiments). Levels were compared with control (Con) Prog-SMCs by ANOVA ($^*P < 0.01$). (**G**) Bar graph showing that lamin B1 reduces cell death in stretched Prog-SMCs (mean ± SEM, n = 3 experiments; Student's t test, $^*P < 0.05$). Dead cells detach from membranes, reducing cell protein on the membranes (12). (**H**) Western blot showing that lamin B1 expression increases the solubility of progerin. Nuclei from Prog-SMCs were sequentially extracted as described in Methods and the soluble extracts analyzed by western blotting. (**I**) Bar graph comparing the extraction profiles for progerin in Prog-SMCs (white) and Prog-SMCs plus lamin B1 (blue) (mean ± SEM, n = 3 experiments; Student's t test, $^*P < 0.02$, $^{**}P < 0.01$, $^{***}P < 0.001$).

lamin B1 construct. Inducing lamin B1 (Figure 3, A and B) did not alter the growth of Prog-SMCs (Figure 3C) but reduced the number of cells with misshapen nuclei (Figure 3D). Induced lamin B1 expression also markedly reduced NM ruptures in Prog-SMCs under both static (61% decrease) and stretched (80% decrease) conditions (Figure 3E). Also, lamin B1 expression resulted in less DNA damage in Prog-SMCs (but not in PreA-SMCs), as judged by H2AXγ levels (Figure 3F). Finally, lamin B1 increased cell survival in stretched Prog-SMCs (Figure 3G).

The farnesyl lipid anchor is thought to tether lamin B1 and progerin to the inner NM (36–38). To determine if increased lamin B1 interferes with progerin's association with the nuclear envelope, Prog-SMC nuclei were sequentially extracted with NaCl, Triton, and urea (39). In the absence of lamin B1 induction (–Dox), approximately 30% of the progerin appeared in the NaCl/Triton fractions, whereas approximately 70% appeared in the urea fractions. With lamin B1 expression (+Dox), 60% of the progerin appeared in the

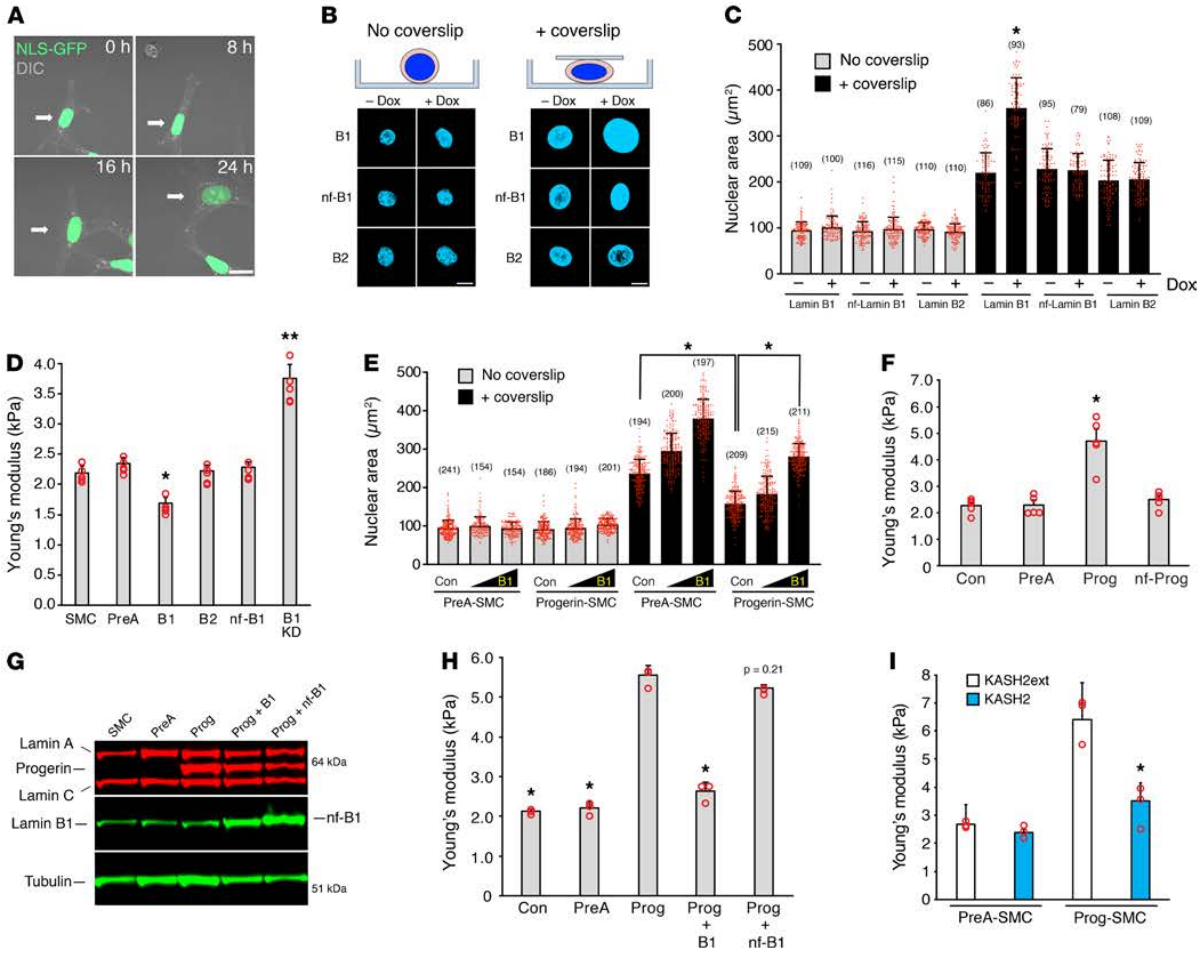

Figure 4. Lamin B1 decreases nuclear stiffness. (**A**) Microscopy images of a live SMC (arrow) expressing Nuc-GFP (green) and increased amounts of lamin B1 (see Supplemental Video 4). Scale bar: 20 μm. (**B**) Microscopy images of Hoechst-stained nuclei in suspended cells expressing lamin B1 (B1), nf-lamin B1 (nf-B1), or lamin B2 (B2) before (left) and after (right) compressing the cells with a glass coverslip. Scale bar: 10 μm. Nuclear lamin expression was induced with Dox (see Supplemental Figure 4A). (**C**) Inducing lamin B1 expression (+Dox) increases nuclear area (mean ± SD, numbers of cells examined are reported above each bar; Student's *t* test, $*P < 0.001$). (**D**) Lamin B1 (B1) decreases nuclear stiffness (Young's modulus) in SMCs, as measured by AFM (mean ± SEM, $n = 5$ experiments). Measurements were compared with noninduced SMCs by ANOVA ($*P < 0.002$, $**P < 0.0001$). (**E**) Lamin B1 increases nuclear size (spreading) in PreA-SMCs and Progerin-SMCs. Nuclei size was measured as in **C** (mean ± SD; Student's *t* test, $*P < 0.001$). (**F**) Progerin (Prog) but not nf-Prog increases nuclear stiffness in SMCs (mean ± SEM, $n = 5$ experiments). Expression data are shown in Supplemental Figure 4F. All measurements were compared with control SMCs (Con) by ANOVA ($*P < 0.0001$). (**G**) Western blot showing increased expression of lamin B1 (B1) and nf-B1 in SMCs examined in **H**. (**H**) Increasing lamin B1 expression but not nf-B1 reduces nuclear stiffness in Prog-SMCs (mean ± SEM, $n = 3$ experiments). Measurements were compared with SMCs expressing progerin by ANOVA ($*P < 0.0001$). (**I**) Disrupting the LINC complex with KASH2 (blue bars) reduces nuclear stiffness in Prog-SMCs (mean ± SEM; $n = 3$ experiments). Nuclear stiffness was compared with cells expressing the inactive mutant KASH2ext (white bars) by the Student's *t* test ($*P < 0.01$).

NaCl/Triton fractions, indicating reduced association of progerin with the nuclear envelope (Figure 3, H and I). In control studies, we found, as expected, a high percentage of nf-Prog (~60%) in the NaCl/Triton fractions (Supplemental Figure 3, A and B).

Lamin B1 decreases nuclear stiffness. In live-cell imaging studies, we noted that SMC nuclei appeared larger in cells expressing lamin B1 (Figure 4A and Supplemental Video 4). Since nuclear size is determined by chromosomal content, nuclear lamina stiffness, and cytoskeletal elements (i.e., microfilaments and microtubules), we hypothesized that lamin B1 increased nuclear size by decreasing nuclear stiffness. To pursue this, we expressed prelamin A, lamin B1, nf-lamin B1, and lamin B2 in SMCs (Supplemental Figure 4A) and examined the nuclear size in suspension cultures stained with Hoechst at baseline and after compressing the cells with a glass coverslip (Figure 4B). The purpose of the coverslip was to mimic the pressure on the nucleus by cytoskeletal

elements and to apply a uniform level of force. The coverslip increased nuclear area in all SMCs, as expected, but the increase was particularly striking in the lamin B1–transduced SMCs (Figure 4C). Increased nuclear area was also observed in fibroblasts transduced with lamin B1 (Supplemental Figure 4, B and C).

We suspected that lamin B1 expression increased nuclear size by decreasing nuclear stiffness. By atomic force microscopy (AFM) measurements over the cell nucleus, lamin B1 expression reduced nuclear stiffness by 23% ($P < 0.002$), whereas a lamin B1 knockdown increased nuclear stiffness by approximately 70% ($P < 0.0001$). Increased expression of prelamin A, lamin B2, and nf-lamin B1 had no effect on nuclear stiffness (Figure 4D and Supplemental Figure 4D). The increase in nuclear area in SMCs expressing lamin B1 (induced with 10 ng/mL Dox) was not accompanied by increased expression of nuclear envelope proteins (Supplemental Figure 4E), suggesting that lamin B1 did not increase nuclear size by inducing larger nuclei.

Lamin B1 expression also increased nuclear area in cells expressing progerin that were compressed with a glass coverslip (Figure 4E). However, the extent of nuclear spreading was significantly lower in Prog-SMCs than in PreA-SMCs, implying that progerin expression made nuclei stiffer. Indeed, by AFM, progerin increased nuclear stiffness more than 2-fold ($P < 0.0001$), whereas prelamin A and nf-Prog had no effect (Figure 4F and Supplemental Figure 4F). The increased nuclear stiffness in Prog-SMCs was reduced by expression of lamin B1 and KASH2, but not by nf-lamin B1 or KASH2ext (Figure 4, G–I).

Progerin levels increase with age in $Lmna^{G609G/+}$ mice whereas lamin B1 levels decrease. NM rupture frequency in cultured SMCs depends on the expression levels of progerin and lamin B1. To explore the relevance of these findings in living mice, we began by using western blots to compare progerin and lamin B1 expression in aortas of 4- and 21-week-old $Lmna^{G609G/+}$ mice (Figure 5A). Progerin levels in the aorta of $Lmna^{G609G/+}$ mice were approximately 50% higher at 21 weeks than at 4 weeks (Figure 5B), while lamin B1 levels were approximately 50% lower (Figure 5C and Supplemental Figure 5, A–C) (both $P < 0.001$). Microscopy revealed that the lower levels of lamin B1 were due to reduced expression in medial SMCs (Figure 5D). The age-dependent change in lamin B1 protein levels was accompanied by a 67% decrease in *Lmnb1* expression; however, the increase in progerin protein levels could not be explained by changes in gene expression (Figure 5E). At 32 weeks, the levels of progerin protein, relative to lamin B1, stabilized (Figure 5F and Supplemental Figure 5, D and E).

The decrease in lamin B1 levels in the aorta from 4–21 weeks was observed only in $Lmna^{G609G/+}$ mice. In WT mice, lamin B1 levels were not significantly reduced at 21 weeks (Figure 5, G and H) ($P = 0.33$), despite the fact that *Lmnb1* transcript levels had fallen by more than 50% (Figure 5I).

NM ruptures and ultrastructural abnormalities in aortic SMCs precede SMC loss in $Lmna^{G609G/G609G}$ mice. Finding high progerin levels but low lamin B1 levels in aortas of $Lmna^{G609G/+}$ mice suggested that we might find NM ruptures in vivo in aortic SMCs. To explore this possibility, we bred WT and $Lmna^{G609G/G609G}$ mice with a nuclear-targeted tdTomato (Nuc-tdTomato) transgene (26). By fluorescence microscopy, Nuc-tdTomato expression was uniform in the thoracic aorta and was confined to the cell nucleus (Figure 6A).

We used fluorescence microscopy to visualize Nuc-tdTomato in aortas of $Lmna^{G609G/G609G}$ mice at 14 weeks of age. At this time point, loss of medial SMCs is clearly evident (12). We found frequent NM ruptures in medial SMCs of $Lmna^{G609G/G609G}$ mice, as judged by the escape of Nuc-tdTomato into the cytoplasm (Figure 6B). No NM ruptures were observed in aortic endothelial cells consistent with the absence of endothelial cell loss in $Lmna^{G609G/G609G}$ mice. In WT mice, Nuc-tdTomato was confined to the nucleus of SMCs (Figure 6B).

We next asked whether the appearance of NM ruptures in the aortic SMCs of $Lmna^{G609G/G609G}$ mice precedes the onset of SMC loss. Loss of SMCs in $Lmna^{G609G/G609G}$ mice was detectable at 10 weeks of age but absent at 8 weeks (Figure 6C). However, at 8 weeks of age, we observed frequent NM ruptures in medial SMCs of $Lmna^{G609G/G609G}$ mice in the ascending aorta and upper descending aorta and less frequent ruptures in the lower descending aorta (Figure 6D and Supplemental Figure 6, A and B).

To determine the frequency of NM ruptures in $Lmna^{G609G/G609G}$ mice, NM ruptures in cross sections of the ascending thoracic aorta in 3 8-week-old $Lmna^{+/+}$ mice and 3 8-week-old $Lmna^{G609G/G609G}$ mice (Figure 7A) were counted and expressed relative to total SMC nuclei. The frequency of NM ruptures in aortic SMCs was significantly higher in $Lmna^{G609G/G609G}$ mice than in $Lmna^{+/+}$ mice (26.7% vs. 2.0%; $P < 0.001$) (Figure 7B). NM ruptures were detected in WT mice but they occurred at a very low frequency. No NM ruptures were detected in endothelial cells in either WT or $Lmna^{G609G/G609G}$ mice (Figure 7B). NM ruptures were also quantified in tissue sections of the upper and lower descending aorta (Supplemental Figure 6, C and D). Consistent with the lower frequency of SMC loss in the descending thoracic aorta (12), NM ruptures were less frequent in the upper and lower descending aorta (Figure 7C). No NM ruptures were detected in the heart or liver of $Lmna^{G609G/G609G}$ mice (Figure 7D).

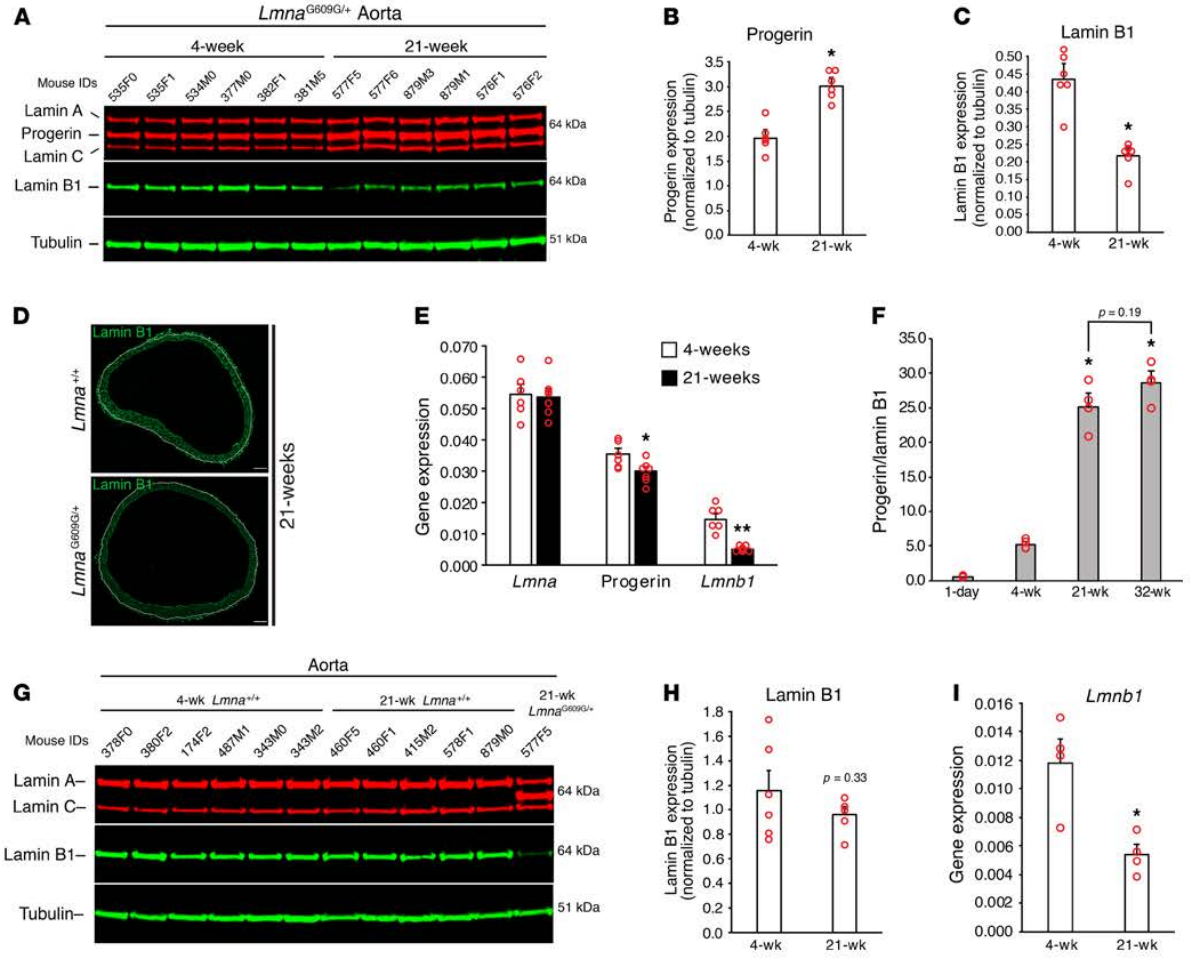

Figure 5. Progerin levels increase with age in *Lmna*$^{G609G/+}$ mice whereas lamin B1 levels decrease. (**A**) Western blot comparing the expression of progerin and lamin B1 in the aorta of 4- and 21-week-old *Lmna*$^{G609G/+}$ mice. Mouse IDs are shown above each sample. (**B** and **C**) Bar graphs showing progerin and lamin B1 levels, relative to tubulin, for the western blot in (**A**) (mean ± SEM, $n = 6$ mice/group; Student's t test, $^*P < 0.001$). (**D**) Immunofluorescence microscopy images of aortic rings showing lamin B1 (green) expression is reduced in SMCs in 21-week-old *Lmna*$^{G609G/+}$ mice. The border between the media and adventitia is marked with a white line. Scale bar: 100 μm. (**E**) Quantitative RT-PCR studies showing *Lmna*, progerin, and *Lmnb1* transcript levels in aortas from 4-week-old ($n = 6$ mice) and 21-week-old ($n = 7$ mice) *Lmna*$^{G609G/+}$ mice (mean ± SEM; Student's t test, $^*P < 0.05$, $^{**}P < 0.001$. (**F**) Bar graph comparing the progerin-to-lamin B1 ratio in the aorta from 1-day-old *Lmna*$^{G609G/+}$ mice ($n = 2$), and from 4-, 21-, and 32-week-old *Lmna*$^{G609G/+}$ mice ($n = 4$) for the western blot in Supplemental Figure 5D. Comparisons were made to 4-week-old *Lmna*$^{G609G/+}$ mice by ANOVA ($^*P < 0.0001$). (**G**) Western blot comparing the expression of lamin B1 in the aorta from 4- ($n = 6$) and 21- ($n = 5$) week-old *Lmna*$^{+/+}$ mice. Mouse IDs are shown above each sample. For comparison, a sample from a 21-week-old *Lmna*$^{G609G/+}$ mouse is included. (**H**) Bar graph showing the expression of lamin B1, relative to tubulin, in the western blot in **G** (mean ± SEM; Student's t test). (**I**) Bar graph showing *Lmnb1* expression in the aorta of 4- and 21-week-old *Lmna*$^{+/+}$ mice (mean ± SEM, $n = 4$ mice/group; Student's t test, $^*P < 0.02$).

Additional studies revealed that NM ruptures were absent in medial SMCs of *Lmna*$^{G609G/G609G}$ mice at 6 weeks of age (0/7 mice) but were easily detectable at 7 weeks, although at a low frequency (5/5 mice). NM ruptures were also observed in older *Lmna*$^{G609G/+}$ mice (Supplemental Figure 7, A and B).

The onset of NM ruptures in *Lmna*$^{G609G/G609G}$ mice coincided with the onset of ultrastructural pathology in SMC nuclei (12), as judged by electron microscopy. At 4 and 6 weeks, the morphology of medial SMCs in *Lmna*$^{G609G/G609G}$ mice was normal by electron microscopy, indistinguishable from the SMCs in WT mice. By 8 weeks, however, intranuclear tubules (the same structures described as intranuclear vesicles in ref. 12) were detected in aortic SMCs of *Lmna*$^{G609G/G609G}$ mice (Supplemental Figure 7C). Intimal endothelial cells were entirely normal. By electron microscopy, there were no abnormalities in SMCs of the urinary bladder in 8- and 16-week-old *Lmna*$^{G609G/G609G}$ mice, nor were there nuclear abnormalities in the heart, quadriceps, or kidney (Supplemental Figure 7D).

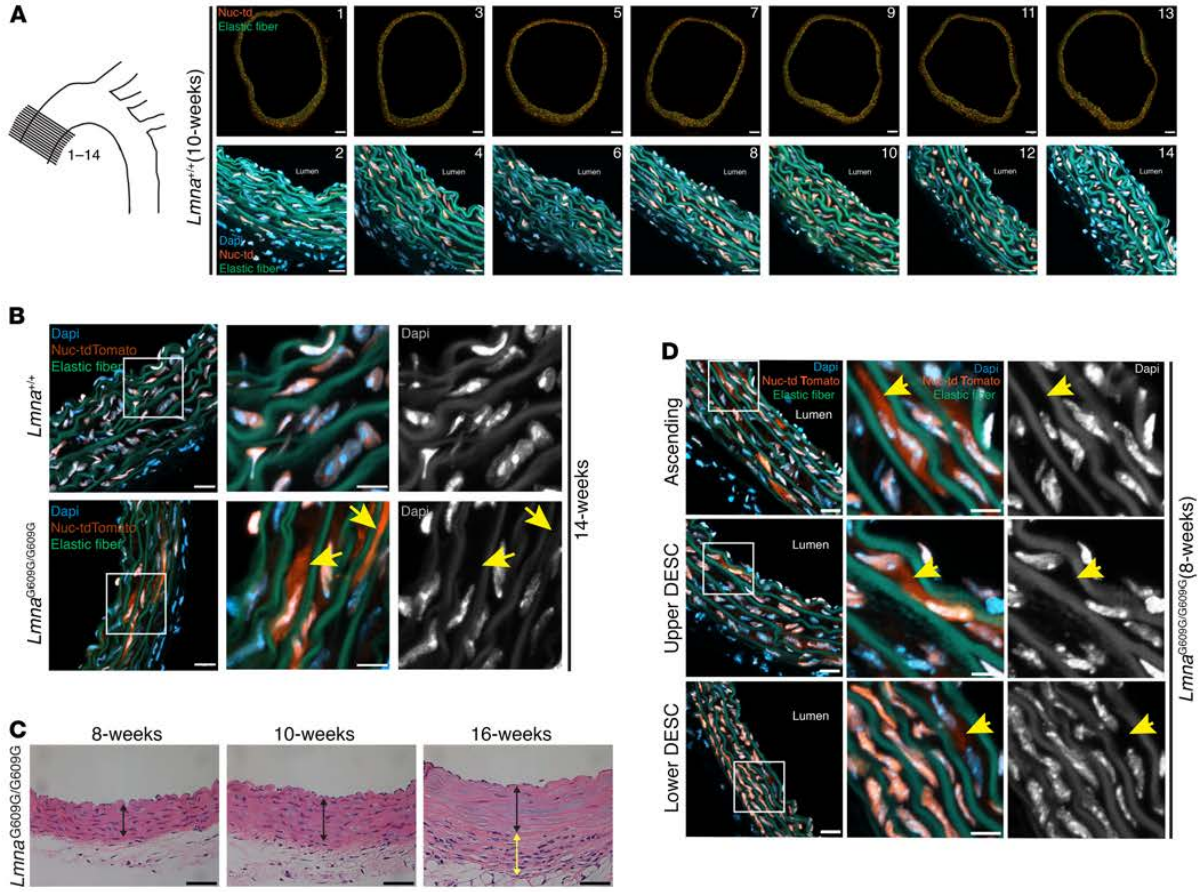

Figure 6. NM ruptures in aortic SMCs precede SMC loss in *Lmna*$^{G609G/G609G}$ mice. (**A**) Expression of Nuc-tdTomato in SMCs is uniform in the ascending aorta. Fourteen sequential cross sections through the ascending aorta were collected every 100 μm from a *Lmna*$^{+/+}$ mouse. Half of the sections (odd-numbered sections; top row) were imaged at low magnification to visualize the entire cross section. Scale bar: 100 μm. The even-numbered sections (bottom row) were imaged at higher magnification to visualize Nuc-tdTomato (orange) in nuclei stained with DAPI (blue). Scale bar: 20 μm. (**B**) Confocal fluorescence microscopy images of the ascending aorta from a 14-week-old *Lmna*$^{+/+}$ and *Lmna*$^{G609G/G609G}$ mouse. The boxed regions are shown at higher magnification in the middle and far-right columns. The colored images show DAPI (blue), elastic fibers (green), and Nuc-tdTomato (orange). The yellow arrows (middle column) point to Nuc-tdTomato outside of an SMC nucleus. To help visualize the boundaries of nuclei, the DAPI stain (white) is shown by itself in the far-right column. Scale bars: 20 μm (left column); 10 μm (middle column). (**C**) H&E-stained sections of the inner ascending aorta from 8-, 10-, and 16-week-old *Lmna*$^{G609G/G609G}$ mice. The black line spans the medial layer and the yellow line spans the thickened and fibrotic adventitia in the 16-week-old mouse. Scale bar: 20 μm. Note the loss of SMC nuclei in the aorta from the 16-week-old mouse. (**D**) Confocal fluorescence microscopy images of the ascending, upper descending, and lower descending thoracic aorta from an 8-week-old *Lmna*$^{G609G/G609G}$ mouse. Boxed regions are analyzed as described in (**B**). Scale bars: 20 μm (left column); 10 μm (middle column).

Discussion

The hallmark of large artery lesions in HGPS is loss of medial SMCs (40), but for years the mechanism has been elusive. In the current study, we found that progerin expression in SMCs, combined with physiologically low levels of lamin B1, trigger NM ruptures, abnormal nuclear morphology, and SMC death. Our findings in progerin-transfected cultured SMCs and aortic SMCs of *Lmna*^{G609G} mice were concordant. In cultured SMCs, progerin expression — at levels matching those in aortas of *Lmna*$^{G609G/+}$ mice — results in NM ruptures, DNA damage, activation of the cGAS-STING pathway, and cell death. The frequency of NM ruptures in SMCs increased with increasing levels of progerin expression. Reducing lamin B1 expression in progerin-expressing SMCs (so as to mirror the physiologically low levels of lamin B1 in aortic SMCs) and subjecting SMCs to uniaxial stretching (so as to mimic the pulsatile stretching of the aortic wall) increased the number of NM ruptures. Conversely, increasing lamin B1 expression or interfering with the transmission of cytoskeletal forces to the cell nucleus reduced NM ruptures. De Vos and colleagues (30) previously identified NM ruptures in transiently transfected human fibroblasts expressing EGFP-tagged progerin, but the incidence of NM ruptures in cells transfected with

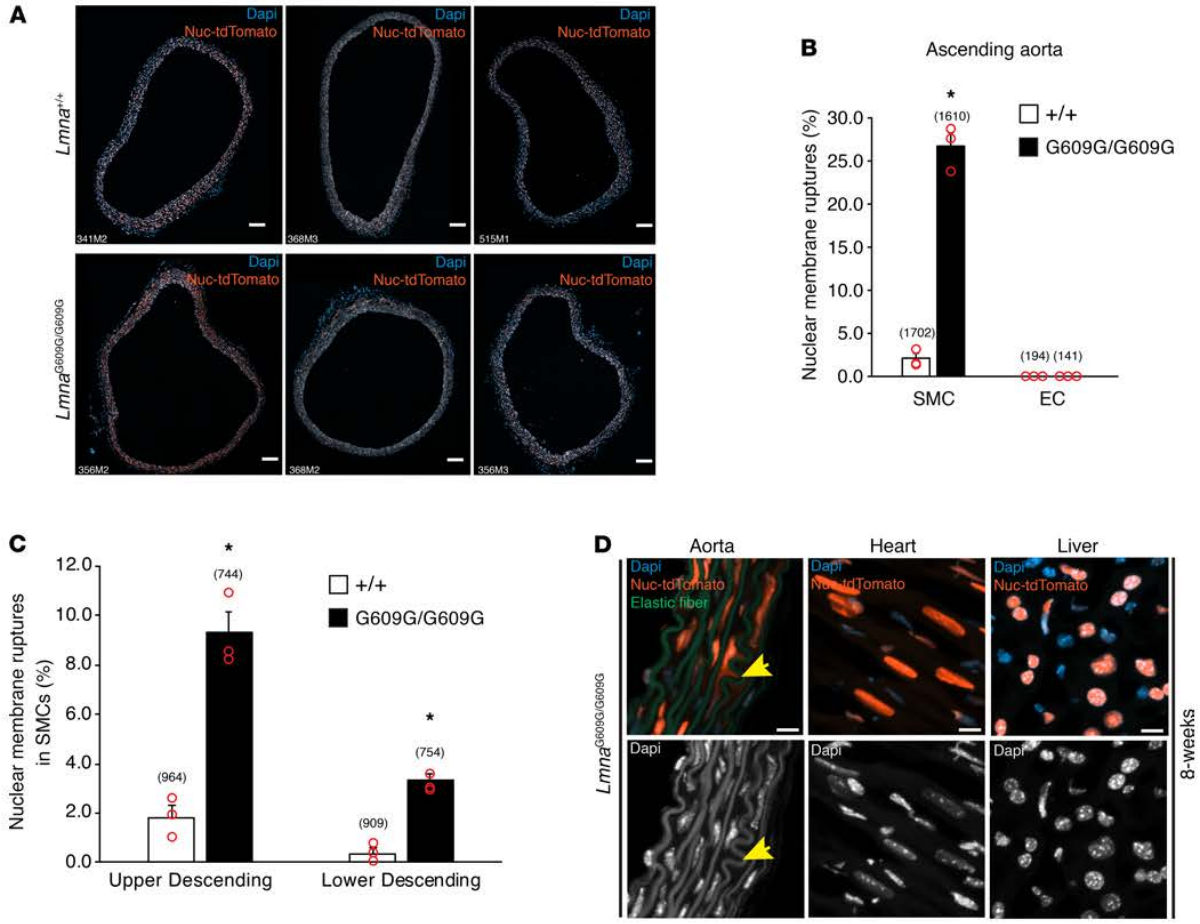

Figure 7. NM ruptures are frequent in aortic SMCs but absent in cardiomyocytes and hepatocytes of $Lmna^{G609G/G609G}$ mice. (**A**) Fluorescence microscopy images of cross sections (10 μm–thick) of the ascending aorta from 3 8-week-old $Lmna^{+/+}$ (top row) and 3 8-week-old $Lmna^{G609G/G609G}$ (bottom row) mice expressing the Nuc-tdTomato transgene. The mouse IDs are shown in the bottom left-hand corner of each image. Nuc-tdTomato (orange); DAPI (blue). Scale bar: 100 μm. (**B**) Quantification of NM ruptures in SMCs and endothelial cells (EC) in the ascending aorta of 8-week-old $Lmna^{+/+}$ and $Lmna^{G609G/G609G}$ mice. The number of NM ruptures is reported as a percentage of total nuclei examined in individual cross sections (**A**) (mean ± SEM; Student's *t* test; $^*P < 0.001$). The total number of nuclei scored is shown in parentheses. (**C**) Quantification of NM ruptures in SMCs in the upper and lower descending aorta of 3 8-week-old $Lmna^{+/+}$ and $Lmna^{G609G/G609G}$ mice. The number of NM ruptures is reported as a percentage of total nuclei examined in individual cross sections (see Supplemental Figure 6C) (mean ± SEM; Student's *t* test; $^*P < 0.001$). The total number of nuclei scored is shown in parentheses. (**D**) Confocal fluorescence microscopy images of the ascending aorta, heart, and liver from an 8-week-old $Lmna^{G609G/G609G}$ mouse. The colored images show DAPI (blue), elastic fibers (green), and Nuc-tdTomato (orange). To assist in visualizing the boundaries of nuclei, the DAPI stain is shown in white (bottom row). The yellow arrow points to Nuc-tdTomato outside of a nucleus in an aortic SMC. Scale bar: 10 μm.

a control plasmid (e.g., EGFP-prelamin A) was not determined. The relevance of our cell culture findings to living animals was established by examining the medial SMCs in aortas of $Lmna^{G609G/G609G}$ mice. In those mice, the expression of progerin in aortic SMCs, combined with very low levels of lamin B1, was accompanied by frequent NM ruptures. The onset of NM ruptures in aortic SMCs was at 7 weeks of age, preceding SMC loss.

Our studies identified nuclear lamin composition as a key factor in the vascular pathology of HGPS. The levels of progerin (which triggers NM ruptures) increased with age in the aorta of $Lmna^{G609G/+}$ mice, whereas levels of lamin B1 (which protects from NM ruptures) decreased. The age-related increase in progerin in the aorta occurred despite decreasing progerin transcript levels, suggesting that progerin is a stable protein with a slow turnover rate. Lamin B1 transcripts declined with age in both WT and $Lmna^{G609G/+}$ mice, but the levels of lamin B1 protein remained stable in WT mice. The preservation of lamin B1 levels in WT mice in the face of reduced transcript levels is consistent with the fact that lamin B1 has a very long half-life in mouse tissues (41, 42). However, given that lamin B1 is a long-lived protein in mice, why did aortic levels of lamin B1 fall with

age in *Lmna*$^{G609G/+}$ mice? The most likely explanation, we believe, is that progerin accelerates the turnover of lamin B1. In any case, the age-related changes in nuclear lamin composition in SMCs of *Lmna*$^{G609G/+}$ mice — high progerin levels and low lamin B1 levels — appear to be "double trouble" for NM integrity, increasing the risk of NM ruptures. We hypothesize that the high levels of progerin and low levels of lamin B1 in SMCs increase nuclear stiffness, rendering nuclei more susceptible to damage from mechanical forces (i.e., that reduced compliance renders the NMs more susceptible to ruptures).

All of the cells in the aorta of *Lmna*^{G609G} mice (intimal endothelial cells, medial SMCs, and adventitial fibroblasts) express high levels of progerin, and all of these cells are subjected to rhythmic stretching from pulsatile blood flow, but both NM ruptures and cell death are confined to the SMCs. We suspect that differences in nuclear lamin composition explain, at least in part, why endothelial and adventitial cells are protected from NM ruptures and cell death. By immunofluorescence microscopy, lamin B1 levels are very low in the medial SMCs of *Lmna*^{G609G} mice but high in endothelial cells and adventitial cells. In cell culture studies, increasing lamin B1 expression in progerin-expressing SMCs markedly reduced nuclear shape abnormalities, NM ruptures, DNA damage, and cell death. For this reason, we suspect that the robust expression of lamin B1 in endothelial and adventitial cells protects those cells from the toxicity of progerin (i.e., NM ruptures and cell death).

Our sequential nuclear extraction experiments provided insights into how lamin B1 reduces progerin-induced NM ruptures. Progerin and lamin B1 both contain carboxyl-terminal modifications (e.g., farnesylation) that promote interaction with the inner NM (36, 43). The nuclear extraction studies revealed that increased lamin B1 expression reduced progerin's association with the nuclear envelope, likely by limiting interactions between progerin's farnesyl lipid with the inner NM. Consistent with this interpretation, the association of nf-Prog with NMs was far weaker than with farnesylated progerin. The reduced association of nf-Prog with NMs likely explains the inability of nf-Prog to trigger NM ruptures. We suspect that increased lamin B1 expression limits NM ruptures in progerin-expressing SMCs in the same way, by competing with progerin for binding sites at the nuclear periphery and reducing progerin's association with the NMs.

In addition to limiting progerin's association with the NMs, increased lamin B1 expression alters the mechanical properties of the cell nucleus. In the past, others have reported, using micropipette aspiration and nuclear strain measurements, that the cell nucleus in progerin-expressing fibroblasts is stiffer than in WT cells (44–46). In the current studies, we used AFM to quantify nuclear stiffness in progerin-expressing SMCs. Consistent with the earlier reports (44–46), we found increased stiffness of the cell nucleus in progerin-expressing SMCs, but we sought to extend this further to determine if boosting lamin B1 expression had an impact on nuclear compliance. Our AFM results were clear: increasing lamin B1 expression decreased nuclear stiffness in SMCs. Lamin B1's capacity to decrease nuclear stiffness in SMCs was unique; nf-lamin B1, lamin A, and lamin B2 did not alter nuclear stiffness whereas knocking down lamin B1 expression increased nuclear stiffness. Remarkably, increased lamin B1 expression also decreased nuclear stiffness in progerin-expressing SMCs, indicating that the baseline levels of lamin B1 are an important factor in determining nuclear compliance (47).

Our discovery that lamin B1 decreases nuclear stiffness was initiated by studies showing that lamin B1 overexpression led to larger nuclei in adherent SMCs. Since cell spreading and cytoskeletal forces can affect nuclear size in adherent cells, we quantified the nuclear area in nonadherent SMCs that were compressed with a glass coverslip. In those studies, we observed larger nuclei in cells that overexpressed lamin B1. Lamin B1 overexpression also increased the nuclear area in progerin-expressing SMCs, but the effect was less pronounced (reflecting progerin's ability to increase nuclear stiffness). We observed consistent findings in lamin B1–transduced fibroblasts. In those cells, we showed that lamin B1 overexpression increased nuclear area at the expense of reduced nuclear height.

The identification of NM ruptures in aortic SMCs of *Lmna*^{G609G} mice adds to our understanding of the vascular pathology in HGPS. Because NM ruptures in SMCs precede any evidence of SMC loss, it seems likely that the ruptures contribute to cell death. The expression of progerin in cultured SMCs, at levels matching those in the aorta of the *Lmna*$^{G609G/+}$ mice, not only leads to NM ruptures but also to DNA damage and activation of the cGAS–STING pathway. The proposal that NM ruptures lead inexorably, directly or indirectly, to SMC death in *Lmna*^{G609G} mice is strengthened by recent studies of cortical neurons in the developing brain of lamin B1–deficient mouse embryos (26). In those studies, there was a clear association between NM ruptures and the death of migrating neurons within the cortical plate. Recently, NM ruptures were proposed to contribute to skeletal myopathy in *Lmna*-deficient mice (48). In those studies, NM ruptures were detected in individual muscle fibers that had been isolated by collagenase treatment and manual pipetting; however, it was unclear whether NM ruptures preceded myopathic changes.

Our current studies focused on progerin-expressing SMCs and the arterial pathology in the ascending thoracic aorta — the region with the most severe arterial disease. We would point out, however, that the disease phenotypes in mouse models of progeria (13, 49–52) are not confined to the aorta. We have not yet explored whether NM ruptures contribute to disease phenotypes in other tissues, but based on the current studies we would not be surprised if future studies found NM ruptures in other sites, particularly in tissues where conditions favor NM ruptures (i.e., high progerin, low lamin B1, and high mechanical stress).

In summary, our current studies showed that the expression of progerin, but not WT prelamin A, in cultured SMCs triggers NM ruptures, DNA damage, and reduced cell survival. We showed that both high levels of progerin and low levels of lamin B1 increase the number of NM ruptures, which are further increased in cells subjected to mechanical stretching. In aortic SMCs of $Lmna^{G609G/+}$ mice, lamin B1 levels in SMCs are very low. With age, aortic lamin B1 levels in these mice decline while the levels of progerin increase. These findings, combined with our cell culture studies, led us to suspect that we would find NM ruptures in the aortic SMCs of $Lmna^{G609G}$ mice. Indeed, we observed frequent NM ruptures in the medial SMCs of $Lmna^{G609G}$ mice. Importantly, the onset of NM ruptures and the appearance of abnormal nuclear morphology preceded SMC loss.

Methods

Mice. Mice with a targeted HGPS mutation ($Lmna^{G609G}$) (11, 12) were bred with Nuc-tdTomato transgenic mice from The Jackson Laboratory (Stock 023035). The Nuc-tdTomato mouse strain was genotyped by PCR with a mutant forward primer 5′-CCAGGCGGGCCATTTACCGTAAG-3′; a WT forward primer 5′-GGAGCGGGAGAAATGGATATG-3′; and a common reverse primer 5′-AAAGTCGCTCTGAGTTGTTAT-3′ (yielding a 320-bp product for the mutant allele and a 603-bp product for the WT allele). Mice were housed in a specific pathogen-free barrier facility with a 12-hour light/dark cycle. The mice were provided pelleted mouse chow (NIH31), water *ad libitum,* and nutritional food cups (DietGel, ClearH_20) as required for supportive care.

Cells. Immortalized mouse aortic SMCs (ATCC, CRL-2797) were cultured in DMEM containing 10% FBS (HyClone), 1× nonessential amino acids, 2 mM glutamine, 1 mM sodium pyruvate, and 0.2 mg/mL G418 (12). For some experiments, SMCs were exposed to UV light (100 mJ/cm^2) with a Stratalinker 2400 (Stratagene). To reduce lamin B1 levels, cells were transfected with 100 nM *Lmnb1* siRNA (Ambion, AM16706) using RNAiMAX (Invitrogen) according to manufacturer's instructions.

Dox-inducible expression of nuclear lamins in SMCs. SMCs harboring Dox-inducible pTRIPZ expression vectors for human prelamin A and human progerin have been described previously (12). The same approach was used to generate SMCs expressing Dox-inducible constructs for lamin B1, lamin B2, nf-Prog, and nf-lamin B1 (Supplemental Table 3). The expression plasmids were constructed by InFusion cloning (Takara Bio) of cDNAs into pTRIPZ. The mouse lamin B1 cDNA was amplified from pCMV6-*Lmnb1* (Origene, MC219388) with forward primer 5′-TACCGGTCCGGAATTATGGCGACCGCGAC-3′ and reverse primer 5′-ATACTCTAGAGCGGCTCACATAATGGCACA-3′. The human lamin B2 cDNA was amplified from pCMV6-*LMNB2* (Origene, SC106163) with forward primer 5′-ATGCGTGGACCTGGAGAAA-3′ and reverse primer 5′-GTAGCCCCTTGAATTTCACATCACGTAGCAGCCTCTTGA-3′. A nf-Prog cDNA was created by changing the C-terminal –CSIM signal sequence in pCMV-XL5-progerin (12) to –SSIM using the QuickChange Lightning mutagenesis kit (Agilent) with forward primer 5′-CAGAGCCCCCAGAACTCCAGCATCATGTAATCT-3′ and reverse primer 5′-AGATTACATGATGCTGGAGTTCTGGGGGCTCTG-3′. A nf-lamin B1 cDNA was created by changing the C-terminal –CAIM signal sequence in pCMV6-*Lmnb1* (Origene, MC219388) to –SAIM with forward primer 5′-GTCAGATCGCACCGGATGGCGACCCGCGA-3′ and reverse primer 5′-GGCTCACATAATGGCACTGCTTTTATTGGATGCTC-3′. All plasmids were verified by DNA sequencing. Packaging of lentivirus and cell transduction were performed by the UCLA Vector Core. Transduced cells were selected with 1.5 μg/mL puromycin for 2 weeks; clones were isolated by limiting dilution.

Constitutive expression of RFP and nuclear lamins in SMCs. SMCs expressing GFP with a nuclear localization signal (NLS-GFP), KASH2-GFP, and extKASH2-GFP have been described previously (12, 26). SMCs expressing NLS-RFP, prelamin A, and progerin were generated by transducing SMCs with pCDH expression plasmids (Supplemental Table 3). The pCDH-NLS-RFP plasmid was created by excising the GFP cDNA in pCDH-NLS-GFP (26) with *Sma*I and *Not*I and replacing it with the RFP cDNA from TurboRFP-H2B (Addgene, 58047) by InFusion cloning. The RFP cDNA was amplified with forward primer 5′-GCGTAAGGTTCCCGGTATGAGCGAGCTGATCAAGGAGA-3′ and reverse primer 5′-CAGATCCTTGCGGCCTTATCTGTGCCCCAGTTTGC-3′. The prelamin A and progerin cDNAs were subcloned into *Eco*RI and *Not*I sites of pCDH by In-Fusion cloning. Human prelamin A was amplified with forward primer 5′-GCTAG-

CGAATTATGGAGACCCCGTCCCAGC-3′ and reverse primer 5′-GATCCTTGCGGCCTTACATGATGCTGCAGT-3′; and human progerin was amplified with forward primer 5′-GCTAGCGAATTATGGAGACCCCGTCCCAGC-3′ and reverse primer 5′-CAGATCCTTGCGGCCTTACATGATGCTGCA-3′. All plasmids were verified by DNA sequencing. Packaging of lentivirus and cell transduction was performed by UCLA's Vector Core. Transduced cells were selected with 3 μg/mL blasticidin (Thermo Fisher Scientific) for 2 weeks; clones were isolated by limiting dilution.

Measurement of NM ruptures in live SMCs. SMCs stably expressing GFP or RFP in the nucleus were seeded into 2-well chamber slides with glass coverslip bottoms (Thermo Fisher Scientific) and cultured in DMEM with 10% FBS (as described earlier). Dox was added to induce nuclear lamin expression and incubated for 24 hours before examination by microscopy. The cell culture chamber slide was mounted into a CO_2 and temperature-controlled stage on a Zeiss LSM 800 confocal laser-scanning microscope controlled by Zen Blue 2.3 software (all from Zeiss). The cells were visualized for 24 hours at 37°C and 5% CO_2 with a Plan-Apochromat 20×/0.8 NA objective. Images of a 3 × 3 tiled field (~1.3 mm^2) were captured every 10 minutes. Differential interface contrast (DIC) was acquired with the transmitted light detector (T-PMT; Zeiss) at the same time as the GFP signal. Composite images of 10 *z*-sections (1 μm sections) were generated and analyzed for NM ruptures. The number of cells with a NM rupture, defined by the escape of GFP (or RFP) in the cytoplasm, was divided by the total number of cells in a field.

Measurement of NM ruptures in stretched SMCs. SMCs stably expressing GFP were seeded onto PDMS membranes and cultured for 48 hours. The membranes were clamped into a custom-built biaxial cell stretching device (12) and stretched 2 mm at 0.5 Hz for 2 hours. The membranes were fixed with 4% paraformaldehyde (PFA; MilliporeSigma) and processed for confocal laser-scanning microscopy. Images from random locations were acquired and scored for NM ruptures. A minimum of 200 cells were scored by 2 trained observers blinded to sample identity.

Measurement of NM ruptures in aortic sections. Mice expressing the Nuc-tdTomato transgene were perfused with 3% PFA in PBS and tissues postfixed in the same solution at 4°C. Frozen tissue sections (10 μm–thick) were stained with DAPI and mounted in Antifade (Invitrogen). Images were captured on a Zeiss LSM 800 laser-scanning confocal microscope controlled by Zen Blue 2.3 software using a Plan-Apochromat 20×/0.8 NA objective. Maximum image projections were generated from scans of the tdTomato and DAPI channels, combined with the autofluorescence signal in the GFP channel. The latter was used to identify the elastic fibers in the media layer. A NM rupture was defined as the appearance of tdTomato fluorescence outside of a nucleus, as judged by DAPI staining. If tdTomato fluorescence was present between 2 adjacent nuclei, this was counted as a single NM rupture. NM ruptures were counted and expressed relative to the total number of nuclei examined.

Measurement of phosphorylated-STING in static and stretched SMCs. SMCs expressing prelamin A or progerin were seeded onto PDMS membranes and cultured for 48 hours. Membranes were stretched for 3 hours (2 mm at 0.5 Hz), fixed with 4% PFA, and processed for immunocytochemistry. Cells were incubated with antibodies against phosphorylated-STING (Cell Signal Technology) and LAP2β, and bound antibodies detected with species-specific fluorescent-labeled antibodies (Supplemental Table 1). Fluorescence microscopy was performed on a Zeiss LSM 800 laser-scanning microscope. Quantification of cells with positive phosphorylated-STING staining was performed by 2 trained observers blinded to sample identity. A minimum of 200 cells were scored per group.

Sequential extraction of SMC nuclei. SMC nuclei were extracted as described by Nmezi and colleagues (38). The sequential extraction of nuclei (with low and high salt, detergent, and urea), and quantification of nuclear lamins in the soluble extracts, provides a measure of the association of nuclear lamins with the nuclear envelope. SMCs in 100 mm tissue culture dishes were collected by scraping into 3 mL of ice-cold PBS and centrifugation at 10,000 *g* for 30 seconds. The cell pellet was resuspended in 1 mL of lysis buffer (ice-cold PBS, 0.1% IGEPAL from Sigma-Aldrich, and protease inhibitors from Sigma-Aldrich) and the lysate centrifuged at 10,000 *g* for 1 minute at 4°C. The pellet was resuspended in 250 μL of nuclear isolation buffer (10 mM HEPES pH 7.4; 2 mM $MgCl_2$; 25 mM KCl; 250 mM sucrose; 1mM DTT; and protease inhibitors), and 50 μL ("nuclei" fraction) was set aside for analysis by western blotting. The remainder was sonicated on ice (five 2-second pulses), centrifuged at 20,000 *g* for 5 minutes at 4°C, and the supernatant ("sonicate" fraction) collected. The pellet was resuspended in 150 μL of nuclear extraction buffer (20 mM HEPES pH 7.4 and protease inhibitors) containing 0.2 M NaCl, and incubated for 20 minutes with end-over-end rotation. The sample was centrifuged at 200,000 *g* for 10 minutes at 4°C and the supernatant ("0.2 M NaCl" fraction) collected. The extraction procedure was repeated with 150 μL of 0.5 M NaCl, 2% Triton X100, 4 M urea, and 8 M urea (all in nuclear extraction buffer). Protein extracts were stored at –80°C until analysis.

Measurement of nuclear area in nonadherent cells. Dox was added to SMCs to induce nuclear lamin expression, and then stained with Hoechst 33342 (5 μg/mL) for 5 minutes in PBS. The cells were washed 3 times with PBS and detached with trypsin. The cells were resuspended in culture media and diluted to 1×10^6 cells per mL. A 5-μL aliquot of stained cells was placed into a glass coverslip-bottom dish (Thermo Fisher Scientific) and allowed to settle for 5 minutes. Images of cell nuclei were recorded with a Zeiss LSM 800 confocal microscope before and after placing a 12 mm coverslip (Fisher Scientific) on top of the cells. The nuclear area was measured with ImageJ (NIH) software.

Measuring nuclear stiffness by AFM. SMCs in 35 mm glass coverslip-bottom dishes (World Precision Instruments) were incubated with Dox for 24 hours to induce nuclear lamin expression. Nuclear stiffness (Young's modulus) in adherent cells was measured on a NanoWizard 4a Bioscience AFM (JPK Instruments) coupled with a Zeiss LSM5 confocal fluorescence microscope (53, 54). A spherical AFM tip with a radius of 500 nm and 0.2 N/m spring constant cantilever (Nanotools, B500-CONT) was placed on top of the cell over the nucleus, identified by staining DNA with Hoechst 33342. Three different areas of the nucleus were sampled with a 2-nN maximum set point. The 3 measurements were used to calculate the average Young's modulus for a single cell. All measurements were performed at 37° C in HEPES-buffered culture medium. The Young's modulus was measured in 25 randomly selected cells for each group, and the force curves analyzed with JPK Data Processing software (JPK Instruments). The Young's modulus was calculated with the Hertz model for a spherical tip and applied to fit the slopes of the approach curve.

Statistics. Statistical analyses were performed with GraphPad Prism software. Experimental groups were analyzed by unpaired 2-tailed Student's *t* test, or 1-way and 2-way ANOVA with Tukey's multiple comparisons test. Statistical significance was considered when the P value was less than 0.05. Red circles in bar graphs show the average values of independent experiments or values for individual animals.

Study approval. All animal studies were approved by UCLA's Animal Research Committee.

Author contributions

PHK, SGY, and LGF designed the research studies. PHK, NYC, YT, PJH, TAW, JLCF, and LGF performed the experiments. NKG and PHK conducted the parallel microfiltration studies. PHK, SGY, and LGF wrote the first draft of the manuscript. PHK, NYC, PJH, YT, TAQ, JLCF, NKG, ACR, SGY, and LGF edited the manuscript.

Acknowledgments

We thank Dino Di Carlo (UCLA) for the use of the plasma cleaner. This work was supported by the National Institutes of Health (AG047192) and the National Center for Advancing Translational Sciences UCLA CTSI (UL1TR001881). Virus production and transduction were performed by the IMTC/UCLA Vector Core, which is supported by CURE/P30 DK041301.

Address correspondence to: Stephan G. Young or Loren G. Fong, UCLA Department of Medicine/Division of Cardiology, 650 Charles E. Young Dr. South, A2-237 CHS, Los Angeles, California 90095, USA. Phone: 310.825.4934; Email: sgyoung@mednet.ucla.edu (SGY). Phone: 310.825.4997; Email: lfong@mednet.ucla.edu (LGF).

1. Eriksson M, et al. Recurrent de novo point mutations in lamin A cause Hutchinson-Gilford progeria syndrome. *Nature*. 2003;423(6937):293–298.
2. De Sandre-Giovannoli A, et al. Lamin a truncation in Hutchinson-Gilford progeria. *Science*. 2003;300(5628):2055.
3. Young SG, et al. Prelamin A, Zmpste24, misshapen cell nuclei, and progeria--new evidence suggesting that protein farnesylation could be important for disease pathogenesis. *J Lipid Res*. 2005;46(12):2531–2358.
4. Glynn MW, Glover TW. Incomplete processing of mutant lamin A in Hutchinson-Gilford progeria leads to nuclear abnormalities, which are reversed by farnesyltransferase inhibition. *Hum Mol Genet*. 2005;14(20):2959–2969.
5. Merideth MA, et al. Phenotype and course of Hutchinson-Gilford progeria syndrome. *N Engl J Med*. 2008;358(6):592–604.
6. Gordon LB, et al. Reduced adiponectin and HDL cholesterol without elevated C-reactive protein: clues to the biology of premature atherosclerosis in Hutchinson-Gilford progeria syndrome. *J Pediatr*. 2005;146(3):336–341.
7. Stehbens WE, et al. Histological and ultrastructural features of atherosclerosis in progeria. *Cardiovasc Pathol*. 1999;8(1):29–39.
8. Stehbens WE, et al. Smooth muscle cell depletion and collagen types in progeric arteries. *Cardiovasc Pathol*. 2001;10(3):133–136.
9. Varga R, et al. Progressive vascular smooth muscle cell defects in a mouse model of Hutchinson-Gilford progeria syndrome. *Proc Natl Acad Sci U S A*. 2006;103(9):3250–3255.
10. Osorio FG, et al. Splicing-directed therapy in a new mouse model of human accelerated aging. *Sci Transl Med*. 2011;3(106):106ra7.

11. Lee JM, et al. Modulation of LMNA splicing as a strategy to treat prelamin A diseases. *J Clin Invest*. 2016;126(4):1592–1602.
12. Kim PH, et al. Disrupting the LINC complex in smooth muscle cells reduces aortic disease in a mouse model of Hutchinson-Gilford progeria syndrome. *Sci Transl Med*. 2018;10(460):eaat7163.
13. Zaghini A, et al. Long term breeding of the Lmna G609G progeric mouse: characterization of homozygous and heterozygous models. *Exp Gerontol*. 2020;130:110784.
14. Capell BC, et al. A farnesyltransferase inhibitor prevents both the onset and late progression of cardiovascular disease in a progeria mouse model. *Proc Natl Acad Sci U S A*. 2008;105(41):15902–15907.
15. Balmus G, et al. Targeting of NAT10 enhances healthspan in a mouse model of human accelerated aging syndrome. *Nat Commun*. 2018;9(1):1700.
16. Hamczyk MR, et al. Progerin accelerates atherosclerosis by inducing endoplasmic reticulum stress in vascular smooth muscle cells. *EMBO Mol Med*. 2019;11(4):e9736.
17. Pitrez PR, et al. Vulnerability of progeroid smooth muscle cells to biomechanical forces is mediated by MMP13. *Nat Commun*. 2020;11(1):4110.
18. Chen X, et al. A small-molecule ICMT inhibitor delays senescence of Hutchinson-Gilford progeria syndrome cells. *Elife*. 2021;10:e63284.
19. Crisp M, et al. Coupling of the nucleus and cytoplasm: role of the LINC complex. *J Cell Biol*. 2006;172(1):41–53.
20. Razafsky D, et al. Validation of a mouse model to disrupt LINC complexes in a cell-specific manner. *J Vis Exp*. 2015;(106):e53318.
21. Song M, et al. Shear stress-induced mechanotransduction protein deregulation and vasculopathy in a mouse model of progeria. *Stem Cell Res Ther*. 2014;5(2):41.
22. Vorburger K, et al. Modification of nuclear lamin proteins by a mevalonic acid derivative occurs in reticulocyte lysates and requires the cysteine residue of the C-terminal CXXM motif. *EMBO J*. 1989;8(13):4007–4013.
23. Vargas JD, et al. Transient nuclear envelope rupturing during interphase in human cancer cells. *Nucleus*. 2012;3(1):88–100.
24. Tamiello C, et al. Soft substrates normalize nuclear morphology and prevent nuclear rupture in fibroblasts from a laminopathy patient with compound heterozygous LMNA mutations. *Nucleus*. 2013;4(1):61–73.
25. Cho S, et al. Mechanosensing by the lamina protects against nuclear rupture, DNA damage, and cell-cycle arrest. *Dev Cell*. 2019;49(6):920–935.
26. Chen NY, et al. An absence of lamin B1 in migrating neurons causes nuclear membrane ruptures and cell death. *Proc Natl Acad Sci U S A*. 2019;116(51):25870–25879.
27. Rober RA, et al. Differential timing of nuclear lamin A/C expression in the various organs of the mouse embryo and the young animal: a developmental study. *Development*. 1989;105(2):365–378.
28. Young SG, et al. Understanding the roles of nuclear A- and B-type lamins in brain development. *J Biol Chem*. 2012;287(20):16103–16110.
29. Zhang J, et al. A human iPSC model of Hutchinson Gilford progeria reveals vascular smooth muscle and mesenchymal stem cell defects. *Cell Stem Cell*. 2011;8(1):31–45.
30. De Vos WH, et al. Repetitive disruptions of the nuclear envelope invoke temporary loss of cellular compartmentalization in laminopathies. *Hum Mol Genet*. 2011;20(21):4175–4186.
31. Denais CM, et al. Nuclear envelope rupture and repair during cancer cell migration. *Science*. 2016;352(6283):353–358.
32. Raab M, et al. ESCRT III repairs nuclear envelope ruptures during cell migration to limit DNA damage and cell death. *Science*. 2016;352(6283):359–362.
33. Stewart-Hutchinson PJ, et al. Structural requirements for the assembly of LINC complexes and their function in cellular mechanical stiffness. *Exp Cell Res*. 2008;314(8):1892–1905.
34. Gonzalo S, Coll-Bonfill N. Genomic instability and innate immune responses to self-DNA in progeria. *Geroscience*. 2019;41(3):255–266.
35. Li T, Chen ZJ. The cGAS-cGAMP-STING pathway connects DNA damage to inflammation, senescence, and cancer. *J Exp Med*. 2018;215(5):1287–1299.
36. Holtz D, et al. The CaaX motif of lamin A functions in conjunction with the nuclear localization signal to target assembly to the nuclear envelope. *Cell*. 1989;59(6):969–977.
37. Mallampalli MP, et al. Inhibiting farnesylation reverses the nuclear morphology defect in a HeLa cell model for Hutchinson-Gilford progeria syndrome. *Proc Natl Acad Sci U S A*. 2005;102(40):14416–14421.
38. Nmezi B, et al. Concentric organization of A- and B-type lamins predicts their distinct roles in the spatial organization and stability of the nuclear lamina. *Proc Natl Acad Sci U S A*. 2019;116(10):4307–4315.
39. Otto H, et al. Identification of tyrosine-phosphorylated proteins associated with the nuclear envelope. *Eur J Biochem*. 2001;268(2):420–428.
40. Worman HJ, Michaelis S. Permanently farnesylated prelamin A, progeria, and atherosclerosis. *Circulation*. 2018;138(3):283–286.
41. Toyama BH, et al. Identification of long-lived proteins reveals exceptional stability of essential cellular structures. *Cell*. 2013;154(5):971–982.
42. Razafsky D, et al. Lamin B1 and lamin B2 are long-lived proteins with distinct functions in retinal development. *Mol Biol Cell*. 2016;27(12):1928–1937.
43. Nigg EA, et al Targeting lamin proteins to the nuclear envelope: the role of CaaX box modifications. *Biochem Soc Trans*. 1992;20(2):500–504.
44. Dahl KN, et al. Distinct structural and mechanical properties of the nuclear lamina in Hutchinson-Gilford progeria syndrome. *Proc Natl Acad Sci U S A*. 2006;103(27):10271–10276.
45. Verstraeten VLRM, et al. Increased mechanosensitivity and nuclear stiffness in Hutchinson-Gilford progeria cells: effects of farnesyltransferase inhibitors. *Aging Cell*. 2008;7(3):383–393.
46. Booth EA, et al. Nuclear stiffening and chromatin softening with progerin expression leads to an attenuated nuclear response to force. *Soft Matter*. 2015;11(32):6412–6418.
47. Shin JW, et al. Lamins regulate cell trafficking and lineage maturation of adult human hematopoietic cells. *Proc Natl Acad Sci U S A*. 2013;110(47):18892–18897.
48. Earle AJ, et al. Mutant lamins cause nuclear envelope rupture and DNA damage in skeletal muscle cells. *Nat Mater*. 2020;19(4):464–473.

49. Bergo MO, et al. Zmpste24 deficiency in mice causes spontaneous bone fractures, muscle weakness, and a prelamin A processing defect. *Proc Natl Acad Sci U S A*. 2002;99(20):13049–13054.
50. Pendás AM, et al. Defective prelamin A processing and muscular and adipocyte alterations in Zmpste24 metalloproteinase-deficient mice. *Nat Genet*. 2002;31(1):94–99.
51. Sagelius H, et al. Targeted transgenic expression of the mutation causing Hutchinson-Gilford progeria syndrome leads to proliferative and degenerative epidermal disease. *J Cell Sci*. 2008;121(Pt 7):969–978.
52. Schmidt E, et al. Expression of the Hutchinson-Gilford progeria mutation during osteoblast development results in loss of osteocytes, irregular mineralization, and poor biomechanical properties. *J Biol Chem*. 2012;287(40):33512–33522.
53. Liu H, et al. In situ mechanical characterization of the cell nucleus by atomic force microscopy. *ACS Nano*. 2014;8(4):3821–3828.
54. Guerrero CR, et al. Subsurface imaging of cell organelles by force microscopy. *ACS Nano*. 2019;13(8):9629–9637.

Supplementary Materials and Methods

Dox-inducible expression of lamin B1 in mouse embryonic fibroblasts (MEFs). MEFs were transduced with the pTRIPZ-*Lmnb1* construct by UCLA's Vector Core. Transduced cells were selected with 3μg/ml puromycin for two weeks; clones were isolated by limiting dilution.

Quantitative real time-PCR. Total RNA was isolated and treated with DNase I (Ambion) according to the manufacture's recommendation. RNA was reverse-transcribed with random primers with SuperScript III cDNA Synthesis Kit (Invitrogen). cDNA samples were diluted in nuclease-free water and stored at –80° C. RT-PCR reactions were performed on a 7900 Fast Real-Time PCR system (Applied Biosystems) with SYBR Green PCR Master Mix (Bioline). Transcript levels were calculated by the comparative cycle threshold method and normalized to cyclophilin A expression. All oligonucleotide primers are listed in Table S2.

Western blotting. Urea-soluble protein extracts from cells and tissues were prepared as described (12). Proteins were size-fractionated on 4–12% gradient polyacrylamide Bis-Tris gels (Invitrogen) and transferred to nitrocellulose membranes. The membranes were blocked with Odyssey Blocking solution (LI-COR Bioscience, Lincoln, NE) for 1 h at RT and incubated with primary antibodies at 4° C overnight. After washing the membranes with PBS containing 0.2% Tween-20, they were incubated with infrared dye (IR)–labeled secondary antibodies at RT for 1 h. The IR signals were quantified with an Odyssey infrared scanner (LI-COR Biosciences). The antibodies and concentrations are listed in Table S1.

Immunofluorescence microscopy. Cells on coverslips or tissue sections (6–10-μm-thick) on glass slides were fixed with 4% paraformaldehyde in PBS and permeabilized with 0.2% Triton. The cells were processed for immunofluorescence microscopy as (12). The antibodies and antibody concentrations are listed in Table S1. Confocal fluorescence microscopy images were

obtained with a Zeiss LSM 800 laser-scanning microscope and images along the *z*-axis were processed by Zen Blue 2.3 software to generate maximum image projections.

Electron microscopy. Mice were perfused *in situ* with PBS followed by ice-cold fixative (2.5% glutaraldehyde, 3% paraformaldehyde in PBS). Tissue samples were processed as described previously (12). Images were acquired with an FEI T12 transmission electron microscope set to 120 kV accelerating voltage and a Gatan 2K × 2K digital camera (Electron Imaging Center).

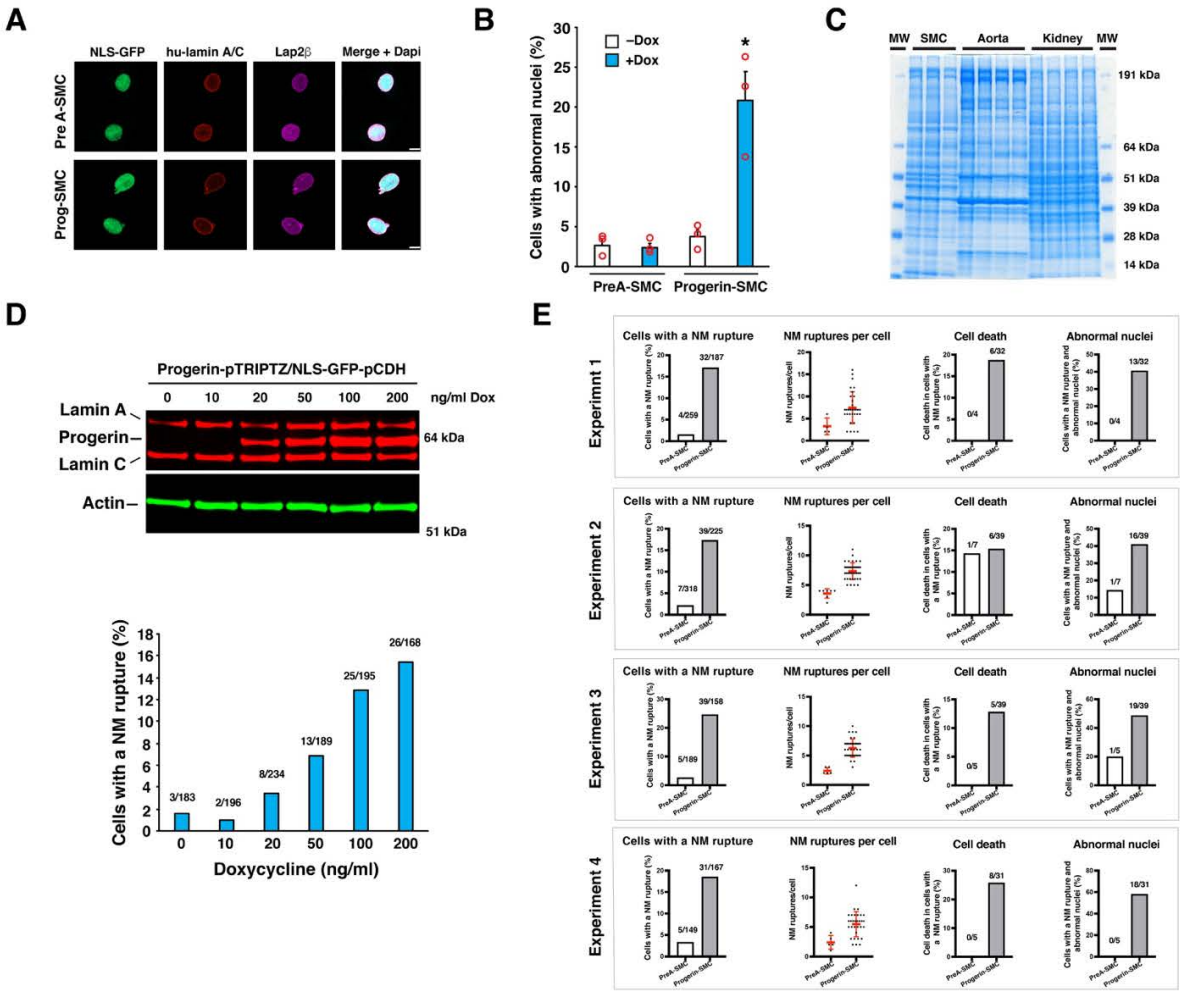

Fig. S1. Progerin causes NM ruptures in SMCs. (A) Confocal fluorescence microscopy images showing the expression of human prelamin A and human progerin in SMCs that express Nuc-GFP (*green*). Cells were stained with antibodies against human lamin A (*red*) and lap2β (*magenta*); nuclei were stained with Dapi (*blue*). Scale bar, 10 μm. **(B)** Bar graph showing that progerin increases abnormally shaped nuclei in fixed SMCs (mean ± SEM, $n = 3$ experiments; *t*-test, $*p < 0.02$). Progerin and prelamin A expression (*blue*) were induced with doxycycline (Dox). *Red* circles show the average values in individual experiments. **(C)** Coomassie Blue–stained SDS-PAGE gel used to quantify total protein for the western blot in Figure 1A. MW, molecular weight. **(D)** Progerin causes a dose-dependent increase in NM ruptures in SMCs. (Top) Western blot showing increasing progerin expression with increasing amounts of Dox. Actin was measured as a loading control. (Bottom) Bar graph showing dose-dependent increase in NM ruptures in SMCs. The ratios above each bar show the numbers of cells with a NM rupture over the total number of cells examined. **(E)** Characterization of NM ruptures in PreA-SMCs and Progerin-SMCs, as judged by time-lapse microscopy ($n = 4$ experiments). Bar graphs show the percentage of cells with a NM rupture; the number of NM ruptures per cell; the percentage of cells with a NM rupture that die; and the percentage of cells with a NM rupture and abnormal shaped nuclei. A total of 915 PreA-SMCs and 735 Prog-SMCs were analyzed.

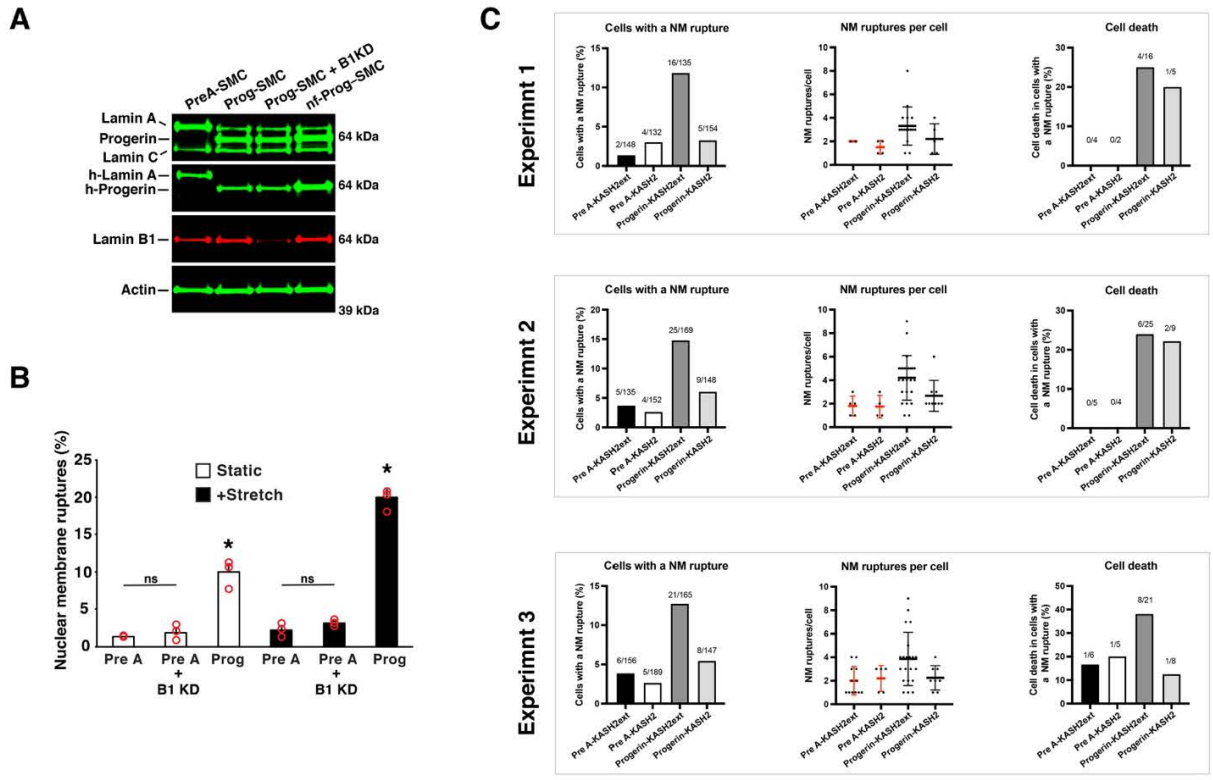

Fig. S2. Disrupting the LINC complex reduces NM ruptures in Prog-SMCs. (A) Western blot showing the expression of prelamin A, progerin, and nonfarnesylated progerin (all human) in SMCs, and the effects of lamin B1 siRNA knockdown (B1KD) in Prog-SMCs. Actin was measured as a loading control. **(B)** Bar graph showing that lamin B1 knockdown (B1 KD) does not increase NM ruptures in PreA-SMCs under either static (*white* bars) or stretched (*black* bars) conditions. Values compared to NM ruptures in static PreA-SMCs (mean ± SEM, $n = 3$ experiments; two-way ANOVA, $*p < 0.0001$). ns, non-significant. *Red* circles show average values in individual experiments. **(C)** Characterization of NM ruptures in PreA-SMC and Prog-SMCs in the presence of either KASH2 or KASH2ext, as judged by time-lapse microscopy ($n = 3$ experiments). Bar graphs show the percentage of cells with a NM rupture; the number of NM ruptures per cell; and the percentage of cells with a NM rupture that die. The total number of cells scored in each experiment is shown in the bar graph on the left.

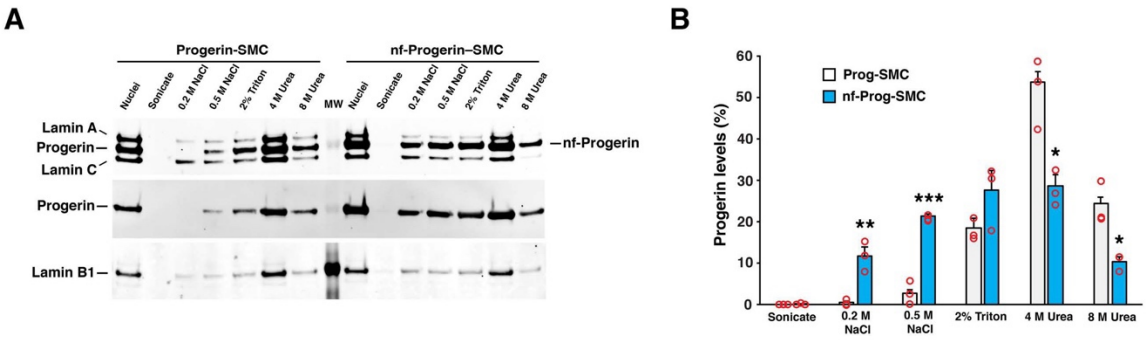

Fig. S3. Nonfarnesylated progerin is bound less tightly to nuclear membranes. (A) Western blot showing the extraction profiles for progerin and nonfarnesylated progerin expressed in SMCs. Nuclei isolated from Prog-SMCs and nf-Prog-SMCs were sequentially extracted with 0.2 M NaCl, 0.5 M NaCl, 2% Triton, 4 M urea, and 8 M urea. The supernatants from each extraction were analyzed by western blotting with antibodies against lamin A/C (to detect all A-type lamins), human lamin A (to detect progerin and nf-progerin), and lamin B1. **(B)** Bar graph comparing the extraction profiles for progerin (*white*) and nf-progerin (*blue*) (mean ± SEM, $n = 3$ experiments; *t*-test, $*p < 0.02$, $**p < 0.01$, $***p < 0.001$). *Red* circles show average values in individual experiments.

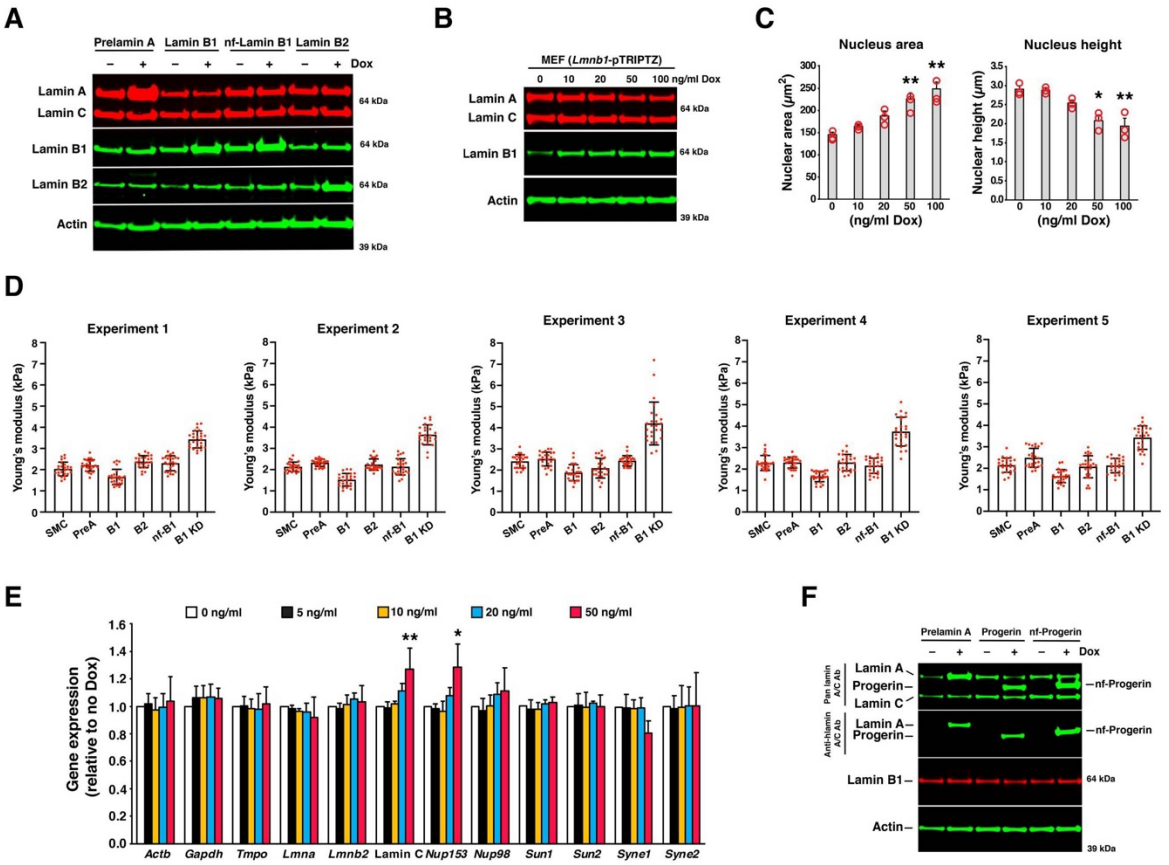

Fig. S4. Lamin B1 decreases nuclear stiffness. (A) Western blot showing the expression of prelamin A, lamin B1, nonfarnesylated lamin B1 (nf-lamin B1), and lamin B2 in SMCs. Lamin expression was induced with Dox. Actin levels were measured as a loading control. **(B)** Western blot showing inducible expression of lamin B1 in mouse embryonic fibroblasts (MEFs). Lamin B1 expression was induced with Dox. Actin levels were measured as a loading control. **(C)** Bar graphs showing the effects of lamin B1 on nuclear size in MEFs. Lamin B1 expression was induced in adherent MEFs with Dox (0–100 ng/ml) for 48 h. The cells were imaged by confocal fluorescence microscopy, and the nucleus area and height determined (mean ± SEM, n = 3 experiments; ANOVA, $*p < 0.01$, $**p < 0.002$). *Red* circles show the average values for independent experiments. **(D)** The effects of prelamin A (PreA), lamin B1 (B1), lamin B2 (B2), nf-lamin B1 (nf-B1), and lamin B1 knockdown (B1 KD) on nuclear stiffness in SMCs were measured by AFM 48 h after changing nuclear lamin expression. Each *red* dot represents an individual cell. Twenty-five cells were examined for each group. Mean ± SD. **(E)** Bar graph comparing the effects of lamin B1 expression on gene expression (mean ± SEM, n = 3 experiments). Comparisons made to SMCs not induced with Dox (*white* bar); ANOVA, $*p < 0.02$, $**p < 0.01$. **(F)** Western blot showing the expression of human prelamin A, human progerin, and human nonfarnesylated–progerin (nf-Progerin) in SMCs. A "pan lamin AC antibody" was used to detect mouse and human A-type lamins; a human lamin A–specific antibody was used to detect human lamin A and progerin. Actin was measured as a loading control.

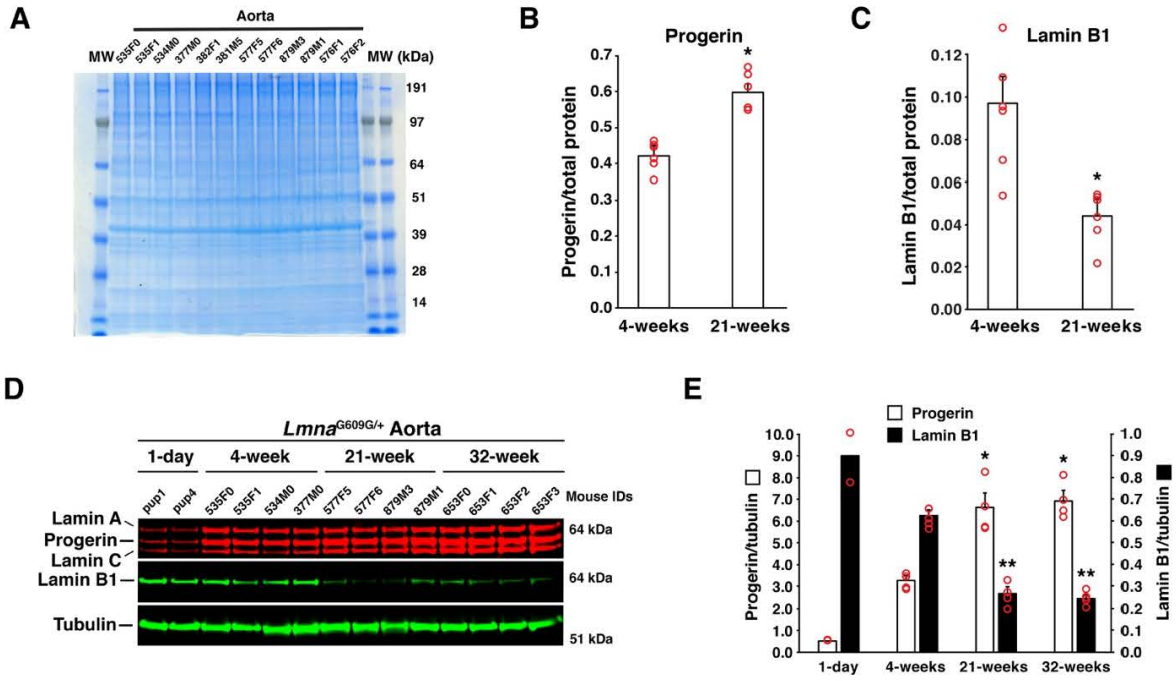

Fig. S5. Progerin and lamin B1 proteins levels change with age in the aorta of *Lmna*$^{G609G/+}$ mice. (A) Coomassie Blue–stained gel corresponding to the western blot in Figure 5A. MW, molecular weight. **(B)** Bar graph showing progerin levels, relative to total protein, for the western blot in Figure 5A (mean ± SEM, $n = 6$ mice/group; *t*-test, $*p < 0.001$). *Red* circles show values for individual animals. **(C)** Bar graph showing lamin B1 levels, relative to total protein, for the western blot in Figure 5A (mean ± SEM, $n = 6$ mice/group; *t*-test, $*p < 0.005$). *Red* circles show values for individual animals. **(D)** Western blot comparing the expression of progerin and lamin B1 in the aorta from 1-day-old, and 4-, 21-, and 32-week–old *Lmna*$^{G609G/+}$ mice. Thoracic aortas (2 or 4 mice per group) were extracted and analyzed as described in Figure 5A. IDs are shown above each sample. **(E)** Bar graph showing the expression of progerin (*white* bars) and lamin B1 (*black* bars), relative to tubulin, for the western blot in panel D. Shown are mean ± SEM ($n = 4$ mice/group), except for the 1-day old mice ($n = 2$). The values for the 21- and 32-week–old mice are compared to 4-week–old mice by ANOVA ($*p < 0.001$, $**p < 0.0001$). *Red* circles show the values for individual animals.

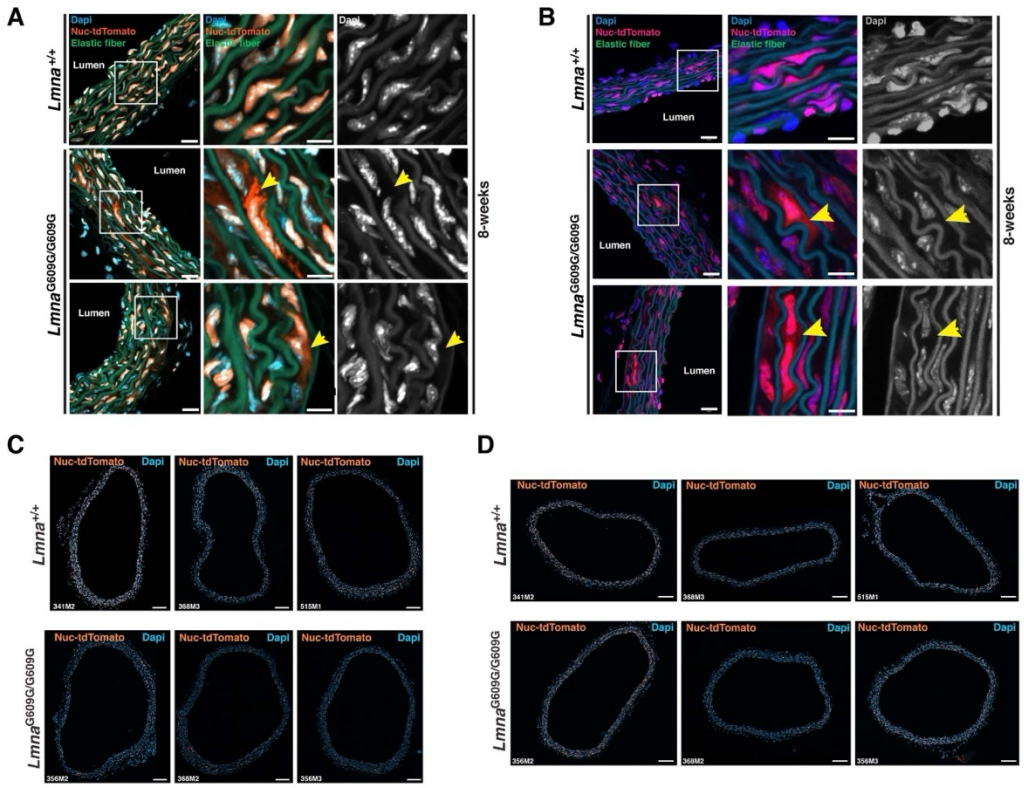

Fig. S6. NM ruptures in SMCs of the ascending thoracic aorta. (A, B) Confocal fluorescence microscopy images of the ascending aorta from 8-week–old *Lmna*$^{+/+}$ and *Lmna*$^{G609G/G609G}$ mice. The boxed regions are shown at higher magnification in the middle and far-right columns. The colored images show Dapi (*blue*), elastic fibers (*green*), and Nuc-tdTomato (*orange* or *red*). The y*ellow* arrows point to Nuc-tdTomato outside of SMC nuclei. To help visualize the boundaries of nuclei, the Dapi stain (*white*) is shown by itself in the far-right column. Scale bars: 20 μm (left column); 10 μm (middle column). **(C, D)** Fluorescence microscopy images of cross sections (10-μm-thick) of the upper (C) and lower (D) descending aorta from three 8-week–old *Lmna*$^{+/+}$ (top row) and three *Lmna*$^{G609G/G609G}$ (bottom row) mice. NM ruptures were quantified in these tissue sections (Fig. 7). The mouse IDs are shown in the bottom left hand corner of each image. Nuc-tdTomato (*orange*); Dapi (*blue*). Scale bars, 100 μm.

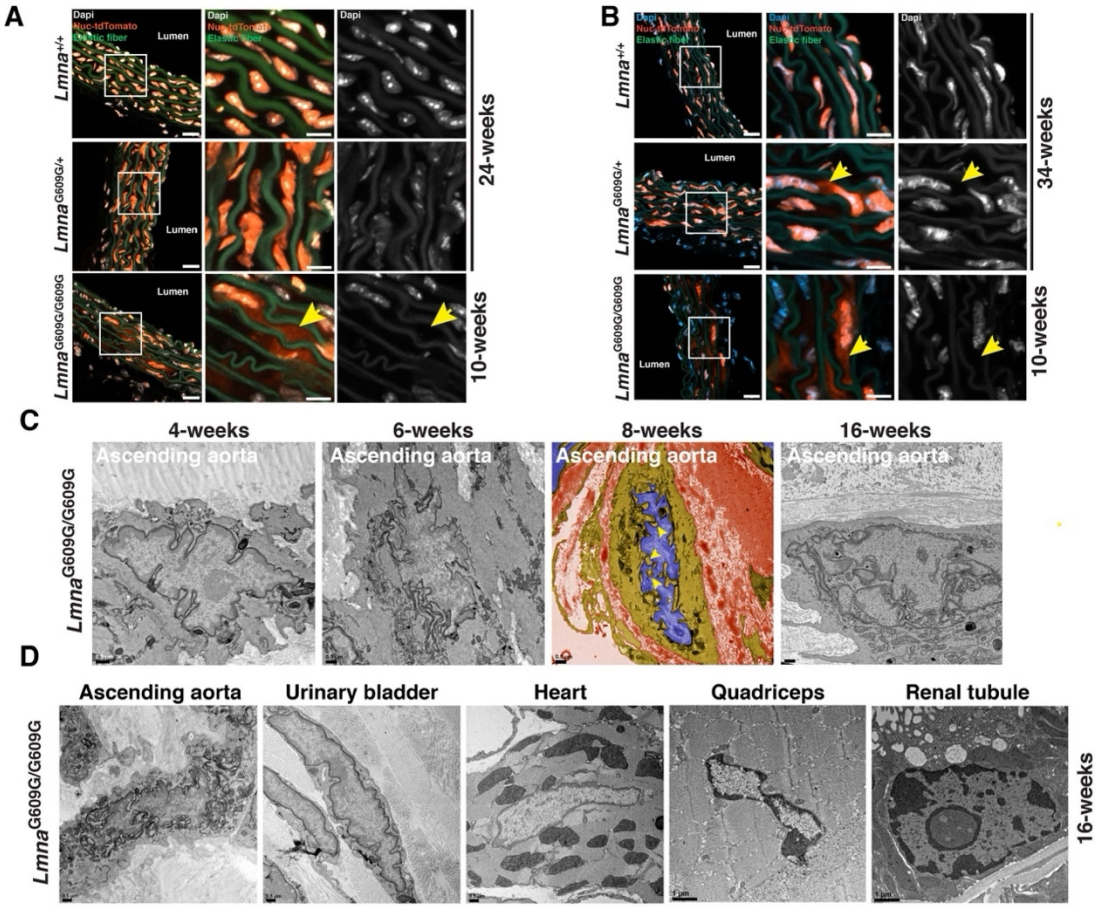

Fig. S7. NM ruptures and intranuclear membranous tubules in aortic SMCs of *Lmna*$^{G609G/+}$ mice. (A) Confocal fluorescence microscopy images of the ascending aorta from 24-week–old *Lmna*$^{+/+}$ and *Lmna*$^{G609G/+}$ mice and a 10-week–old *Lmna*$^{G609G/G609G}$ mouse. The boxed regions are shown at higher magnification on the right. The colored images show Dapi (*white*), elastic fibers (*green*), and Nuc-tdTomato (*orange*). The *yellow* arrow (middle column) points to Nuc-tdTomato outside of an SMC nucleus in the *Lmna*$^{G609G/G609G}$ mouse. To help visualize the boundaries of nuclei, the Dapi stain (*white*) is shown in the right column. Scale bars: 20 µm (left column); 10 µm (middle column). **(B)** Confocal fluorescence microscopy images of the ascending aorta from 34-week–old *Lmna*$^{+/+}$ and *Lmna*$^{G609G/+}$ mice and a 10-week–old *Lmna*$^{G609G/G609G}$ mouse. The boxed regions are shown at higher magnification to the right. Images were generated exactly as described in panel A except that the Dapi signal is colored *blue*. *Yellow* arrows point to Nuc-tdTomato outside of nucleus in the 34-week–old *Lmna*$^{G609G/+}$ mouse and the 10-week–old *Lmna*$^{G609G/G609G}$ mouse. Scale bars: 20 µm (left column); 10 µm (middle column). **(C)** Representative electron micrographs of SMC nuclei in the ascending aorta from 4-, 6-, 8-, and 16-week–old *Lmna*$^{G609G/G609G}$ mice. The image from the 8-week-old mouse was colored to make it easier to identify the cell nucleus (*blue*), cytoplasm (*tan*), and connective tissue (*reddish-brown*). *Yellow* arrowheads point to intranuclear tubules. Scale bars are shown in the images. **(D)** Representative electron micrographs of nuclei in the ascending aorta, urinary bladder, heart, quadriceps, and renal tubule from a 16-week–old *Lmna*$^{G609G/G609G}$ mouse. Scale bars are shown in the images.

Table S1. Antibodies used for western blotting and immunohistochemistry.

Antibody Description	Species	Source	Catalog #	Use	Dilution
β-actin	Goat	Santa Cruz Biotech	SC1616	WB, IF	1:3000
GFP	Rabbit	ThermoFisher	A11122	WB, IF	1:1000
Human lamin A	Mouse	Millipore	MAB3211	WB, IF	1:1500
Lamin A/C	Mouse	Santa Cruz Biotech	SC376248	WB, IF	1:1500
Lamin B1	Goat	Santa Cruz Biotech	SC6217	WB, IF	1:1500
Lamin B2	Mouse	Invitrogen	332100	WB, IF	1:1000
LAP2β	Mouse	BD Pharmingen	611000	IF	1:2000
Phospho-H2AX	Mouse	Millipore	05-636	WB, IF	1:3000
Phospho-STING (Ser365)	Rabbit	Cell Signaling Technology	72971S	IF	1:1000
Phospho-p53(Ser15)	Rabbit	Cell Signaling Technology	9284	WB, IF	1:3000
Tubulin	Rat	Novus Bio	NB600-506	WB	1:3000
Anti-rabbit IR800	Donkey	LI-COR	926-32213	WB	1:10000
Anti-goat IR800	Donkey	LI-COR	926-32214	WB	1:10000
Anti-rat IR800	Donkey	ThermoFisher	SA5-10032	WB	1:5000
Anti-mouse IR800	Donkey	ThermoFisher	SA5-10172	WB	1:5000
Anti-rabbit IR680	Donkey	LI-COR	926-32221	WB	1:5000
Anti-rat IR680	Goat	LI-COR	925-68076	WB	1:5000
Anti-goat IR680	Donkey	LI-COR	926-68074	WB	1:5000
Anti-mouse IR680	Donkey	ThermoFisher	SA5-10170	WB	1:5000
Anti-mouse Alexa 488	Donkey	Invitrogen	A21202	IF	1:2000
Anti-rabbit Alexa 488	Donkey	Invitrogen	A21206	IF	1:2000
Anti-goat Alexa 488	Donkey	Invitrogen	A11055	IF	1:2000
Anti-goat Alexa 555	Donkey	Invitrogen	A21432	IF	1:2000
Anti-rabbit Alexa 555	Donkey	Invitrogen	A31572	IF	1:200
Anti-rabbit Alexa 568	Donkey	Invitrogen	A10042	IF	1:2000
Anti-mouse Alexa 568	Donkey	Invitrogen	A10037	IF	1:2000

Anti-mouse Alexa 647	Donkey	Invitrogen	A31571	IF	1:2000
Anti-rabbit Alexa 647	Donkey	Invitrogen	A31573	IF	1:2000
Anti-goat Alexa 647	Donkey	Invitrogen	A21447	IF	1:2000
Anti-rat Alexa 650	Donkey	ThermoFisher	SA5-10029	IF	1:200

Table S2. Quantitative RT-PCR primers.

Gene or transcript	Forward (5′–3′)	Reverse (5′–3′)
Actb	GGCTGTATTCCCCTCCATCG	CCAGTTGGTAACAATGCCATGT
Ppia	TGAGCACTGGAGAGAAAGGA	CCATTATGGCGTGTAAAGTCA
Gapdh	GCACAGTCAAGGCCGAGAAT	GCCTTCTCCATGGTGGTGAA
Lmna	CCTATCGAAAGCTGCTGGAG	CCTGAGACTGGGATGAGTGG
Lmnb1	CAACTGACCTCATCTGGAAGAAC	TGAAGACTGTGCTTCTCTGAGC
Lmnb2	GAGGACATTGCCTACAAGTTCAC	TTCCACACAAGGGTTGATG
Lamin C	GACAATGAGGATGACGACGAG	TTAATGAAAAGACTTTGGCATGG
Nup153	AAGCGAAGTGCTCCTTGTGAGG	TGGTAGTGGGTTGAAGAGCAGG
Nup98	CCTCTTGGTACAGGAGCCTTTG	TTGAGGTGCTGCTGGAGAACAG
Progerin	CTGAGTACAACCTGCGCTCA	AGTTCTGGGAGCTCTGGGCT
Snf7b	GCAGGACATTGCTGACCAGCAA	CAAGTTCCTCCAACTCTGCCATG
Sun1	AGCATCCTAAGCACTCGGT	TAGATGTCGGGCTGGATCAC
Sun2	CAGGATTGGAATGGTGGATTA	AGTGCCGTCTTGGTCTCATAA
Syne1	CTGCTGCTTATTGGACTCACCT	GAGGAGGACCGTTGGTATATCTG
Syne2	CAGGAGTATCCAGAACATTCCCG	AGACTGCTGTGCCTGGATTTCG
Tmpo	GGAGTGAATCCTGGTCCCATTG	GACTGTTGGAAGAGGAGTAGAGG
Vps2	AACCGAGCCATGAGAGAACTGG	ACGCACCAGGTCTTTTGCCATG
Vps20	GAGCAACTGCTCGATAGGACAG	CCCTCCATCACCTTCATCTCGA
Vps24	TCAGGTCAAGGAAAGCCGTGAG	TGCAGAGAACCAGCTACTCGCA
Vps4	GAGAACCAGAGTGAAGGCAAGG	TCCACCGTATGTTCGGCTTCTC
Vps60	GATGAGAGAGGGTCCTGCTAAG	CAGGTTGTCTCGCTGTTGCTCA

Table S3. Plasmid constructs.

Plasmid name	Protein	Constitutive or inducible	Drug selection
Prelamin A-pTRIPZ	Prelamin A	Inducible	Puromycin
Progerin-pTRIPZ	Progerin	Inducible	Puromycin
nf-Progerin-pTRIPZ	Non-farnesylated progerin	Inducible	Puromycin
Lmnb1-pTRIPZ	Lamin B1	Inducible	Puromycin
nf-*Lmnb1*-pTRIPZ	Non-farnesylated lamin B1	Inducible	Puromycin
LMNB2-pTRIPZ	Lamin B2	Inducible	Puromycin
Prelamin A-pCDH	Prelamin A	Constitutive	Blasticidin
Progerin-pCDH	Progerin	Constitutive	Blasticidin
NLS-CopGFP-pCDH	Nuclear localized GFP	Constitutive	Blasticidin
NLS-TurboRFP-pCDH	Nuclear localized RFP	Constitutive	Blasticidin
pLenti6-GFP-KASH2	GFP–KASH2	Constitutive	Blasticidin
pLenti6-GFP-KASH2ext	GFP–KASH2ext	Constitutive	Blasticidin

Full unedited gel for Figure 1A.

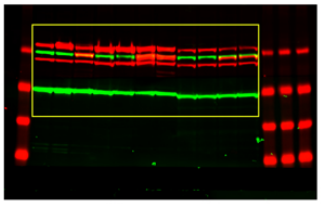

Antibodies
Lamin A/C
Lamin B1
Tubulin

Full unedited gel for Figure 3A.

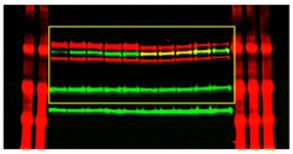

Antibodies
Lamin A/C
Lamin B1
Tubulin
Actin

Full unedited gel for Figure 3H.

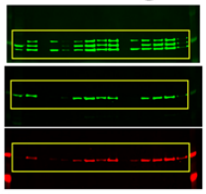

Antibodies
Lamin A/C
hLamin A/C
Lamin B1

Full unedited gel for Figure 4G.

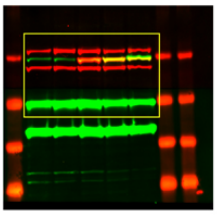

Antibodies
Lamin A/C
Lamin B1
Tubulin
Actin

Full unedited gel for Figure 5A.

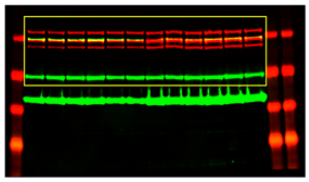

Antibodies
Lamin A/C
Lamin B1
Tubulin
Actin

Full unedited gel for Figure 5G.

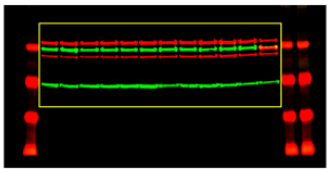

Antibodies
Lamin A/C
Lamin B1
Tubulin

Full unedited gel for Figure S1B.

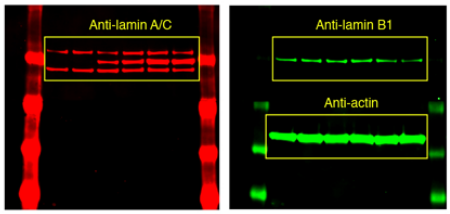

Full unedited gel for Figure S2A.

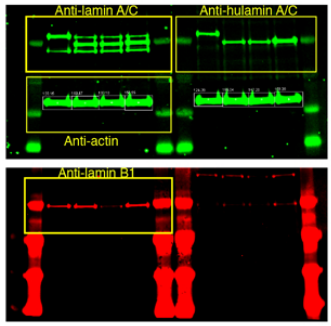

Full unedited gel for Figure S3A.

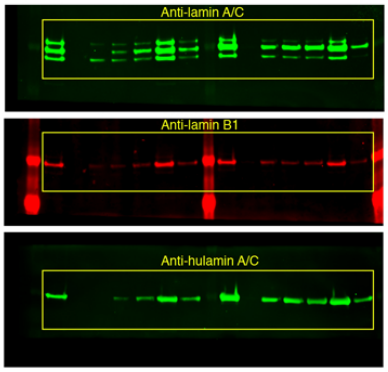

Full unedited gel for Figure S4A.

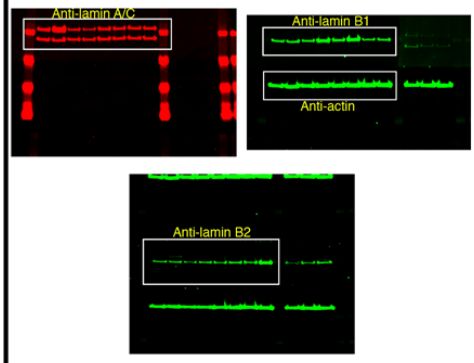

Full unedited gel for Figure S4B.

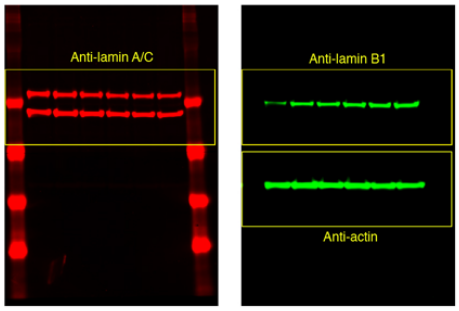

Full unedited gel for Figure S4F.

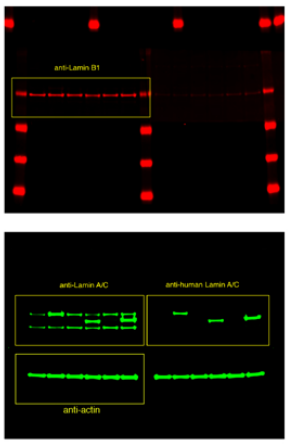

Full unedited gel for Figure S5D.

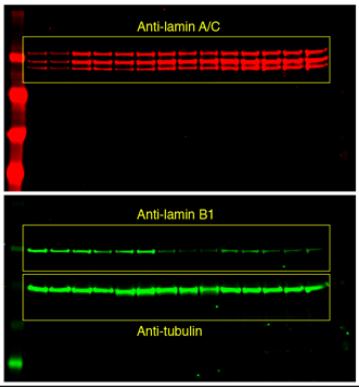

Chapter 4:

Progerin Forms an Abnormal Meshwork and Has a Dominant-negative Effect on the Nuclear Lamina

PNAS

Progerin forms an abnormal meshwork and has a dominant-negative effect on the nuclear lamina

Paul H. Kim[a,b], Joonyoung R. Kim[a], Yiping Tu[a], Hyesoo Jung[a], JY Brian Jeong[c], Anh P. Tran[a], Ashley Presnell[a], Stephen G. Young[a,d,*], and Loren G. Fong[a,*]

[a]Department of Medicine, David Geffen School of Medicine, University of California, Los Angeles, Los Angeles, CA 90095; [b]Department of Bioengineering, University of California, Los Angeles, Los Angeles, CA 90095; [c]Advanced Light Microscopy and Spectroscopy Laboratory, California NanoSystems Institute, University of California, Los Angeles, Los Angeles, CA 90095; [d]Department of Human Genetics, David Geffen School of Medicine, University of California, Los Angeles, Los Angeles, CA 90095

[*]Correspondence: lfong@mednet.ucla.edu, sgyoung@mednet.ucla.edu

ORCID: 0000-0001-7270-3176 (S.G.Y.), 0000-0002-4465-5290 (L.G.F.)

Author Contributions: P.H.K., S.G.Y., L.G.F. designed research; P.H.K., J.R.K., Y.T., H.J., J.B.J., A.P.T., A.P., L.G.F. performed research; P.H.K., S.G.Y., L.G.F. analyzed data; P.H.K., S.G.Y., L.G.F. wrote the paper.

Competing interest statement: The authors have no financial or personal competing interests in connection with the manuscript.

Data availability: All study data are included in this article and *SI Appendix.*

Classification: Biological Sciences, Medical Sciences

Running title: Progerin alters the nuclear lamina meshwork

Key Words: progeria, smooth muscle cells, nuclear membrane ruptures, nuclear lamina, high-resolution confocal microscopy, time-lapse fluorescence microscopy, nuclear blebs

This PDF file includes:

Main Text, Figures 1–8, *SI Appendix*

Abstract

Progerin, the protein that causes Hutchinson-Gilford progeria syndrome, triggers nuclear membrane (NM) ruptures and blebs, but the mechanisms are unclear. We suspected that the expression of progerin changes the overall structure of the nuclear lamina. High-resolution microscopy of smooth muscle cells revealed that lamin A and lamin B1 form independent meshworks with uniformly spaced openings (~0.085 μm^2). The expression of progerin in smooth muscle cells resulted in the formation of an irregular meshwork with clusters of large openings (up to 1.4 μm^2). The expression of progerin acted in a dominant-negative fashion to disrupt the morphology of the endogenous lamin B1 meshwork, triggering irregularities and large openings that closely resembled the irregularities and openings in the progerin meshwork. These abnormal meshworks were strongly associated with NM ruptures and blebs. Of note, the progerin meshwork was markedly abnormal in nuclear blebs that were deficient in lamin B1 (~50% of all blebs). That observation suggested that higher levels of lamin B1 expression might normalize the progerin meshwork and prevent NM ruptures and blebs. Indeed, increased lamin B1 expression reversed the morphological abnormalities in the progerin meshwork and markedly reduced the frequency of NM ruptures and blebs. Thus, progerin expression disrupts the overall structure of the nuclear lamina, but that effect—along with NM ruptures and blebs—can be abrogated by increased lamin B1 expression.

Significance Statement

Progerin, the mutant lamin A in Hutchinson-Gilford progeria syndrome, triggers multiple disease phenotypes despite persistent synthesis of wild-type lamin A, prompting speculation that progerin acts in a dominant-negative fashion to disrupt the structure and function of the nuclear lamina. Thus far, however, there has been no evidence that progerin disrupts lamin protofilament formation or that it interferes with the structure of nuclear lamin meshworks in cells. We showed that progerin forms an abnormal meshwork with large openings and that it triggers remarkably similar abnormalities in an independent meshwork formed by lamin B1 (*i.e.*, arguably a dominant-negative effect). These meshwork abnormalities, along with frequent nuclear membrane ruptures and nuclear blebs could be reversed by increased expression of lamin B1 or LAP2β.

Introduction

Hutchinson–Gilford progeria syndrome (HGPS), a progeroid disorder in children, is caused by the synthesis of progerin, a mutant form of lamin A (M. Eriksson et al., 2003). Children with HGPS develop disease phenotypes in multiple tissues (*e.g.*, bone, connective tissue, skin, hair, heart, vasculature) and typically die during their teenage years from atherosclerotic cardiovascular disease (Merideth et al., 2008). Progerin is caused by a *de novo* point mutation in *LMNA* [most often p.G608G(GGC>GGT)] that promotes usage of a cryptic splice donor site and leads to a mutant transcript with an in-frame deletion of 150 nucleotides, resulting in the production of progerin, an internally truncated lamin A that retains a C-terminal farnesyl lipid anchor (S G Young, L G Fong, & S Michaelis, 2005). Progerin is unequivocally the culprit in HGPS. The expression of progerin in genetically modified mice triggers disease phenotypes similar to those in children with HGPS (*e.g.*, skeletal abnormalities, osteoporosis, alopecia, vascular disease, sclerodermatous changes in the skin) (Sánchez-López et al., 2021; Varga et al., 2006; Yang et al., 2006). When progerin is expressed in cultured cells, it triggers phenotypes that are observed in fibroblasts from children with HGPS (*e.g.*, abnormal nuclear shape, DNA damage, senescence) (M. Eriksson et al., 2003; Glynn & Glover, 2005).

Progerin is targeted to the nuclear lamina, a 14–16 nm-thick fibrillar structure located adjacent to the inner nuclear membrane (Turgay & Medalia, 2017). In most somatic cells, the main components of the nuclear lamina are the A-type lamins (lamin A and lamin C; products of *LMNA*) and the B-type lamins (lamin B1 and lamin B2; products of *LMNB1* and *LMNB2*, respectively) (Dittmer & Misteli, 2011). The A- and B-type lamins assemble into separate but interacting net-like fibrillar meshworks (Nmezi et al., 2019; Shimi et al., 2015; Turgay et al., 2017). The nuclear lamina provides structural support for the nucleus and protects the integrity of the nuclear

membranes. Fibroblasts lacking all nuclear lamins (*Lmna*$^{-/-}$*Lmnb1*$^{-/-}$*Lmnb2*$^{-/-}$) exhibit frequent and prolonged nuclear membrane (NM) ruptures, resulting in DNA damage (Chen et al., 2021). Nuclear lamins also interact with nuclear membrane proteins, DNA-binding proteins, and transcription factors impacting critical cellular functions (*e.g.*, cell migration, heterochromatin anchoring, nuclear positioning, gene expression, cell division) (Worman & Schirmer, 2015).

When progerin is expressed in cultured cells, it alters properties associated with the nuclear envelope (Chang et al., 2019; De Vos et al., 2011; Glynn & Glover, 2005; Kelley et al., 2011; Mallampalli, Huyer, Bendale, Gelb, & Michaelis, 2005; Verstraeten, Ji, Cummings, Lee, & Lammerding, 2008; J. Zhang et al., 2011). In smooth muscle cells (SMCs), progerin increases nuclear stiffness, as judged by atomic force microscopy (Kim et al., 2021). It also triggers replicative stress (Coll-Bonfill et al., 2023), reduced DNA repair (H. Zhang, Xiong, & Cao, 2014), ER stress (Hamczyk et al., 2019), DNA damage and NM ruptures (Kim et al., 2021). Progerin also renders nuclei of SMCs more susceptible to mechanical stress, resulting in increased numbers of NM ruptures, greater DNA damage, and more cell death (Kim et al., 2021; Kim et al., 2018b). In a mouse model of HGPS, we observed NM ruptures in SMCs in the medial layer of the aorta (Kim et al., 2021). The fact that progerin triggered NM ruptures in SMCs (but not in adjacent endothelial cells or adventitial cells) helped to explain the histopathologic hallmark in HGPS (loss of medial SMCs in large arteries) (W. Stehbens, Delahunt, Shozawa, & Gilbert-Barness, 2001).

While the expression of progerin promotes nuclear blebs and NM ruptures, the mechanisms have not been clear. We formulated a simple hypothesis—that progerin expression results in overt structural abnormalities in the nuclear lamina—not only in the progerin meshwork but also in the meshworks of other nuclear lamins. To test this hypothesis, we used doxycycline-inducible vectors to create SMCs that express prelamin A (which is processed to mature lamin A) as well as SMCs

that express progerin. With these inducible cell lines in hand, we were able to characterize cells that produced identical amounts of progerin or mature lamin A. We were also able to compare, by high-resolution confocal fluorescence microscopy (Nmezi et al., 2019; Shimi et al., 2015), the structure of the nuclear lamina meshwork formed by progerin, and the meshwork formed by mature lamin A. These studies allowed us to test whether the structure of the progerin meshwork was abnormal, and if so, whether progerin adversely affected the structure of meshworks of other nuclear lamins (*e.g.*, lamin B1). We were also able to determine whether abnormalities in nuclear lamin meshworks were associated with NM ruptures and blebs. We also used live cell imaging to investigate the relationship between NM ruptures and blebs.

With our studies underway, it was quickly evident that the lamin A meshwork in SMCs was uniform and regular, whereas the progerin meshwork was irregular and contained large gaps. We also found that an abnormal progerin meshwork was associated with low levels of lamin B1. The latter observation prompted us to test whether increased lamin B1 expression would eliminate the structural irregularities in the progerin meshwork, and if so, whether that would be accompanied by reduced numbers of NM ruptures and blebs.

Results

The nuclear lamin meshwork is abnormal in progerin-expressing SMCs. Nuclear lamins assemble into filamentous meshworks adjacent to the inner nuclear membrane. To characterize progerin and lamin A meshworks, we used doxycycline (Dox)-inducible vectors to create clonal aortic smooth muscle cells (SMCs) that expressed human progerin or human prelamin A (which is processed to mature lamin A). Dox levels in the medium were adjusted to achieve progerin and lamin A levels similar to levels in the aorta of *Lmna*$^{G609G/+}$ mice (Figure 1A). After 48 h of Dox induction, SMCs were stained with an antibody that detects human lamin A and progerin (but not mouse lamin A/C). Images of the nuclear lamin meshwork at the upper surface of the nucleus were collected by high-resolution confocal fluorescence microscopy (Figure 1B). Human lamin A formed a meshwork with uniform gaps of ~0.085 μm^2. The meshwork in ~80% of progerin-expressing SMCs appeared indistinguishable from lamin A–expressing cells; however, ~20% of the progerin-expressing cells exhibited an abnormal meshwork with irregularities and large gaps (Figure 1, B and C). These observations were confirmed by super-resolution STED microscopy (Figure 1D). The gaps in the abnormal regions of the progerin meshwork ranged in size from 0.01 to 1.4 μm^2 (*vs*. 0.01–0.27 μm^2 in the lamin A meshwork) and on average were larger (0.25 μm^2 *vs*. 0.085 μm^2 in prelamin A-expressing SMCs) (Figure 1, E and F).

Progerin has a dominant-negative effect on the structure of the meshworks formed by other nuclear lamins. We examined the lamin B1 meshwork in SMC cell lines that expressed progerin, prelamin A, or a nonfarnesyl-progerin in which the *CaaX* motif was changed from –CSIM to –SSIM (Mallampalli et al., 2005) (*SI Appendix*, Figure S1A). The endogenous lamin B1 meshwork in wild-type SMCs and prelamin A–expressing SMCs was regular, with openings averaging ~0.08 μm^2 (Figure 2, A and B). Progerin expression changed the structure of the lamin B1 meshwork

(Figure 2, A and B), resulting in irregularities and large openings that mirrored the abnormalities in the progerin meshwork, as judged by confocal (Figure 2A) and STED (Figure 2C) microscopy. The gaps in the lamin B1 meshwork in progerin-expressing SMCs were larger than in prelamin A–expressing SMCs (0.142 ± 0.016 μm^2 *vs.* 0.090 ± 0.011 μm^2; P = 0.0012, *n* = 45 nuclei/group) (Figure 2B). An abnormal lamin B1 meshwork was restricted to cells with a morphologically abnormal progerin meshwork. Also, the sizes of the openings in the lamin B1 meshwork were virtually identical to those in the progerin meshwork (Figure 2D).

Nonfarnesyl-progerin did not alter the structure of the lamin B1 meshwork (Figure 2, A and B). Much of the nonfarnesyl-progerin was in the nucleoplasm (*SI Appendix*, Figure S1, B–D), but some of it was located at the nuclear rim (colocalizing with lamin B1 and LAP2β) (*SI Appendix*, Figure S1, B–D). The nonfarnesyl-progerin along the nuclear rim formed a regular meshwork with small openings (Figure 2A).

We used a lamin C–specific antibody to define the distribution of endogenous lamin C. [The lamin C–specific antibody was validated by western blotting and immunocytochemistry (*SI Appendix*, Figure S2).] Lamin C staining in wild-type SMCs had a punctate pattern, both at the nuclear rim and in the nucleoplasm (Figure 3, A and B). While the staining was predominantly punctate, in some cases lamin C appeared to line one or two sides of an opening in the lamin A meshwork. In progerin-expressing cells, lamin C puncta bordered openings in the progerin meshwork, including in regions of the meshwork containing large gaps and irregularities (Figure 3B).

Nuclear membrane (NM) ruptures and nuclear blebs are associated with an abnormal progerin meshwork. Progerin triggers nuclear blebs and NM ruptures in SMCs (Kim et al., 2021). We suspected that the ruptures and blebs were associated with abnormalities in the progerin

meshwork. To test that suspicion, progerin-expressing SMCs were fixed and stained with a human lamin A–specific antibody. Cells with nuclear blebs (n = 171) and without nuclear blebs (n = 132) were identified on low-magnification images and then characterized further by high-resolution confocal microscopy (Figure 4A). Nuclear blebs and an abnormal progerin meshwork were strongly correlated; 71% of cells with a nuclear bleb had an abnormal progerin meshwork, whereas only 14% of cells without a bleb exhibited an abnormal meshwork (Figure 4B). Similar analyses were performed for NM ruptures. NM ruptures were identified by live-cell imaging in progerin-SMCs that expressed a nuclear-targeted GFP reporter (nls-GFP) (Vargas, Hatch, Anderson, & Hetzer, 2012) (De Vos et al., 2011). NM ruptures were identified by leakage of nls-GFP into the cytoplasm (Figure 4C). After 48 h of imaging, the cells were fixed and examined by immunofluorescence confocal microscopy. An abnormal progerin meshwork was observed in 72% of cells with a NM rupture (n = 120) but in only 16% of cells without a NM rupture (n = 273) (Figure 4D). Nuclear blebs and NM ruptures were also strongly correlated; 84% of cells with a NM rupture had a nuclear bleb (Figure 4E), and 91% cells with a nuclear bleb had a NM rupture (Figure 4F).

An abnormal progerin meshwork in nuclear blebs is associated with low lamin B1 levels. We stained progerin-expressing SMCs with antibodies against human lamin A (to detect progerin), lamin B1, and LAP2β and then imaged cells with nuclear blebs by high-resolution confocal microscopy. Nuclear blebs contained both progerin and LAP2β, and the intensity of progerin and LAP2β staining in blebs was similar to that along the nuclear rim (Figure 5A). In contrast, lamin B1 staining of blebs was heterogenous. In ~50% of nuclear blebs, lamin B1 expression was barely detectable (Figure 5, A and B). Maximum intensity projections confirmed low amounts of lamin B1 expression in the bleb relative to amounts at the nuclear rim. In blebs with very low levels of

lamin B1, the progerin meshwork was irregular with large openings (Figure 5C). The irregular pattern was observed in 96% of blebs with low levels of lamin B1 (n = 98 cells). In contrast, only 3% of blebs with strong lamin B1 staining had a morphologically abnormal progerin meshwork (n = 102 cells) (Figure 5D).

Nuclear blebs form at sites of NM ruptures. We observed a strong association between NM ruptures and nuclear blebs in progerin-expressing SMCs (Figure 4F). To understand that association, we used live-cell imaging to monitor bleb formation and NM ruptures in progerin-expressing SMCs that expressed nls-GFP and cGAS-mCherry [to mark NM rupture sites; (Civril et al., 2013; Denais et al., 2016)]. After Dox-induction of progerin expression, the frequency of nuclear blebs and NM ruptures increased. After 48 h, 14% of the cells had a nuclear bleb or a NM rupture (Figure 6A). Consistent with earlier studies (Hatch & Hetzer, 2016; Vargas et al., 2012), NM ruptures occurred more frequently in cells with nuclear blebs (Figure 6B). Of note, cGAS-mCherry was often found in nuclear blebs (Figure 6C and *SI Appendix*, Video 1), suggesting that blebs formed at a NM rupture site. Indeed, live-cell imaging revealed that 81% of new blebs formed at a NM rupture site (Figure 6D). Because progerin causes repetitive NM ruptures in SMCs (Kim et al., 2021) and because NM ruptures are more frequent in cells with a nuclear bleb (Figure 6B), we suspected that we would find NM ruptures within blebs. Indeed, we observed NM ruptures (as judged by cGAS-mCherry labeling) at a nuclear bleb, which was associated with the formation of smaller blebs within the nuclear bleb (Figure 6E).

Because we had previously documented NM ruptures *in vivo* in aortic SMCs of *Lmna*^{G609G} mice (Kim et al., 2021), we predicted that we might also encounter nuclear blebs in aortic SMCs. Indeed, we found nuclear blebs in SMCs in the aorta of 10-week-old *Lmna*$^{G609G/G609G}$ mice (Figure

6F and *SI Appendix*, Figure S3B). In some of those cells, we observed (with a lamin A/C–specific antibody) an abnormal nuclear lamina meshwork (Figure 6F and *SI Appendix*, Figure S3B).

NM ruptures and nuclear blebs are associated with an abnormal nuclear lamin meshwork in *Lmnb1*$^{-/-}$ and *Zmpste24*$^{-/-}$ SMCs. To further explore the relationship between nuclear blebs and NM ruptures, we created *Zmpste24*$^{-/-}$ and *Lmnb1*$^{-/-}$ SMCs. Immunocytochemistry studies identified increased nuclear blebs in *Zmpste24*$^{-/-}$ and *Lmnb1*$^{-/-}$ cells (*SI Appendix*, Figure S4), and live-cell imaging revealed increased NM ruptures (Figure 7A). At the end of the live-cell imaging, the SMCs were fixed and stained with antibodies against lamin A/C (to identify cells with a nuclear bleb) and cGAS (to identify NM rupture sites). In both *Zmpste24*$^{-/-}$ and *Lmnb1*$^{-/-}$ cells, NM ruptures were strongly correlated with blebs. In *Zmpste24*$^{-/-}$ cells with a bleb (n = 126 cells), 69% had a NM rupture. In *Zmpste24*$^{-/-}$ cells without a nuclear bleb (n = 187 cells), only 8% had a NM rupture (Figure 7B). In *Lmnb1*$^{-/-}$ cells with a nuclear bleb (n = 174 cells), 91% had a NM rupture; in *Lmnb1*$^{-/-}$ cells without a nuclear bleb (n = 145 cells), 27% had a NM rupture (Figure 7B).

Irregular lamin A meshworks with large gaps were identified in both *Lmnb1*$^{-/-}$ and *Zmpste24*$^{-/-}$ SMCs (Figure 7C). In *Zmpste24*$^{-/-}$ cells with a nuclear bleb (n = 110 cells), 61.2% had an abnormal lamin A meshwork; in cells without a bleb (n = 198 cells), 2.5% had an abnormal lamin A meshwork (Figure 7D). In *Lmnb1*$^{-/-}$ cells with a nuclear bleb (n = 156), 90.2% had an abnormal lamin A meshwork; in cells without a nuclear bleb (n = 129), 43.9% had an abnormal lamin A meshwork (Figure 7D).

Lamin B1 and LAP2β expression normalized the meshwork in progerin-SMCs and reduced the frequency of nuclear blebs and NM ruptures. The observation that lamin B1 levels were low in nuclear blebs that exhibited a structurally abnormal progerin meshwork led us to hypothesize that increased lamin B1 expression would normalize the morphology of the progerin

meshwork. To test that hypothesis, we generated SMCs that expressed progerin constitutively and then introduced Dox-inducible constructs for lamin B1, nonfarnesyl–lamin B1, or HA-tagged LAP2β. Dox levels were adjusted to increase endogenous levels of lamin B1 and LAP2β by approximately threefold (*SI Appendix*, Figure S5, A and B). After 48 h, cells were stained with antibodies against lamin A/C and lamin B1, and the nuclear lamin meshworks were examined by immunofluorescence confocal microscopy. Lamin B1 expression normalized the progerin meshwork (Figure 8A), reducing the percentage of cells with an abnormal progerin meshwork from 20% to 4% (n = 86–114 cells/group in three independent experiments) (Figure 8B). Nonfarnesyl–lamin B1 had no effect on the frequency of abnormal progerin meshworks (P = 0.57). Of note, LAP2β also reduced the percentage of cells with an abnormal progerin meshwork from 20% to 4% (Figure 8B). High-resolution imaging of LAP2β in wild-type and progerin-SMCs revealed a uniform net-like staining pattern similar to that of the nuclear lamins (*SI Appendix*, Figure S5, C and D).

Increased lamin B1 and LAP2β expression reduced the frequency of NM ruptures and blebs in progerin-expressing SMCs, consistent with their ability to improve the morphology of the progerin meshwork. Live-cell imaging studies revealed that lamin B1 and LAP2β reduced the percentage of progerin-expressing cells with NM ruptures from 20% to <6% (Figure 8C) and reduced the frequency of nuclear blebs from ~16% to <4% (Figure 8C). Nonfarnesyl–lamin B1 had no effect on the frequency of NM ruptures or blebs (Figure 8C).

Discussion

Lamin A, an intermediate filament protein, is a major component of the nuclear lamina. Lamin A dimers assemble into head-to-tail protofilaments and then into higher-order filaments to form a fibrillar meshwork that lines the inner nuclear membrane. Half-normal amounts of lamin A synthesis (*LMNA* haploinsufficiency) cause late-onset muscular dystrophy in humans and mice (Bonne et al., 1999; Wolf et al., 2008). A distinct genetic disease, HGPS, is caused by a *de novo* *LMNA* point mutation that leads to the production of progerin—an internally truncated lamin A containing a farnesyl lipid anchor. In children with HGPS, progerin causes multiple disease phenotypes and does so despite production of lamin A from the unaffected *LMNA* allele. The ability of progerin to trigger severe disease—despite ongoing lamin A synthesis—prompted speculation that progerin exerts a dominant-negative effect on the nuclear lamina (M. Eriksson et al., 2003). Thus far, however, the mechanisms by which progerin causes disease have remained unclear. In the current study, our efforts to characterize the impact of progerin on the structure of the nuclear lamina uncovered fresh insights into the mechanisms of disease. We used mouse SMCs as a model system to better understand mechanisms responsible for the progerin-induced NM ruptures and SMC loss in the aorta of *Lmna*^{G609G} mice (Kim et al., 2021). High-resolution confocal microscopy of cultured SMCs revealed that lamin A and lamin B1 form similar but distinct meshworks—consistent with earlier studies (Nmezi et al., 2019; Shimi et al., 2015). We found that the two meshworks were similar in appearance but that the precise location of the fibrils and the openings in the meshworks differed. We showed that the expression of prelamin A in SMCs results in the formation of an orderly lamin A meshwork with very small openings. In contrast, progerin resulted in the formation of an irregular meshwork with large openings. Unexpectedly, progerin expression also resulted in an abnormal lamin B1 meshwork with large openings (corresponding to openings

in the progerin meshwork), suggesting that progerin exerts a dominant-negative effect on the structure of the nuclear lamina. We suspect that progerin's capacity to impact on the structure of the lamin B1 meshwork reflects direct protein–protein interactions between the two meshworks.

The similar abnormalities in the progerin and lamin B1 meshworks in progerin-expressing SMCs were associated with a markedly increased frequency of NM ruptures and nuclear blebs. We found that increasing lamin B1 expression in progerin-expressing cells normalized the morphology of both the progerin and lamin B1 meshworks and resulted in a markedly reduced frequency of NM ruptures and blebs. In earlier studies (Kim et al., 2021), we found that increased lamin B1 expression in SMCs reduced progerin-induced nuclear stiffness, DNA damage, and cell death. Because progerin and lamin B1 both contain C-terminal modifications (*i.e.*, farnesylation, carboxyl methylation) that promote their association with the inner nuclear membrane (Holtz, Tanaka, Hartwig, & McKeon, 1989; Nigg, Kitten, & Vorburger, 1992), we proposed that lamin B1 and progerin could compete for a limited number of binding sites at the nuclear rim (Kim et al., 2021). We further proposed that increasing lamin B1 expression reduces progerin's association with the inner nuclear membrane and thereby reduces its toxicity. In support of that proposal, nuclear extraction studies revealed that increased expression of lamin B1 reduces the amount of progerin in the nuclear membrane fraction (Kim et al., 2021). Our current studies revealed that increased lamin B1 expression minimizes progerin toxicity (*i.e.*, NM ruptures and blebs) by normalizing the progerin and lamin B1 meshworks. We suspect that the normalization of the meshworks is related, at least in part, to displacement of progerin from inner nuclear membrane binding sites.

Our use of doxycycline (Dox)-inducible vectors to express prelamin A and progerin was crucial; this approach allowed us to examine SMC clones that expressed equivalent amounts of prelamin

A and progerin. It is not possible to achieve comparable expression levels with transiently transfected SMCs or "mixed stable" SMCs—or with studies with human fibroblast cell lines. In our current studies, we matched progerin levels in cultured SMCs to levels in aortas of *Lmna*$^{G609G/+}$ mice. Lamin A levels in aortas of *Lmna*$^{+/+}$ mice and progerin levels in aortas of *Lmna*$^{G609G/+}$ mice are 4–5-fold higher than lamin C levels and are 15–25-fold higher than levels of lamin B1 (Kim et al., 2018b). We produced progerin-expressing SMC clones with a progerin:lamin C ratio of ~3:1 and a progerin:lamin B1 ratio of ~4.4:1. At those levels, we found morphological abnormalities in both the progerin meshwork and the lamin B1 meshwork. The use of the Dox-inducible expression system in SMCs held another advantage—aside from allowing us to fine-tune protein expression levels. Because the SMC clones were grown in Dox-free medium, we were able—by adding Dox to the medium—to examine the impact of progerin expression in naïve SMCs. Had we performed studies in SMCs that expressed progerin constitutively, we would have needed to consider long-term effects of progerin toxicity (*e.g.*, DNA damage, cell senescence, altered gene expression) on the morphology of the nuclear lamina and on the frequency of NM ruptures and nuclear blebs.

In recent studies, Buxboim *et al.* (Buxboim et al., 2023) examined the nuclear lamina by cryo-electron tomography and reported that nuclear lamin filaments in progerin-expressing fibroblasts were more densely packed than in wild-type fibroblasts. While the cryo-EM studies could not identify which nuclear lamins contributed to increased filament density, they succeeded in showing that the nuclear lamina in progerin-expressing cells was morphologically distinct. Their finding of increased filament density is consistent with our finding that progerin expression results in morphologically abnormal progerin and lamin B1 meshworks.

The ability of progerin to induce morphological abnormalities in the nuclear lamin meshwork depended on progerin farnesylation. The expression of nonfarnesyl-progerin in SMCs resulted in

a morphologically normal meshwork at the nuclear rim (colocalizing with lamin B1 and LAP2β), although a substantial fraction of nonfarnesyl-progerin was in the nucleoplasm. Consistent with an absence of disease phenotypes in knock-in mice expressing nonfarnesylated progerin (Yang et al., 2011), nonfarnesyl-progerin expression in SMCs did not increase the frequency of NM ruptures and blebs. We suspect that the ability of nonfarnesyl-progerin to reach the nuclear rim and form a morphologically normal meshwork was dependent on direct interactions with other nuclear lamins. Another reason to suspect that nonfarnesyl-progerin interacts with other nuclear lamins was the fact that nonfarnesyl-progerin triggered abnormalities in the distribution of lamin B1. In wild-type SMCs, lamin B1 is located at the nuclear rim, whereas in nonfarnesyl-progerin–expressing SMCs some of the lamin B1 was in the nucleoplasm, likely trapped there by interactions with nucleoplasmic nonfarnesyl-progerin. In any case, we suspect that the reduced toxicity of nonfarnesyl-progerin in SMCs results from its ability to form a regular meshwork and its inability to trigger NM ruptures and blebs.

When wild-type cells are incubated in medium containing a protein farnesyltransferase inhibitor (FTI), nonfarnesyl–prelamin A can be detected in the nucleoplasm and at the nuclear rim (Glynn & Glover, 2005; Toth et al., 2005). Similarly, when progerin-expressing cells are incubated with an FTI, nonfarnesyl-progerin can be detected in the nucleoplasm (Glynn & Glover, 2005; Mallampalli et al., 2005; Toth et al., 2005; Wang et al., 2012; Yang et al., 2005) and at the nuclear rim. Based in part on those findings, FTIs have been tested as a potential treatment for HGPS. In both human and mouse studies, FTIs were reported to reduce disease in mouse models of progeria (Capell et al., 2008; Fong, Frost, et al., 2006; Gordon et al., 2014a; Yang et al., 2006). In our studies with a gene-targeted HGPS mouse model, we found that adding an FTI to the drinking water resulted in modest short-term improvements in body weight and bony abnormalities, but the

progression of disease was relentless and severe (Yang et al., 2006). Given current data, we believe that treatment of children with FTIs is reasonable. However, in considering FTIs as a therapeutic strategy, one must also consider the potential impact of the FTI on lamin B1 farnesylation. In our studies, we found that increased expression of wild-type (farnesyl-)lamin B1 in SMCs improved the morphology of the progerin meshwork and reduced the frequency of NM ruptures and blebs. In contrast, a comparable amount of nonfarnesyl-lamin B1 had no effect on the morphology of the progerin meshwork, nor did it reduce the frequency of NM ruptures and blebs. Thus, inhibiting the farnesylation of progerin with an FTI could minimize the toxicity of progerin, but it seems possible that any salutary effects of the drug could be blunted by inhibition of lamin B1 farnesylation.

In our studies, we examined, by confocal microscopy, the distribution of lamin C in prelamin A–expressing and progerin-expressing SMCs. The lamin C antibody that we used was specific; there was no binding of the antibody to *Lmna*$^{-/-}$ cells, nor was there any binding of the antibody to other nuclear lamins on western blots. In WT SMCs, prelamin A–expressing SMCs and progerin-expressing SMCs, the distribution of lamin C was predominantly punctate. Lamin C puncta were found immediately adjacent to lamin A, progerin, and lamin B1 fibrils within the nuclear lamin meshworks. Occasionally, lamin C lined one or more sides of small openings in a nuclear lamin meshwork, but it did not form a *bona fide* net-like meshwork resembling the meshworks formed by lamin A, progerin, or lamin B1. Also, lamin C was absent from the voids created by large openings in the progerin meshwork. It is possible that the absence of a *bona fide* lamin C net-like meshwork reflects low amounts of lamin C within cells (Shimi et al., 2008).

In earlier studies (Chen et al., 2021), we found that overexpression of an inner nuclear membrane protein, LAP2β, eliminated NM ruptures in *Lmna*$^{-/-}$*Lmnb1*$^{-/-}$*Lmnb2*$^{-/-}$ fibroblasts. In the current studies, we found that expression of LAP2β in progerin-expressing SMCs normalized

the morphology of the progerin meshwork—and did so as effectively as lamin B1. Like lamin B1, LAP2β expression reduced the frequency of nuclear blebs and ruptures. The mechanism by which LAP2β normalizes the progerin meshwork is not understood, but our confocal microscopy studies showed that LAP2β adopts a net-like pattern resembling the lamin A and lamin B1 meshworks. We suspect that the net-like distribution of LAP2β functions to normalize the progerin meshwork and minimize NM ruptures and blebs. The nucleoplasmic domain of LAP2β has been reported to interact with nuclear lamins, in particular lamin B1, but it is unclear whether that property is responsible for LAP2β's net-like distribution or its capacity to improve the morphology of the progerin network. It is interesting that the nucleoplasmic portion of emerin (an inner nuclear membrane protein related to LAP2β) forms filamentous structures *in vitro* (Samson et al., 2017), but thus far there have been no reports that LAP2β shares that property.

Our studies are consistent with earlier studies showing that NM ruptures are more frequent in cells with a nuclear bleb (Hatch & Hetzer, 2016; Vargas et al., 2012), presumably due to a weakened nuclear envelope (Shah, Wolf, & Lammerding, 2017). In our studies, we found, with live-cell imaging studies, that ~80% of *new* nuclear blebs in progerin-expressing SMCs form at a NM rupture site, explaining the strong correlation between NM ruptures and blebs. NM ruptures occurred more frequently in progerin-expressing cells with an abnormal meshwork, suggesting that the irregularities and large openings in the meshwork weakened the nuclear lamina and were causally related to the emergence of NM ruptures and blebs. In *Zmpste24*$^{-/-}$ and *Lmnb1*$^{-/-}$ SMCs, we also observed a very strong association between NM ruptures, nuclear blebs, and irregularities and gaps in the nuclear lamin meshworks. Those observations provided additional support for the notion that a weakened, structurally abnormal meshwork contributes to NM ruptures and bleb formation.

Increasing lamin B1 expression in progerin-expressing SMCs counteracted the impact of progerin on the structure of the nuclear lamina and reduced the frequency of nuclear blebs and ruptures. We suspect that lamin B1's capacity to mitigate progerin-induced phenotypes in SMCs is physiologically relevant, with high levels of lamin B1 in tissues protecting against disease and low levels increasing the severity of disease. In this context, we have been intrigued by a hallmark histopathologic finding in HGPS—loss of SMCs in the medial layer of the aorta (W. Stehbens et al., 2001). In wild-type mice, the lamin A:lamin B1 ratio is extremely high in the aorta (the highest among a comparison of 13 tissues, including bone and skin) (Kim et al., 2018b). In the setting of progerin expression in *Lmna*$^{G609G/+}$ mice, where progerin protein accumulates with age while lamin B1 levels fall, the progerin:lamin B1 ratio in the aorta rises to very high levels; the progerin:lamin B1 ratio in the aorta is ~25–30, whereas it is only ~2.5 in left ventricular myocardium (Kim et al., 2018b). We suspect that the low amounts of lamin B1 render progerin-expressing SMCs more susceptible to progerin toxicity, resulting in an abnormal progerin meshwork and an increased susceptibility to mechanical stress associated with pulsatile blood flow. In support of that proposal, we found an abnormal lamin A/C meshwork in aortic SMCs of *Lmna*$^{G609G/G609G}$ mice. The arterial pathology in mouse HGPS is restricted to medial SMCs. We have never observed loss of intimal endothelial cells or adventitial mesenchymal cells even though the intima and adventitia are also exposed to mechanical stress. We suspect that the substantially higher amounts of lamin B1 in intimal and adventitial cells (Kim et al., 2018b) render them less susceptible to disease.

Materials and Methods

Mice. Mice with a targeted HGPS mutation (*Lmna*^{G609G}) (Kim et al., 2018b; Lee et al., 2016) were housed in a specific pathogen–free barrier facility with a 12-h light/dark cycle. The mice were provided pelleted mouse chow (NIH31) and water *ad libitum* and nutritional food cups (Westbrook, ME) as required for supportive care. All animal studies were approved by UCLA's Animal Research Committee.

Cells. Immortalized mouse aortic smooth muscle cells (SMCs) (ATCC, #CRL-2797) were cultured in DMEM (Invitrogen) supplemented with 10% (v/v) fetal bovine serum (HyClone), 1× nonessential amino acids, 2 mM glutamine, 1 mM sodium pyruvate, and 0.2 mg/ml G418 at 37°C with 5% CO_2.

***Lmnb1*-deficient SMCs**. Guide RNAs targeting *Lmnb1*-deficient SMCs (*Lmnb1*$^{-/-}$) (lacking any detectable lamin B1 by western blot or immunocytochemical staining) were created by CRISPR/Cas9-induced homology-directed repair. A detailed description is provided in *SI Appendix*.

***Zmpste24*-deficient SMC.** *Zmpste24*-deficient SMCs were created in a similar fashion as *Lmnb1*-deficient SMCS. A detailed description is provided in *SI Appendix*.

Western blotting. Western blotting of cell and tissue samples was performed as previously described (Kim et al., 2018b) (Kim et al., 2021). A description is provided in *SI Appendix.* The antibodies and concentrations are listed in *SI Appendix*, Table SI.

Quantitative real time-PCR. Quantitative real time-PCR was performed as previously described (Kim et al., 2021). A detailed description is provided in *SI Appendix*. All primers used in the experiments are listed in *SI Appendix*, Table SII.

Doxycycline (Dox)-inducible expression in SMCs. SMCs harboring Dox-inducible pTRIPZ expression vectors for human prelamin A, human progerin, non-farnesylated human progerin (progerin-SSIM), lamin B1, and non-farnesylated lamin B1 (lamin B1-SAIM) have been described previously (Kim et al., 2018b) (Kim et al., 2021). A similar approach was used to generate SMCs expressing Dox-inducible constructs for LAP2β. A detailed description is provided in *SI Appendix.* The primer sequences are listed in *SI Appendix*, Table SIII.

Constitutive expression of nuclear localized GFP, cGAS-mCherry, and lamins in SMCs. SMCs expressing green fluorescent protein (GFP) with a nuclear localization signal (nls-GFP) have been described previously (Kim et al., 2021). The creation of SMCs expressing constitutive plasmids for prelamin A and progerin is described in *SI Appendix.*

Measurement of nuclear membrane (NM) ruptures in live SMCs. The detection of nuclear membrane ruptures was performed as previously described (Kim et al., 2021). A description is provided in *SI Appendix.*

High-resolution confocal fluorescence microscopy. 50,000 cells were grown in a chambered coverslip with a #1.5H (170 μm ± 5μm) glass bottom (ibidi USA). After 48 h, cells (with or without doxycycline) were fixed with 4% paraformaldehyde in PBS for 10 min at room temperature and permeabilized with 0.3% Triton X-100 in PBS for 10 min. The cells were processed for immunofluorescence microscopy as described (Kim et al., 2021). The antibodies and concentrations are listed in *SI Appendix*, Table SI. Airyscan images were acquired with a LSM980 with Airyscan2 in super-resolution (SR) imaging mode with a scan-speed of 5 with a Plan-Apochromat 63×/1.4 NA oil-immersion objective (Zeiss). Excitation wavelengths and filter settings for the respective dyes were selected with the integrated dye presets in the ZEN Blue 2.3 software. Identical settings were used throughout the entire imaging session. *Z*-stacks were

recorded at a recommended optimal section of 0.14 μm from the bottom (close to glass bottom) to the top of a nucleus. Images acquired in SR imaging mode were further processed with Airyscan Joint Deconvolution (jDCV) available in Zen Blue software. jDCV parameters were: sample structure, standard; maximum iterations, 10; and quality threshold of 0.00. High-resolution confocal fluorescence microscopy images were processed by Zen Blue 2.3 software to generate cross-sectional projection and maximum intensity projection images ranging from equatorial to top (away from glass bottom) of a nucleus.

Quantification of lamina meshwork gap. *Z*-axis images from equatorial to top of a nucleus were compiled and converted to 8-bit grayscale in ImageJ (NIH). Brightness and contrast were adjusted to enhance the visibility of the lamina meshwork. The meshwork was outlined using the "Overlay" tool with a paintbrush set to a width of 1 pixel. A threshold was then applied to delineate the meshwork, and the area of the gaps within the meshwork was quantified with the "Analyze Particles" function. A global scale was established with a scale bar from the original image. Meshwork gaps adjacent to the image borders were excluded from quantification. The quantification results were exported to GraphPad Prism software for graphical illustrations.

STED microscopy. Samples were analyzed using a Leica TCS SP8 STED laser scanning confocal microscope equipped with a 93×/1.3 GLYC STED WHITE objective lens with a motorized correction collar. The sample was excited using 488nm and 561nm laser lines from a white light laser continuum and STED depletion occurred at 660nm for both channels. Single molecule HyD detectors collected the fluorescence emission within two windows at 503nm–555nm and 583nm–643nmm, scanning at 8000Hz with 8 line average and 12 frame average. Images were taken at 12.1nm × 12.1nm pixel size, using 141nm z-step size with the pinhole at 130.6 μm. Images were deconvolved and processed by the Leica Lightning adaptive method.

Statistical analysis. Statistical analyses were performed with Microsoft Excel for Mac 2011 and GraphPad Prism software. Experimental groups were analyzed by unpaired 2-tailed Student's *t* test, or one-way and two-way ANOVA with Tukey's multiple comparisons test. Statistical significance was considered when the P value was < 0.05. Red circles in bar graphs show the average values of independent experiments or values for individual animals.

Data availability statement

The data underlying Figs. 1, 2, 4, 5, 6, 7, and 9 are openly available in the publicly accessible database UCLA Dataverse at https://urldefense.com/v3/__https://dataverse.ucla.edu/dataset.xhtml?persistentId=doi:10.25346*S6*GA8STV__;Ly8!!F9wkZZsI-LA!BcuXqMkGf1l9IA-7Y8NaSmy_Y4isFXtG-Mnbz7wYlsFKheXWga_4cSDj88Z8uM48JxocHTDgxr684In4G3ntatqu_g$. All other study data are included in this article and Supplementary files.

Acknowledgments

We thank Stella Choi for assistance with the measurement of nuclear lamin meshwork gap sizes. This work was supported by the National Center for Advancing Translational Sciences UCLA CTSI (UL1TR001881). Virus production and transduction were performed by the IMTC/UCLA Vector Core, which is supported by CURE/P30 DK041301. STED microscopy was performed at the Advanced Light Microscopy/Spectroscopy Laboratory and Leica Microsystems Center of Excellence at the California NanoSystems Institute at UCLA (RRID:SCR_022789) with funding support from NIH Shared Instrumentation Grant S10OD025017 and NSF Major Research Instrumentation grant CHE-0722519. The authors declare no competing financial interests.

References

Aebi, U., Cohn, J., Buhle, L., & Gerace, L. (1986). The nuclear lamina is a meshwork of intermediate-type filaments. *Nature, 323*(6088), 560-564. doi:10.1038/323560a0

Atchison, L., Abutaleb, N. O., Snyder-Mounts, E., Gete, Y., Ladha, A., Ribar, T., . . . Truskey, G. A. (2020). iPSC-Derived Endothelial Cells Affect Vascular Function in a Tissue-Engineered Blood Vessel Model of Hutchinson-Gilford Progeria Syndrome. *Stem Cell Reports, 14*(2), 325-337. doi:10.1016/j.stemcr.2020.01.005

Baker, P. B., Baba, N., & Boesel, C. P. (1981). Cardiovascular abnormalities in progeria. Case report and review of the literature. *Arch Pathol Lab Med, 105*(7), 384-386. Retrieved from https://www.ncbi.nlm.nih.gov/pubmed/6894691

Benedicto, I., Dorado, B., & Andres, V. (2021). Molecular and Cellular Mechanisms Driving Cardiovascular Disease in Hutchinson-Gilford Progeria Syndrome: Lessons Learned from Animal Models. *Cells, 10*(5). doi:10.3390/cells10051157

Beyret, E., Liao, H. K., Yamamoto, M., Hernandez-Benitez, R., Fu, Y., Erikson, G., . . . Izpisua Belmonte, J. C. (2019). Single-dose CRISPR-Cas9 therapy extends lifespan of mice with Hutchinson-Gilford progeria syndrome. *Nat Med, 25*(3), 419-422. doi:10.1038/s41591-019-0343-4

Bonne, G., Di Barletta, M. R., Varnous, S., Bécane, H.-M., Hammouda, E.-H., Merlini, L., . . . Schwartz, K. (1999). Mutations in the gene encoding lamin A/C cause autosomal dominant Emery-Dreifuss muscular dystrophy. *Nat. Genet., 21*, 285–288.

Burke, B., & Stewart, C. L. (2013). The nuclear lamins: flexibility in function. *Nat Rev Mol Cell Biol, 14*(1), 13-24. doi:10.1038/nrm3488

Buxboim, A., Kronenberg-Tenga, R., Salajkova, S., Avidan, N., Shahak, H., Thurston, A., & Medalia, O. (2023). Scaffold, mechanics and functions of nuclear lamins. *FEBS Lett, 597*(22), 2791-2805. doi:10.1002/1873-3468.14750

Cao, K., Graziotto, J. J., Blair, C. D., Mazzulli, J. R., Erdos, M. R., Krainc, D., & Collins, F. S. (2011). Rapamycin reverses cellular phenotypes and enhances mutant protein clearance in Hutchinson-Gilford progeria syndrome cells. *Sci Transl Med, 3*(89), 89ra58. doi:10.1126/scitranslmed.3002346

Capell, B. C., Erdos, M. R., Madigan, J. P., Fiordalisi, J. J., Varga, R., Conneely, K. N., . . . Collins, F. S. (2005). Inhibiting farnesylation of progerin prevents the characteristic nuclear

blebbing of Hutchinson-Gilford progeria syndrome. *Proc. Natl. Acad. Sci. USA, 102*(36), 12879-12884. Retrieved from http://www.ncbi.nlm.nih.gov/entrez/query.fcgi?cmd=Retrieve&db=PubMed&dopt=Citation&list_uids=16129833

Capell, B. C., Olive, M., Erdos, M. R., Cao, K., Faddah, D. A., Tavarez, U. L., . . . Collins, F. S. (2008). A farnesyltransferase inhibitor prevents both the onset and late progression of cardiovascular disease in a progeria mouse model. *Proc Natl Acad Sci U S A, 105*(41), 15902-15907. doi:10.1073/pnas.0807840105

Chang, W., Wang, Y., Luxton, G. W. G., Östlund, C., Worman, H. J., & Gundersen, G. G. (2019). Imbalanced nucleocytoskeletal connections create common polarity defects in progeria and physiological aging. *Proc Natl Acad Sci U S A, 116*(9), 3578-3583. doi:10.1073/pnas.1809683116

Chen, N. Y., Kim, P. H., Tu, Y., Yang, Y., Heizer, P. J., Young, S. G., & Fong, L. G. (2021). Increased expression of LAP2β eliminates nuclear membrane ruptures in nuclear lamin-deficient neurons and fibroblasts. *Proc Natl Acad Sci U S A, 118(25)*(25), e2107770118. doi:10.1073/pnas.2107770118

Civril, F., Deimling, T., de Oliveira Mann, C. C., Ablasser, A., Moldt, M., Witte, G., . . . Hopfner, K. P. (2013). Structural mechanism of cytosolic DNA sensing by cGAS. *Nature, 498*(7454), 332-337. doi:10.1038/nature12305

Coll-Bonfill, N., Mahajan, U., Shashkova, E. V., Lin, C. J., Mecham, R. P., & Gonzalo, S. (2023). Progerin induces a phenotypic switch in vascular smooth muscle cells and triggers replication stress and an aging-associated secretory signature. *Geroscience, 45*(2), 965-982. doi:10.1007/s11357-022-00694-1

Cong, L., Ran, F. A., Cox, D., Lin, S., Barretto, R., Habib, N., . . . Zhang, F. (2013). Multiplex genome engineering using CRISPR/Cas systems. *Science, 339*(6121), 819-823. doi:10.1126/science.1231143

De Vos, W. H., Houben, F., Kamps, M., Malhas, A., Verheyen, F., Cox, J., . . . Broers, J. L. (2011). Repetitive disruptions of the nuclear envelope invoke temporary loss of cellular compartmentalization in laminopathies. *Hum Mol Genet, 20*(21), 4175-4186. doi:10.1093/hmg/ddr344

Debusk, F. L. (1972). The Hutchinson-Gilford progeria syndrome. *J. Pediatr., 80*, 697–724.

Denais, C. M., Gilbert, R. M., Isermann, P., McGregor, A. L., te Lindert, M., Weigelin, B., . . . Lammerding, J. (2016). Nuclear envelope rupture and repair during cancer cell migration. *Science, 352*(6283), 353-358. doi:10.1126/science.aad7297

Dittmer, T. A., & Misteli, T. (2011). The lamin protein family. *Genome Biol, 12*(5), 222. doi:10.1186/gb-2011-12-5-222

Eriksson, M., Brown, W. T., Gordon, L. B., Glynn, M. W., Singer, J., Scott, L., . . . Collins, F. S. (2003). Recurrent de novo point mutations in lamin A cause Hutchinson-Gilford progeria syndrome. *Nature, 423*(6937), 293-298. doi:10.1038/nature01629

Eriksson, M., Brown, W. T., Gordon, L. B., Glynn, M. W., Singer, J., Scott, L., . . . Collins, F. S. (2003). Recurrent *de novo* point mutations in lamin A cause Hutchinson–Gilford progeria syndrome. *Nature, 423*, 293–298.

Fawcett, D. W. (1966). On the occurrence of a fibrous lamina on the inner aspect of the nuclear envelope in certain cells of vertebrates. *Am J Anat, 119*(1), 129-145. doi:10.1002/aja.1001190108

Fong, L. G., Frost, D., Meta, M., Qiao, X., Yang, S. H., Coffinier, C., & Young, S. G. (2006). A protein farnesyltransferase inhibitor ameliorates disease in a mouse model of progeria. *Science, 311*(5767), 1621-1623. doi:10.1126/science.1124875

Fong, L. G., Ng, J. K., Lammerding, J., Vickers, T. A., Meta, M., Cote, N., . . . Young, S. G. (2006). Prelamin A and lamin A appear to be dispensable in the nuclear lamina. *J Clin Invest, 116*(3), 743-752. doi:10.1172/jci27125

Gerace, L., & Blobel, G. (1980). The nuclear envelope lamina is reversibly depolymerized during mitosis. *Cell, 19*(1), 277-287. doi:10.1016/0092-8674(80)90409-2

Gerhard-Herman, M., Smoot, L. B., Wake, N., Kieran, M. W., Kleinman, M. E., Miller, D. T., . . . Gordon, L. B. (2012). Mechanisms of premature vascular aging in children with Hutchinson-Gilford progeria syndrome. *Hypertension, 59*(1), 92-97. doi:10.1161/HYPERTENSIONAHA.111.180919

Glynn, M. W., & Glover, T. W. (2005). Incomplete processing of mutant lamin A in Hutchinson-Gilford progeria leads to nuclear abnormalities, which are reversed by farnesyltransferase inhibition. *Hum. Mol. Genet., 14*, 2959-2969. Retrieved from http://www.ncbi.nlm.nih.gov/entrez/query.fcgi?cmd=Retrieve&db=PubMed&dopt=Citation&list_uids=16126733

Goldman, R. D., Gruenbaum, Y., Moir, R. D., Shumaker, D. K., & Spann, T. P. (2002). Nuclear lamins: building blocks of nuclear architecture. *Genes Dev, 16*(5), 533-547. doi:10.1101/gad.960502

Goldman, R. D., Shumaker, D. K., Erdos, M. R., Eriksson, M., Goldman, A. E., Gordon, L. B., . . . Collins, F. S. (2004). Accumulation of mutant lamin A causes progressive changes in nuclear architecture in Hutchinson-Gilford progeria syndrome. *Proc. Natl. Acad. Sci. USA, 101*, 8963-8968.

Gordon, L. B., Kleinman, M. E., Miller, D. T., Neuberg, D. S., Giobbie-Hurder, A., Gerhard-Herman, M., . . . Kieran, M. W. (2012). Clinical trial of a farnesyltransferase inhibitor in children with Hutchinson-Gilford progeria syndrome. *Proc Natl Acad Sci U S A, 109*(41), 16666-16671. doi:10.1073/pnas.1202529109

Gordon, L. B., Massaro, J., D'Agostino, R. B., Sr., Campbell, S. E., Brazier, J., Brown, W. T., . . . Kieran, M. W. (2014a). Impact of farnesylation inhibitors on survival in Hutchinson-Gilford progeria syndrome. *Circulation, 130*(1), 27-34. doi:10.1161/circulationaha.113.008285

Gordon, L. B., Massaro, J., D'Agostino, R. B., Sr., Campbell, S. E., Brazier, J., Brown, W. T., . . . Kieran, M. W. (2014b). Impact of farnesylation inhibitors on survival in Hutchinson-Gilford progeria syndrome. *Circulation, 130*(1), 27–34. doi:10.1161/circulationaha.113.008285

Gordon, L. B., Shappell, H., Massaro, J., D'Agostino, R. B., Sr., Brazier, J., Campbell, S. E., . . . Kieran, M. W. (2018). Association of Lonafarnib Treatment vs No Treatment With Mortality Rate in Patients With Hutchinson-Gilford Progeria Syndrome. *Jama, 319*(16), 1687-1695. doi:10.1001/jama.2018.3264

Hamczyk, M. R., Villa-Bellosta, R., Gonzalo, P., Andres-Manzano, M. J., Nogales, P., Bentzon, J. F., . . . Andres, V. (2018). Vascular Smooth Muscle-Specific Progerin Expression Accelerates Atherosclerosis and Death in a Mouse Model of Hutchinson-Gilford Progeria Syndrome. *Circulation, 138*(3), 266-282. doi:10.1161/CIRCULATIONAHA.117.030856

Hamczyk, M. R., Villa-Bellosta, R., Quesada, V., Gonzalo, P., Vidak, S., Nevado, R. M., . . . Andrés, V. (2019). Progerin accelerates atherosclerosis by inducing endoplasmic reticulum stress in vascular smooth muscle cells. *EMBO Mol Med, 11*(4). doi:10.15252/emmm.201809736

Harborth, J., Elbashir, S. M., Bechert, K., Tuschl, T., & Weber, K. (2001). Identification of essential genes in cultured mammalian cells using small interfering RNAs. *J Cell Sci, 114*(Pt 24), 4557-4565. doi:10.1242/jcs.114.24.4557

Hatch, E. M., & Hetzer, M. W. (2016). Nuclear envelope rupture is induced by actin-based nucleus confinement. *J Cell Biol, 215*(1), 27-36. doi:10.1083/jcb.201603053

Holtz, D., Tanaka, R. A., Hartwig, J., & McKeon, F. (1989). The CaaX motif of lamin A functions in conjunction with the nuclear localization signal to target assembly to the nuclear envelope. *Cell, 59*(6), 969-977. doi:0092-8674(89)90753-8 [pii]

Kang, S. M., Seo, S., Song, E. J., Kweon, O., Jo, A. H., Park, S., . . . Park, B. J. (2023). Progerinin, an Inhibitor of Progerin, Alleviates Cardiac Abnormalities in a Model Mouse of Hutchinson-Gilford Progeria Syndrome. *Cells, 12*(9). doi:10.3390/cells12091232

Kelley, J. B., Datta, S., Snow, C. J., Chatterjee, M., Ni, L., Spencer, A., . . . Paschal, B. M. (2011). The defective nuclear lamina in Hutchinson-gilford progeria syndrome disrupts the nucleocytoplasmic Ran gradient and inhibits nuclear localization of Ubc9. *Mol Cell Biol, 31*(16), 3378-3395. doi:10.1128/mcb.05087-11

Kim, P. H., Chen, N. Y., Heizer, P. J., Tu, Y., Weston, T. A., Fong, J. L., . . . Fong, L. G. (2021). Nuclear membrane ruptures underlie the vascular pathology in a mouse model of Hutchinson-Gilford progeria syndrome. *JCI Insight, 6(16)*(16), e151515. doi:10.1172/jci.insight.151515

Kim, P. H., Luu, J., Heizer, P., Tu, Y., Weston, T. A., Chen, N., . . . Fong, L. G. (2018a). Disrupting the LINC complex in smooth muscle cells reduces aortic disease in a mouse model of Hutchinson-Gilford progeria syndrome. *Sci Transl Med, 10*(460). doi:10.1126/scitranslmed.aat7163

Kim, P. H., Luu, J., Heizer, P., Tu, Y., Weston, T. A., Chen, N., . . . Fong, L. G. (2018b). Disrupting the LINC complex in smooth muscle cells reduces aortic disease in a mouse model of Hutchinson-Gilford progeria syndrome. *Sci Transl Med, 10(460)*(460), eaat7163. doi:10.1126/scitranslmed.aat7163

Koblan, L. W., Erdos, M. R., Gordon, L. B., Collins, F. S., Brown, J. D., & Liu, D. R. (2021). Base editor treats progeria in mice. *Nature*. doi:10.1038/d41586-021-01114-8

Lee, J. M., Nobumori, C., Tu, Y., Choi, C., Yang, S. H., Jung, H. J., . . . Fong, L. G. (2016). Modulation of LMNA splicing as a strategy to treat prelamin A diseases. *J Clin Invest, 126*(4), 1592-1602. doi:10.1172/JCI85908

Lin, F., & Worman, H. J. (1993). Structural organization of the human gene encoding nuclear lamin A and nuclear lamin C. *J Biol Chem, 268*(22), 16321-16326. Retrieved from https://www.ncbi.nlm.nih.gov/pubmed/8344919

Lopez-Otin, C., Blasco, M. A., Partridge, L., Serrano, M., & Kroemer, G. (2013). The hallmarks of aging. *Cell, 153*(6), 1194-1217. doi:10.1016/j.cell.2013.05.039

Mallampalli, M. P., Huyer, G., Bendale, P., Gelb, M. H., & Michaelis, S. (2005). Inhibiting farnesylation reverses the nuclear morphology defect in a HeLa cell model for Hutchinson-Gilford progeria syndrome. *Proc. Natl. Acad. Sci. USA, 102*(40), 14416-14421. Retrieved from http://www.ncbi.nlm.nih.gov/entrez/query.fcgi?cmd=Retrieve&db=PubMed&dopt=Citation&list_uids=16186497

McClintock, D., Ratner, D., Lokuge, M., Owens, D. M., Gordon, L. B., Collins, F. S., & Djabali, K. (2007). The mutant form of lamin A that causes Hutchinson-Gilford progeria is a biomarker of cellular aging in human skin. *PLoS One, 2*(12), e1269. doi:10.1371/journal.pone.0001269

Merideth, M. A., Gordon, L. B., Clauss, S., Sachdev, V., Smith, A. C., Perry, M. B., . . . Introne, W. J. (2008). Phenotype and course of Hutchinson-Gilford progeria syndrome. *N Engl J Med, 358*(6), 592-604. doi:10.1056/NEJMoa0706898

Nigg, E. A., Kitten, G. T., & Vorburger, K. (1992). Targeting lamin proteins to the nuclear envelope: the role of CaaX box modifications. *Biochem Soc Trans, 20*(2), 500-504. doi:10.1042/bst0200500

Nmezi, B., Xu, J., Fu, R., Armiger, T. J., Rodriguez-Bey, G., Powell, J. S., . . . Padiath, Q. S. (2019). Concentric organization of A- and B-type lamins predicts their distinct roles in the spatial organization and stability of the nuclear lamina. *Proc Natl Acad Sci U S A, 116*(10), 4307-4315. doi:10.1073/pnas.1810070116

Olive, M., Harten, I., Mitchell, R., Beers, J. K., Djabali, K., Cao, K., . . . Gordon, L. B. (2010). Cardiovascular pathology in Hutchinson-Gilford progeria: correlation with the vascular

pathology of aging. *Arterioscler Thromb Vasc Biol, 30*(11), 2301-2309. doi:10.1161/atvbaha.110.209460

Puttaraju, M., Jackson, M., Klein, S., Shilo, A., Bennett, C. F., Gordon, L., . . . Misteli, T. (2021). Systematic screening identifies therapeutic antisense oligonucleotides for Hutchinson-Gilford progeria syndrome. *Nat Med, 27*(3), 526-535. doi:10.1038/s41591-021-01262-4

Samson, C., Celli, F., Hendriks, K., Zinke, M., Essawy, N., Herrada, I., . . . Zinn-Justin, S. (2017). Emerin self-assembly mechanism: role of the LEM domain. *Febs j, 284*(2), 338-352. doi:10.1111/febs.13983

Sánchez-López, A., Espinós-Estévez, C., González-Gómez, C., Gonzalo, P., Andrés-Manzano, M. J., Fanjul, V., . . . Andrés, V. (2021). Cardiovascular Progerin Suppression and Lamin A Restoration Rescue Hutchinson-Gilford Progeria Syndrome. *Circulation, 144*(22), 1777-1794. doi:10.1161/circulationaha.121.055313

Santiago-Fernandez, O., Osorio, F. G., Quesada, V., Rodriguez, F., Basso, S., Maeso, D., . . . Lopez-Otin, C. (2019). Development of a CRISPR/Cas9-based therapy for Hutchinson-Gilford progeria syndrome. *Nat Med, 25*(3), 423-426. doi:10.1038/s41591-018-0338-6

Scaffidi, P., & Misteli, T. (2006). Lamin A-dependent nuclear defects in human aging. *Science, 312*(5776), 1059-1063. doi:10.1126/science.1127168

Shah, P., Wolf, K., & Lammerding, J. (2017). Bursting the Bubble - Nuclear Envelope Rupture as a Path to Genomic Instability? *Trends Cell Biol, 27*(8), 546-555. doi:10.1016/j.tcb.2017.02.008

Shimi, T., Kittisopikul, M., Tran, J., Goldman, A. E., Adam, S. A., Zheng, Y., . . . Goldman, R. D. (2015). Structural organization of nuclear lamins A, C, B1, and B2 revealed by superresolution microscopy. *Mol Biol Cell, 26*(22), 4075-4086. doi:10.1091/mbc.E15-07-0461

Shimi, T., Pfleghaar, K., Kojima, S., Pack, C. G., Solovei, I., Goldman, A. E., . . . Goldman, R. D. (2008). The A- and B-type nuclear lamin networks: microdomains involved in chromatin organization and transcription. *Genes Dev, 22*(24), 3409-3421. doi:10.1101/gad.1735208

Stehbens, W., Delahunt, B., Shozawa, T., & Gilbert-Barness, E. (2001). Smooth muscle cell depletion and collagen types in progeric arteries. *Cardiovasc. Pathol., 10*, 133–136.

Stehbens, W. E., Wakefield, S. J., Gilbert-Barness, E., Olson, R. E., & Ackerman, J. (1999). Histological and ultrastructural features of atherosclerosis in progeria. *Cardiovasc Pathol, 8*(1), 29-39. doi:10.1016/s1054-8807(98)00023-4

Toth, J. I., Yang, S. H., Qiao, X., Beigneux, A. P., Gelb, M. H., Moulson, C. L., . . . Fong, L. G. (2005). Blocking protein farnesyltransferase improves nuclear shape in fibroblasts from humans with progeroid syndromes. *Proc. Natl. Acad. Sci. USA, 102*(36), 12873-12878. Retrieved from http://www.ncbi.nlm.nih.gov/entrez/query.fcgi?cmd=Retrieve&db=PubMed&dopt=Citation&list_uids=16129834

Turgay, Y., Eibauer, M., Goldman, A. E., Shimi, T., Khayat, M., Ben-Harush, K., . . . Medalia, O. (2017). The molecular architecture of lamins in somatic cells. *Nature, 543*(7644), 261-264. doi:10.1038/nature21382

Turgay, Y., & Medalia, O. (2017). The structure of lamin filaments in somatic cells as revealed by cryo-electron tomography. *Nucleus, 8*(5), 475-481. doi:10.1080/19491034.2017.1337622

Ullrich, N. J., Kieran, M. W., Miller, D. T., Gordon, L. B., Cho, Y. J., Silvera, V. M., . . . Kleinman, M. E. (2013). Neurologic features of Hutchinson-Gilford progeria syndrome after lonafarnib treatment. *Neurology, 81*(5), 427-430. doi:10.1212/WNL.0b013e31829d85c0

Varga, R., Eriksson, M., Erdos, M. R., Olive, M., Harten, I., Kolodgie, F., . . . Collins, F. S. (2006). Progressive vascular smooth muscle cell defects in a mouse model of Hutchinson-Gilford progeria syndrome. *Proc Natl Acad Sci U S A, 103*(9), 3250-3255. doi:10.1073/pnas.0600012103

Vargas, J. D., Hatch, E. M., Anderson, D. J., & Hetzer, M. W. (2012). Transient nuclear envelope rupturing during interphase in human cancer cells. *Nucleus, 3*(1), 88-100. doi:10.4161/nucl.18954

Verstraeten, V. L., Ji, J. Y., Cummings, K. S., Lee, R. T., & Lammerding, J. (2008). Increased mechanosensitivity and nuclear stiffness in Hutchinson-Gilford progeria cells: effects of farnesyltransferase inhibitors. *Aging Cell, 7*(3), 383-393. doi:10.1111/j.1474-9726.2008.00382.x

Wang, Y., Ostlund, C., Choi, J. C., Swayne, T. C., Gundersen, G. G., & Worman, H. J. (2012). Blocking farnesylation of the prelamin A variant in Hutchinson-Gilford progeria syndrome alters the distribution of A-type lamins. *Nucleus, 3*(5), 452-462. doi:10.4161/nucl.21675

Wolf, C. M., Wang, L., Alcalai, R., Pizard, A., Burgon, P. G., Ahmad, F., . . . Seidman, J. G. (2008). Lamin A/C haploinsufficiency causes dilated cardiomyopathy and apoptosis-triggered cardiac conduction system disease. *J Mol Cell Cardiol, 44*(2), 293-303. doi:S0022-2828(07)01313-2 [pii]
10.1016/j.yjmcc.2007.11.008

Worman, H. J., & Bonne, G. (2007). "Laminopathies": a wide spectrum of human diseases. *Exp. Cell. Res., 313*(10), 2121–2133. Retrieved from http://www.ncbi.nlm.nih.gov/entrez/query.fcgi?cmd=Retrieve&db=PubMed&dopt=Citation&list_uids=17467691

Worman, H. J., & Schirmer, E. C. (2015). Nuclear membrane diversity: underlying tissue-specific pathologies in disease? *Curr Opin Cell Biol, 34*, 101-112. doi:10.1016/j.ceb.2015.06.003

Yang, S. H., Bergo, M. O., Toth, J. I., Qiao, X., Hu, Y., Sandoval, S., . . . Fong, L. G. (2005). Blocking protein farnesyltransferase improves nuclear blebbing in mouse fibroblasts with a targeted Hutchinson-Gilford progeria syndrome mutation. *Proc. Natl. Acad. Sci. USA, 102*(29), 10291-10296. Retrieved from http://www.ncbi.nlm.nih.gov/entrez/query.fcgi?cmd=Retrieve&db=PubMed&dopt=Citation&list_uids=16014412

Yang, S. H., Chang, S. Y., Ren, S., Wang, Y., Andres, D. A., Spielmann, H. P., . . . Young, S. G. (2011). Absence of progeria-like disease phenotypes in knock-in mice expressing a non-farnesylated version of progerin. *Hum Mol Genet, 20*(3), 436-444. Retrieved from http://www.ncbi.nlm.nih.gov/entrez/query.fcgi?cmd=Retrieve&db=PubMed&dopt=Citation&list_uids=21088111

Yang, S. H., Meta, M., Qiao, X., Frost, D., Bauch, J., Coffinier, C., . . . Fong, L. G. (2006). A farnesyltransferase inhibitor improves disease phenotypes in mice with a Hutchinson-Gilford progeria syndrome mutation. *J Clin Invest, 116*(8), 2115-2121. doi:10.1172/jci28968

Young, S. G., Fong, L. G., & Michaelis, S. (2005). Prelamin A, Zmpste24, misshapen cell nuclei, and progeria--new evidence suggesting that protein farnesylation could be important for disease pathogenesis. *J Lipid Res, 46*(12), 2531-2558. doi:10.1194/jlr.R500011-JLR200

Young, S. G., Fong, L. G., & Michaelis, S. (2005). Prelamin A, Zmpste24, misshapen cell nuclei, and progeria—New evidence suggesting that protein farnesylation could be important for disease pathogenesis. *J. Lipid. Res., 46*, 2531–2558.

Zhang, H., Xiong, Z. M., & Cao, K. (2014). Mechanisms controlling the smooth muscle cell death in progeria via down-regulation of poly(ADP-ribose) polymerase 1. *Proc Natl Acad Sci U S A, 111*(22), E2261-2270. doi:10.1073/pnas.1320843111

Zhang, J., Lian, Q., Zhu, G., Zhou, F., Sui, L., Tan, C., . . . Colman, A. (2011). A human iPSC model of Hutchinson Gilford Progeria reveals vascular smooth muscle and mesenchymal stem cell defects. *Cell Stem Cell, 8*(1), 31-45. doi:10.1016/j.stem.2010.12.002

Abbreviations

Cas9, CRISPR associated protein 9

cGAS, cyclic GMP–AMP synthase

Dox, doxycycline

HGPS, Hutchinson-Gilford progeria syndrome

Hu, human

LAP2β, lamina-associated polypeptide-2 β isoform

Mo, mouse

NM, nuclear membrane

SMC, smooth muscle cell

Figure 1

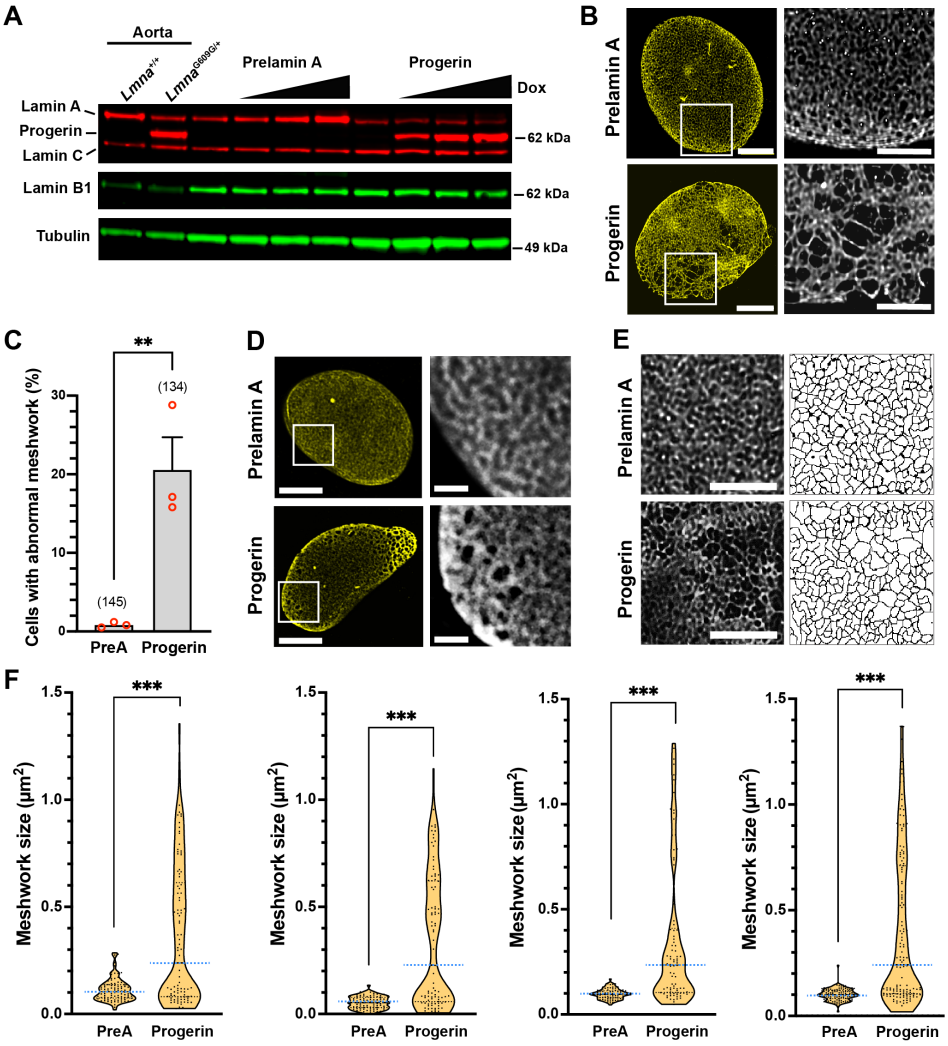

Figure 1. The nuclear lamin meshwork is abnormal in progerin-expressing SMCs. A. Western blot comparing the expression of lamin A and progerin in the mouse aorta and in cultured SMCs expressing doxycycline (Dox)-inducible constructs for human (hu)-prelamin A and hu-progerin. Tubulin was measured as a loading control. B. Confocal fluorescence microscopy images of the prelamin A (upper) and progerin (lower) meshworks in SMCs stained with an antibody against hu-lamin A (yellow). High-magnification images of the boxed regions are shown to the right. Scale bar, 2 µm. C. The percentage of cells with an abnormal nuclear lamin meshwork in SMCs expressing prelamin A (PreA) or progerin. The total numbers of cells examined in three independent experiments (circles) are shown in parentheses. Mean ± SEM. **, $P < 0.01$. D. STED microscopy images of the prelamin A (upper) and progerin (lower) meshworks in SMCs stained with an antibody against hu-lamin A (yellow). High-magnification images of the boxed regions are shown to the right. Scale bar, 1 µm. E. Representative microscopy images (left) and line drawings (right) of 4 × 4-µm regions in the prelamin A (upper) and progerin (lower) meshworks in SMCs. Scale bar, 2 µm. F. Violin plots comparing the distribution (tan) and average sizes (blue dotted lines) of the openings in the prelamin A (PreA) and progerin meshworks in four pairs of nuclei. ***, $P < 0.001$.

Figure 2

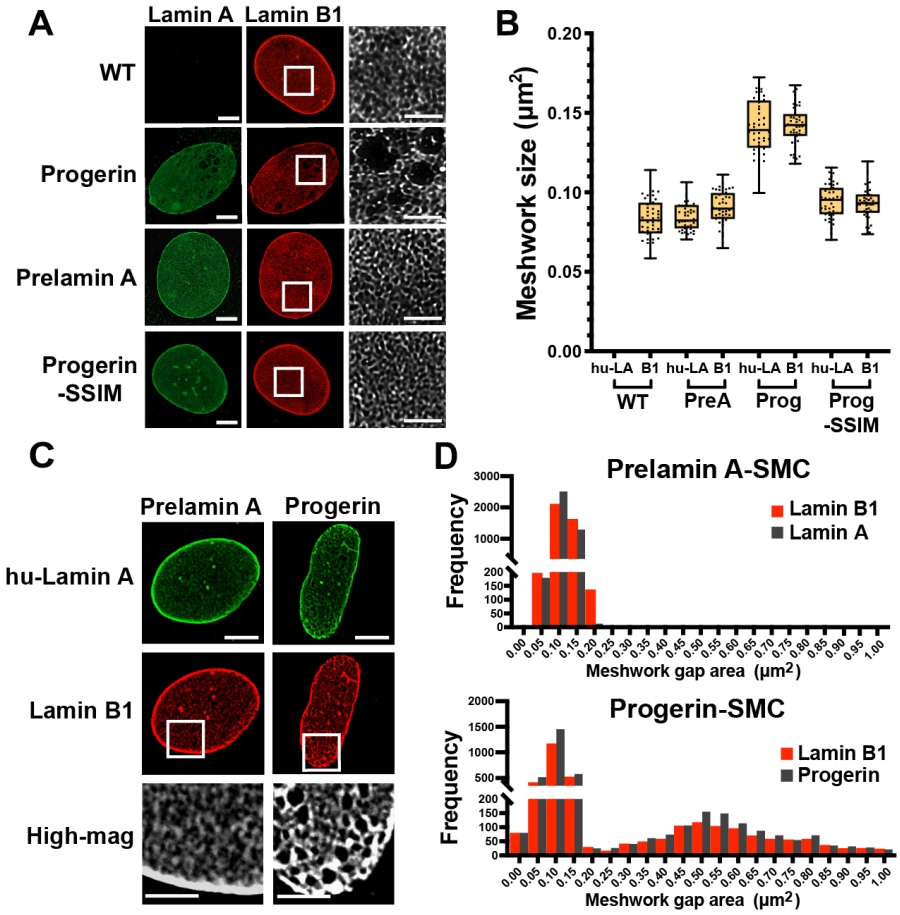

Figure 2. Progerin has a dominant-negative effect on the structure of the lamin B1 meshwork. A. Representative confocal fluorescence microscopy images of wild-type SMCs (WT) and SMCs expressing hu-progerin, hu-prelamin A, and hu-progerin-SSIM. Cells were stained with antibodies against hu-lamin A (green) and lamin B1 (red). Scale bar, 2.5 μm. High-magnification images of the boxed regions are shown to the right. Scale bar, 2 μm. B. Box and whisker plots comparing the average sizes (solid black line) and ranges of the openings in the meshworks of WT SMCs, and SMCs expressing hu-prelamin A (hu-PreA), hu-progerin (hu-Prog), and hu-Prog-SSIM. The cells were stained with antibodies against hu-lamin A and mouse lamin B1. Mean ± SEM. *, $P < 0.05$ (n = 45 nuclei/group). C. STED microscopy images of SMCs expressing prelamin A (left) or progerin (right) stained with antibodies against hu-lamin A (green) and lamin B1 (red). Scale bar, 5 μm. High-magnification images of the boxed regions are shown at the bottom. Scale bar, 1.0 μm. D. Bar graphs showing the sizes of the openings in the lamin A (black) and lamin B1 (red) meshworks in SMCs expressing hu-prelamin A (top) and the progerin (black) and lamin B1 (red) meshworks in SMCs expressing hu-progerin (bottom). A break in the Y-axis was used to optimize viewing of the sizes of lower-frequency openings in the meshwork.

Figure 3

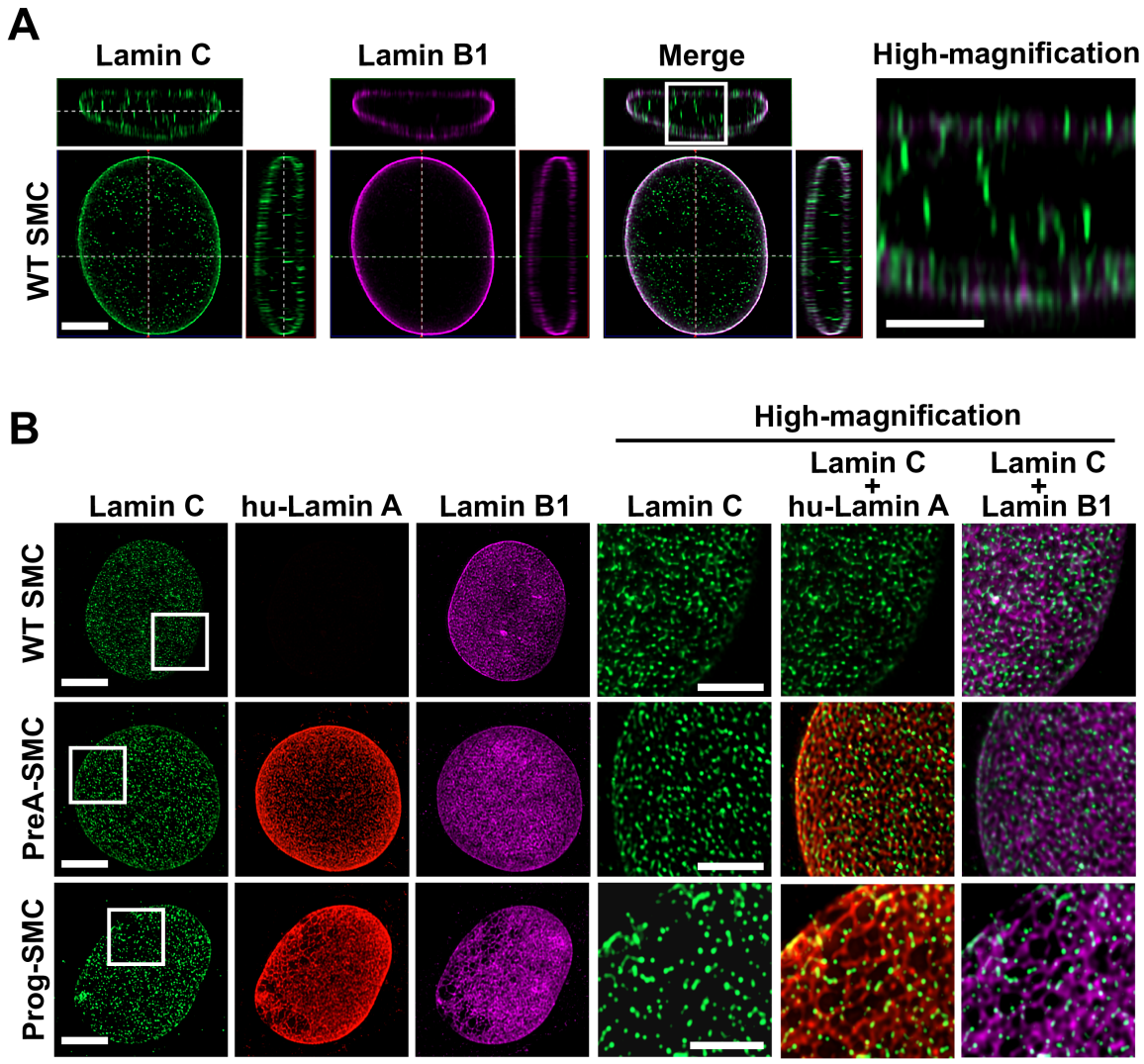

Figure 3. Lamin C in progerin-SMCs is present along the borders of openings in the progerin meshwork. A. Orthogonal views of a nucleus from a wild-type SMC (WT SMC) stained with antibodies against lamin C (green) and lamin B1 (magenta). Lamin C is located at the nuclear rim and in the nucleoplasm. Scale bar, 5 µm. A high-magnification image of the boxed region is shown to the right. Scale bar, 2 µm. B. Representative confocal fluorescence microscopy images of nuclei from WT-SMCs and SMCs expressing hu-prelamin A (PreA-SMC) and hu-progerin (Prog-SMC). Cells were stained with antibodies against lamin C (green), hu-lamin A (red), and lamin B1 (magenta). Scale bar, 5 µm. High-magnifications images of the boxed areas are shown to the right. Scale bar, 2 µm.

Figure 4

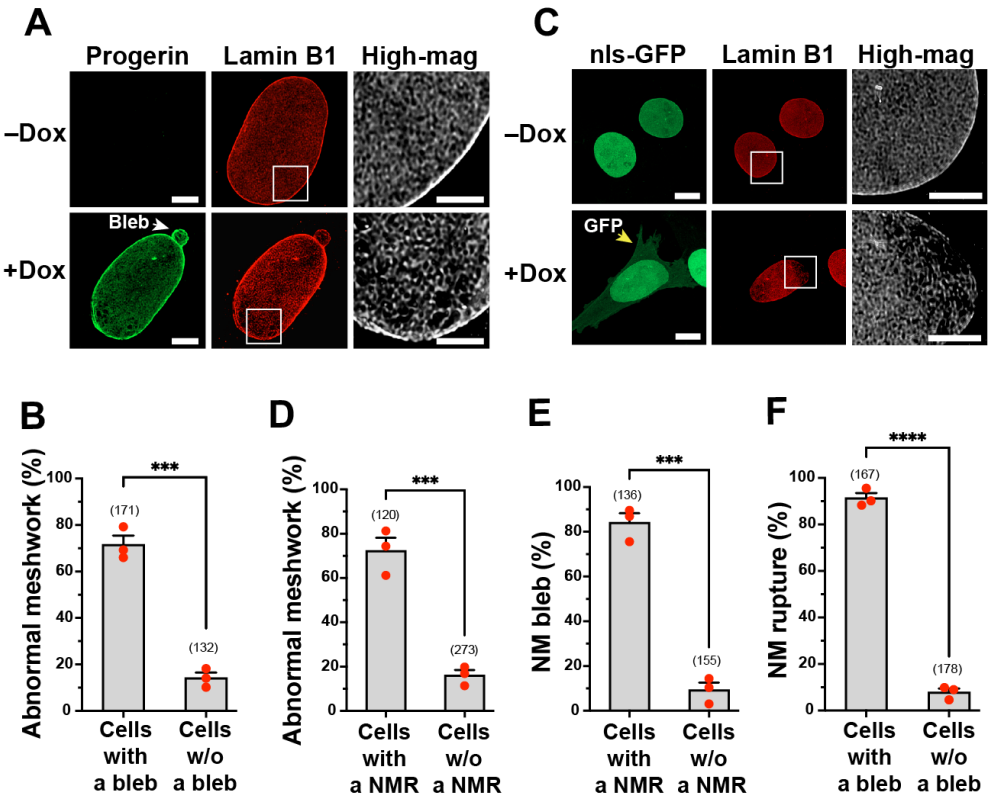

Figure 4. Nuclear membrane (NM) ruptures and nuclear blebs are associated with an abnormal progerin meshwork. A. Representative confocal fluorescence microscopy images of non-induced (–Dox) and induced (+Dox) progerin-SMCs stained with antibodies against hu-lamin A (green) and lamin B1 (red). Scale bar, 5 µm. Boxed regions are shown at higher magnification to the right. Scale bar, 2 µm. The arrow points to a nuclear bleb. B. Percentage of progerin-SMCs with a nuclear bleb that have an abnormal progerin meshwork. The total numbers of cells examined in 3 different experiments (circles) are shown in parentheses. Mean ± SEM. ***, $P < 0.001$. C. Representative confocal fluorescence microscopy images of non-induced (–Dox) and induced (+Dox) progerin-SMCs expressing nls-GFP (green) and stained with an antibody against lamin B1 (red). Scale bar, 5 µm. Boxed regions are shown at higher magnification to the right. Scale bar, 2 µm. A cell with a NM rupture was identified by nls-GFP in the cytoplasm (yellow arrow). D. Percentage of progerin-SMCs with a NM rupture (NMR) and an abnormal progerin meshwork. The total numbers of cells examined in 3 independent experiments (circles) are shown in parentheses. Mean ± SEM. ***, $P < 0.001$. E. Percentage of progerin-SMCs with a NMR that had a nuclear bleb. The total numbers of cells examined in 3 independent experiments (circles) are shown in parentheses. Mean ± SEM. ***, $P < 0.001$. F. Percentage of progerin-SMCs with a nuclear bleb that had a NMR. The total numbers of cells examined in 3 independent experiments (circles) are shown in parentheses. Mean ± SEM. ****, $P < 0.0001$.

Figure 5

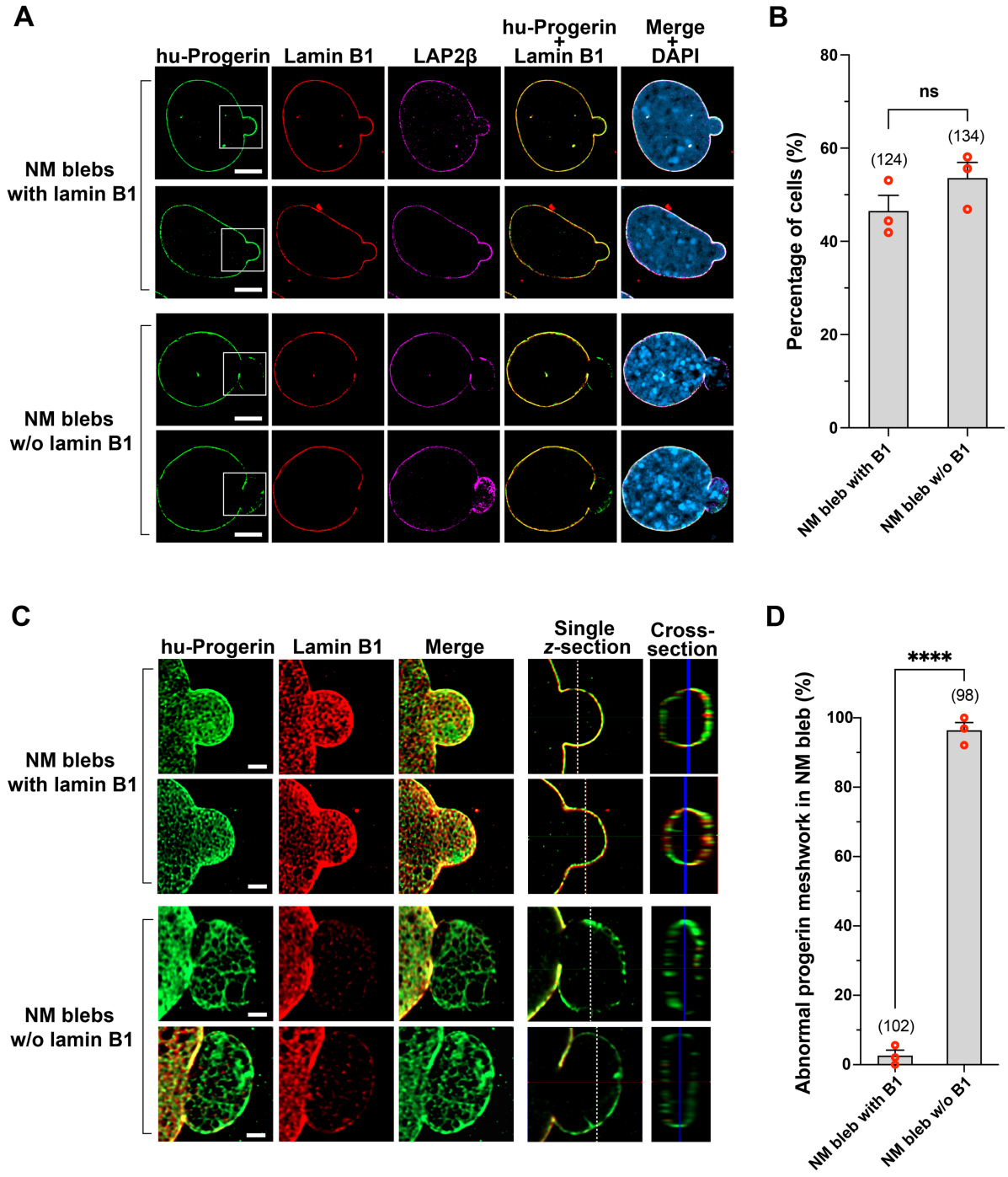

Figure 5. An abnormal progerin meshwork in nuclear blebs is associated with low lamin B1 levels. A. Representative confocal fluorescence microscopy images of progerin-SMCs stained with antibodies against hu-lamin A (green), lamin B1 (red), and LAP2β (magenta). DNA was stained with Dapi (blue). Scale bar, 5 µm. Single microscopy sections were collected through the middle of the nuclear bleb. The boxed areas are shown at higher magnification in panel C. B.

Percentage of nuclear blebs in progerin-SMCs with normal levels of lamin B1 or low levels of lamin B1. The total numbers of cells examined in three experiments (circles) are shown in parentheses. Mean ± SEM. ns, not significant. C. High-resolution microscopy images of the progerin and lamin B1 meshworks in the nuclear blebs boxed in panel A. Scale bar, 1 μm. D. Percentage of nuclear blebs with an abnormal progerin meshwork in blebs with lamin B1 and blebs without lamin B1. The total numbers of cells examined in three independent experiments (circles) are shown in parentheses. Mean ± SEM. ****, $P < 0.001$.

Figure 6

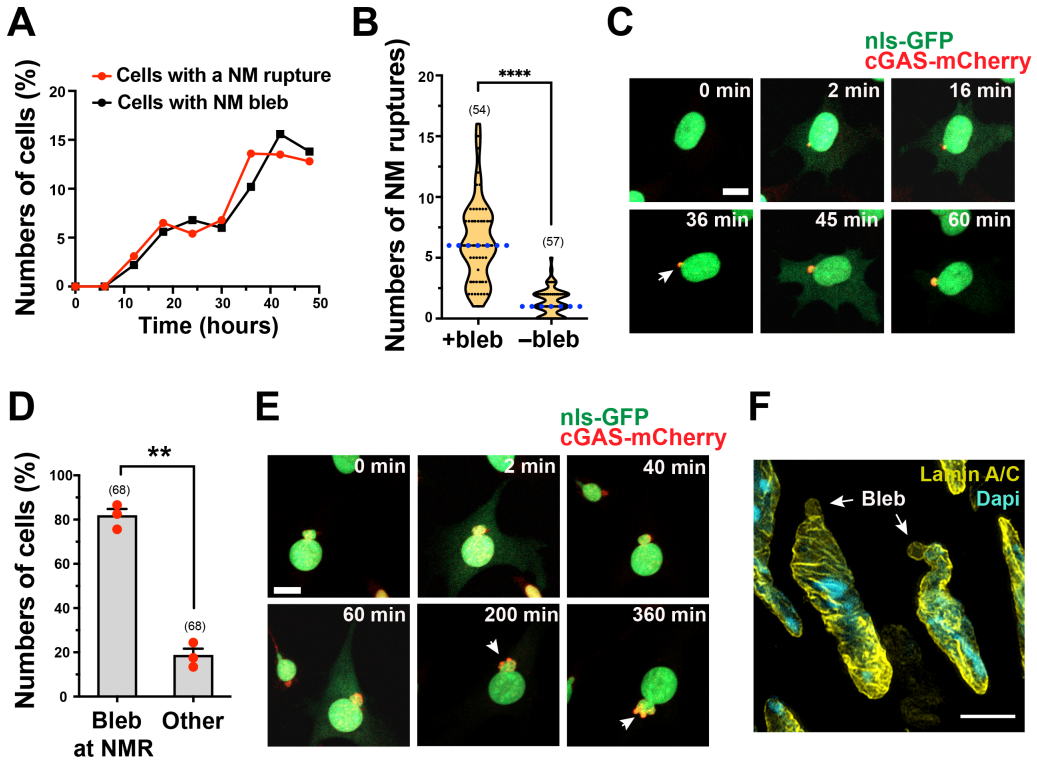

Figure 6. Nuclear blebs form at sites of nuclear membrane ruptures. A. Kinetics of nuclear bleb formation (black squares) and NM ruptures (red circles) after adding Dox to induce progerin synthesis. B. Frequency of NM ruptures in progerin-SMCs with a nuclear bleb and without a nuclear bleb. The total numbers of cells examined are shown in parentheses. Mean ± SD. ****, $P < 0.0001$. C. Still images from a live-cell recording (Supplemental video 1) of progerin-SMCs expressing nls-GFP (green) and cGAS-mCherry (red). A NM rupture at 2 min (identified by the appearance of GFP in the cytoplasm) was followed by the formation of a nuclear bleb labeled with cGAS-mCherry (arrow). Scale bar, 10 µm. The time mark (relative to the first image) is shown in the upper right. D. Bar graph showing the frequency of a nuclear bleb forming at a NM rupture (NMR) site. The total numbers of cells examined from three experiments (circles) are shown above each bar. Mean ± SEM. **, $P < 0.01$. E. Still images from a time-lapse video (Supplemental video 2) of progerin-SMCs showing the formation of nuclear bleb on an existing bleb after a NM rupture. Scale bar, 10 µm. The arrow points to two small nuclear blebs that formed on a larger nuclear bleb. F. Confocal fluorescence microscopy image of aortic SMCs from a 10-week–old *Lmna*$^{G609G/G609G}$ mouse stained with an antibody against lamin A/C (yellow). DNA was stained with Dapi (blue). Scale bar, 5 µm. The arrows point to nuclear blebs.

Figure 7

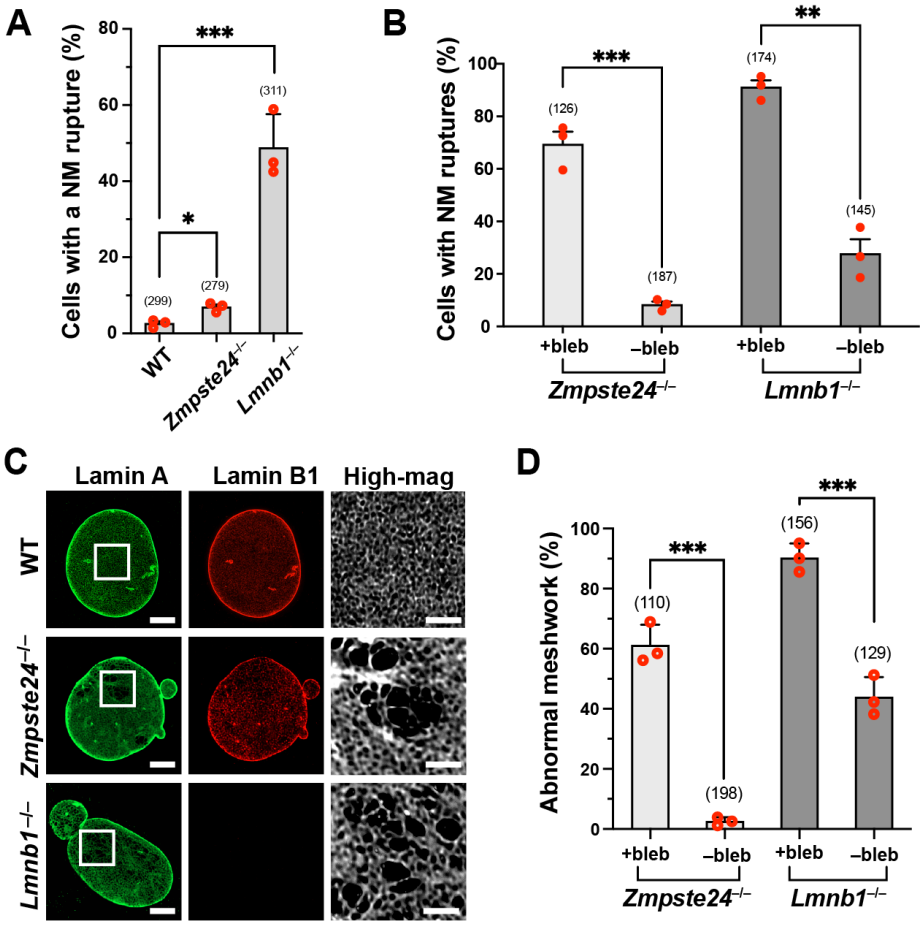

Figure 7. NM ruptures and nuclear blebs are associated with an abnormal nuclear lamin meshwork in *Lmnb1*$^{-/-}$ and *Zmpste24*$^{-/-}$ SMCs. A. Bar graph showing the percentage of cells with a NM rupture in wild-type (WT), *Zmpste24*$^{-/-}$, and *Lmnb1*$^{-/-}$ SMCs. The total numbers of cells examined in 3 independent experiments (circles) are shown in parentheses. Mean ± SEM. *, P < 0.05 ***; P < 0.001. B. Bar graph showing the frequency of NM ruptures in *Zmpste24*$^{-/-}$ and *Lmnb1*$^{-/-}$ SMCs with and without a nuclear bleb. The total numbers of cells examined in 3 independent experiments (circles) are shown in parentheses. Mean ± SEM. **, P < 0.01; ***, P < 0.001 C. Representative high-resolution microscopy images of cells stained with antibodies against lamin A (green) and lamin B1 (red) in WT, *Zmpste24*$^{-/-}$, and *Lmnb1*$^{-/-}$ SMCs. Scale bar, 5 µm. Boxed areas are shown at higher magnification on the right. D. Bar graph showing the frequency of an abnormal lamin A meshwork in *Zmpste24*$^{-/-}$ and *Lmnb1*$^{-/-}$ SMCs with and without a nuclear bleb. The numbers of cells scored in 3 independent experiments (circles) are shown in parentheses. Mean ± SEM. ***, P < 0.001.

Figure 8

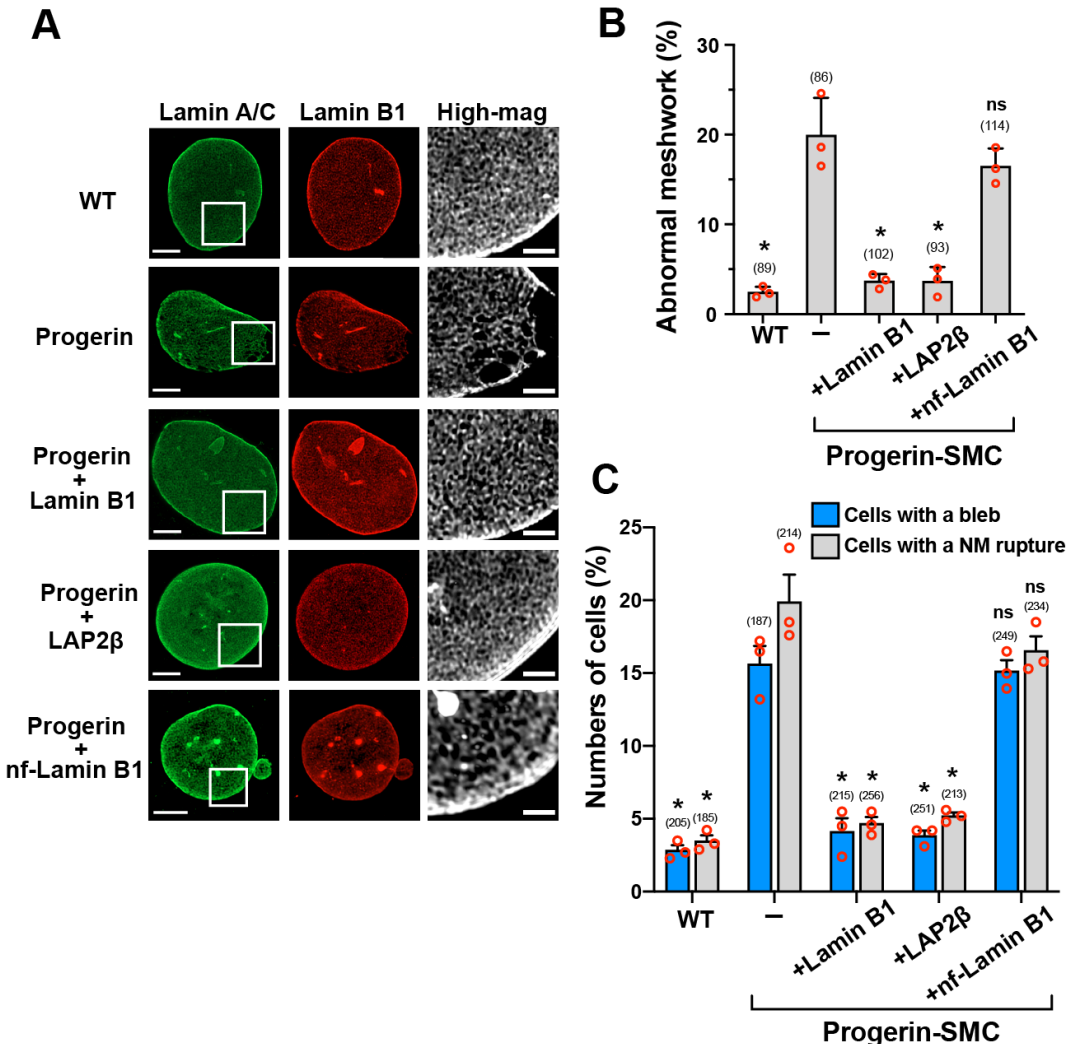

Figure 8. Lamin B1 and LAP2β expression normalized the meshwork in progerin-SMCs and reduced the frequency of NM ruptures and nuclear blebs. A. Representative high-resolution microscopy images of WT SMCs, and SMCs expressing progerin, progerin + lamin B1, progerin + LAP2β, or progerin + nonfarnesyl-lamin B1 (nf-lamin B1); cells were stained with antibodies against lamin A/C (green) and lamin B1 (red). High-magnification images of the boxed regions are shown on the right (white). Scale bar, 5 µm. B. Percentage of cells with an abnormal nuclear lamin meshwork in WT-SMCs, progerin-SMCs, and progerin-SMCs expressing lamin B1, LAP2β, or nf-lamin B1. The numbers of cells examined in 3 independent experiments (circles) are shown in parentheses. Mean ± SEM. *, $P < 0.05$. One-way ANOVA showing comparisons to progerin-SMCs. C. Percentage of cells with a nuclear bleb (blue) or NM rupture (grey) in WT-SMCs, progerin-SMCs, and progerin-SMCs expressing lamin B1, LAP2β, or nf-lamin B1. The numbers of cells examined in 3 independent experiments (circles) are shown in parentheses. Mean ± SEM. *, $P < 0.05$. Two-way ANOVA showing comparisons to progerin-SMCs. ns, not significant.

PNAS

Supporting Information for

Progerin forms an abnormal meshwork and has a dominant-negative effect on the nuclear lamina

Paul H. Kim, Joonyoung R. Kim, Yiping Tu, Hyesoo Jung, JY Brian Jeong, Anh P. Tran, Ashley Presnell, Stephen G. Young, and Loren G. Fong

Loren G. Fong

Email: lfong@mednet.ucla.edu

This PDF file includes:

Supporting text (Materials and Methods)

Figures S1 to S5

Tables S1 to S3

Legends for Movies S1 to S2

SI References

Other supporting materials for this manuscript include the following:

Movies S1 to S2

Materials and Methods

***Lmnb1*-deficient SMCs**. Guide RNAs targeting *Lmnb1*-deficient SMCs (*Lmnb1*$^{-/-}$) (lacking any detectable lamin B1 by western blot or immunocytochemical staining) were created by CRISPR/Cas9-induced homology-directed repair. Guide RNAs targeting *Lmnb1* 5′ upstream sequences (5′-GCTGGAACCACTCCACGTGT-3′ and 5′-GGCGAGAGGCGGGCAGGAGG-3′) and *Lmnb1* 3′ untranslated region (5′-TAGTCACCATGTACGCACTC-3′ and 5′-ATCTTACAACGTGTATGGAT-3′) were subcloned into the CRISPR/Cas9 vector pX458-GFP (Addgene). To facilitate the selection of genetically modified SMCs, blasticidin and zeocin-resistant knock-in cassettes flanked by LoxP sequences and incorporating homology arms (1,702 bp and 1,519 bp for the blasticidin-resistant cassette; 1,724 bp and 1,747 bp for the zeocin-resistant cassette) were constructed. This strategy made it possible to isolate clones that had undergone successful integration of the cassettes. A Nucleofector II apparatus (Lonza) and the Cell line T Nucleofector kit (Lonza) were used to electroporate 3 μg of each vector and insert cassette into 2 × 10^6 SMCs. After 48 h, SMCs were treated by blasticidin and zeocin. Following a 14-day selection period, genomic DNA was extracted from SMC clones with the DNeasy kit (Qiagen) and subjected to PCR analysis with *Lmnb1*-specific primers (5′ upstream: 5′-GCTACCCAGGGAATCTCAGGC-3′; 3′ UTR: 5′-TGGCAGCTCCAGAGGAAGAATG-3′). The PCR products (6,510 bp for blasticidin-resistant and 4,836 bp for zeocin-resistant integrated alleles) were sequenced with *Lmnb1* sequencing primers (5′ upstream: 5′-AGGTCCGCTCGATCCTCACC-3′ and 5′-CGCATCAGCAGGTAAAGGGAC-3′; 3′ UTR: 5′-CCAATCAACAGCTCTGTAGAACCTC-3′ and 5′-CAGACCACCCATCTAGGGAGAG-3′). Sequencing confirmed the targeted integration of each cassette into each allele. Subsequently, a clone was expanded in a 6-well plate and treated with an adenovirus expressing *Cre* recombinase

under the CMV promoter to excise the integrated cassettes. Confirmation of the sequences post-*Cre* treatment was achieved through the previously mentioned PCR sequencing analyses.

***Zmpste24*-deficient SMC.** *Zmpster24*-deficient SMCs were created in a similar fashion as *Lmnb1*-deficient SMCS. Guide RNAs targeting exon 6 of *Zmpste24* (5′-GGTAAGGCTACCTGGAGGTG-3′) and (5′-ACAACATACACCTTAGTCAA-3′) were subcloned into pX458-GFP CRISPR/Cas9 vector linearized with *Bbs*I. PCR primers outflanking the gRNA cut sites (5′-ATTGCCTGTGTCTGCCCTTCTGCT-3′ and 5′-GAACACTGGTTTTGTTTTGCAGCC-3′) were used to amplify the gene fragment from the genomic DNA. Sequencing primer (5′-TCCACCAGCATGAACAAGGGTGTGT-3′) was used to verify the sequence deletion between the two guide RNA cut sites. Clonal cell lines were further tested by qPCR and western blot to confirm the absence and inactivity of ZMPSTE24.

Western blotting. SMCs were prepared by collecting cells with TrypLE (ThermoFisher), washing briefly in cold PBS and centrifuged at 500 × *g* for 5 min. Cell pellets were lysed in urea lysis buffer [8M urea, 100mM NaCl, 10mM Tris, 1mM EDTA, 1× phosphatase inhibitor (Bimake), 0.1mM PMSF, 0.1% Triton-X 100, 1× protease inhibitor (Roche) dissolved in water] by vortexing for 10 sec followed by centrifugation for 10 min at 18,000 × *g*. The supernatant was transferred to a clean Eppendorf tube, mixed with LDS sample buffer (Invitrogen), and heated at 70°C for 10 min. Urea-soluble protein extracts were size-fractionated on 4–12% gradient polyacrylamide Bis-Tris gels (Invitrogen) and transferred to nitrocellulose membranes. The membranes were blocked with Odyssey Blocking solution (LI-COR Bioscience, Lincoln, NE) for 1 h at RT and incubated with primary antibodies at 4°C overnight. After washing the membranes with PBS containing 0.2% Tween-20 (3 times for 10 min each), they were incubated with infrared dye (IR)–labeled secondary antibodies at RT for 1 h. Membranes were washed with 0.2% PBS-T (3 times for 10 min each).

The IR signals were quantified with an Odyssey infrared scanner (LI-COR Biosciences). The antibodies and concentrations are listed in *SI Appendix*, Table SI.

Quantitative real time-PCR. Total RNA was extracted with the RNeasy kit (Qiagen) and treated with DNase I (Ambion) according to the manufacturer's recommendation. RNA was reverse-transcribed with random primers using SuperScript III cDNA Synthesis Kit (Invitrogen). cDNA samples were diluted in nuclease-free water and stored at –80°C. RT-PCR reactions were performed on a QuantStudio5 system (ThermoFisher Scientific) with SYBR Green PCR Master Mix (Bioland). Transcript levels were calculated by the comparative cycle threshold method and normalized to cyclophilin A expression. All primers used in the experiments are listed in *SI Appendix*, Table SII.

Doxycycline (Dox)-inducible expression in SMCs. SMCs harboring Dox-inducible pTRIPZ expression vectors for human prelamin A, human progerin, non-farnesylated human progerin (progerin-SSIM), lamin B1, and non-farnesylated lamin B1 (lamin B1-SAIM) have been described previously (Kim et al., 2018b) (Kim et al., 2021). The same approach was used to generate SMCs expressing Dox-inducible constructs for LAP2β (*SI Appendix*, Table SIII). The expression plasmid was constructed by InFusion cloning (Takara Bio, Japan) of cDNAs into pTRIPZ. The mouse *Tmpo* cDNA was amplified from mouse cDNA with forward primer 5′-GTCAGATCGCACCGGATGCCGGAGTTCCTAGAGG-3′ and reverse primer 5′-CATGGTGGCGGGATCGTTGGATATTTTAGTATCTT-3′. All plasmids were verified by DNA sequencing. Packaging of lentivirus and transduction of cells were performed by UCLA's Vector Core. Transduced cells were selected with 3 μg/ml puromycin for two weeks; individual clones were isolated by limiting dilution in 96-well plates. Clones were screened by western blotting and immunofluorescence staining. A minimum of 2 clones were isolated for each cell line.

Constitutive expression of nuclear localized GFP, cGAS-mCherry, and lamins in SMCs. SMCs expressing green fluorescent protein (GFP) with a nuclear localization signal (nls-GFP) have been described previously (Kim et al., 2021). Constitutive expression of prelamin A and progerin in SMCs was performed by transducing SMCs with pCLNR (#17735; Addgene) expression plasmids. The prelamin A and progerin cDNAs were subcloned into *Hind*III and *Not*I sites of pCLNR by InFusion cloning. Human prelamin A was amplified with forward primer 5′-GCTAGCGAATTATGGAGACCCCGTCCCAGC-3′ and reverse primer 5′-GATCCTTGCGGCCTTACATGATGCTGCAGT-3′; human progerin was amplified with forward primer 5′-GCTAGCGAATTATGGAGACCCCGTCCCAGC-3′ and reverse primer 5′-CAGATCCTTGCGGCCTTACATGATGCTGCA-3′. cGAS-mCherry-Puro-pCDH (#132771; Addgene) was purchased from Addgene. All plasmids were verified by DNA sequencing. Packaging of lentivirus, retrovirus, and SMC transduction were performed by UCLA's Vector Core. Transduced cells were selected with 3 μg/ml blasticidin or puromycin for two weeks; individual clones were isolated by limiting dilution. A minimum of 2 clones were isolated for each cell line.

Measurement of nuclear membrane (NM) ruptures in live SMCs. SMCs stably expressing GFP in the nucleus were seeded into 2-well chamber slides with glass coverslip bottoms (ThermoFisher Scientific) and cultured in complete culture media. Mitomycin C (1 μg/ml) was added to the medium to trigger cell-cycle arrest. The inhibition of cell proliferation facilitated NM rupture quantification by eliminating mitotic cells. Doxycycline was added to induce nuclear lamin expression and incubated for 24 h before examination by microscopy. The cell culture chamber slide was mounted into a CO_2- and temperature-controlled stage on a Zeiss LSM800 confocal laser scanning microscope controlled by Zen Blue 2.3 software (all from Zeiss). The cells were visualized for 48 h at 37°C and 5% CO_2 with a Plan-Apochromat 20×/0.8 NA objective. Images

from randomly selected fields of view were captured every 1–2 min. The numbers of cells with a NM rupture, defined by the appearance of GFP in the cytoplasm, was divided by the total number of cells in a field.

Supplemental Figure 1.

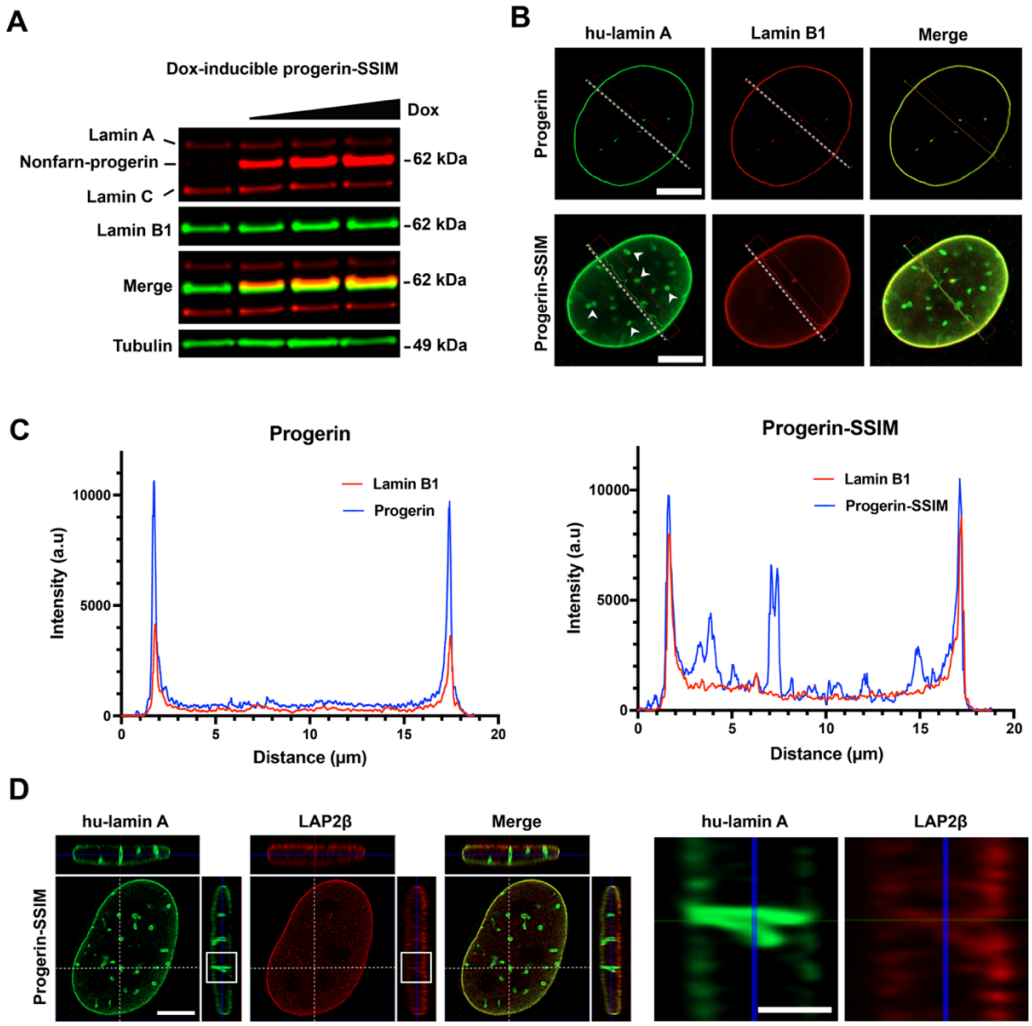

Supplemental Figure 1. Nonfarnesyl-progerin is expressed in the nucleoplasm and at the nuclear periphery. A. Western blot showing the doxycycline (Dox)-inducible expression of nonfarnesylated hu-progerin (hu-progerin-SSIM) in cultured SMCs. Tubulin was measured as a loading control. (The gel was cropped from a gel shown in Figure 1A.) B. Representative images of single microscopy sections through the middle of SMC nuclei stained with antibodies against hu-lamin A (green) and lamin B1 (red). Scale bar, 5 μm. Note hu-progerin-SSIM staining in the nucleoplasm (white arrowheads). The dotted lines mark the locations of the fluorescence intensity profiles reported in panel C. C. The relative fluorescence intensity profiles for antibodies against hu-lamin A (blue) and lamin B1 (red) in SMCs expressing hu-progerin (left) and hu-progerin-SSIM (right). D. Orthogonal views of a progerin-SSIM nucleus stained with antibodies against hu-lamin A (green) and LAP2β (red). Scale bar, 5 μm. Boxed regions are shown at higher magnification to the right. Scale bar, 2 μm.

Supplemental Figure 2.

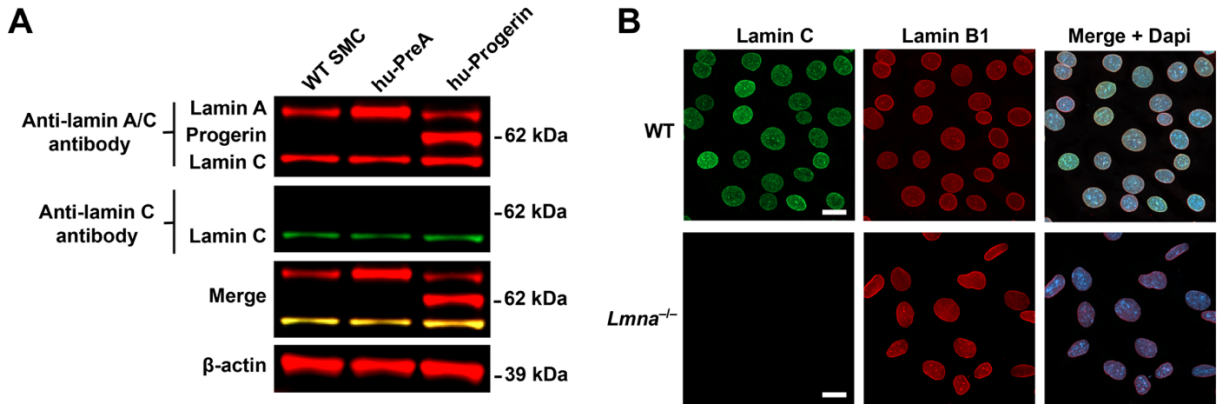

Supplemental Figure 2. The antibody used to detect lamin C is specific. A. Western blot demonstrating the specificity of the anti-lamin C antibody. Extracts from non-transduced wild-type SMCs (WT SMC), and SMCs expressing hu-prelamin A (hu-PreA) or hu-progerin were fractionated by SDS-PAGE and membranes blotted with antibodies against anti-lamin A/C (red) and anti-lamin C (green). The individual and merged images are shown. β-actin was measured as a loading control. B. Immunofluorescence study showing the absence of lamin C antibody binding in *Lmna*$^{-/-}$ SMCs. Wild-type (WT) and *Lmna*$^{-/-}$ SMCs were stained with antibodies against lamin C (green) and lamin B1 (red). DNA was stained with Dapi (blue). Scale bar, 20 μm.

Supplemental Figure 3.

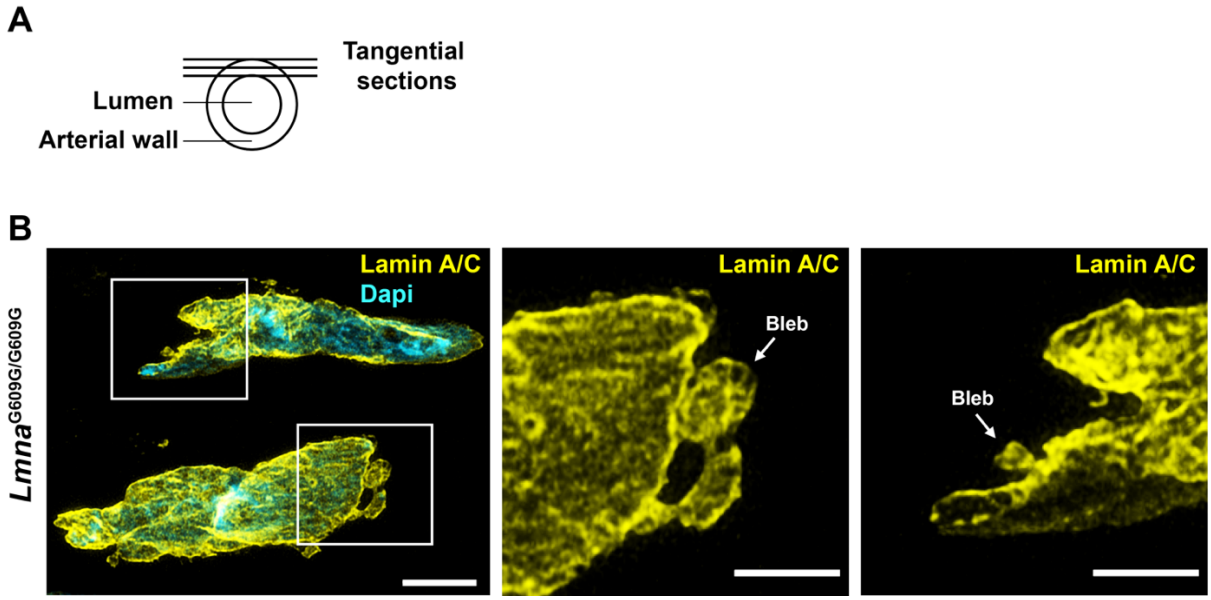

Supplemental Figure 3. Detection of nuclear blebs in *Lmna*$^{G609G/G609G}$ aortic SMCs. A. Picture showing the orientation of the tissue sections collected from mouse aortas to examine SMC nuclei by immunohistochemistry. B. Confocal fluorescence microscopy images of aortic SMCs from a 10-week–old *Lmna*$^{G609G/G609G}$ mouse stained with antibodies against lamin A/C (yellow). DNA was stained with Dapi (blue). Scale bar, 5 µm. Arrows point to nuclear membrane blebs in two different SMCs. The boxed regions are shown at higher magnification to the right. Scale bar, 2.5 µm.

Supplemental Figure 4.

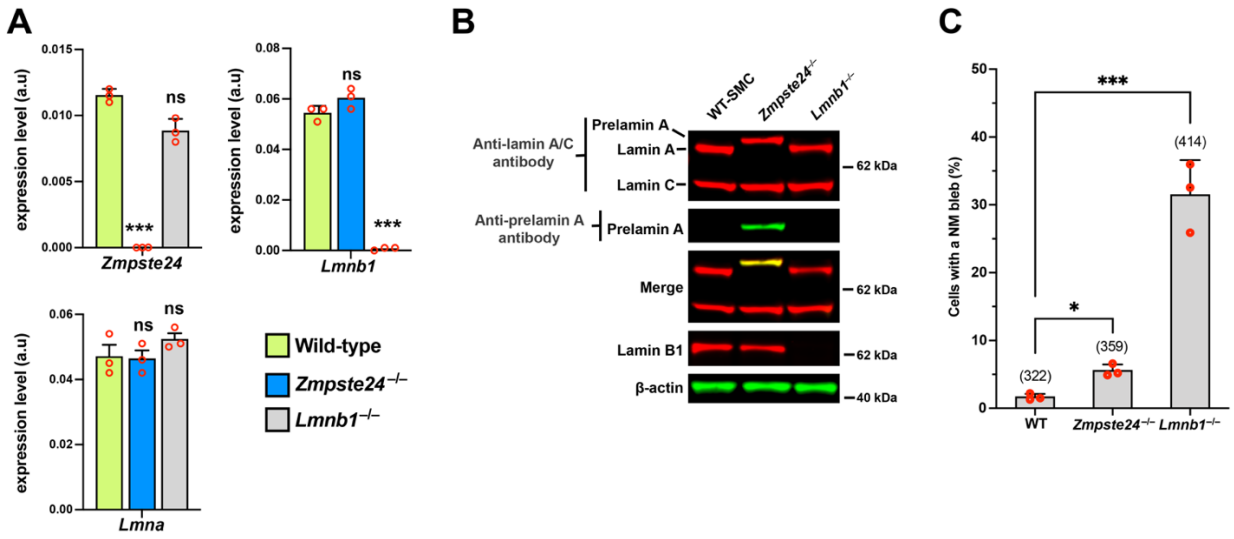

Supplemental Figure 4. Characterization of *Zmpste24*$^{-/-}$ and *Lmnb1*$^{-/-}$ SMCs. A. Bar graph comparing the expression of *Zmpste24*, *Lmnb1*, and *Lmna* in wild-type (green), *Zmpste24*$^{-/-}$ (blue), and *Lmnb1*$^{-/-}$ (grey) SMCs by quantitative RT-PCR. Gene expression was normalized to *Ppia.* Mean ± SEM *(n* = 3 experiments). One-way ANOVA showing comparisons made to wild-type SMCs. ***, P < 0.001; ns, not significant. B. Western blot comparing the expression of lamin A, lamin C, lamin B1, and prelamin A in wild-type (WT), *Zmpste24*$^{-/-}$, and *Lmnb1*$^{-/-}$ SMCs. Prelamin A was detected with an anti-prelamin A antibody (clone 3C8). β-actin was measured as an internal control. The individual channels and merged image are shown. C. Bar graph showing the fraction of cells with a NM bleb identified by immunocytochemistry in WT, *Zmpste24*$^{-/-}$, and *Lmnb1*$^{-/-}$ SMCs. The numbers of cells examined are shown in parentheses from three independent experiments (circles). Mean ± SEM. One-way ANOVA showing comparisons made to WT SMCs. *, P < 0.05; ***, P < 0.001.

Supplemental Figure 5.

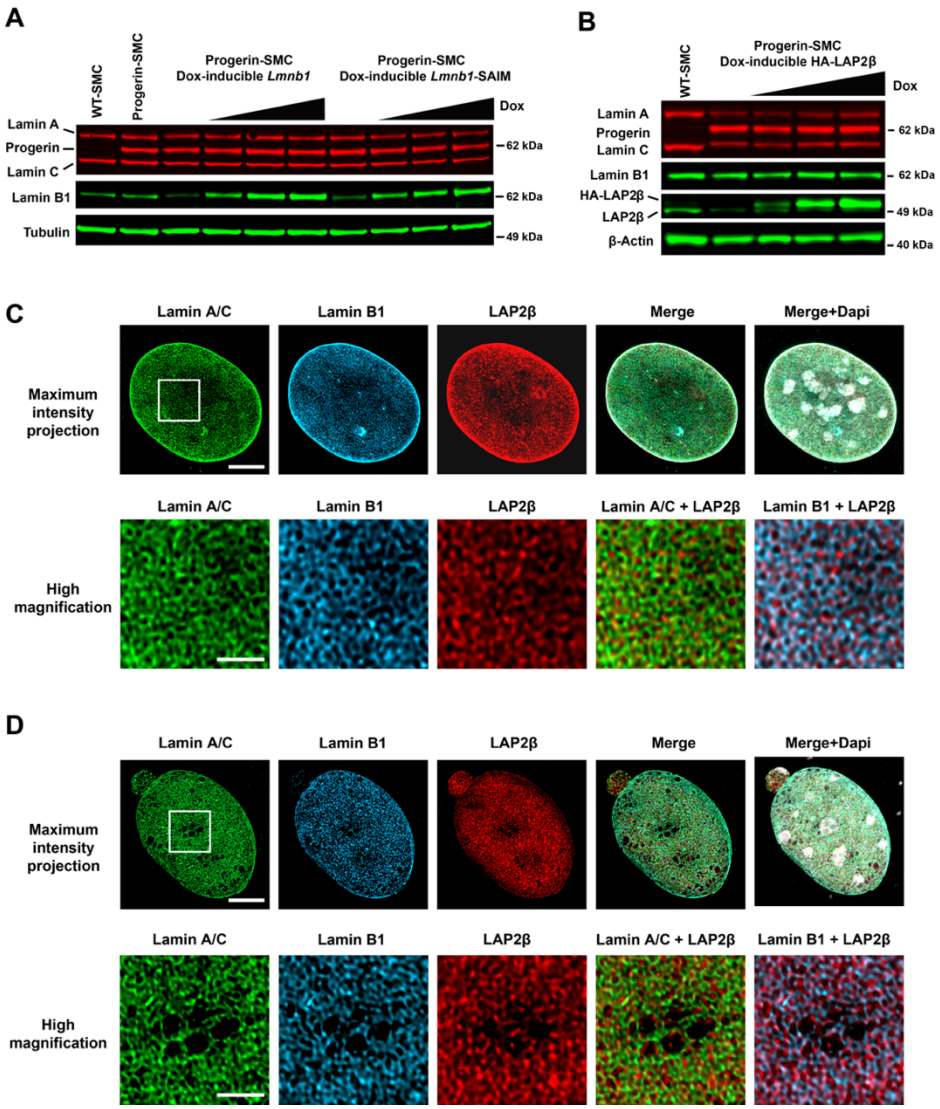

Supplemental Figure 5. Inducible expression of lamin B1, nonfarnesyl-lamin B1, and HA-tagged LAP2β in progerin-SMCs. A. Western blot comparing the expression of lamin A, progerin, lamin C, and lamin B1 in wild-type SMCs (WT-SMC), progerin-SMCs, and progerin-SMCs expressing Dox-inducible constructs for lamin B1 and nonfarnesyl-lamin B1 (*Lmnb1*-SAIM). Tubulin was measured as an internal control. B. Western blot comparing the expression of lamin A, progerin, lamin C, lamin B1, and LAP2β in WT-SMCs, and progerin-SMCs expressing a Dox-inducible construct for HA-tagged LAP2β (HA-LAP2β). Actin was measured as an internal control. Note the slower migration of HA-LAP2β as compared to endogenous LAP2β. C–D. Confocal fluorescence microscopy images of WT-SMCs (C) and progerin-SMCs (D) stained with antibodies against lamin A/C (green), lamin B1 (blue), and LAP2β (red). DNA was stained with Dapi (white). Scale bar, 5 μm. High magnification images of the boxed regions are shown below. Scale bar, 2 μm.

Table S1. Antibodies used for western blotting and immunocytochemistry.

Antibody Description	Species	Source	Catalog #	Use	Dilution
β-actin	Goat	Santa Cruz Biotech	SC1616	WB, IF	1:3000
β-actin	Mouse	Santa Cruz Biotech	SC47778	WB	1:3000
cGAS	Rabbit	Cell Signal	31659S	IF	1:1000
Human lamin A	Mouse	Millipore	MAB3211	WB, IF	1:1500
Human lamin A/C	Rabbit	Abcam	Ab108595	WB, IF	1:1000
Human lamin A/C-Alexa 488 conjugated	Rabbit	Abcam	Ab185014	IF	1:1000
Human lamin A/C-Alexa 594 conjugated	Rabbit	Abcam	Ab215324	IF	1:1000
Lamin B1	Goat	Santa Cruz Biotech	SC6217	WB, IF	1:1500
Lamin C	Rabbit	Pro Sci	71-055	WB, IF	1:1000
LAP2β	Mouse	BD Pharmingen	611000	IF	1:2000
Prelamin A	Rat	In-house	clone 3C8	WB	1:1000
Tubulin	Rat	Novus Bio	NB600-506	WB	1:3000
Anti-rabbit IR800	Donkey	LI-COR	926-32213	WB	1:10000
Anti-goat IR800	Donkey	LI-COR	926-32214	WB	1:10000
Anti-rat IR800	Donkey	ThermoFisher	SA5-10032	WB	1:5000
Anti-mouse IR800	Donkey	ThermoFisher	SA5-10172	WB	1:5000
Anti-rabbit IR680	Donkey	LI-COR	926-32221	WB	1:5000
Anti-rat IR680	Goat	LI-COR	925-68076	WB	1:5000
Anti-goat IR680	Donkey	LI-COR	926-68074	WB	1:5000
Anti-mouse IR680	Donkey	ThermoFisher	SA5-10170	WB	1:5000
Anti-mouse Alexa 488	Donkey	Invitrogen	A21202	IF	1:2000
Anti-rabbit Alexa 488	Donkey	Invitrogen	A21206	IF	1:2000
Anti-goat Alexa 488	Donkey	Invitrogen	A11055	IF	1:2000
Anti-goat Alexa 555	Donkey	Invitrogen	A21432	IF	1:2000
Anti-rabbit Alexa 555	Donkey	Invitrogen	A31572	IF	1:200

Anti-rabbit Alexa 568	Donkey	Invitrogen	A10042	IF	1:2000
Anti-mouse Alexa 568	Donkey	Invitrogen	A10037	IF	1:2000
Anti-mouse Alexa 647	Donkey	Invitrogen	A31571	IF	1:2000
Anti-rabbit Alexa 647	Donkey	Invitrogen	A31573	IF	1:2000
Anti-goat Alexa 647	Donkey	Invitrogen	A21447	IF	1:2000
Anti-mouse Alexa 647 Plus	Donkey	Invitrogen	A32787	IF	1:2000
Anti-rabbit Alexa 647 Plus	Donkey	Invitrogen	A32795	IF	1:2000
Anti-rat Alexa 650	Donkey	ThermoFisher	SA5-10029	IF	1:200
Anti-rabbit Alexa 680	Donkey	Invitrogen	A21109	IF	1:1000

Table S2. Quantitative RT-PCR primers.

Gene or transcript	**Forward (5′–3′)**	**Reverse (5′–3′)**
Ppia	TGAGCACTGGAGAGAAAGGA	CCATTATGGCGTGTAAAGTCA
Lmna	CCTATCGAAAGCTGCTGGAG	CCTGAGACTGGGATGAGTGG
Lmnb1	CAACTGACCTCATCTGGAAGAAC	TGAAGACTGTGCTTCTCTGAGC
Zmpste24	CCTCTGTTTGACAAATTCACACC	AACGCTTAGATCCTTCAACAACA

Table S3. Description of cell lines.

Cell line	Modification	Source	Validation method	Mycoplasma contamination
hu-prelamin A-SMC	human (hu)-prelamin A-pTRIPZ	In-house	Western blotting	No
hu-progerin-SMC	hu-progerin-pTRIPZ	In-house	Western blotting	No
hu-progerin-SMC-SSIM	hu-progerin-SSIM-pTRIPZ	In-house	Western blotting	No
Lmna$^{-/-}$-SMC	CRISPR/Cas9 deletion of *Lmna*	In-house	Western blotting and qPCR	No
hu-prelamin A-SMC + nls-GFP	hu-prelamin A-pTRIPZ + nls-GFP-pCLNR	In-house	Microscopy	No
hu-progerin-SMC + nls-GFP	hu-progerin-pTRIPZ + nls-GFP-pCLNR	In-house	Microscopy	No
hu-progerin-SMC + nls-GFP + cGAS-mCherry	hu-progerin-pTRIPZ + nls-GFP-pCLNR + *cGAS-mCherry-pCDH*	In-house	Microscopy	No
Zmpste24$^{-/-}$-SMC	CRISPR/Cas9 deletion of *Zmpste24*	In-house	Western blotting and qPCR	No
Lmnb1$^{-/-}$-SMC	CRISPR/Cas9 deletion of *Lmnb1*	In-house	Western blotting and qPCR	No
Zmpste24$^{-/-}$-SMC + nls-GFP	*Zmpste24*$^{-/-}$ + nls-GFP-pCLNR	In-house	Microscopy	No
Lmnb1$^{-/-}$-SMC + nls-GFP	*Lmnb1*$^{-/-}$ + nls-GFP-pCLNR	In-house	Microscopy	No
Lamin B1-SMC	hu-progerin-pCLNR + *Lmnb1*-pTRIPZ	In-house	Western blotting	No
Lamin B1-SMC-SIAM	hu-progerin-pCLNR + *Lmnb1*-SAIM-pTRIPZ	In-house	Western blotting	No
HA-LAP2β-SMC	hu-progerin-pCLNR + HA-*Tmpo*-pTRIPZ	In-house	Western blotting	No

Chapter 5:

Conclusion

The goal of this study was to investigate the underlying mechanisms of vascular smooth muscle cell loss in HGPS by studying an HGPS mouse model and an *in vitro* doxycycline-inducible cell system. I discovered several properties of progerin and aortic wall conditions that contribute to SMC loss in large arteries as outlined in Chapter 2, 3, and 4. These findings are organized into a diagram which depicts our current view on the mechanisms contributing to vascular SMC loss in HGPS (Figure 5.1).

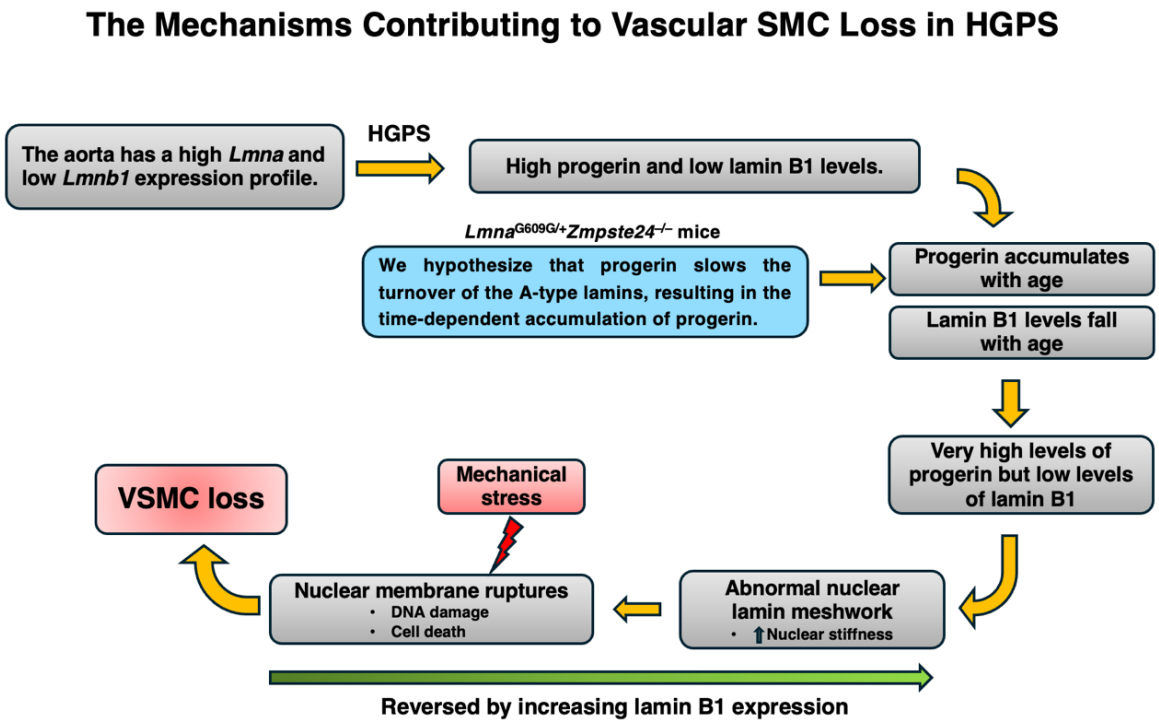

Figure 5.1. Our current view on the mechanisms contributing to vascular smooth muscle cell loss in HGPS.

In Chapter 2, I identified a unique lamin expression profile in the aorta compared to other tissues. Various tissues were harvested from wild-type mice, and quantitative western blotting was performed with lamin A/C, lamin B1, and tubulin antibodies. Upon quantifying the lamin A to lamin B1 ratio, the aorta had an ~10-fold higher ratio compared to the kidney. In the setting of HGPS, this results in high progerin and low lamin B1 expression in the aorta. In Chapter 3, we

compared young and old progeria mice and showed that progerin accumulated with age, whereas lamin B1 protein levels fell with age. This ultimately resulted in very high levels of progerin but low levels of lamin B1.

Our quantitative western blotting studies of mouse tissues revealed why the aorta was most severely affected in progeria mice; it exhibited the highest progerin to lamin B1 ratio among all the tissues we tested. This finding led us to the next question: "Why are vascular smooth muscle cells affected but not endothelial cells or adventitial cells?" Consequently, we became curious about potential differences across the various layers of the aorta. To explore this, we performed immunohistochemical staining of aorta sections using an antibody against lamin B1. Notably, the staining intensity of lamin B1 varied significantly across different layers of the aorta. The endothelial and adventitia layers exhibited much brighter lamin B1 staining compared to the medial layer. This expression pattern suggested that lamin B1 may play distinct roles in these vascular regions. The elevated levels of lamin B1 in the endothelial layer, which lines the interior surface of blood vessels, could be related to its role in maintaining nuclear structure and regulating gene expression in endothelial cells, which are critical for vascular function and integrity. Similarly, the strong lamin B1 staining in the adventitia, the outermost layer of the aorta composed mainly of connective tissue, might reflect its involvement in structural support and cellular organization. In contrast, the medial layer, predominantly composed of smooth muscle cells, showed relatively lower lamin B1 expression, indicating possible differences in nuclear architecture or cellular requirements for this protein in the contractile functions of these cells. These findings open new avenues for exploring the specific functions of lamin B1 in vascular biology and its implications in vascular diseases.

We were particularly interested in understanding the impact of high progerin and low lamin B1 expression profiles on the nuclear lamina of smooth muscle cells. Our investigation revealed that approximately 25% of SMCs expressing progerin developed an abnormal nuclear meshwork characterized by clusters of large gaps. This structural aberration contrasts sharply with the more regular meshwork observed in SMCs expressing prelamin A, where gap openings within the meshwork were consistently sized around $0.1\mu m^2$. These observations led us to hypothesize that the structural defects induced by progerin in the nuclear lamina meshwork may have deleterious effects on cellular health. Furthermore, we found that the presence of progerin not only disrupts the meshwork but also alters the organization of other key nuclear lamins, such as lamin B1, and nuclear envelope proteins, including LAP2β. The disruption of these proteins suggests that progerin exerts a dominant-negative effect, compromising the integrity and function of the nuclear lamina and nuclear envelope. This finding is significant as it highlights the extensive impact of progerin on nuclear architecture, potentially contributing to cellular dysfunction and disease pathology.

To further investigate the downstream effects of an abnormal nuclear meshwork on cellular health, we conducted a detailed examination of various phenotypes and properties of progerin, as documented in Chapters 3 and 4. Our research uncovered that the expression of progerin significantly increased nuclear stiffness. This increase in stiffness was quantitatively measured using techniques such as Atomic Force Microscopy (AFM) and the "coverslip assay," both of which confirmed the substantial rigidity imparted by progerin. Conversely, lamin B1 exhibited an opposite effect; its presence rendered the nucleus more pliable and softer, indicating a fundamental difference in how these proteins influence nuclear mechanics. Moreover, the expression of progerin was correlated with a notable increase in NM ruptures. These ruptures likely result from

decreased nuclear integrity and occurred with greater frequency in progerin-expressing cells. The consequence of these nuclear membrane ruptures was profound, leading to significant DNA damage and ultimately resulting in cell death. This finding was further corroborated *in vivo*. In *Lmna*^{G609G} mice with a Nuc-Tomato reporter, we observed that NM ruptures occurred specifically in vascular SMCs and not in endothelial cells. This *in vivo* evidence strengthens our understanding of the detrimental effects of progerin on nuclear integrity, particularly within the vascular SMCs.

The aorta is subjected to various mechanical forces, including wall shear stress, blood pressure, and matrix-driven stress, which means that vascular SMCs are constantly under mechanical stress. To investigate the effects of this stress, we used a custom-built cell stretching device. Our findings revealed that SMCs expressing progerin were significantly more susceptible to mechanical stress, leading to a higher incidence of NM ruptures, DNA damage, and cell death. In contrast, SMCs expressing prelamin A did not exhibit increased susceptibility to mechanical stress, regardless whether stretching was applied or not. To further validate our hypothesis, we utilized KASH2-EGFP, a construct capable of disrupting the LINC complex, thereby eliminating the transmission of extracellular forces to the nucleus. Both *in vitro* and *in vivo* models confirmed that this intervention effectively rescued nuclear membrane ruptures and reduced cell death in progerin-expressing cells. This finding supports our hypothesis that mechanical stress exacerbates the detrimental effects of progerin on nuclear integrity and highlights the potential of targeting the LINC complex to mitigate these effects.

Lastly, there is an intriguing puzzle in the field of lamin research: the absence of vascular disease in *Zmpste24*$^{-/-}$ mice. Both farnesyl–prelamin A and progerin terminate with a farnesylcysteine methyl ester group and exhibit similar toxicities, as verified in cell culture studies. *Zmpste24* KO mice develop phenotypes akin to those observed in progeria mice, including brittle

bones, growth failure, and shortened lifespan. Despite these similarities, a notable distinction remains: the absence of HGPS vascular disease in *Zmpste24*$^{-/-}$ mice. We proposed that studying both *Zmpste24*$^{-/-}$ and *Lmna*^{G609G} progeria mice could uncover unique properties of progerin and the 50-amino acid deleted segment that contribute to vascular disease. At the early age of five weeks, both progerin and farnesylated prelamin A are expressed at similar levels in the aortas of these mice. However, as previously mentioned, progerin accumulates with age. Moreover, not only does progerin accumulate, but it also causes the accumulation of other A-type lamins, such as lamin A and lamin C. However, the level of farnesylated prelamin A, lamin A, and lamin C did not change with age in *Zmpste24*$^{-/-}$ mouse aortas.

We hypothesize that the lack of vascular disease in *Zmpste24*$^{-/-}$ mice is due to the non-accumulation of farnesylated prelamin A, preventing it from reaching a threshold level necessary to induce vascular pathology. The mechanisms underlying progerin's unique ability to accumulate remain unclear. We suspect that the absence of phosphorylation sites within the missing 50 amino acid sequence of progerin or the involvement of protein kinase Akt/PKB may be responsible. Further research is needed to elucidate these mechanisms and fully understand the distinct effects of progerin on the accumulation of A-type lamins.

In conclusion, we identified several unique properties of progerin and its effects on the aorta that elucidate the mechanisms contributing to vascular smooth muscle cell loss in Hutchinson-Gilford progeria syndrome. Our studies highlighted potential therapeutic targets for further investigation. Notably, we discovered the crucial role and properties of lamin B1, which could rescue the abnormal meshwork, nuclear membrane ruptures, DNA damage, abnormal nuclear morphology, nuclear stiffness, and cell death induced by progerin. Moving forward, our research will focus on a newly created transgenic mouse model that expresses lamin B1

specifically in smooth muscle cells. This model will enable us to explore the therapeutic potential of lamin B1 in greater detail and develop new strategies to mitigate the vascular complications associated with Hutchinson-Gilford progeria syndrome.